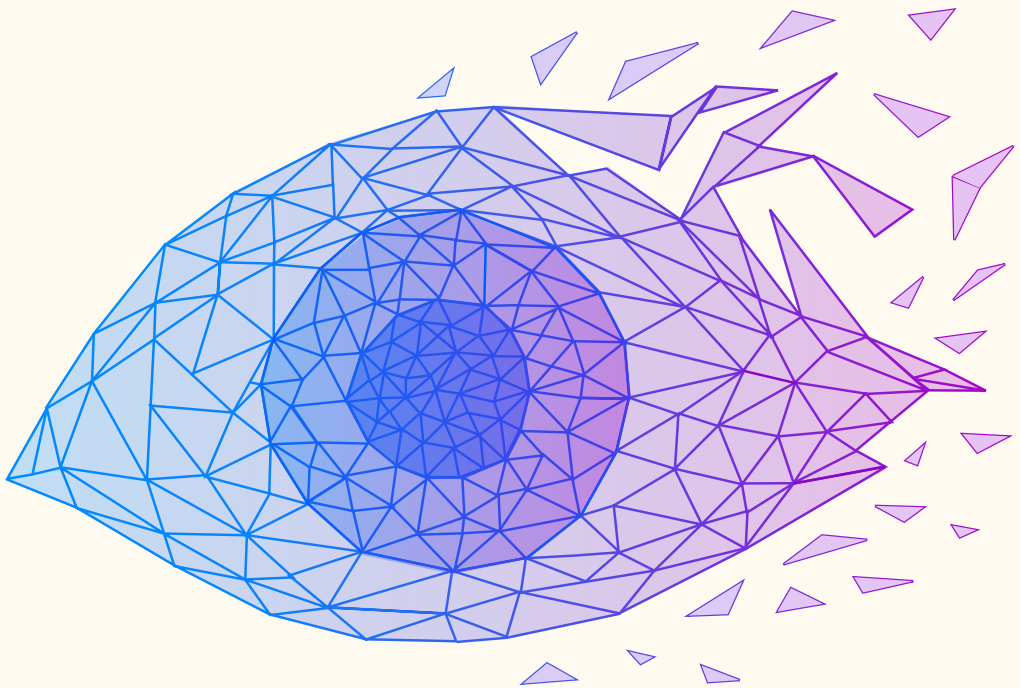


IMAGE-BASED OCULAR PROTON THERAPY

MRI in treatment planning and evaluation



Lisa Klaassen

Image-based ocular proton therapy
MRI in treatment planning and evaluation

1. MRI van het oog is nauwkeuriger dan conventionele oogheelkundige modaliteiten om tumoromvang te bepalen, met name bij anterieur gelegen tumoren. (dit proefschrift)
2. Polynome tumormodellen zijn in theorie in staat om een oogmelanoom volledig te beschrijven, maar de echte uitdaging ligt in het juist positioneren van de tumorbasis in de conventionele planningssystemen voor protonentherapie. (dit proefschrift)
3. Ellipsoïde tumormodellen van het oogmelanoom geven geen goede weergave van tumorvolume en zouden niet gebruikt moeten worden voor prognose, omdat ze geen informatie toevoegen aan de veelgebruikte AJCC-classificatie. (dit proefschrift)
4. Farmacokinetische analyse van perfusiegewogen MRI heeft voor het beoordelen van therapierespons geen toegevoegde waarde boven de semi-kwantitatieve analyse die in de kliniek gebruikt wordt. (dit proefschrift)
5. De systematische overschatting van de tumor, ontstaan door bij meerdere modaliteiten altijd de veiligste optie te kiezen, heeft een vergelijkbaar effect op het bestraalde gebied als de reguliere marge.
6. Voor een behandeling waarbij we mensen op 0.2 mm nauwkeurig positioneren, is het onbegrijpelijk dat we zo weinig verificatie hebben over de geometrie van het oog en de locatie van organen at risk.
7. Uitkomsten van radiotherapie van oogmelanomen zouden per centrum gerapporteerd moeten worden en niet alleen per behandelmethode.
8. Gezien de zeldzaamheid van het oogmelanoom is samenwerking tussen protonencentra die oogtumoren behandelen essentieel. De MDR helpt hier, in zijn huidige vorm, niet bij.
9. Het uitstellen van congresdeadlines is een belediging voor de mensen die hun werk wel op tijd hebben ingediend.
10. Zorgen voor mensen zonder om te kijken naar het klimaat en dieren is zowel inconsistent als ineffectief. Daarom zou in ziekenhuizen plantaardig eten de standaard moeten zijn.

Image-based ocular proton therapy

MRI for treatment planning and evaluation

Lisa Klaassen

Image-based ocular proton therapy: MRI in treatment planning and evaluation

Thesis, Leiden University, the Netherlands

© Lisa Klaassen, 2025

Cover design: Lisa Klaassen

Layout: Arul Raja | www.ridderprint.nl

Printing: Ridderprint

The work in this thesis was financially supported by:

Varian, a Siemens Healthineers Company, through a Varian-HollandPTC Consortium grant (project number 2020016)

Landelijke Stichting voor Blinden en Slechtzienden, Algemene Nederlandse Vereniging Ter Voorkoming van Blindheid and Oogfonds, who contributed through UitZicht.

Financial support for the printing of this thesis was kindly provided by:

Stichting Leids Oogheelkundig Ondersteuningsfonds

No part of this thesis may be reproduced or transmitted in any form without prior written permission from the author.

Image-based ocular proton therapy
MRI in treatment planning and evaluation

Proefschrift

ter verkrijging van

de graad van doctor aan de Universiteit Leiden,

op gezag van rector magnificus prof.dr. S. de Rijcke,

volgens besluit van het college voor promoties

te verdedigen op donderdag 23 april 2026

klokke 10:00 uur

door

Lisa Klaassen

geboren te Almelo

in 1996

Promotoren

Dr. J.W.M. Beenakker

Prof. dr. G.P.M. Luyten

Prof. dr. C.R.N. Rasch

Promotiecommissie

Prof. dr. R. Kalmann

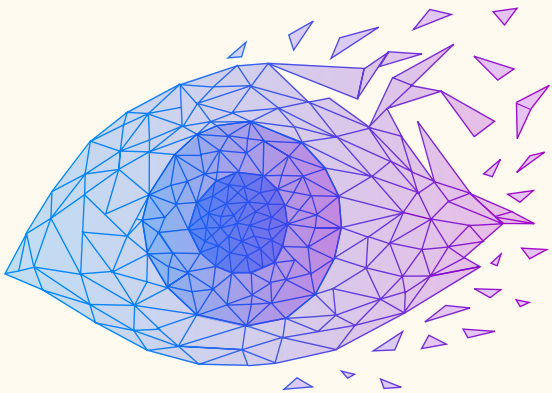
Prof. dr. C.L. Creutzberg

Prof. dr. M.S. Hoogeman (HollandPTC/Erasmus Medical Center)

Dr. J. Hrbacek (Paul Scherrer Institute)

INHOUDSOPGAVE

Nederlandse samenvatting		7
English summary		11
Chapter 1	Introduction	15
Chapter 2	Magnetic Resonance Imaging in the Clinical Care for Uveal Melanoma Patients: A Systematic Review from an Ophthalmic Perspective	39
Chapter 3	Geometrical accuracy of magnetic resonance imaging for ocular proton therapy planning	71
Chapter 4	Automatic three-dimensional magnetic resonance-based measurements of tumour prominence and basal diameter for treatment planning of uveal melanoma	99
Chapter 5	Comparing model-based and delineation-based target volume definition for ocular proton beam therapy planning	133
Chapter 6	Estimating uveal melanoma volume with ellipsoid tumour models	159
Chapter 7	Quantitative Perfusion-Weighted Magnetic Resonance Imaging in Uveal Melanoma	177
Chapter 8	Reproducibility of perfusion-weighted and diffusion-weighted MRI in uveal melanoma	203
Chapter 9	Discussion	219
Appendix		
	Portfolio	240
	List of publications	246
	Dankwoord	247
	Curriculum vitae	249



Nederlandse samenvatting

NEDERLANDSE SAMENVATTING

Het oogmelanoom is een zeldzame vorm van kanker. Elk jaar krijgen ongeveer 200 tot 250 mensen in Nederland deze ziekte. Het oogmelanoom kan behandeld worden met bestraling of door het oog te verwijderen. Voor grotere tumoren, of tumoren die dicht bij de oogzenuw liggen, is bestraling met protonen de beste behandeling. Deze bestraling maakt de tumor onschadelijk, maar zorgt er vaak voor dat mensen minder goed gaan zien. Ook is er nu nog een operatie nodig om metalen clips op het oog te plaatsen voordat de bestraling kan beginnen.

De onderzoeken in dit proefschrift maken deel uit van een groter project. Dat project heeft als doel om in de toekomst nauwkeuriger te bestralen, en dat te doen zonder de metalen clips. De onderzoeken gaan vooral over hoe MRI-scans van het oog kunnen helpen bij het maken van het bestralingsplan en bij het beoordelen van het resultaat van de behandeling.

In hoofdstuk 2 geef ik een overzicht van de rol van MRI bij verschillende delen in het proces: bij het stellen van de diagnose, het maken van het bestralingsplan en achteraf om te zien of de behandeling heeft gewerkt.

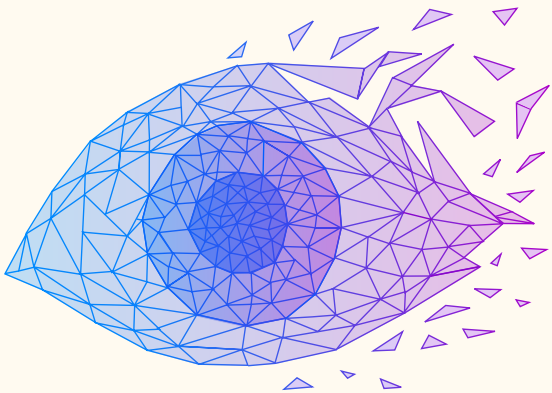
In hoofdstuk 3 heb ik onderzocht of de MRI-scans die we gebruiken geschikt zijn voor het maken van een bestralingsplan. We ontdekten dat de MRI-scans van het oog niet vervormd zijn en dus goed gebruikt kunnen worden.

Hoofdstukken 4 en 5 vergelijken MRI met de huidige methodes. In hoofdstuk 4 kijken we naar de metingen van de dikte en diameter van de tumor. Hiervoor ontwikkelden we eerst een automatische methode om de dikte en diameter te bepalen. We zagen dat de verschillen tussen MRI en echo meestal klein zijn, maar dat MRI nauwkeuriger is voor tumoren die aan de voorkant van het oog liggen. In hoofdstuk 5 vergelijken we tumormodellen, die gebruikt worden bij het maken van het bestralingsplan, met een 3D-intekening van de tumor. Hierbij kwamen we erachter dat de huidige tumormodellen weliswaar zorgen dat we de hele tumor bestralen, maar dat ze ook een overschatting geven van de daadwerkelijke tumor.

Hoofdstuk 6 gaat over een ander type tumormodel dat door andere onderzoekers wordt gebruikt om het volume van een tumor te berekenen. Hier laten we zien dat dit model het werkelijke tumorvolume overschat, en dat er ook grote verschillen tussen verschillende patiënten zijn. Daarom is het niet verstandig is om dit type tumormodel voor individuen te gebruiken.

Hoofdstukken 7 en 8 gaan over het beoordelen van de effecten van de behandeling. In hoofdstuk 7 tonen we aan dat een kwantitatieve analyse van perfusiegewogen MRI (een manier om bloedtoevoer en -afvoer te bekijken) veranderingen na bestraling aan kan tonen. Toch blijkt dat een eenvoudigere methode die nu in de kliniek wordt gebruikt meestal voldoende is. In hoofdstuk 8 laten we zien dat de klinisch gebruikte analyse van de perfusiegewogen MRI een reproduceerbare methode is. Dat geldt ook voor diffusiegewogen MRI van het oog, een methode die de beweging van moleculen in het weefsel laat zien.

In hoofdstuk 9, de discussie, beschrijf ik de verschillen tussen de huidige werkwijze en een nieuwe werkwijze. In deze nieuwe werkwijze zouden we beeldgestuurde bestralingsplannen maken, zonder het gebruik van de metalen clips. Deze werkwijze duurt in totaal korter, en heeft minder onzekerheden dan de huidige workflow. Daardoor weten we met de nieuwe werkwijze, met MRI, waarschijnlijk beter waar de tumor is in het oog. Maar zonder clips is het wel lastiger om zeker te weten waar het oog naartoe kijkt. In dit hoofdstuk beschrijf ik de stappen die we nog nodig hebben om deze werkwijze te gaan toepassen.



English summary

ENGLISH SUMMARY

Uveal melanoma is a rare form of cancer of the eye. Each year, about 200 to 250 people in the Netherlands are diagnosed with this disease. Treatment usually consists of radiation therapy or removal of the affected eye. For larger tumours, or those located close to the optic nerve, proton therapy is the treatment of choice. This technique effectively treats the tumour, but often results in loss of vision. In addition, a surgery is currently required to place tantalum clips on the eye before the radiation treatment can begin.

The studies presented in this thesis are part of a larger project aimed at improving the accuracy of proton therapy for ocular tumours and enabling treatment without the need for metal clips. Specifically, the research focuses on the role of ocular MRI in both treatment planning and treatment evaluation.

Chapter 2 provides an overview of the potential roles of MRI in several stages, such as diagnosis, radiotherapy planning, and post-treatment evaluation.

In Chapter 3, we investigated whether the MRI scans used in our centre are suitable for treatment planning. We found that the ocular MRI images are geometrically accurate and can therefore be reliably used for this purpose.

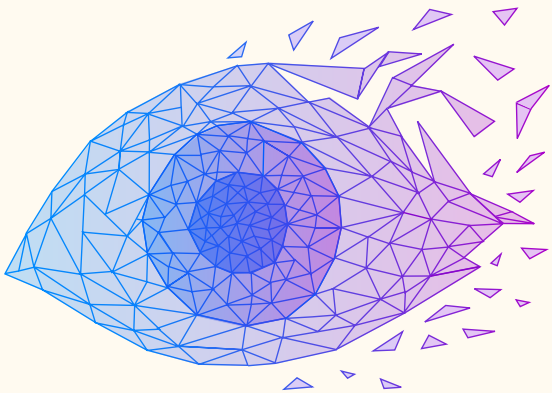
Chapters 4 and 5 compare MRI with conventional clinical methods. In Chapter 4, we developed an automatic method to measure tumour thickness and diameter and compared these measurements between MRI and ultrasound. Differences between the two modalities were generally small, but MRI proved to be more accurate for tumours located at the front of the eye.

In Chapter 5, we compared tumour models, which are commonly used in treatment planning, with three-dimensional tumour delineations based on MRI. We found that while current models ensure adequate tumour coverage, they also tend to overestimate the actual tumour size.

Chapter 6 focuses on ellipsoid tumour models, which are used in the literature to estimate tumour volume. We show that this model systematically overestimates the true tumour volume and that there is large variability between patients. Therefore, this type of model is not suitable for individual use.

Chapters 7 and 8 deal with evaluating the effects of radiation therapy. In Chapter 7, we demonstrate that quantitative analysis of perfusion-weighted MRI can detect post-radiation changes in the tumour. However, we also show that a simpler analysis method, which is currently used in clinical practice, is generally sufficient. In Chapter 8, we confirm that this simpler perfusion analysis is reproducible, and the same holds true for diffusion-weighted MRI, which measures the microscopic movement of molecules within tissue.

Finally, in Chapter 9, the discussion, I describe the differences between the current clinical workflow and a proposed new workflow. In the new approach, treatment planning would be based directly on MRI images, without using metal clips. This image-based workflow is faster and introduces fewer uncertainties, which likely improves the accuracy of tumour localization within the eye. However, without clips, determining the exact direction of gaze remains a challenge. This chapter outlines the additional steps required before such an MRI-based workflow can be implemented in clinical practice.



Chapter 1

Introduction

UVEAL MELANOMA

Uveal melanoma is an ocular malignancy that arises from melanocytes in the uveal tract, consisting of the choroid, ciliary body and iris (Figure 1). Although it is the most frequently occurring primary ocular malignancy in adults, it is a rare disease with an incidence from 2 to 10 per million per year, varying per region [1-3]. In the Netherlands, between 200 and 250 patients are affected each year [4]. The disease affects both men and women equally and most patients are approximately 50 to 70 years old at diagnosis. Risks factors include a fair skin colour, many skin naevi, light iris colour, congenital ocular melanocytosis and having family members with cutaneous or uveal melanoma [5, 6].

Patients often present with complaints such as blurred or distorted vision, light flashes, visual field loss or photopsia [2]. However, about 30% of patients do not experience any symptoms and are referred after routine examinations [7]. The nature and amount of symptoms depend on tumour size and location. Furthermore, symptoms may also be caused by accompanying exudative retinal detachment, which occurs more frequently in larger uveal melanoma [8].

Patients are diagnosed by an ophthalmologist specialized in ocular oncology, most often based on clinical examination of the lesion with indirect fundus ophthalmoscopy, supported by several ophthalmological and radiological imaging modalities [9, 10]. In some cases, histopathological confirmation of the diagnosis is necessary. More details about the different imaging modalities used in the clinical care for uveal melanoma patients are described in chapter 1.2.

Several treatment options of the primary tumour exist. Eye-sparing treatment modalities include plaque brachytherapy and external beam radiation therapy with protons or photons. Furthermore, enucleation (surgical removal of the eye) may still be the treatment of choice for very large uveal melanomas. High local control is achieved with all aforementioned treatment modalities [11, 12], although complication rates differ. Treatment options are further described in chapter 1.3.

Despite the high local control, disease-related death is high with about half of uveal melanoma patients succumbing to metastatic disease in 15 years [13]. The most common sites of metastases are liver and lungs [14]. Metastatic risk is related to tumour size [15] and several cytogenetic features such as monosomy of chromosome 3 and alterations in the BAP1 gene [2, 12].

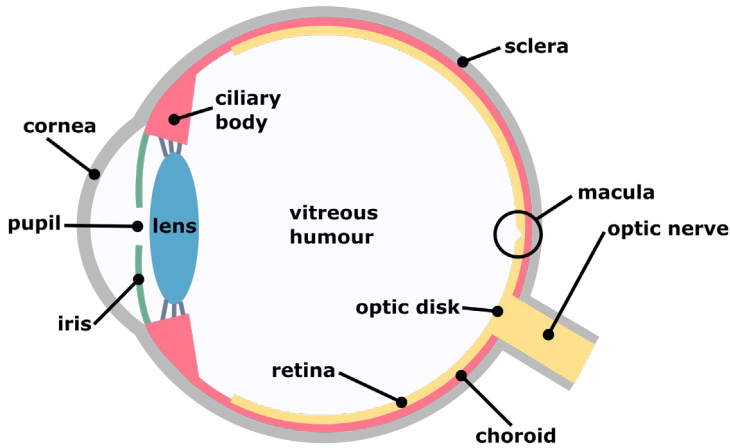


Figure 1: Anatomy of a healthy right eye (transversal plane). Uveal melanomas can arise from the choroid (~90%), the ciliary body (~6%) or the iris (~4%) [2].

IMAGING OF UVEAL MELANOMA

Several ophthalmological and radiological imaging modalities are combined in the clinical care for uveal melanoma patients, with usage depending on application and availability. In Figure 2, several imaging modalities are shown for a patient with uveal melanoma. Below, their working mechanisms and usage are described.

Fundus photography

Fundus photography is one of the most frequently used imaging methods in the ophthalmology practice. The patient's pupils are dilated, after which an optical image of the retinal surface using visible light is acquired. This is a widely available and non-invasive technique, giving information on the presence of ocular lesions, their shape, location, approximate size, and location. However, it yields a two-dimensional view of the retinal surface without any depth information. Its use is limited with unclear media such as cataract, vitreous haemorrhage, and silicon oil after vitrectomies. Due to the limited field of view of 40 to 60 degrees in traditional systems [16, 17], stitching of several separate photographs is necessary to obtain a composite view of the retina. Furthermore, peripherally located lesions are sometimes difficult to visualize, although modern wide-field systems are able to image up to 200 degrees of the retina [18]. Additionally, obtaining tumour measurements from fundus photographs is not possible, due to the patient-specific refraction characteristics [19, 20].

Information from fundus photography is used in differential diagnosis, in treatment planning and follow-up after treatment [21-23].

Confocal scanning laser ophthalmoscopy

Comparable to conventional fundus photography systems, confocal scanning laser ophthalmoscopy (CSLO) systems are used to create an image of the retinal surface through the patient's pupil. However, CSLO uses a laser to scan the retina. Its applications are similar to fundus photography systems, although CSLO is able to produce an image with increased contrast compared to modern wide-field fundus photography systems, at a similar resolution of 6-8 μm [24].

Fluorescein angiography and indocyanine green angiography

Tumour vasculature can be visualized using fluorescein angiography (FAG) and indocyanine green angiography (ICGA) [25]. Both are based on the intravenous injection of a fluorescent dye, which is visualized with blue light in the case of FAG and near-infrared light for ICGA in intervals of several seconds up to seven minutes after injection. Due to the larger size of the indocyanine green molecules, it has an affinity for choroidal vasculature, while FAG is used to visualize retinal vasculature [22]. Both methods only visualize the surface of the lesion and do not offer 3D information about the tumour. FAG and ICGA often have a role in differential diagnosis and may aid in tumour delineation for treatment planning. Furthermore, changes in FAG and ICGA imaging has been described after treatment of uveal melanoma [26].

Fundus autofluorescence

Fundus autofluorescence (FAF), comparable to FAG and ICGA, enables visualization of fluorophore emission in the patient's fundus after excitation. In contrast to these dye-based methods, FAF exploits intrinsic autofluorescence, eliminating the need for intravenous contrast administration [27]. FAF can contribute to differential diagnosis. Furthermore, changes in FAF images after brachytherapy have been observed, possibly enabling early treatment response assessment [28, 29].

Ocular ultrasonography and ultrasound biomicroscopy

In ultrasonography and ultrasound biomicroscopy (UBM), imaging is performed based on high-frequency sound waves, which are reflected by ocular structures. Since these sound waves have a higher penetration depth than light, ultrasound imaging is able to obtain depth information, enabling measurements of tumour thickness and diameters. However, ultrasound is operator-dependent, with standard deviations in tumour thickness and diameter of 0.2 mm and 0.8 mm between different observers [30]. Additionally, ultrasound has limited soft tissue contrast and the correct measurement

angles have to be selected during the exam, as image reconstruction in other planes is not possible afterwards.

B-scan ultrasonography (10-20 MHz) is used most often for tumour dimensions of posterior uveal melanoma, with an axial and lateral spatial resolutions of around 0.15 and 0.45 mm, respectively [22]. Ultrasound biomicroscopy uses higher frequencies (35-100 MHz), enabling axial resolutions of around 0.05 mm, at the cost of penetration depth (~3-6 mm). This allows high-resolution visualization of the anterior segment and the relationship between tumour and surrounding structures, such as the ciliary body [31].

Optical coherence tomography and OCT-angiography

Optical coherence tomography (OCT) is imaging based on the interference patterns of low-coherence near-infrared light, reflected by ocular structures. Used in several retinal and macular diseases, it can image the layers of the retina and choroid. OCT has a high resolution of 10-20 μm , but a limited penetration depth of about 1-2 mm [32]. In uveal melanoma, it may be used for thickness measurements of very thin lesions and for imaging of subretinal fluid. In the context of proton therapy planning, OCT can be used to measure the distance between macula and fovea [33].

With OCT-angiography, intratumoral vasculature can be visualized by comparing several OCT scans performed at different timepoints at the same location. It can aid in the distinction between small uveal melanoma and naevi [34, 35] and is proposed as a non-invasive marker for macular and peripapillary blood flow reduction after radiation therapy [36, 37].

Ocular biometry

Ocular biometry is not necessarily an imaging modality, but a measurement technique to determine characteristics of the eye. Although primarily used for the calculation of intra-ocular lens power in cataract surgery, measurements such as axial length and anterior chamber depth are used in the context of proton therapy planning as well [38, 39]. Measurements in eyes with posteriorly located tumours must be interpreted with caution [40], as the signal might be reflected by the tumour surface instead of the scleral wall.

Magnetic resonance imaging

Magnetic resonance imaging (MRI) is a three-dimensional imaging modality with excellent soft tissue contrast, offering both anatomical and functional information. Although first described in the year 1983, the clinical use of MRI was initially limited [41]. However, since the last decade, its use has been increasing due to the development of eye-specific surface coils and dedicated scan protocols [42-45]. The current role of MRI in the clinical care for uveal melanoma patients is elaborately described in the systematic review in chapter 2.

X-ray imaging

X-ray imaging uses a stationary X-ray source and detector to form a 2D image based on X-ray attenuation. Due to the limited soft tissue contrast, it does not have a role in differential diagnosis or follow-up. However, lateral and axial X-ray images are used in position verification for ocular proton beam therapy. Here, tantalum clips, which are sutured to the sclera, can be visualized.

Computed tomography

Computed tomography (CT) uses a rotating X-ray source and detectors to form a 3D anatomical image. Spatial resolutions of 0.5 to 1.0 mm can be achieved [46]. However, due to its limited soft tissue contrast, the role of CT in differential diagnosis is limited. In treatment planning for stereotactic radiotherapy and in some proton therapy centres, CT is used to determine stopping power [39, 46-48]. Furthermore, CT of the lungs and liver has a role in the detection of metastatic disease.

Radionuclide-based imaging modalities

Radionuclide-based imaging modalities, such as single photon emission computed tomography (SPECT) and positron emission tomography (PET) provide functional assessment of tumours. Both use intravenously administered radionuclides to assess tissue perfusion and metabolic activity. Although larger uveal melanomas are described to be visible on both modalities [49, 50], their use in clinical practice is limited due to their spatial resolution of 4 to 8 millimetres [50, 51], availability and cost. However, especially PET-CT has been described to have a role in the detection of metastatic disease and in differential diagnosis, if the ocular lesion is suspected to be a metastasis of another primary tumour.

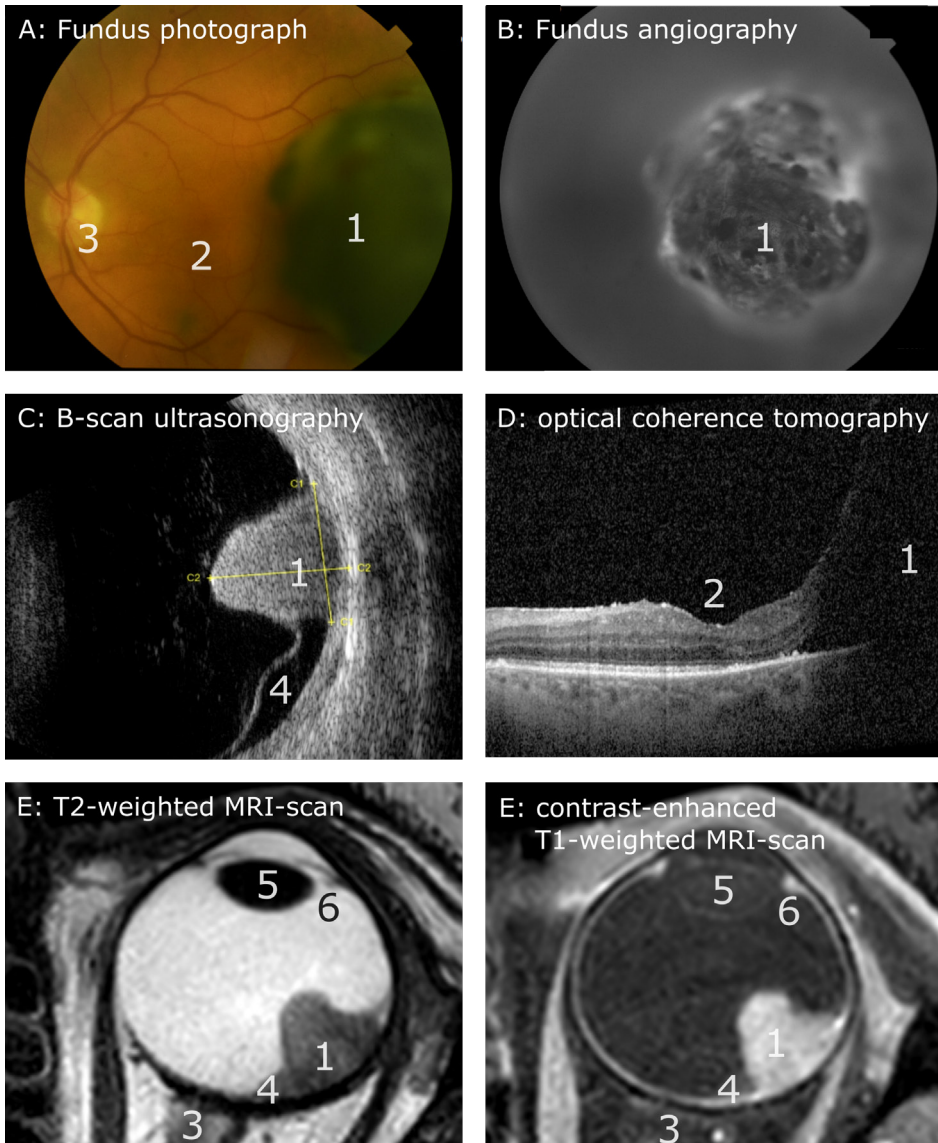


Figure 2: Several imaging modalities for a patient with a large mushroom-shaped uveal melanoma located temporally from the optic nerve of the left eye. (A) Fundus photograph, (B) fundus angiography, (C) B-scan ultrasound, (D) OCT-scan, (E) T2-weighted MRI-scan, (F) contrast-enhanced T1-weighted MRI-scan. Several structures are annotated: (1) tumour, (2) macula, (3) optic nerve, (4) retinal detachment, (5) lens and (6) ciliary body.

TREATMENT OPTIONS AND SELECTION

History of uveal melanoma treatment

Historically, enucleation (surgical removal of the eye) was the only treatment for uveal melanomas. Eye-sparing techniques emerged in the 1900s, with the first mention of radiation treatment in 1903, when a 3-year-old patient with retinoblastoma was treated with X-ray exposure through a lead plate perforated to treat both eyes [52]. In 1915, the first report of a choroidal melanoma treated with an implant with a radium isotope was published [53]. In 1930, the insertion of a radon seed in a choroidal sarcoma was reported [54]. In this era, radiation therapy was mostly used as a salvage option for patients with a tumour in their only functional eye. Around the 1960s, curved brachytherapy plaques gained popularity, first with cobalt-60 [55], and later with ruthenium-106 [56]. In the 1980s, iodine-125 brachytherapy emerged in the United States.

First reports of the use of proton therapy date back to 1978, when the first patients were irradiated in Boston [57]. Interestingly, the current set-up still shows many similarities to the set-up described in this paper. Charged particle therapy with helium ions was performed from the 1980s [58]. In Europe, proton therapy was used for uveal melanoma from 1984 at the Paul Scherrer Institut in Switzerland [59], from 1989 at Clatterbridge in the United Kingdom [60] and from 1991 at the Centre Antoine Lacassagne in Nice [61].

The major shift from enucleation to eye-sparing techniques was driven by the Collaborative Ocular Melanoma Study (COMS). In a randomized trial, enucleation was compared to iodine-125 plaque brachytherapy, resulting in no significant difference in survival at 5, 10, and 12 years [62, 63]. Because of these findings, eye-sparing treatments have increasingly become standard options when feasible, with enucleation reserved for very large tumours.

Current availability and treatment selection

Worldwide, treatment availability for uveal melanoma varies considerably. Ruthenium-106 brachytherapy is offered in approximately 100 centres in the world [64], while iodine-125 is mainly used in large ocular oncology centres in the United States [65]; in Europe, the use of iodine-125 has been described in Sweden [66] and Spain [67]. Currently, about 20 centers in the world perform ocular proton therapy (OPT). Most of the treatments are performed with a dedicated fixed horizontal beam line, although newer centres often use non-dedicated gantry-based solutions [68]. Photon-based techniques, such as stereotactic radiotherapy, are more

widely available, as is enucleation. Treatment selection generally depends on local availability, tumour size, tumour location, and patient preferences. In the Netherlands, treatment options include ruthenium-106 brachytherapy, proton beam therapy, stereotactic radiotherapy, and enucleation. Below, several available treatment options are discussed in more detail.

Ruthenium-106 brachytherapy is the preferred option for smaller tumours (<7 mm in thickness and <16 mm in basal diameter) and is performed at the Leiden University Medical Center (LUMC) for about 50% of uveal melanoma patients in the Netherlands. This modality delivers highly localized beta radiation and provides excellent local control, but its limited penetration depth restricts its use to smaller lesions, and it is less suitable for tumours adjacent to the optic nerve, where placement of the plaque is technically challenging and local recurrence rates are higher [69].

Compared with ruthenium-106, iodine-125 brachytherapy offers greater penetration depth, which allows treatment of larger tumours. However, iodine-125 also has a less steep dose fall-off than ruthenium and a more heterogeneous dose distribution compared with protons. Trofimov et al. [70] conducted plan comparisons between iodine-125 brachytherapy and proton therapy for a large number of virtual tumours: proton therapy was more favourable across most metrics, but iodine-125 performed better for a small number of cases, such as large nasally located tumours. In the Netherlands, iodine-125 brachytherapy is not currently available. Any consideration of its use should weigh factors such as costs, quality assurance requirements, and the number of patients who might benefit relative to proton therapy.

Stereotactic (photon) radiotherapy (SRT) is more widely available than proton therapy and is performed for ocular tumours in the Netherlands at the Erasmus Medical Center. Many centres have described a high local control with stereotactic radiotherapy [71-73]. However, in the Netherlands, uveal melanoma is a standard indication for proton therapy, due to the more favourable toxicity profile compared to SRT [74]. Several treatment planning comparison studies describe dosimetric advantages of proton therapy compared to stereotactic radiotherapy. For example, Fleury et al. [46] described higher mean doses on the optic nerve, macula, retina, anterior segment and lacrimal gland with SRT, although the D2% on the anterior segment was higher with proton therapy. Similarly, Gerard et al. [75] and Weber et al. [76] describe higher doses on the optic disk, macula, lacrimal gland and contralateral eye with SRT. In contexts where proton therapy is also available, SRT might especially be considered in a palliative setting or for patients who are unable to undergo clip surgery, which is still needed for proton therapy [77].

Enucleation remains an important option for very large tumours or when patients prefer not to undergo radiotherapy, and it is performed in about 25% of cases. Importantly, there is no strict cut-off for the choice between proton therapy and enucleation; the decision is always made in close consultation between the patient, ocular oncologist, and radiation oncologist.

Proton therapy in detail

Ocular proton therapy is generally recommended for larger tumours and tumours with a juxtapapillary location, which together account for about 25% of patients in the Netherlands. Its clinical value stems from the depth-dose characteristics of protons, most notably the Bragg peak, which enables the delivery of high radiation doses to the tumour while minimizing exposure to surrounding ocular structures, especially compared to photons [78].

Ocular proton therapy differs from proton therapy for other tumour sites in several important ways. Compared to most extraocular targets, uveal melanomas are small (typically less than 10 mm in thickness and under 20 mm in diameter) and located at shallow depths, usually within 3 cm of the surface [33]. The small scale is further emphasized by the close proximity of critical structures such as the optic nerve and macula, which necessitates a sharp lateral penumbra. In addition, the mobility of the globe presents unique challenges for treatment delivery. These factors have historically led to the development of dedicated horizontal passive-scattering beamlines equipped with patient-specific brass apertures to minimize the lateral penumbra, the use of fixation lights to stabilize gaze, and the surgical placement of tantalum clips to facilitate precise target definition and patient positioning [79].

Below, several steps in the clinical workflow at HollandPTC are described. Details may differ per treatment centre and alternatives are described in chapter 9.

Pre-treatment imaging

Pre-treatment imaging typically consists of fundus photography, ocular ultrasonography, ocular MRI, and biometry [40, 80]. These modalities are used to obtain detailed measurements of both the eye and the tumour, providing the anatomical information necessary for accurate treatment planning. An overview of the measurements obtained for treatment planning is provided in Table 1, with further details discussed in chapter 1.2.

Table 1: Measurements obtained for treatment planning of ocular proton therapy.

Measurement	Modality
<i>Eye</i>	
Axial length	Biometry, MRI
Transversal diameter	MRI
Anterior chamber depth	Biometry
Limbus diameter	Biometry
Thickness of the sclera	MRI
<i>Tumour</i>	
Prominence	Ultrasound, MRI
Diameter	Ultrasound, MRI
Clip-tumour distances	Surgical measurements, MRI
Distance to optic nerve	MRI, fundus imaging, OCT
Distance to macula	Fundus imaging, OCT
Shape of the tumour base*	Fundus imaging, FAG*

* Tumour shape is not measured quantitatively, but these modalities can aid in the assessment of the delineated target volume.

Clip placement surgery

Prior to treatment, tantalum clips are surgically placed on the surface of the sclera by an ocular oncologist at the referring hospital (Figure 3A). Each clip has a diameter of 2.5 mm and a thickness of 0.2 mm. The procedure is performed under general anaesthesia. During the subsequent radiotherapy workflow, the clips serve a dual purpose: they provide markers that aid in accurate tumour delineation during treatment planning, and they function as reference points for patient positioning [80].

Treatment planning

Treatment planning for ocular proton therapy can be performed with different treatment planning systems, most of which use a model-based approach. This contrasts with conventional radiotherapy planning, where delineation, dose calculation and optimization are generally performed with 3D CT-images, often co-registered with MR imaging. Examples of model-based treatment planning systems are EYEPLAN and OCTOPUS [81, 82], which were both in-house developed and used for the majority of ocular proton therapy patients up to now. Varian Medical Systems developed a similar system called Eclipse Ocular Proton Planning (EOPP), which is used at HollandPTC. More recently, RayStation developed the RayOcular module, which enables the integration of the eye model with 3D imaging [48].

In model-based planning, an ellipsoidal eye model with a predefined density is formed based on measurements of the axial length and transverse diameter of the patient's eye. This eye model is fitted onto the position of the tantalum clips (Figure 3B). A fundus view, which is a 2D schematic map of the inner eye, is used for the delineation of the tumour base (Figure 3C-D). The tumour base is drawn based on the clip-tumour distances, tumour diameters and measurements to structures such as the optic nerve. The tumour top is then formed using a polynomial, the degree of which can be chosen by the user to reflect the tumour shape (Figure 3E) [83].

After definition of the target volume, several gazing angles can be evaluated, and the best gazing angle is chosen based on dose to organs at risk and feasibility. For example, in Figure 4, gazing direction to the right results in sparing of the anterior chamber, while the dose to the macula is lower with a left gazing direction.

In many proton centres, among which HollandPTC, ocular proton therapy is performed using a passive scattering horizontal beam [80, 84]. Therefore, a patient-specific brass aperture is manufactured, based on the treatment plan, which is used to shape the proton beam. Here, a lateral and distal margin of 2.5 mm are used [85].

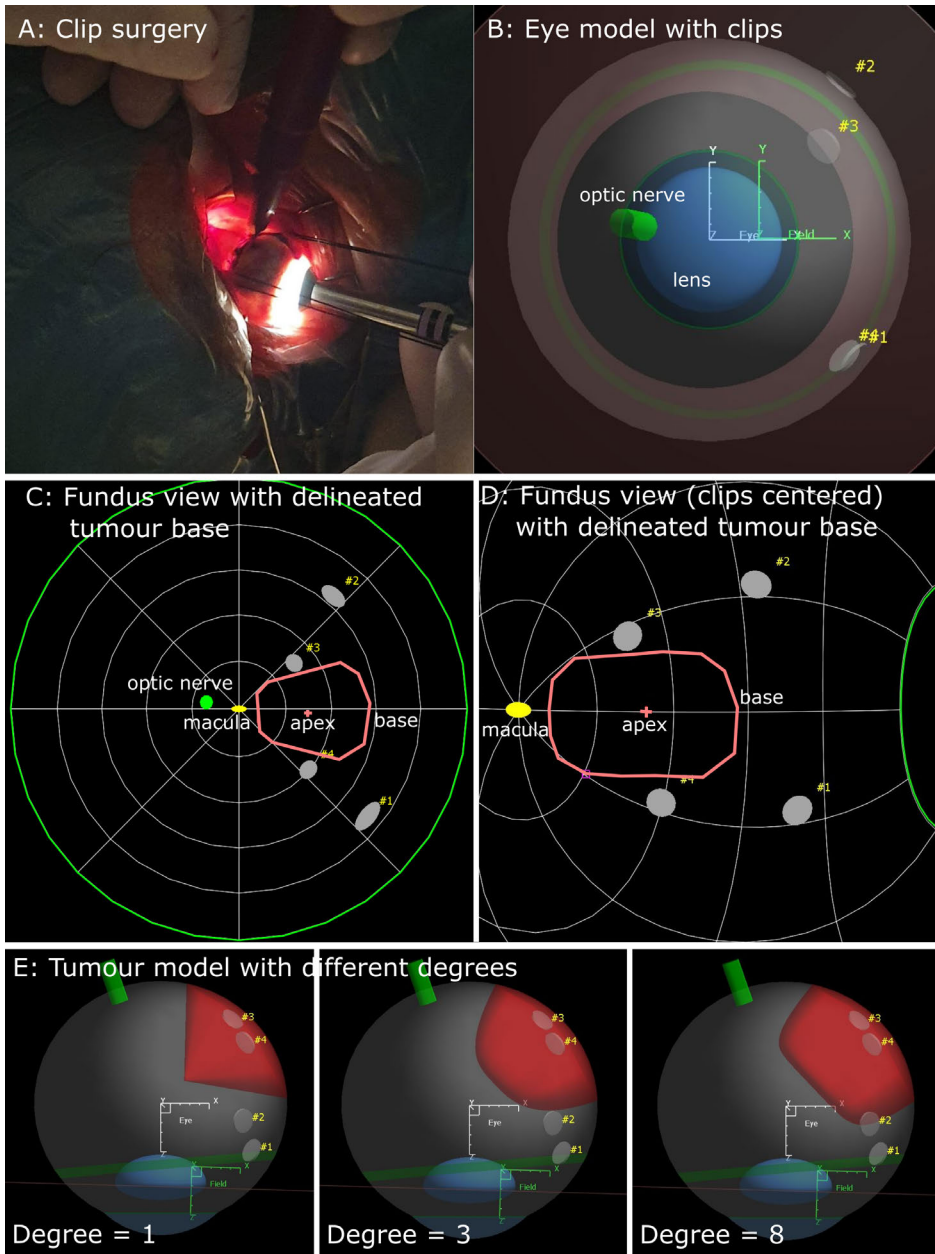


Figure 3: Target volume delineation in Eclipse Ocular Proton Planning. (A) Clips are placed surgically by an ocular oncologist. (B) The ellipsoid eye model is based on eye measurements and fitted onto the four clips. (C,D) Two different angles from the fundus view with clips: tumour base is delineated, using clip-tumour measurements and diameters. (E) The most appropriate degree of the polynomial is chosen to form the tumour top.

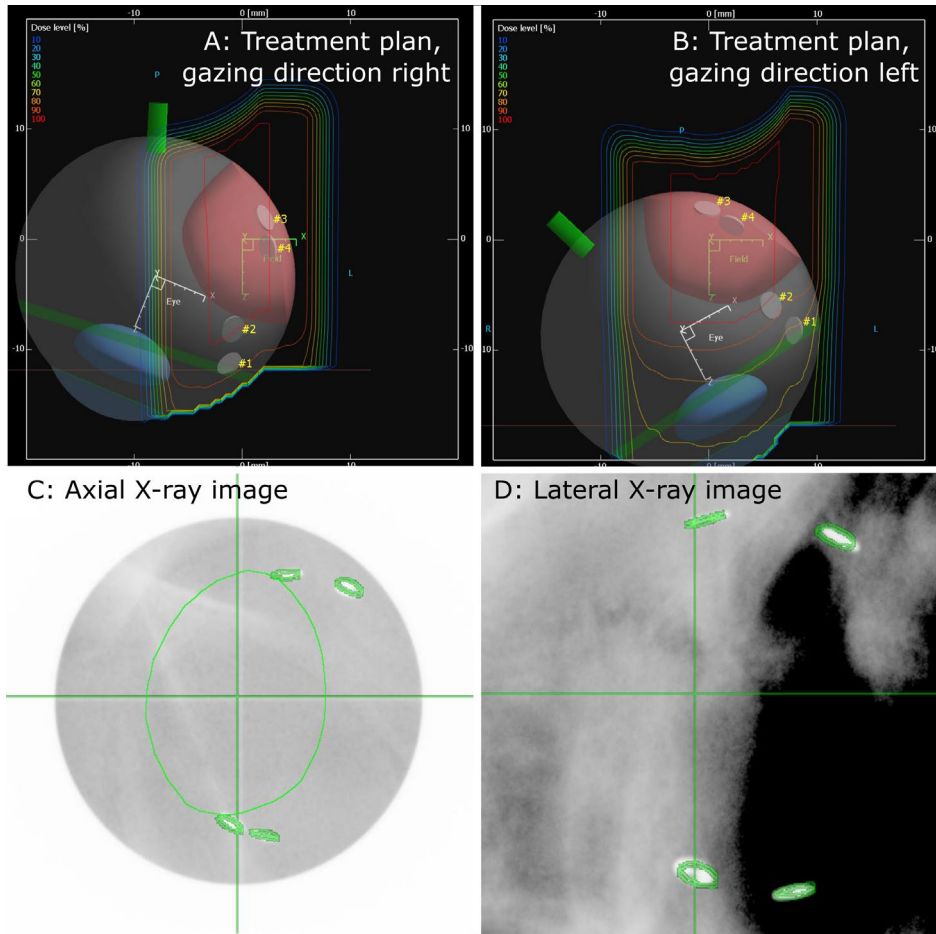


Figure 4: Treatment planning and resulting DRR. (A) An example of a treatment plan with gazing direction right (polar angle 25 degrees), sparing the anterior chamber. (B) Example of a treatment plan with gazing direction left (polar angle 25 degrees), lowering the macula dose but with a higher dose on the anterior chamber. (C, D) X-ray images (axial and lateral) taken during patient positioning with overlay of the aperture shape and clips (green lines).

Delivery

At HollandPTC, ocular proton therapy is delivered in four consecutive daily fractions to a total dose of 60 GyE (Figure 5). For head immobilization, patients are fitted with a front-shell thermoplastic mask in combination with a bite block and a band at the back of the head to ensure stable head positioning. Prior to each fraction, the treated eye is anesthetized with topical drops, and the eyelids are displaced using either an eyelid retractor or adhesive strips to provide an unobstructed beam path and to protect the eyelids. Patient positioning and gazing direction are verified with

orthogonal X-rays, which visualize the surgically placed tantalum clips (Figure 4). The clips are then matched to the digitally reconstructed radiograph (DRR), which is produced by the treatment planning system. During beam delivery, a live video feed is used to monitor of eye position. The beam delivery takes approximately 40 to 60 seconds per fraction.

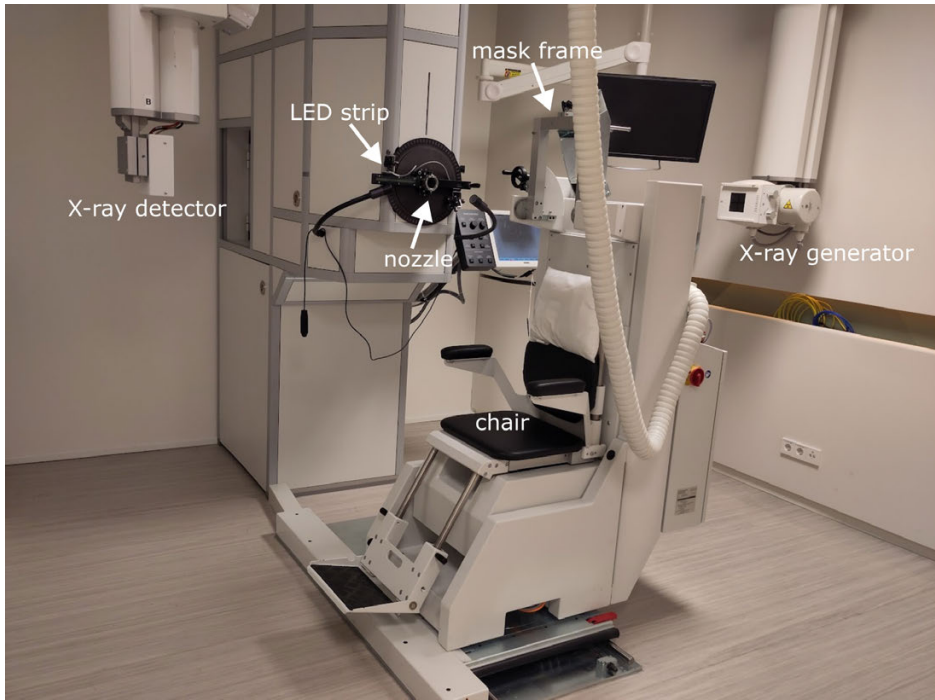


Figure 5: Eye treatment room at HollandPTC.

Follow-up methods and treatment outcomes

After proton therapy, treatment response assessment is usually performed using ultrasound and fundoscopy. Tumour regression after proton beam therapy for uveal melanoma is typically slow, with ultrasound studies showing that measurable shrinkage may take up to 32 months [86], and early increases in prominence can represent transient changes rather than true progression [87]. MRI may aid in early surveillance, as semi-quantitative perfusion-weighted MRI techniques have shown favourable changes three months after treatment, a timepoint when for most patients no change in size is visible yet [88].

Local tumour control after ocular proton therapy is excellent, with large series reporting 5-year local control rates around 95–96% [79, 89-92]. Loss of visual acuity,

however, remains one of the main side effects: most series document a substantial decline in visual acuity during the first two years after treatment and high rates of severe visual impairment by five years (results vary by cohort and pre-treatment vision, with some series showing >70% of patients with severe visual impairment at 5 years [91]).

The pathologies behind post-treatment vision loss often co-exist: radiation retinopathy and maculopathy (radiation damage to retinal microvasculature, with maculopathy referring to disease of the retinal vessels at the macula), optic neuropathy, exudative retinal detachment, cataract (treatable with lens replacement), and vitreous haemorrhage may all have an impact on visual acuity. Radiation retinopathy is a chronic, progressive, dose-dependent occlusive vasculopathy that most commonly develops in the irradiated retina and macula but may have functional consequences beyond the highest-dose region [93]. Larger tumours and those associated with pre-existing exudative retinal detachment are at greater risk of post-treatment retinal detachment and related complications [79].

Neovascular glaucoma is one of the leading reasons for secondary enucleation after proton therapy, although rates of enucleation for toxicity have declined with improved management (including anti-VEGF therapy) [94, 95]. Other late effects such as, light sensitivity, dry eye and eyelash loss also contribute to reduced quality of life.

THIS THESIS

The work in this thesis was performed in the context of the clipless proton therapy project, a HollandPTC-Varian project with researchers from the LUMC, ErasmusMC, TU Delft and HollandPTC. This project aims to enable clipless ocular proton therapy with several milestones: (1) the development of a setup for clipless positioning, (2) the use of MRI in ocular treatment planning, (3) the validation of a clipless MR-based workflow and (4) the development of a blood serum-based staging method.

This thesis describes several steps towards the second milestone. Chapter 2 discusses the different applications of MRI in the clinical care for uveal melanoma patients. Chapter 3 evaluates the geometric accuracy of the dedicated eye-specific MRI protocol to determine its suitability for radiotherapy planning. In chapter 4, conventional ultrasound tumour dimension measurements are compared with MRI-based measurements, while chapter 5 extends this comparison to model-based versus MRI-based target volume definition. Chapter 6 contrasts commonly used ellipsoidal

tumour models for prognostication with delineated tumour volumes. Shifting focus to treatment response assessment, chapter 7 explores quantitative perfusion-weighted MRI in a large cohort of patients before and after therapy, and chapter 8 investigates the reproducibility of the clinically used semi-quantitative perfusion-weighted MRI. Chapter 9 provides a discussion of the key findings in this thesis, their implications, and potential future directions.

REFERENCES

1. Hou X, Rokohl AC, Li X, Guo Y, Ju X, Fan W, et al. Global incidence and prevalence in uveal melanoma. *Adv Ophthalmol Pract Res*. 2024;4:226-32. doi: 10.1016/j.aopr.2024.10.001.
2. Jager MJ, Shields CL, Cebulla CM, Abdel-Rahman MH, Grossniklaus HE, Stern MH, et al. Uveal melanoma. *Nat Rev Dis Primers*. 2020;6:24. doi: 10.1038/s41572-020-0158-0.
3. Wu M, Yavuziyigitoglu S, Brosens E, Ramdas WD, Kilic E, Rotterdam Ocular Melanoma Study G. Worldwide Incidence of Ocular Melanoma and Correlation With Pigmentation-Related Risk Factors. *Invest Ophthalmol Vis Sci*. 2023;64:45. doi: 10.1167/iovs.64.13.45.
4. NKR Cijfers. Incidentie per jaar. <https://nkr-cijfers.iknl.nl/>: Integraal Kankercentrum Nederland; 2025
5. Richtig E, Langmann G, Mullner K, Smolle J. Ocular melanoma: epidemiology, clinical presentation and relationship with dysplastic nevi. *Ophthalmologica*. 2004;218:111-4. doi: 10.1159/000076146.
6. Weis E, Shah CP, Lajous M, Shields JA, Shields CL. The association between host susceptibility factors and uveal melanoma: a meta-analysis. *Arch Ophthalmol*. 2006;124:54-60. doi: 10.1001/archophth.124.1.54.
7. Damato EM, Damato BE. Detection and time to treatment of uveal melanoma in the United Kingdom: an evaluation of 2,384 patients. *Ophthalmology*. 2012;119:1582-9. doi: 10.1016/j.ophtha.2012.01.048.
8. Kivela T, Eskelin S, Makitie T, Summanen P. Exudative retinal detachment from malignant uveal melanoma: predictors and prognostic significance. *Invest Ophthalmol Vis Sci*. 2001;42:2085-93.
9. Chattopadhyay C, Kim DW, Gombos DS, Oba J, Qin Y, Williams MD, et al. Uveal melanoma: From diagnosis to treatment and the science in between. *Cancer*. 2016;122:2299-312. doi: 10.1002/cncr.29727.
10. Kaliki S, Shields CL. Uveal melanoma: relatively rare but deadly cancer. *Eye (Lond)*. 2017;31:241-57. doi: 10.1038/eye.2016.275.
11. Carvajal RD, Sacco JJ, Jager MJ, Eschelmann DJ, Olofsson Bagge R, Harbour JW, et al. Advances in the clinical management of uveal melanoma. *Nat Rev Clin Oncol*. 2023;20:99-115. doi: 10.1038/s41571-022-00714-1.
12. Yang J, Manson DK, Marr BP, Carvajal RD. Treatment of uveal melanoma: where are we now? *Ther Adv Med Oncol*. 2018;10:1758834018757175. doi: 10.1177/1758834018757175.
13. Kujala E, Makitie T, Kivela T. Very long-term prognosis of patients with malignant uveal melanoma. *Invest Ophthalmol Vis Sci*. 2003;44:4651-9. doi: 10.1167/iovs.03-0538.
14. Diener-West M, Reynolds SM, Agugliaro DJ, Caldwell R, Cumming K, Earle JD, et al. Development of metastatic disease after enrollment in the COMS trials for treatment of choroidal melanoma: Collaborative Ocular Melanoma Study Group Report No. 26. *Arch Ophthalmol*. 2005;123:1639-43. doi: 10.1001/archophth.123.12.1639.
15. Shields CL, Kaliki S, Furuta M, Fulco E, Alarcon C, Shields JA. American Joint Committee on Cancer classification of posterior uveal melanoma (tumor size category) predicts prognosis in 7731 patients. *Ophthalmology*. 2013;120:2066-71. doi: 10.1016/j.ophtha.2013.03.012.
16. Nagiel A, Lalane RA, Sadda SR, Schwartz SD. ULTRA-WIDEFIELD FUNDUS IMAGING: A Review of Clinical Applications and Future Trends. *Retina*. 2016;36:660-78. doi: 10.1097/IAE.0000000000000937.
17. Domalpally A, Barrett N, Reimers J, Blodi B. Comparison of Ultra-Widefield Imaging and Standard Imaging in Assessment of Early Treatment Diabetic Retinopathy Severity Scale. *Ophthalmol Sci*. 2021;1:100029. doi: 10.1016/j.xops.2021.100029.

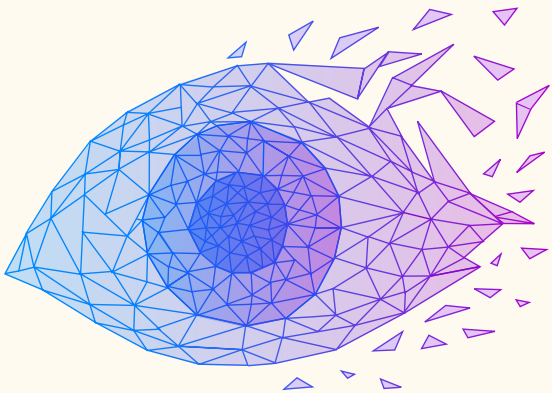
18. Kumar V, Surve A, Kumawat D, Takkar B, Azad S, Chawla R, et al. Ultra-wide field retinal imaging: A wider clinical perspective. *Indian J Ophthalmol.* 2021;69:824-35. doi: 10.4103/ijjo.IJO_1403_20.
19. Haasjes C, Vu THK, Beenakker JM. Patient-specific mapping of fundus photographs to three-dimensional ocular imaging. *Med Phys.* 2025;52:2330-9. doi: 10.1002/mp.17576.
20. Pors LJ, Haasjes C, van Vught L, Hoes NP, Luyten GPM, van Rijn GA, et al. Correction Method for Optical Scaling of Fundoscopy Images: Development, Validation, and First Implementation. *Invest Ophthalmol Vis Sci.* 2024;65:43. doi: 10.1167/iovs.65.1.43.
21. Wulff J, Koska B, Giese M, Baumer C, Richter R, Foerster A, et al. Evaluation of OPTOS wide-field fundus image projections for radiotherapy planning of uveal melanoma. *J Appl Clin Med Phys.* 2025;26:e70009. doi: 10.1002/acm2.70009.
22. Solnik M, Padaszyska N, Czarnaacka AM, Synoradzki KJ, Yousef YA, Choragiewicz T, et al. Imaging of Uveal Melanoma-Current Standard and Methods in Development. *Cancers (Basel).* 2022;14. doi: 10.3390/cancers14133147.
23. Psomiadi A, Haas G, Edlinger M, Bechrakis NE, Blatsios G. Ultra-wide-field imaging of choroidal melanoma before and after proton beam radiation therapy. *Eur J Ophthalmol.* 2020;30:1397-402. doi: 10.1177/1120672119873210.
24. In: Bille JF, editor. *High Resolution Imaging in Microscopy and Ophthalmology: New Frontiers in Biomedical Optics.* Cham (CH)2019.
25. Shields CL, Shields JA, De Potter P. Patterns of indocyanine green videoangiography of choroidal tumours. *Br J Ophthalmol.* 1995;79:237-45. doi: 10.1136/bjo.79.3.237.
26. Krause L, Bechrakis NE, Heinrich S, Kreusel KM, Foerster MH. Indocyanine green angiography and fluorescein angiography of malignant choroidal melanomas following proton beam irradiation. *Graefes Arch Clin Exp Ophthalmol.* 2005;243:545-50. doi: 10.1007/s00417-004-1029-1.
27. Bindewald-Wittich A, Holz FG, Ach T, Fiorentzis M, Bechrakis NE, Willerding GD. Fundus Autofluorescence Imaging in Patients with Choroidal Melanoma. *Cancers (Basel).* 2022;14. doi: 10.3390/cancers14071809.
28. Bindewald-Wittich A, Swenshon T, Carasco E, Dreyhaupt J, Willerding GD. Blue-Light Fundus Autofluorescence Imaging following Ruthenium-106 Brachytherapy for Choroidal Melanoma. *Ophthalmologica.* 2020;243:303-15. doi: 10.1159/000504715.
29. Navaratnam J, Baerland TP, Eide NA, Faber RT, Rekstad BL, Vavvas DG, et al. Fundus Autofluorescence Change as an Early Indicator of Treatment Effect of Brachytherapy for Choroidal Melanomas. *Ocul Oncol Pathol.* 2019;5:445-53. doi: 10.1159/000499403.
30. Haritoglou C, Neubauer AS, Herzum H, Freeman WR, Mueller AJ. Interobserver and intraobserver variability of measurements of uveal melanomas using standardised echography. *Br J Ophthalmol.* 2002;86:1390-4. doi: 10.1136/bjo.86.12.1390.
31. Conway RM, Chew T, Golchet P, Desai K, Lin S, O'Brien J. Ultrasound biomicroscopy: role in diagnosis and management in 130 consecutive patients evaluated for anterior segment tumours. *Br J Ophthalmol.* 2005;89:950-5. doi: 10.1136/bjo.2004.059535.
32. Obuchowska I, Konopinska J. Importance of Optical Coherence Tomography and Optical Coherence Tomography Angiography in the Imaging and Differentiation of Choroidal Melanoma: A Review. *Cancers.* 2022;14. doi: 10.3390/cancers14143354.
33. Wulff J, Koska B, Khalil DA, Richter R, Backer CM, Bäumer C, et al. Uncertainties in ocular proton planning and their impact on required margins. *Phys Medica.* 2024;121. doi:10.1016/j.ejmp.2024.103358.
34. Ghassemi F, Mirshahi R, Fadakar K, Sabour S. Optical coherence tomography angiography in choroidal melanoma and nevus. *Clin Ophthalmol.* 2018;12:207-14. doi: 10.2147/OPHT.148897.

35. Greig EC, Laver NV, Mendonca LSM, Levine ES, Baumal CR, Waheed NK, et al. Swept-Source Optical Coherence Tomography Angiography in Small Choroidal Melanomas and Choroidal Nevi. *Retina*. 2021;41:1182-92. doi: 10.1097/IAE.0000000000003053.
36. Cennamo G, Breve MA, Velotti N, Sparnelli F, Iovino C, Farella A, et al. Evaluation of Vascular Changes with Optical Coherence Tomography Angiography after Plaque Radiotherapy of Choroidal Melanoma. *Ophthalmic Res*. 2018;60:238-42. doi: 10.1159/000490571.
37. Jung SK, Lee EH, Mishra KK, Daftari IK, Park SS. OCT Angiography Analysis of Retinal and Choroidal Flow after Proton Beam Therapy for Choroidal Melanoma. *Ophthalmol Sci*. 2025;5:100674. doi: 10.1016/j.xops.2024.100674.
38. Damato B, Kacperek A, Errington D, Heimann H. Proton beam radiotherapy of uveal melanoma. *Saudi J Ophthalmol*. 2013;27:151-7. doi: 10.1016/j.sjopt.2013.06.014.
39. Wulff J, Koska B, Janson M, Baumer C, Denker A, Geismar D, et al. Technical note: Impact of beam properties for uveal melanoma proton therapy-An in silico planning study. *Med Phys*. 2022;49:3481-8. doi: 10.1002/mp.15573.
40. Jaarsma-Coes MG, Ferreira TA, Marinkovic M, Vu THK, van Vught L, van Haren GR, et al. Comparison of Magnetic Resonance Imaging-Based and Conventional Measurements for Proton Beam Therapy of Uveal Melanoma. *Ophthalmol Retina*. 2023;7:178-88. doi: 10.1016/j.oret.2022.06.019.
41. Moseley I, Brant-Zawadski M, Mills C. Nuclear magnetic resonance imaging of the orbit. *Br J Ophthalmol*. 1983;67:333-42. doi: 10.1136/bjo.67.6.333.
42. Beenakker JW, Ferreira TA, Soemarwoto KP, Genders SW, Teeuwisse WM, Webb AG, et al. Clinical evaluation of ultra-high-field MRI for three-dimensional visualisation of tumour size in uveal melanoma patients, with direct relevance to treatment planning. *MAGMA*. 2016;29:571-7. doi: 10.1007/s10334-016-0529-4.
43. Ferreira TA, Grech Fonk L, Jaarsma-Coes MG, van Haren GGR, Marinkovic M, Beenakker JM. MRI of Uveal Melanoma. *Cancers (Basel)*. 2019;11. doi: 10.3390/cancers11030377.
44. Ferreira TA, Jaarsma-Coes MG, Marinkovic M, Verbist B, Verdijk RM, Jager MJ, et al. MR imaging characteristics of uveal melanoma with histopathological validation. *Neuroradiology*. 2022;64:171-84. doi: 10.1007/s00234-021-02825-5.
45. Lemke AJ, Alai-Omid M, Hengst SA, Kazi I, Felix R. Eye imaging with a 3.0-T MRI using a surface coil--a study on volunteers and initial patients with uveal melanoma. *Eur Radiol*. 2006;16:1084-9. doi: 10.1007/s00330-005-0087-z.
46. Fleury E, Pignol JP, Kilic E, Milder M, van Rij C, Naus N, et al. Comparison of stereotactic radiotherapy and protons for uveal melanoma patients. *Phys Imaging Radiat Oncol*. 2024;31:100605. doi: 10.1016/j.phro.2024.100605.
47. Marnitz S, Cordini D, Bendl R, Lemke AJ, Heufelder J, Simiantonakis I, et al. Proton therapy of uveal melanomas: intercomparison of MRI-based and conventional treatment planning. *Strahlenther Onkol*. 2006;182:395-9. doi: 10.1007/s00066-006-1512-1.
48. Wulff J, Koska B, Heufelder J, Janson M, Backer CM, Siregar H, et al. Commissioning and validation of a novel commercial TPS for ocular proton therapy. *Med Phys*. 2023;50:365-79. doi: 10.1002/mp.16006.
49. Singh AD, Bhatnagar P, Bybel B. Visualization of primary uveal melanoma with PET/CT scan. *Eye (Lond)*. 2006;20:938-40. doi: 10.1038/sj.eye.6702044.
50. Kato K, Kubota T, Ikeda M, Tadokoro M, Abe S, Nakano S, et al. Low efficacy of 18F-FDG PET for detection of uveal malignant melanoma compared with 123I-IMP SPECT. *J Nucl Med*. 2006;47:404-9. doi:

51. Papastefanou VP, Islam S, Szyszko T, Grantham M, Sagoo MS, Cohen VM. Metabolic activity of primary uveal melanoma on PET/CT scan and its relationship with monosomy 3 and other prognostic factors. *Br J Ophthalmol.* 2014;98:1659-65. doi: 10.1136/bjophthalmol-2014-305304.
52. Hilgartner HL. Report of Case of Double Glioma Treated with X-Ray. *Tex Med J (Austin).* 1903;18:322-3.
53. Deutschmann R. Ueber intraokularen Tumor und Strahlentherapie. *Z Augenheilkd.* 1915;33:206-9.
54. Moore RF. Choroidal Sarcoma Treated by the Intraocular Insertion of Radon Seeds. *Br J Ophthalmol.* 1930;14:145-52. doi: 10.1136/bjo.14.4.145.
55. Stallard HB. Radiotherapy for malignant melanoma of the choroid. *Br J Ophthalmol.* 1966;50:147-55. doi: 10.1136/bjo.50.3.147.
56. Lommatzsch PK. beta-Irradiation of choroidal melanoma with 106Ru/106Rh applicators. 16 Years' experience. *Arch Ophthalmol.* 1983;101:713-7. doi: 10.1001/archophth.1983.01040010713002.
57. Gradoudas ES, Goitein M, Koehler A, Constable IJ, Wagner MS, Verhey L, et al. Proton irradiation of choroidal melanomas. Preliminary results. *Arch Ophthalmol.* 1978;96:1583-91. doi: 10.1001/archophth.1978.03910060217006.
58. Castro JR, Char DH, Petti PL, Daftari IK, Quivey JM, Singh RP, et al. 15 years experience with helium ion radiotherapy for uveal melanoma. *Int J Radiat Oncol Biol Phys.* 1997;39:989-96. doi: 10.1016/s0360-3016(97)00494-x.
59. Zografos L, Perret C, Egger E, Gailloud C, Greiner R. Proton beam irradiation of uveal melanomas at Paul Scherrer Institute (former SIN). *Strahlenther Onkol.* 1990;166:114. doi:
60. Kacperek A. Protontherapy of eye tumours in the UK: a review of treatment at Clatterbridge. *Appl Radiat Isot.* 2009;67:378-86. doi: 10.1016/j.apradiso.2008.06.012.
61. Hérault J, Gerard A, Carnicer A, Aloï D, Peyrichon ML, Barnel C, et al. 30 years of ocular proton therapy, the Nice view. *Cancer Radiother.* 2022;26:1016-26. doi: 10.1016/j.canrad.2022.03.004.
62. Collaborative Ocular Melanoma Study G. The COMS randomized trial of iodine 125 brachytherapy for choroidal melanoma: V. Twelve-year mortality rates and prognostic factors: COMS report No. 28. *Arch Ophthalmol.* 2006;124:1684-93. doi: 10.1001/archophth.124.12.1684.
63. Diener-West M, Earle JD, Fine SL, Hawkins BS, Moy CS, Reynolds SM, et al. The COMS randomized trial of iodine 125 brachytherapy for choroidal melanoma, III: initial mortality findings. COMS Report No. 18. *Arch Ophthalmol.* 2001;119:969-82. doi: 10.1001/archophth.119.7.969.
64. De Brabandere M, Placidi E, Siebert FA, Carlsson Tedgren A, Stocker Escarpa A, Tagliaferri L, et al. GEC-ESTRO survey of (106)Ru eye applicator practice for ocular melanoma - Physicist survey. *Radiother Oncol.* 2024;193:110114. doi: 10.1016/j.radonc.2024.110114.
65. Binder C, Mruthyunjaya P, Scheffler AC, Seider MI, Crilly R, Hung A, et al. Practice Patterns for the Treatment of Uveal Melanoma with Iodine-125 Plaque Brachytherapy: Ocular Oncology Study Consortium Report 5. *Ocul Oncol Pathol.* 2020;6:210-8. doi: 10.1159/000504312.
66. Gill VT, Stalhammar G. Incidence, risk factors and outcomes of cataract surgery after plaque brachytherapy for posterior uveal melanoma. *Heliyon.* 2024;10:e23447. doi: 10.1016/j.heliyon.2023.e23447.

67. Vicente N, Saornil MA, Almaraz A, Munoz-Moreno MF. Long-term results of visual function in posterior uveal melanoma patients treated with I125 episcleral brachytherapy in a Spanish referral Ocular Oncology Unit. *Arq Bras Oftalmol.* 2021;84:330-8. doi: 10.5935/0004-2749.20210047.
68. Mortimer LAS, R.; Mazal, A.; Beenakker, J.W.M.; Dendale, R.; Denker, A.; Fleury, E.; Groulier, A.; Kacperek, A.; Mishra, K.; Saini, J.; Trofimov, A.V.; Thariat, J.; Trnkova, P.; Vidal, M.; Shih, H.A.; Hrbacek, J.; Heufelder, J. PTCOG Ocular Survey - Perspective on Ocular Particle Therapy: Current Practices and Emerging Trends. Submitted to the International Journal of Particle Therapy. 2025. doi:
69. Pors LJ, Marinkovic M, Deuzeman HH, Vu THK, Kerkhof EM, van Wieringen-Warmenhoven KM, et al. Clinical outcomes and risk factors for local failure and visual impairment in patients treated with Ru-106 brachytherapy for uveal melanoma. *Clin Transl Radiat Oncol.* 2025;52:100939. doi: 10.1016/j.ctro.2025.100939.
70. Trofimov AV, Aronow ME, Gragoudas ES, Keane FK, Kim IK, Shih HA, et al. A Systematic Comparison of Dose Distributions Delivered in (125)I Plaque Brachytherapy and Proton Radiation Therapy for Ocular Melanoma. *Int J Radiat Oncol Biol Phys.* 2023;115:501-10. doi: 10.1016/j.ijrobp.2022.07.017.
71. Dieckmann K, Georg D, Zehetmayer M, Bogner J, Georgopoulos M, Potter R. LINAC based stereotactic radiotherapy of uveal melanoma: 4 years clinical experience. *Radiother Oncol.* 2003;67:199-206. doi: 10.1016/s0167-8140(02)00345-6.
72. Muller K, Nowak PJ, de Pan C, Marijnissen JP, Paridaens DA, Levendag P, et al. Effectiveness of fractionated stereotactic radiotherapy for uveal melanoma. *Int J Radiat Oncol Biol Phys.* 2005;63:116-22. doi: 10.1016/j.ijrobp.2005.01.058.
73. Zehetmayer M, Kitz K, Menapace R, Ertl A, Heinzl H, Ruhswurm I, et al. Local tumor control and morbidity after one to three fractions of stereotactic external beam irradiation for uveal melanoma. *Radiother Oncol.* 2000;55:135-44. doi: 10.1016/s0167-8140(00)00164-x.
74. College voor zorgverzekeringen. Indicaties voor protonentherapie (deel 1). 2010. Available from: <https://www.zorginstituutnederland.nl/documenten/2010/03/23/protonentherapie-indicaties-voor-protonentherapie-deel-1---intra-oculaire-tumoren-chordomen-chondrosarcomen-en-pediatische-tumoren>.
75. Gerard A, Peyrichon ML, Vidal M, Barnel C, Sauerwein W, Carnicer A, et al. Ocular proton therapy, pencil beam scanning high energy proton therapy or stereotactic radiotherapy for uveal melanoma; an in silico study. *Cancer Radiother.* 2022;26:1027-33. doi: 10.1016/j.canrad.2022.03.003.
76. Weber DC, Bogner J, Verwey J, Georg D, Dieckmann K, Escude L, et al. Proton beam radiotherapy versus fractionated stereotactic radiotherapy for uveal melanomas: A comparative study. *Int J Radiat Oncol Biol Phys.* 2005;63:373-84. doi: 10.1016/j.ijrobp.2005.01.057.
77. van Beek JGM, van Rij CM, Baart SJ, Yavuziyigitoglu S, Bergmann MJ, Paridaens D, et al. Fractionated stereotactic radiotherapy for uveal melanoma: Long-term outcome and control rates. *Acta Ophthalmol.* 2022;100:511-9. doi: 10.1111/aos.15029.
78. Char DH, Phillips T, Daftari I. Proton teletherapy of uveal melanoma. *Int Ophthalmol Clin.* 2006;46:41-9. doi: 10.1097/O1.iio.0000195853.85581.c0.
79. Mishra KK, Daftari IK. Proton therapy for the management of uveal melanoma and other ocular tumors. *Chin Clin Oncol.* 2016;5:50. doi: 10.21037/cco.2016.07.06.
80. Hrbacek J, Kacperek A, Beenakker JM, Mortimer L, Denker A, Mazal A, et al. PTCOG Ocular Statement: Expert Summary of Current Practices and Future Developments in Ocular Proton Therapy. *Int J Radiat Oncol Biol Phys.* 2024;120:1307-25. doi: 10.1016/j.ijrobp.2024.06.017.

81. Goitein M, Miller T. Planning proton therapy of the eye. *Med Phys.* 1983;10:275-83. doi: 10.1118/1.595258.
82. Dobler B, Bendl R. Precise modelling of the eye for proton therapy of intra-ocular tumours. *Phys Med Biol.* 2002;47:593-613. doi: 10.1088/0031-9155/47/4/304.
83. Varian Medical Systems. Planning Reference Guide for Eclipse Ocular Proton Planning Eclipse Ocular Proton Planning. 2007;(September):1-286.
84. Hrbacek J, Mishra KK, Kacperek A, Dendale R, Nauraye C, Auger M, et al. Practice Patterns Analysis of Ocular Proton Therapy Centers: The International OPTIC Survey. *Int J Radiat Oncol Biol Phys.* 2016;95:336-43. doi: 10.1016/j.ijrobp.2016.01.040.
85. Fleury E, Trnkova P, Spruijt K, Herault J, Lebbink F, Heufelder J, et al. Characterization of the HollandPTC proton therapy beamline dedicated to uveal melanoma treatment and an interinstitutional comparison. *Med Phys.* 2021;48:4506-22. doi: 10.1002/mp.15024.
86. Gillam M, Fenech GA, Chadwick O, Nairn J, Chadha V, Connolly J, et al. When Is the Optimum Radiological Response to Proton Beam Therapy in Uveal Melanoma? *Ocul Oncol Pathol.* 2023;9:130-7. doi: 10.1159/000533308.
87. Maschi C, Thariat J, Herault J, Caujolle JP. Tumour Response in Uveal Melanomas Treated with Proton Beam Therapy. *Clin Oncol (R Coll Radiol).* 2016;28:198-203. doi: 10.1016/j.clon.2015.08.007.
88. Tang MCY, Ferreira TA, Marinkovic M, Jaarsma-Coes MG, Klaassen L, Vu THK, et al. MR-based follow-up after brachytherapy and proton beam therapy in uveal melanoma. *Neuroradiology.* 2023;65:1271-85. doi: 10.1007/s00234-023-03166-1.
89. Dendale R, Lumbroso-Le Rouic L, Noel G, Feuvret L, Levy C, Delacroix S, et al. Proton beam radiotherapy for uveal melanoma: results of Curie Institut-Orsay proton therapy center (ICPO). *Int J Radiat Oncol Biol Phys.* 2006;65:780-7. doi: 10.1016/j.ijrobp.2006.01.020.
90. Egger E, Schalenbourg A, Zografos L, Bercher L, Boehringer T, Chamot L, et al. Maximizing local tumor control and survival after proton beam radiotherapy of uveal melanoma. *Int J Radiat Oncol Biol Phys.* 2001;51:138-47. doi: 10.1016/s0360-3016(01)01560-7.
91. Marinkovic M, Pors LJ, van den Berg V, Peters FP, Schalenbourg A, Zografos L, et al. Clinical Outcomes after International Referral of Uveal Melanoma Patients for Proton Therapy. *Cancers (Basel).* 2021;13. doi: 10.3390/cancers13246241.
92. Seibel I, Cordini D, Rehak M, Hager A, Riechardt AI, Boker A, et al. Local Recurrence After Primary Proton Beam Therapy in Uveal Melanoma: Risk Factors, Retreatment Approaches, and Outcome. *Am J Ophthalmol.* 2015;160:628-36. doi: 10.1016/j.ajo.2015.06.017.
93. Sahoo NK, Ranjan R, Tyagi M, Agrawal H, Reddy S. Radiation Retinopathy: Detection and Management Strategies. *Clin Ophthalmol.* 2021;15:3797-809. doi: 10.2147/OPHT.S219268.
94. Mantel I, Schalenbourg A, Bergin C, Petrovic A, Weber DC, Zografos L. Prophylactic use of bevacizumab to avoid anterior segment neovascularization following proton therapy for uveal melanoma. *Am J Ophthalmol.* 2014;158:693-701 e2. doi: 10.1016/j.ajo.2014.07.002.
95. Shields CL, Dalvin LA, Chang M, Mazloumi M, Fortin P, McGarrey M, et al. Visual Outcome at 4 Years Following Plaque Radiotherapy and Prophylactic Intravitreal Bevacizumab (Every 4 Months for 2 Years) for Uveal Melanoma: Comparison With Nonrandomized Historical Control Individuals. *JAMA Ophthalmol.* 2020;138:136-46. doi: 10.1001/jamaophthalmol.2019.5132.



Chapter 2

Magnetic Resonance Imaging in the Clinical Care for Uveal Melanoma Patients: A Systematic Review from an Ophthalmic Perspective

Collaboration chapter

M.G. Jaarsma-Coes & L. Klaassen*, M. Marinkovic, G.P.M. Luyten
T.H.K. Vu, T.A. Ferreira, J.W.M. Beenakker

Cancers (2023). doi: 10.3390/cancers15112995

** These authors contributed equally*

ABSTRACT

Conversely to most tumour types, magnetic resonance imaging (MRI) was rarely used for eye tumours. As recent technical advances have increased ocular MRI's diagnostic value, various clinical applications have been proposed. This systematic review provides an overview of the current status of MRI in the clinical care of uveal melanoma (UM) patients, the most common eye tumour in adults. In total, 158 articles were included. Two- and three-dimensional anatomical scans and functional scans, which assess the tumour micro-biology, can be obtained in routine clinical setting. The radiological characteristics of the most common intra-ocular masses have been described extensively, enabling MRI to contribute to diagnoses. Additionally, MRI's ability to non-invasively probe the tissue's biological properties enables early detection of therapy response and potentially differentiates between high- and low-risk UM. MRI-based tumour dimensions are generally in agreement with conventional ultrasound (median absolute difference 0.5 mm), but MRI is considered more accurate in a subgroup of anteriorly located tumours. Although multiple studies propose that MRI's 3D tumour visualisation can improve therapy planning, an evaluation of its clinical benefit is lacking. In conclusion, MRI is a complementary imaging modality for UM of which the clinical benefit has been shown by multiple studies.

INTRODUCTION

Although magnetic resonance imaging (MRI) has been used to image uveal melanoma patients since its introduction in the 1980s [1,2], it was sparsely used in clinical practice as eye-motion resulted in a low image quality. As a result, the diagnosis and treatment of intra-ocular tumours was primarily based on ophthalmic imaging modalities, such as fundoscopy and ultrasound, conversely to tumours in other parts of the body, where advances in MR- and CT-imaging have significantly improved clinical care. In the last decade, however, technical developments have enabled the acquisition of high-quality MR-images of the eye and orbit [3,4,5,6,7,8,9,10]. As a result, MR-imaging has been proposed for different ocular conditions such as inflammation, refractive conditions, glaucoma and several malignancies [10,11,12,13,14,15,16,17,18,19,20,21].

For uveal melanoma (UM) patients specifically, multiple clinical applications of ocular MRI have been proposed [11,22,23,24,25,26,27,28,29,30]. MRI makes it possible to obtain a complete 3D visualisation of the eye and orbit, without the limited penetration depth of ultrasound or fundoscopy [31,32]. This 3D visualisation makes MRI more accurate in measuring the dimension of anterior tumours, especially if conventional ultrasound is not able to visualise the entire tumour due to its limited penetration depth or limitations in probe placement [32]. Furthermore, a study comparing MRI and histopathological findings suggests that MRI is more reliable than ultrasound in the detection of optic nerve invasion and extrascleral extension [28]. Different studies, therefore, propose methods to use MRI to further advance the treatment planning of these patients [33]. Additionally, MRI can probe different biological aspects of the tumour without the need of a biopsy. These new imaging biomarkers have proven to aid in the diagnosis and follow-up of patients with UM and other intraocular masses and may also provide prognostic information [15,26,28,34,35,36,37,38,39].

With MRI emerging as a clinically valuable imaging modality for the eye, it is important to understand its strengths and limitations from an ophthalmic perspective, especially since a high level of care has already been attained with the conventional techniques. However, as most ocular-MRI studies are described from a radiological or physics perspective, their implications for ophthalmic clinical practice are often not fully explored. Therefore, we systematically reviewed the ocular MRI literature from an ophthalmic perspective, with particular attention to the clinical implications of MRI for patients with uveal melanoma. In this review, we will describe the characteristics of UM on MRI, followed by possible clinical applications of MRI in the differential diagnosis, treatment planning and follow-up of these patients. Finally, these evaluations will be combined into indications for ocular MRI in the care of patients with an intraocular mass.

MATERIALS AND METHODS

This systematic review was carried out according to the PRISMA 2020 statement [40]. PubMed and the Cochrane Library were searched for full-text articles in English, published between January 2000 and December 2022 using the following term:

("ocular ma*" OR "intraocular ma*" "Uveal melanoma" OR "Choroidal melanoma" OR "iris melanoma") AND ("magnetic resonance imaging [MeSH] OR "MRI")

In Rayyan [41], all records were screened jointly by two authors (MJC, JWB) based on the title and abstract. The full text was read for all potentially eligible records. Articles were excluded if no details were provided on the use of MRI (full text only), it did not involve an intraocular mass or only considered metastatic disease outside the orbit. Additionally, studies that did not include in vivo MR-imaging were excluded. Single case studies were excluded when larger studies were available on a similar topic. These case studies are listed in Appendix A. The remaining articles were assessed to determine the contribution of MRI in the clinical care for patients with an intraocular mass. Furthermore, records were identified from reference lists of included studies. An overview of the search and inclusion process is shown in Figure 1.

In this review, data from several studies were combined for quantitative MRI measures of the tumour perfusion and diffusivity [11,26,28,34,35,36,37,38,42,43,44,45]. Moreover, the data comparing ultrasound-based and MRI-based tumour dimensions of different studies were combined in a Bland–Altman plot in order to provide a comprehensive evaluation of the agreement between these modalities [3,28,32,33,46,47]. The methods for this review were not previously registered.

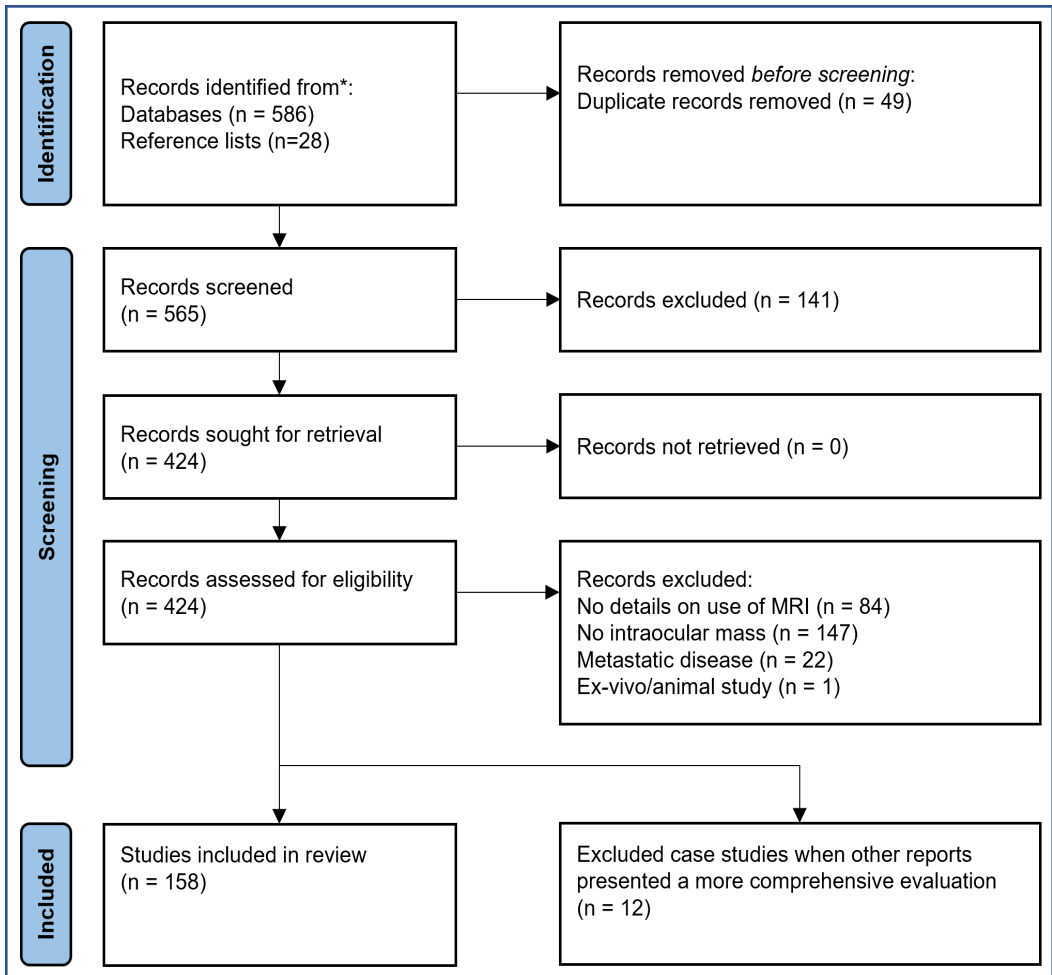


Figure 1. Flowchart of the search and inclusion process.

UVEAL MELANOMA ON MRI

Modern ocular MRI scans are preferably performed on a 3T MRI scanner with a surface coil as the increased signal to noise ratio delivers a higher diagnostic value compared to scans acquired with a head coil or a 1.5 tesla scanner [10,21,48]. These protocols preferably contain both two- and three-dimensional anatomical sequences complemented with functional imaging [10,11,21]. The two-dimensional sequences are particularly useful to evaluate anatomy, layer of origin and to assess the margins of the lesion, while the three-dimensional sequences allow for a comprehensive assessment of tumour geometry through multiplanar reconstructions. This three-

dimensional evaluation proved to be particularly valuable in the determination of the tumour dimensions in the context of therapy selection, planning and follow-up [3,10,47]. In addition to these anatomical scans, functional MRI-scans provide different quantitative imaging biomarkers which can aid in the differential diagnosis, staging and assessment of therapy response [26,28,34,37,38,39]. It has been shown that these MRI scans can be performed safely and reliably at field strengths up to 7 tesla, in patients with modern intraocular lenses (IOL) or a Baerveldt glaucoma implant, after silicon oil tamponade and with tantalum markers sutured to the sclera [33,49,50,51,52,53,54,55].

Anatomical Evaluation

In MRI, multiple images with different contrasts are generally jointly evaluated. These different contrasts provide the complementary information needed to distinguish different pathologies such as intraocular masses, associated retinal detachment, necrosis and other treatment related effects [21,22,28,56,57,58]. For the eye, these contrasts should at least include T2-weighted scans and T1-weighted scans, the latter before and after administration of an intravenous gadolinium-based contrast agent (Figure 2A–C).

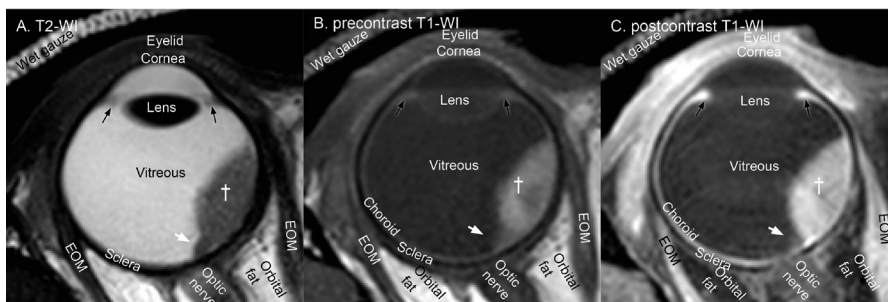


Figure 2. Transversal anatomical MR-images of a patient with a uveal melanoma (dagger) and associated retinal detachment (white arrow). (A) On T2-weighted images, most lesions are hypointense compared to the vitreous. (B,C) T1-weighted imaging before (B) and after (C) contrast showing an hyperintense mass which is enhancing. Note that the choroid, extra ocular muscles (EOM), ciliary body (black arrow) and eyelid also enhance.

The signal intensity characteristics of UM on these types of MR-images have been described extensively [10,11,26,28,34,36,37,45,56,59,60,61,62,63,64,65,66,67,68,69,70,71,72,73,74,75,76]. As almost all intraocular lesions, including UM, are hyperintense on T1- and hypointense on T2-weighted imaging compared to the vitreous, Ferreira [28] proposed to use the choroid and nearby extraocular muscle as reference on T1- and on T2-weighted imaging, respectively. Using these tissues as a reference, she

described that UM are mostly hyperintense on T2-weighted imaging and hyperintense or isointense on T1-weighted imaging. The signal intensity on T1-weighted imaging correlated significantly to pigmentation [28,72], which is also clearly visible in Figure 3B, where the melanotic part (blue arrow) is more hyperintense than the amelanotic part (pink arrow). As opposed to retinal detachment, all UM, but also retinoblastomas and haemangiomas, enhance after contrast administration [11,28,74,77,78]. These characteristics are an important first step to differentiate UM from accompanying phenomena, such as detachments of the retina and choroid, which can be identified based on signal intensity and morphology [22,79]. The signal intensity of retinal detachment varies based on its contents [11] and can have a similar signal intensity as the UM on non-enhanced scans (Figure 2A,B, arrow). Therefore, contrast-enhanced T1-weighted scans are important to differentiate retinal detachment from UM, as the retinal detachment does not enhance (Figure 2B,C, arrow) [10,22,28]. Retinal detachment can be observed reliably on MRI [28,75]; however, small retinal detachments might be missed on MR-images with poorer image quality [48,80,81]. Haemorrhagic retinal detachment and other intraocular haemorrhages are easier to recognise in their subacute stage when they are hyperintense on native T1-weighted images and do not enhance after contrast administration [10,11]. In contrast to retinal detachment, necrosis and inflammation are better depicted on T2-weighted imaging, as is illustrated in Figure 3 [22,56]. Using the aforementioned features, MRI is able to distinguish UM from accompanying features or other pathologies, such as peripheral exudative haemorrhagic chorioretinopathy [25].

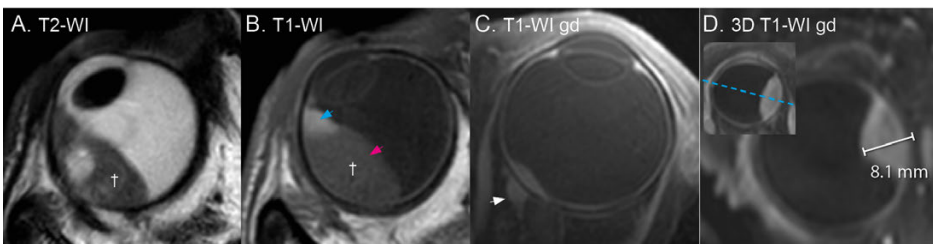


Figure 3. (A,B) patient with necrosis (A) in a bipartite uveal melanoma (cross). The amelanotic part (B), pink arrow) is isointense, while the melanotic part (B), blue arrow) is hyperintense compared to the choroid on T1. (C) Extraocular extension (white arrow) is best visualised on the contrast-enhanced T1-weighted scan with fat suppression. (D) A volumetric scan allows for three-dimensional visualisation of the tumour and surrounding structures and provides the most accurate dimension measurements (line) as the measurement plane (D) can be reconstructed perpendicular to the sclera (dotted line).

One of the advantages of MRI compared to ultrasound and fundoscopy is that the complete orbit can be evaluated. This allows for a more accurate screening for extrascleral extension, optic nerve invasion and inflammatory processes [11,15,27,28,29,30,82,83,84,85,86,87,88,89,90,91,92,93,94,95]. MRI generally outperforms ultrasound in screening for extrascleral extension (Figure 3C) [27,28,29,30]. Only small extrascleral extensions have been reported to be missed on both MRI and ultrasound [28,29]. In the screening for extrascleral extension, it is important to use fat-suppressed scans, as they provide better differentiation of a potential extrascleral extension of the tumour and orbital fat [10]. Additionally, a three-dimensional assessment of the enhancing extraocular component is advised, as the muscle insertions might be mistaken for extrascleral extension [28,29,30]. Brisse et al. reported only a limited accuracy in identifying optic nerve invasion in retinoblastoma on their contrast enhanced T1 sequences (AUC = 0.64; 95% CI, 0.55–0.72) [96]. On the other hand, MRI was found to reliably demonstrate or exclude optic nerve invasion in fourteen UM cases [28]. In this particular series, one case of optic nerve invasion was missed on ultrasound, but seen on MRI. Therefore, Seibel et al. recommend performing an MRI for all patients with a juxtapapillary located UM, as even small melanoma might invade the optic nerve [97].

Functional Scans

In addition to these anatomical assessments, functional MRI can provide multiple types of quantitative information on function and biology of an intraocular mass [15,26,28,34,35,36,37,38,39,68,72,98,99,100]. In oncology, perfusion weighted imaging (PWI) and diffusion weighted imaging (DWI) are the most commonly used functional MRI techniques and have proven to be valuable in the differential diagnosis and assessment of therapy response in other tumour sites.

Similar to fluorescein angiography, in PWI, an image is acquired every few seconds during and after the administration of an intravenous contrast agent (Figure 4A,B). Current clinical MRI scanners can acquire a three-dimensional image of the complete eye with an isotropic resolution of at least 1.5 mm every 2 s [28,72]. As a result, the complete lesion, and not only its ventral surface, can be assessed with PWI. Additionally, the concentration of contrast agent can be determined on these images, which, through pharmacokinetic modelling [72,101], provides quantitative information of the tissue's microvasculature [37,72,102].

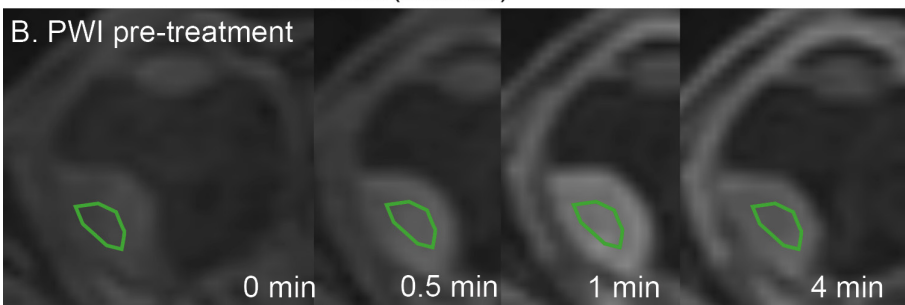
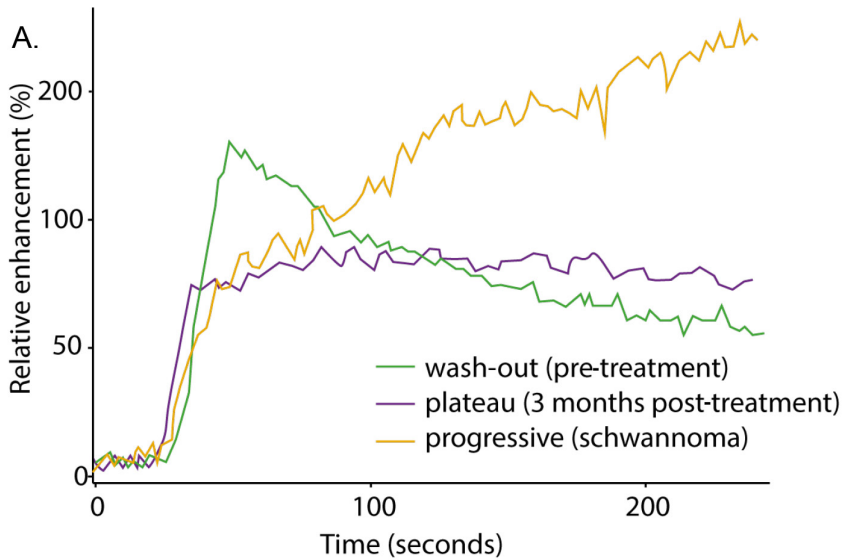


Figure 4. (A) The three different time intensity curves (TICs): A wash-out TIC of a UM patient before treatment, a plateau TIC from the same patient 3 months after treatment and a progressive curve in a patient with a schwannoma. (B) Four timepoints of the PWI-MRI of the same UM patient before treatment, showing an increase in signal intensity in the tumour at timepoint 0.5 and 1 min and decrease towards the end of the acquisition (4 min), resulting in the green time intensity curve (A).

In clinical practice, the amount of signal enhancement, the peak intensity and the temporal evolution of the enhancement are assessed [10,22,28,43,74]. This proves a relatively straightforward description of the uptake and potential outflow of contrast agent. For UM, a combined analysis of two studies showed a peak intensity of 1.60 ± 0.39 ($n = 51$) [28,43]. Absence of enhancement or lower peak intensities are indicative for retinal detachment [10,22,28] or benign lesions [43], although haemangiomas show a stronger enhancement than UM [74]. For the interpretation of these metrics,

it is important to acknowledge that the lesion's pigmentation is a confounding factor on the observed enhancement [72].

Temporal evolution of the contrast uptake is visualised by a Time Intensity Curve (TIC) and is commonly characterised as progressive, plateau or wash-out (Figure 4A) [28]. Similar to other masses, the TIC shape of intraocular masses is indicative of its malignancy. Benign lesions generally have a progressive or plateau TIC, whereas malignant lesions often show a wash-out or plateau TIC [34]. A combined analysis of two studies [28,34] shows that most UM showed a wash-out TIC (69%), whereas the remaining UM showed a plateau TIC (31%). As a result, a progressive curve is considered a clear indication that the lesion is of another aetiology, as it was not observed in any of the UM patients. In UM, the amount of wash-out is reported to decrease after radiotherapy and in these patients, progressive curves have been observed (Figure 4A) [46]. Interestingly, these perfusion changes were observed before changes in size became apparent, making PWI a potential early biomarker of therapy response [46]. Quantitative analysis of these data, for example, through pharmacokinetic modelling, is reported to be indicative for patient prognosis. For example, higher peak intensities and transfer rates between blood plasma and extravascular extracellular space were found in UM with monosomy 3, an important genetic marker for metastatic risk [28,37].

The second commonly used functional MRI technique in oncology is DWI, a technique which assesses the diffusion (i.e., mobility) of water molecules within a tissue. This diffusion, quantified as an apparent diffusion coefficient (ADC) [102], is a reflection of the tissue's density and cell size and has been found to be a non-invasive biomarker of a lesion's malignancy [15]. For the eye, obtaining DWI has been challenging due to eye motion and the magnetic field inhomogeneities present in the orbit, but several DWI techniques have been developed, enabling ocular applications of this technique [10,35,103,104,105,106].

In the orbit, a low ADC is indicative of malignant lesions, whereas benign lesions, retinal detachment, inflammation and lesions after treatment tend to have an ADC above $1.35 \times 10^{-3} \text{ mm}^2/\text{s}$ [38,39]. Several studies measured the ADC of UM [11,28,36,37,44,45] and found a combined ADC of $1.11 \pm 0.24 \times 10^{-3} \text{ mm}^2/\text{s}$ (Figure 5). Interestingly, one of these studies consistently reported lower ADC values for both the UM and vitreous [36], illustrating the importance of locally validating the used protocol against the values presented in literature [107].

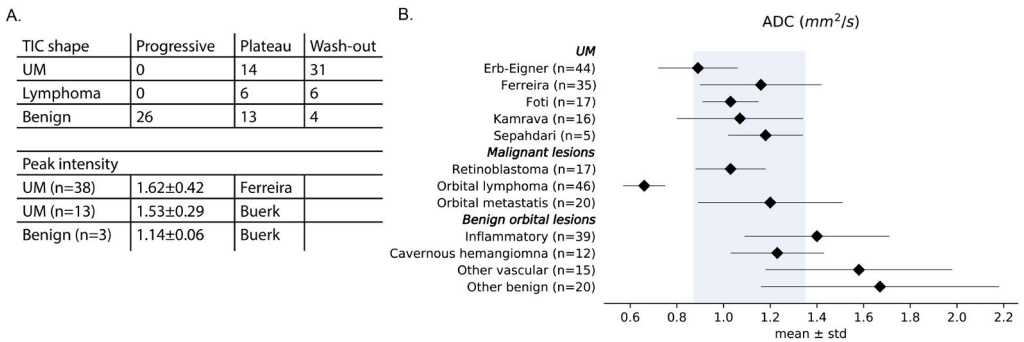


Figure 5. (A) Two-thirds of the perfusion classifications in UMs show a wash-out TIC, whereas most benign lesions have a progressive curve, which is not observed in UM. Plateau TICs are observed in both benign and malignant ocular masses [28,34,41]. On average, UMs show a relative enhancement of 1.6 after contrast administration [28,42]. (B) The ADC value, a measure of diffusion, of UM is $1.11 \pm 0.24 \times 10^{-3} mm^2/s$ (gray area), which is lower than most benign orbital lesions and higher than orbital lymphoma [26,28,35,36,37,38].

DIFFERENTIAL DIAGNOSIS

Conventional ophthalmic imaging, such as ultrasound and fundoscopy, is generally sufficient to differentiate UM from other intraocular masses [108,109]. However, in some patients, not all necessary criteria can be accurately evaluated due to the size and/or location of the mass or due to the presence of opaque media such as cataract, vitreous haemorrhage or massive choroidal effusion [11,28,110,111]. In these cases, MRI can contribute to the differential diagnosis, as it can assess different aspects of the lesion such as its origin, signal intensities and functional parameters. Although prospective studies on the accuracy of MR-based differential diagnosis of intraocular masses are still lacking, several studies and case reports provide indications of its current value.

Different studies showed that by using only anatomical information, such as location, origin and signal intensity, MRI can contribute to the differential diagnosis for various intraocular masses including retinal pigment epithelium adenomas [73], cysts [112], retinoblastoma [21,77,113,114,115], Coats disease [116], uveitis [15,117], choroidal effusion [118], neurofibroma [119] and UM [120,121]. Additionally, different reports showed that anatomical MRI can identify choroidal haemangioma [74,122], schwannoma [123,124] and scleritis [125,126]. However, other studies report that relying on anatomical characteristics alone can result in an inconclusive or even

erroneous interpretation of the images, as the anatomical characteristics are often similar for distinct pathologies. For example, although UM are commonly hyperintense on T1 due to their pigmentation, making this an important clue in the differential diagnosis, melanocytomas are also hyperintense on T1. Furthermore, as approximately 15% of UM are unpigmented [28,127,128], the lack of T1-hyperintensity alone is not sufficient to exclude UM from the differential diagnosis. As a result, an MR-based diagnosis without inclusion of functional scans has been reported to be inconclusive for teratocarcinoma [129], malignant rhabdoid tumour [130], leiomyoma [131,132], lymphoma [133] and intraocular metastasis [75,94].

Given the different perfusion and diffusion characteristics of distinct intraocular and orbital masses, it is recommended to include functional imaging when the presence of a mass in the eye or orbit is expected [11,15,17,28,134]. Based on signal intensities alone, schwannomas, for example, can appear similar to an amelanotic UM [123], although the observed heterogeneous enhancement is less typical for UM [94,113,124]. PWI, however, provides a much stronger differentiation, as the observed progressive TIC (Figure 4) has not been found in any UM [124]. Similarly, lymphomas can be difficult to differentiate from UM on T1- and T2-weighted imaging [133]. However, the very low ADC values observed in lymphoma, $0.66 \pm 0.09 \times 10^{-3} \text{ mm}^2/\text{s}$ compared to $1.11 \pm 0.24 \times 10^{-3} \text{ mm}^2/\text{s}$ for UM, can provide a clear indication of the lesion's diagnosis [38,135,136,137,138]. Furthermore, one study reported the use of an MRI-based radiomics model to differentiate uveal melanoma from other intraocular masses, such as ocular metastases and melanocytomas [100].

THERAPY PLANNING

Conventionally, MRI has had a limited role in ocular radiotherapy [139,140]. A notable exception has been stereotactic radiosurgery, where MRI is reportedly being used to complement CT imaging [141,142,143,144,145,146,147] and has shown to contribute to an increase in local control [148]. However, for other forms of ocular radiotherapy, such as brachytherapy and proton beam therapy, the therapy is planned using a dome-shaped model to approximate the tumour geometry. This model is conventionally based on the tumours prominence and basal diameters as obtained by ultrasound, complemented by intra-operative data and optical imaging [139]. In contrast to this approximate description of the tumour geometry, MRI is proposed to provide a complete three-dimensional visualisation of the tumour and surrounding structures [3].

In general, a good agreement between ultrasound and MRI-based tumour dimensions is found (Figure 6) [30,32,33,46,47]. However, MRI was considered more reliable when the full tumour extent could not be visualised on ultrasound [32]. In these cases, a discrepancy between the modalities was often observed. Four studies [28,32,33,46] compared ultrasound- and MRI-based tumour dimension measurements using a modern MRI protocol, including three-dimensional contrast enhanced scans [48] with an isotropic acquisition resolution of at least 1.0 mm. A combined analysis of 72 patients (Figure 6) showed that, on average, the ultrasound measurements were slightly larger than the MRI measurements ($p < 0.01$, Prominence; median 6.3 mm vs. 6.1 mm and largest basal diameter (LBD); 14.7 mm vs. 14.0 mm). The full tumour extent was more often not visible in anterior tumours compared to posterior tumours (78% and 22% respectively, $p < 0.001$), which resulted in an increased median absolute difference in prominence of 0.2 mm and LBD of 1.2 mm, respectively (Figure 6C), with both MRI and ultrasound measurements performed including sclera.

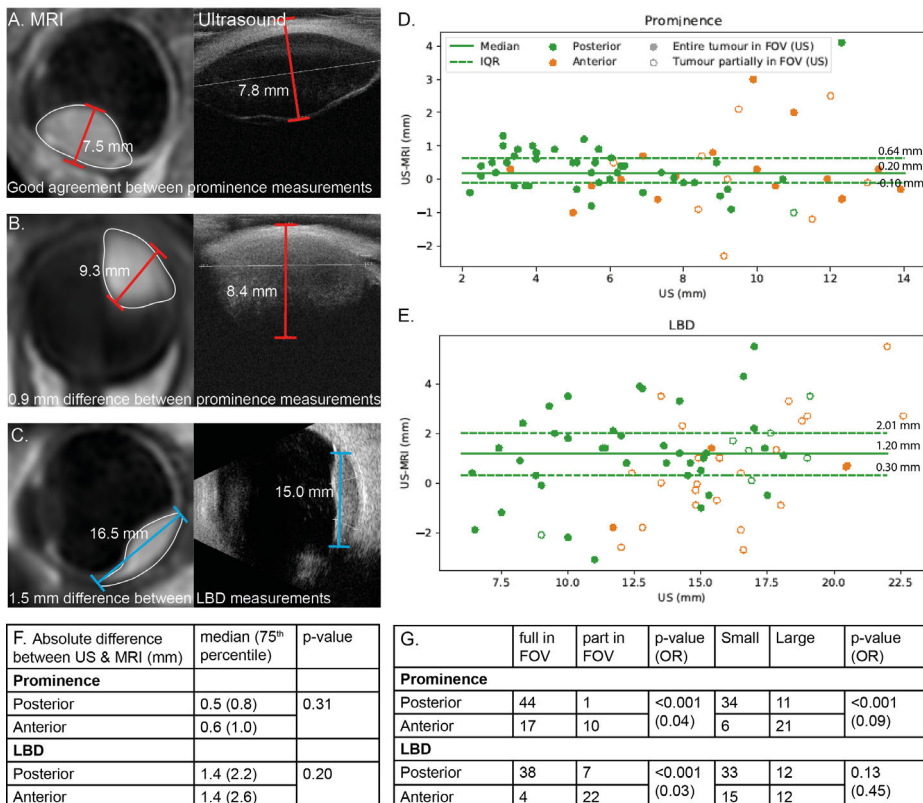


Figure 6. Comparison between MRI and ultrasound-based tumour measurements. Although both modalities generally are in agreement (A), larger differences are found for anterior

Figure 6 Continued

tumours (A,B), orange markers in (D,E) and when the full tumour extent was not visible on ultrasound ((C), open circles in (D,E)). Overall, the prominence and LBD measurements were larger on ultrasound (Wilcoxon signed-rank test, $p < 0.01$) (F) and anterior tumours were more often not fully visible on ultrasound ($p < 0.001$) (G). Small tumours were defined as tumours with a prominence including sclera < 7 mm and an LBD < 16 mm.

Although several studies have shown the feasibility of fully three-dimensional MRI-based therapy planning [97,135,136,149,150,151,152], none of these methods are available clinically. A recent study showed that MRI can also improve the conventional model-based, planning, as in specific cases, it provided more accurate axial length and tumour–marker distance measurements [33]. Moreover, modern planning systems such as OCTOPUS, RayOcular and Plaque Simulator do provide the option to show MR-images in the therapy planning, which can subsequently be used to verify, and, when needed, adapt, the model-based treatment plan to conform the three-dimensional visualisation of the MRI [139,153,154,155,156]. Others propose therapy planning by fusing MR-images with fundus photographs, to provide a better localisation of the fovea, one of the main organs at risk in ocular radiotherapy, which is unfortunately not visible on MRI [81]. In this context of increasing the accuracy of ocular radiotherapy, it is comforting to know that no significant changes were observed in tumour and eye shape between the prone MRI-scanning position and the sitting position used during ocular proton therapy [157].

Furthermore, two studies have shown the feasibility of verifying brachytherapy plaque position with 1.5 tesla MRI [152,158]. However, the clinical benefit of this application still needs to be demonstrated.

FOLLOW-UP

A reduction in tumour prominence or volume, as obtained by ultrasound, is clinically one of the primary signs of therapy response [46,159,160,161]. In general, a rapid reduction in tumour prominence is observed after brachytherapy, while after ocular proton beam therapy, an initial stable or even a temporarily increase in prominence is not uncommon. For UM patients, 3 months post ruthenium brachytherapy, a clinically significant reduction in prominence is already apparent on both MRI and ultrasound [46]. In proton therapy, however, this reduction can take months up to a year to occur and a temporary increase in tumour prominence is not uncommon [161].

Several studies showed that MRI can be used to quantify the reduction in tumour size after treatment [46,162,163,164,165]. One study prospectively compared MRI and ultrasound-based prominence measurements for patients treated with proton beam therapy or brachytherapy [46]. In this study, ultrasound and MRI were generally in agreement, but treatment-induced effects, such as extraocular inflammation, resulted in an overestimation of the tumour prominence on ultrasound in some patients at 3 and 6 months post treatment. Additionally, this study reported that the volumetric assessment provided by MRI enabled a more reliable evaluation of the small changes in volume in the first months after proton therapy.

Different studies propose that functional MR-imaging can provide early biomarkers of therapy response [26,44,46]. Favourable PWI changes, such as a decrease in wash-out, have been observed as early as 3 months after treatment, and also when changes in size were not yet apparent [46]. Other studies propose an increase in ADC as a measure for therapy response [26,44,46,163]. Although, on average, the diffusivity indeed increases after therapy, the confounding effect of (micro)necrosis might not make it a useful biomarker on the individual patient level [46,56];' by a '.

Finally, exudative retinal detachment and sick tumour syndrome, a known side effect of irradiation in patients with an intraocular mass, is sometimes treated with vitrectomy with tumourectomy and silicon oil tamponade. As the silicon oil prevents accurate ultrasound imaging, follow-up with conventional ophthalmic imaging is hindered. Monitoring these patients with MRI has been reported to prevent secondary enucleation by differentiating local tumour recurrence from scarred tumour residue [53].

DISCUSSION

In recent years, different MRI techniques dedicated for imaging the eye and orbit have become clinically available, enabling the acquisition of high quality MR-images of the eye in regular clinical care. As a result, an increasing number of ophthalmic applications of MRI has been proposed in the last five years, especially related to ocular oncology. This increase can also be observed in the scientific literature, where the number of ocular oncology-related MRI-studies increased from 55 in 2000–2005 to 151 for the last 5 years. Moreover, since the radiological characteristics of the most common primary ocular tumours, UM and retinoblastoma, have now been extensively described, MRI can provide a similar contribution to the care for ocular oncology patients as it does for patient groups with other tumours.

From an imaging point of view, the eye is a relatively unique organ as it can be accurately imaged with optical techniques. Conversely to other tumour sites, adequate care can often be provided for intraocular masses without radiological imaging, as the ophthalmic imaging modalities provide sufficient information for its diagnosis, treatment and follow-up [11,28]. Notwithstanding the clinical importance of these conventional modalities, multiple studies show the added value of MRI in specific cases, as MRI can provide information not attainable with optical and ultrasonic imaging. In particular, three-dimensional visualisation of the eye and tumour, and functional assessments of the lesion's biology, especially diffusion and perfusion weighted imaging, provide clinically valuable complementary information.

Although fundoscopic and ultrasonic imaging are generally sufficient for accurate diagnosis of intraocular masses, in various situations they cannot provide a definite diagnosis, such as for lesions behind the iris, and in cases with an accompanying vitreous haemorrhage or dense cataracts. Now, the anatomical and functional characteristics of a lesion on MRI can aid in the diagnosis for these cases, instead of an invasive biopsy. For a reliable evaluation of the MR-images, it is, however, critical that the radiologist is sufficiently acquainted with the appearance of intraocular masses on MRI, especially since not all radiological characteristics of all types of intraocular masses are known, nor have a 100% specificity. As a result, definite diagnoses based on MRI alone can be challenging. However, as a comprehensive radiological description of UM is available, a differentiation between UM and other masses is, in our experience, often possible, especially in a combined evaluation with ophthalmic data. In this context, communication between the radiology and ophthalmology professions is vital. In our experience, an MRI can also be beneficial in an atypical presentation of a mass, for example, for a very young patient with a lesion which, on ophthalmic imaging, appears as a UM. While especially the functional MRI measures can provide an independent confirmation of the diagnosis, we have also seen different cases where these biomarkers combined with MRI's visualisation of the mass's internal structures, point towards a different diagnosis, which was then later confirmed through biopsy. In general, MRI can be used as an additional diagnostic tool, especially for atypical presentations of intraocular lesions, if visualisation is impossible with conventional ophthalmic imaging methods or in situations where the diagnosis is uncertain.

For the treatment selection of intraocular masses, the benefit of MRI mainly depends on the type of lesion and the available treatment options. For example, in retinoblastoma, the main goal of the MRI is diagnostic confirmation and detection of local tumour extent

[21]. Although for UM, three-dimensional visualisation on MRI generally provides a more accurate size determination than conventional ultrasound [32,33], the current treatment protocols effectively incorporate these uncertainties, resulting in high rates of local control (>95%) [166,167]. When, however, multiple treatment options are available for the patient based on tumour dimensions, for example, brachytherapy and proton therapy, a small change in tumour dimensions can have a direct impact on the choice of treatment modality [3]. As small UM are generally accurately assessed with ophthalmic imaging, an MRI is generally not indicated for treatment selection and planning. However, for larger and anteriorly located UM, larger differences are observed between MRI and ultrasound measurements. In these cases, especially when the full tumour extent cannot be visualised on ultrasound, we advise performing an MRI, given the >0.5 mm difference in prominence in 72% of these patients (Figure 6). In addition to these size measurements, MRI can reportedly provide a more reliable screening for optic nerve invasion and extrascleral extension. For juxtapapillary tumours, an MRI has, therefore, been advised [97]. When an extrascleral component is suspected, we do advise performing an MRI, as it might not only impact treatment selection, but also aid in surgical planning.

Given the relatively the set dimensions of ruthenium plaques used in ocular brachytherapy, an MRI is generally of limited value for treatment planning purposes in ruthenium brachytherapy. When treating with COMS iodine plaques, which allow for a customisation of the spatial dose profile [168], MRI could be incorporated in treatment planning. Although in the Eye Physics Plaque Simulator, a planning software for these plaques, MR-images can be used as an input for the planning; the clinical benefits of this step have not yet been published. For ocular proton therapy, MRI is increasingly being used, and was considered the second most important area of future developments [169]. While the conventional model-based approach to treatment planning, as used in EyePlan and EOPP, does not rely on radiological imaging, more modern treatment planning software, including OCTOPUS and RayOcular, do provide the incorporation of MR-images in the planning. Although an evaluation of the benefit of adding three-dimensional MRI-visualisation to the ophthalmic imaging is still subject of current studies [81,135,149], we recently showed that adding MR-based measurements to the conventional model-based planning can provide a more accurate description in 20/23 patients [33].

Compared to the diagnosis and treatment of intraocular masses, the value of MRI in the follow-up after treatment has been studied less extensively. Conventionally, a reduction in tumour prominence is considered the primary sign of therapy response. UM treated with brachytherapy generally show a rapid reduction in prominence, making the use of MRI for follow-up of little clinical value for these patients. For patients

treated with ocular proton therapy, however, such a reduction in prominence can take up to a year to become apparent, suggesting that an alternative biomarker of therapy response could be of value. Until present, only two studies have prospectively assessed MRI in the follow-up of these patients [26,46]. Although functional MRI, especially perfusion weighted imaging, is proposed as an early biomarker of therapy response, independent validation of these findings in a larger cohort is still needed.

With the advent of new treatments for specific types of metastatic spread of UM [170,171], MRI-based staging and prognostication of intraocular masses might become clinically relevant in the coming years. Different studies have shown that known histopathological variants, such as monosomy 3 and the presence of microvascular loops, result in different perfusion characteristics that can be detected with MRI [28,37]. Future studies should validate these findings in larger patient groups, as well as investigating the relation of perfusion-weighted MRI with other genetic factors, such as BAP1, EIF1AX and 8q status. An additional area that warrants further prospective evaluation is the benefit of MRI in the differential diagnosis. In this respect, it would be beneficial to provide a diagnostic framework that combines the information of optical and MR-imaging, as, in our experience, this combination of disciplines provides pivotal clues for an unambiguous diagnosis.

Although performing an MRI-scan has proven to be cost-effective for specific indications, such as for treatment decision-making in tumours with an intermediate size [33,172], the wide availability and immediate access of the ophthalmic modalities will most certainly make them stay the primary imaging modality for ocular masses for the coming decade. Nevertheless, given the increase in (biological) information attainable by MRI, an increasing contribution of MRI in ocular oncology is expected.

CONCLUSIONS

With the advances of ocular MRI, a new way of visualising the eye and orbit has emerged which complements the information provided by the more commonly used fundoscopic and ultrasound imaging. MRI can aid differential diagnosis for atypical presentations of intraocular lesions, especially when visualisation is impossible or limited with conventional ophthalmic imaging methods. For these patients, the additional information provided by MRI might mitigate the need for an intra-ocular biopsy. Furthermore, when the tumour thickness and basal diameters make the patient eligible for multiple treatments, the three-dimensional visualisation of MRI can aid treatment decision making. Furthermore, we advise performing an MRI if optic nerve invasion or an extrascleral component is suspected. Finally, first evidence has been provided of the benefit of including MRI for

ocular proton beam therapy planning and the use of perfusion-weighted MRI as an early biomarker for treatment response assessment.

APPENDIX A

A list of case studies which were excluded when larger studies were available on a similar topic.

1. Rahman, A.M.; Selva, D.; Davis, G. Choroidal melanoma with extrascleral extension in an Australian Aboriginal man. *Clin. Exp. Ophthalmol.* **2007**, *35*, 187–189.
2. Wagle, A.M.; Wu, B.C.; Gopal, L.; Sundar, G. Necrosis of uveal melanoma post-COVID-19 vaccination. *Indian J. Ophthalmol.* **2022**, *70*, 1837–1840.
3. Das, D.; Deka, P.; Verma, G.; Kuri, G.C.; Bhattacharjee, H.; Bharali, G.; Pandey, D.; Koul, A.; Das, B.; Deka, A. IgG4-related intraocular inflammation masquerading as ciliary body melanoma in a young girl. *Indian J. Ophthalmol.* **2016**, *64*, 601–603.
4. Kimura, D.; Kida, T.; Sato, T.; Fukumoto, M.; Kohmoto, R.; Kojima, S.; Mizuno, H.; Sakaguchi, H.; Sugasawa, J.; Ikeda, T. A Case of Retinal Detachment with Unique Optical Coherence Tomography Findings after Gamma Knife® Radiosurgery Treatment for Choroidal Melanoma. *Case Rep. Ophthalmol.* **2018**, *9*, 17–23.
5. Shields, J.A.; Shields, C.L.; Kimmel, A.S.; Eagle, R.C., Jr. Contralateral blindness from chiasmal extension of unsuspected choroidal melanoma. *Ophthalmic Plast. Reconstr. Surg.* **2004**, *20*, 384–387.
6. Arevalo, J.F.; Shields, C.L.; Shields, J.A. Giant nodular posterior scleritis simulating choroidal melanoma and birdshot retinochoroidopathy. *Ophthalmic Surg. Lasers Imaging Retin.* **2003**, *34*, 403–405.
7. Cotliar, J.M.; Shields, C.L.; Meyer, D.R. Chronic orbital inflammation and fibrosis after retrobulbar alcohol and chlorpromazine injections in a patient with choroidal melanoma. *Ophthalmic Plast. Reconstr. Surg.* **2008**, *24*, 410–411.
8. Sheck, L.H.; Ng, Y.S.; Watson, M.; Vincent, A.L. Clinical findings and molecular diagnosis of retinoblastoma in older children. *Ophthalmic Genet.* **2013**, *34*, 238–242.
9. Tsukikawa, M.; Akinpelu, B.; Wangaryattawanich, P.; Scherpelz, K.; Stacey, A.W. Uveal melanoma incidentally diagnosed with neuroimaging, a case series of 3 patients. *Radiol. Case Rep.* **2022**, *17*, 54–59.
10. Richter, M.N.; Bechrakis, N.E.; Stoltenburg-Didinger, G.; Foerster, M.H. Transscleral resection of a ciliary body leiomyoma in a child: Case report and review of the literature. *Graefes Arch. Clin. Exp. Ophthalmol.* **2003**, *241*, 953–957.
11. Lindner, T.; Langner, S.; Falke, K.; Walter, U.; Krüger, P.C.; Pohlmann, A.; Zimpfer, A.; Stahnke, T.; Hadlich, S.; Guthoff, R.; et al. Anatomic and pathological characterization of choroidal melanoma using multimodal imaging: what is practical, what is needed? *Melanoma Res.* **2015**, *25*, 252–258.
12. Wei, W.; Mo, J.; Jie, Y.; Li, B. Adenoma of the retinal pigment epithelium: A report of 3 cases. *Can. J. Ophthalmol.* **2010**, *45*, 166–170.

REFERENCES

1. Hawkes, R.C.; Holland, G.N.; Moore, W.S.; Rizk, S.; Worthington, B.S.; Kean, D.M. NMR imaging in the evaluation of orbital tumors. *AJNR Am. J. Neuroradiol.* **1983**, *4*, 254–256.
2. De Keizer, R.; Vielvoye, G.; de Wolff-Rouendaal, D. Nuclear Magnetic Resonance Imaging of Intraocular Tumors. *Am. J. Ophthalmol.* **1986**, *102*, 438–441.
3. Beenakker, J.-W.M.; Ferreira, T.A.; Soemarwoto, K.P.; Genders, S.W.; Teeuwisse, W.M.; Webb, A.G.; Luyten, G.P.M. Clinical evaluation of ultra-high-field MRI for three-dimensional visualisation of tumour size in uveal melanoma patients, with direct relevance to treatment planning. *Magn. Reson. Mater. Phys. Biol. Med.* **2016**, *29*, 571–577.
4. Berkowitz, B.A.; McDonald, C.; Ito, Y.; Tofts, P.; Latif, Z.; Gross, J. Measuring the human retinal oxygenation response to a hyperoxic challenge using MRI: Eliminating blinking artifacts and demonstrating proof of concept. *Magn. Reson. Med.* **2001**, *46*, 412–416.
5. Lindner, T.; Langner, S.; Graessl, A.; Rieger, J.; Schwerter, M.; Muhle, M.; Lysiak, D.; Kraus, O.; Wuerfel, J.; Guthoff, R.F.; et al. High spatial resolution in vivo magnetic resonance imaging of the human eye, orbit, nervus opticus and optic nerve sheath at 7.0 Tesla. *Exp. Eye Res.* **2014**, *125*, 89–94.
6. Lemke, A.J.; Alai-Omid, M.; Hengst, S.A.; Kazi, I.; Felix, R. Eye imaging with a 3.0-T MRI using a surface coil—A study on volunteers and initial patients with uveal melanoma. *Eur. Radiol.* **2006**, *16*, 1084–1089.
7. Richdale, K.; Wassenaar, P.; Teal Bluestein, K.; Abduljalil, A.; Christoforidis, J.A.; Lanz, T.; Knopp, M.V.; Schmalbrock, P. 7 Tesla MR imaging of the human eye in vivo. *J. Magn. Reson. Imaging JMRI* **2009**, *30*, 924–932.
8. Graessl, A.; Muhle, M.; Schwerter, M.; Rieger, J.; Oezerdem, C.; Santoro, D.; Lysiak, D.; Winter, L.; Hezel, F.; Waiczies, S.; et al. Ophthalmic Magnetic Resonance Imaging at 7 T Using a 6-Channel Transceiver Radiofrequency Coil Array in Healthy Subjects and Patients with Intraocular Masses. *Investig. Radiol.* **2014**, *49*, 260–270.
9. Beenakker, J.W.M.; van Rijn, G.A.; Luyten, G.P.M.; Webb, A.G. High-resolution MRI of uveal melanoma using a microcoil phased array at 7 T. *NMR Biomed.* **2013**, *26*, 1864–1869.
10. Ferreira, T.A.; Fonk, L.G.; Jaarsma-Coes, M.G.; van Haren, G.G.R.; Marinkovic, M.; Beenakker, J.-W.M. MRI of Uveal Melanoma. *Cancers* **2019**, *11*, 377.
11. Foti, P.V.; Travalì, M.; Farina, R.; Palmucci, S.; Spatola, C.; Raffaele, L.; Salamone, V.; Caltabiano, R.; Broggi, G.; Puzzo, L.; et al. Diagnostic methods and therapeutic options of uveal melanoma with emphasis on MR imaging—Part I: MR imaging with pathologic correlation and technical considerations. *Insights Into Imaging* **2021**, *12*, 1–27.
12. Van Vught, L.; Dekker, C.E.; Stoel, B.C.; Luyten, G.P.M.; Beenakker, J.M. Evaluation of intraocular lens position and retinal shape in negative dysphotopsia using high-resolution magnetic resonance imaging. *J. Cataract. Refract. Surg.* **2021**, *47*, 1032–1038.
13. Kang, L.; Wan, C. Application of advanced magnetic resonance imaging in glaucoma: A narrative review. *Quant. Imaging Med. Surg.* **2022**, *12*, 2106–2128.
14. Niendorf, T.; Beenakker, J.W.M.; Langner, S.; Erb-Eigner, K.; Bach Cuadra, M.; Beller, E.; Millward, J.M.; Niendorf, T.M.; Stachs, O. Ophthalmic Magnetic Resonance Imaging: Where Are We (Heading to)? *Curr. Eye Res.* **2021**, *46*, 1251–1270.
15. Ferreira, T.A.; Saraiva, P.; Genders, S.W.; Buchem, M.V.; Luyten, G.P.M.; Beenakker, J.-W.M. CT and MR imaging of orbital inflammation. *Neuroradiology* **2018**, *60*, 1253–1266.
16. Diogo, M.; Jager, M.; Ferreira, T. CT and MR Imaging in the Diagnosis of Scleritis. *AJNR Am. J. Neuroradiol.* **2016**, *37*, 2334–2339.
17. Ferreira, T.A.; Pinheiro, C.F.; Saraiva, P.; Jaarsma-Coes, M.G.; Van Duinen, S.G.; Genders, S.W.; Marinkovic, M.; Beenakker, J.-W.M. MR and CT Imaging of the Normal Eyelid and its Application in Eyelid Tumors. *Cancers* **2020**, *12*, 658.

18. Sims, J.R.; Chen, A.M.; Sun, Z.; Deng, W.; Colwell, N.A.; Colbert, M.K.; Zhu, J.; Sainulabdeen, A.; Faiq, M.A.; Chan, K.C.; et al. Role of Structural, Metabolic, and Functional MRI in Monitoring Visual System Impairment and Recovery. *J. Magn. Reson. Imaging* **2021**, *54*, 1706–1729.
19. Gracitelli, C.P.; Gerente, V.M.; Furlanetto, R.L.; Amaro, E.; Paranhos, A. Magnetic Resonance Imaging for Glaucoma Evaluation. *Eur. J. Gastroenterol. Hepatol.* **2020**, *29*, 622–626.
20. Lemke, A.J.; Kazi, I.; Felix, R. Magnetic resonance imaging of orbital tumors. *Eur. Radiol.* **2006**, *16*, 2207–2219.
21. De Graaf, P.; on behalf of the European Retinoblastoma Imaging Collaboration (ERIC); Göricke, S.; Rodjan, F.; Galluzzi, P.; Maeder, P.; Castelijns, J.A.; Brisse, H.J. Guidelines for imaging retinoblastoma: Imaging principles and MRI standardization. *Pediatr. Radiol.* **2012**, *42*, 2–14.
22. Foti, P.V.; Travali, M.; Farina, R.; Palmucci, S.; Spatola, C.; Liardo, R.L.E.; Milazzotto, R.; Raffaele, L.; Salamone, V.; Caltabiano, R.; et al. Diagnostic methods and therapeutic options of uveal melanoma with emphasis on MR imaging—Part II: Treatment indications and complications. *Insights Into Imaging* **2021**, *12*, 1–24.
23. Neupane, R.; Gaudana, R.; Boddu, S.H. Imaging Techniques in the Diagnosis and Management of Ocular Tumors: Prospects and Challenges. *AAPS J.* **2018**, *20*, 97.
24. Solnik, M.; Padaszyńska, N.; Czarnecka, A.M.; Synoradzki, K.J.; Yousef, Y.A.; Chorągiewicz, T.; Rejdak, R.; Toro, M.D.; Zweifel, S.; Dyndor, K.; et al. Imaging of Uveal Melanoma—Current Standard and Methods in Development. *Cancers* **2022**, *14*, 3147.
25. Singh, M.; Durairaj, P.; Yeung, J. Uveal Melanoma: A Review of the Literature. *Oncol. Ther.* **2018**, *6*, 87–104.
26. Foti, P.V.; Longo, A.; Reibaldi, M.; Russo, A.; Privitera, G.; Spatola, C.; Raffaele, L.; Salamone, V.; Farina, R.; Palmucci, S.; et al. Uveal melanoma: Quantitative evaluation of diffusion-weighted MR imaging in the response assessment after proton-beam therapy, long-term follow-up. *Radiol. Med.* **2017**, *122*, 131–139.
27. Tartaglione, T.; Pagliara, M.M.; Sciandra, M.; Caputo, C.G.; Calandrelli, R.; Fabrizi, G.; Gaudino, S.; Blasi, M.A.; Colosimo, C. Uveal melanoma: Evaluation of extrascleral extension using thin-section MR of the eye with surface coils. *La Radiol. Med.* **2014**, *119*, 775–783.
28. Ferreira, T.A.; Jaarsma-Coes, M.G.; Marinkovic, M.; Verbist, B.; Verdijk, R.M.; Jager, M.J.; Luyten, G.P.M.; Beenakker, J.-W.M. MR imaging characteristics of uveal melanoma with histopathological validation. *Neuroradiology* **2021**, *64*, 171–184.
29. Récsán, Z.; Karlinger, K.; Fodor, M.; Zalatnai, A.; Papp, M.; Salacz, G. MRI for the Evaluation of Scleral Invasion and Extrascleral Extension of Uveal Melanomas. *Clin. Radiol.* **2002**, *57*, 371–376.
30. Hosten, N.; Bornfeld, N.; Wassmuth, R.; Lemke, A.J.; Sander, B.; E Bechrakis, N.; Félix, R. Uveal melanoma: Detection of extraocular growth with MR imaging and US. *Radiology* **1997**, *202*, 61–67.
31. Coleman, D.J.; Silverman, R.H.; Rondeau, M.J.; O Lloyd, H.; Daly, S. Explaining the current role of high-frequency ultrasound in ophthalmic diagnosis. *Expert. Rev. Ophthalmol.* **2006**, *1*, 63–76.
32. Klaassen, L.; Jaarsma-Coes, M.G.; Verbist, B.M.; Vu, T.K.; Marinkovic, M.; Rasch, C.R.; Luyten, G.P.; Beenakker, J.-W.M. Automatic Three-Dimensional Magnetic Resonance-based measurements of tumour prominence and basal diameter for treatment planning of uveal melanoma. *Phys. Imaging Radiat. Oncol.* **2022**, *24*, 102–110.

33. Jaarsma-Coes, M.G.; Ferreira, T.A.; Marinkovic, M.; Vu, T.K.; van Vught, L.; van Haren, G.R.; Rodrigues, M.F.; Klaver, Y.L.; Verbist, B.M.; Luyten, G.P.; et al. Comparison of MRI-based and conventional measurements for proton beam therapy of uveal melanoma. *Ophthalmol. Retina* **2022**, *7*, 178–188.
34. Yuan, Y.; Kuai, X.-P.; Chen, X.-S.; Tao, X.-F. Assessment of dynamic contrast-enhanced magnetic resonance imaging in the differentiation of malignant from benign orbital masses. *Eur. J. Radiol.* **2013**, *82*, 1506–1511.
35. De Graaf, P.; Pouwels, P.; Rodjan, F.; Moll, A.; Imhof, S.; Knol, D.; Sanchez, E.; van der Valk, P.; Castelijns, J. Single-Shot Turbo Spin-Echo Diffusion-Weighted Imaging for Retinoblastoma: Initial Experience. *AJNR Am. J. Neuroradiol.* **2012**, *33*, 110–118.
36. Erb-Eigner, K.; Willerding, G.; Taupitz, M.; Hamm, B.; Asbach, P. Diffusion-Weighted Imaging of Ocular Melanoma. *Investig. Radiol.* **2013**, *48*, 702–707.
37. Kamrava, M.; Sepahdari, A.R.; Leu, K.; Wang, P.-C.; Roberts, K.; Demanes, D.J.; McCannel, T.; Ellingson, B.M. Quantitative multiparametric MRI in uveal melanoma: Increased tumor permeability may predict monosomy 3. *Neuroradiology* **2015**, *57*, 833–840.
38. Sepahdari, A.R.; Politi, L.S.; Aakalu, V.K.; Kim, H.J.; Razeq, A.A. Diffusion-weighted imaging of orbital masses: Multi-institutional data support a 2-ADC threshold model to categorize lesions as benign, malignant, or indeterminate. *AJNR Am. J. Neuroradiol.* **2014**, *35*, 170–175.
39. Sepahdari, A.R.; Aakalu, V.K.; Setabutr, P.; Shiehmorteza, M.; Naheedy, J.H.; Mafee, M.F. Indeterminate Orbital Masses: Restricted Diffusion at MR Imaging with Echo-planar Diffusion-weighted Imaging Predicts Malignancy. *Radiology* **2010**, *256*, 554–564.
40. Page, M.J.; Moher, D.; Bossuyt, P.M.; Boutron, I.; Hoffmann, T.C.; Mulrow, C.D.; Shamseer, L.; Tetzlaff, J.M.; Akl, E.A.; Chou, R.; et al. The PRISMA 2020 statement: An updated guideline for reporting systematic reviews. *BMJ* **2021**, *372*, n71.
41. Uzzani, M.; Hammady, H.; Fedorowicz, Z.; Elmagarmid, A. Rayyan—A web and mobile app for systematic reviews. *Syst. Rev.* **2016**, *5*, 210.
42. Li, D.J.; Yang, W.L.; Wang, Z.Y.; Chen, W.; Zhao, Q.; Li, Y.F.; Cui, R.; Shen, L.; Wei, W.B. [Comparative analysis on the significances of contrast-enhanced ultrasound and dynamic contrast-enhanced magnetic resonance imaging in uveal melanoma diagnosis]. *Zhonghua Yan Ke Za Zhi* **2018**, *54*, 194–198.
43. Buerk, B.M.; Pulido, J.S.; Chiong, I.; Folberg, R.; Edward, D.P.; Duffy, M.T.; Thulborn, K.R. Vascular perfusion of choroidal melanoma by 3.0 tesla magnetic resonance imaging. *Trans. Am. Ophthalmol. Soc.* **2004**, *102*, 209–218.
44. Russo, A.; Mariotti, C.; Longo, A.; Foti, P.V.; Avitabile, T.; Uva, M.G.; Franco, L.M.; Bonfiglio, V.; Milone, P.; Ettorre, G.C.; et al. Diffusion-weighted magnetic resonance imaging and ultrasound evaluation of choroidal melanomas after proton-beam therapy. *La Radiol. Med.* **2015**, *120*, 634–640.
45. Sepahdari, A.; Kapur, R.; Aakalu, V.; Villablanca, J.; Mafee, M. Diffusion-Weighted Imaging of Malignant Ocular Masses: Initial Results and Directions for Further Study. *AJNR Am. J. Neuroradiol.* **2012**, *33*, 314–319.
46. Tang, M.; Ferreira, T.; Jaarsma-Coes, M.; Klaassen, L.; Marinkovic, M.; Vu, K.; Rasch, C.; Creutzberg, C.; Horeweg, N.; Klaver, Y.; et al. MR-based follow-up after brachytherapy and proton beam therapy in uveal melanoma. *Acta Ophthalmol.* **2022**, *100*.
47. Schueller, P.; Dogan, A.; Panke, J.E.; Micke, O.; Willich, N. Does the imaging method have an influence on the measured tumor height in ruthenium plaque therapy of uveal melanoma? *Strahlenther. Onkol.* **2005**, *181*, 320–325.
48. Beenakker, J.-W.M.; Rasch, C.R. Letter to the Editor of Radiotherapy and Oncology regarding the paper titled “MRI and FUNDUS image fusion for improved ocular biometry in Ocular Proton Therapy” by Via et al. *Radiother. Oncol.* **2022**, *176*, 251.

49. Oberacker, E.; Paul, K.; Huelnhagen, T.; Oezerdem, C.; Winter, L.; Pohlmann, A.; Boehmert, L.; Stachs, O.; Heufelder, J.; Weber, A.; et al. Magnetic resonance safety and compatibility of tantalum markers used in proton beam therapy for intraocular tumors: A 7.0 Tesla study. *Magn. Reson. Med.* **2017**, *78*, 1533–1546.
50. Bustin, A. Editorial for “A Comparison of 3T and 7T MRI for the Clinical Evaluation of Uveal Melanoma”. *J. Magn. Reson. Imaging* **2022**, *55*, 1516–1517.
51. Tang, M.C.; Jaarsma-Coes, M.G.; Ferreira, T.A.; Fonk, L.Z.G.; Marinkovic, M.; Luyten, G.P.; Beenakker, J.M. A Comparison of 3 T and 7 T MRI for the Clinical Evaluation of Uveal Melanoma. *J. Magn. Reson. Imaging* **2022**, *55*, 1504–1515.
52. Gach, H.M.; Mackey, S.L.; Rehman, S.; Kadbi, M.; Zoberi, J.E.; Garcia-Ramirez, J.; Grigsby, P.W. Magnetic resonance imaging metal artifact reduction for eye plaque patient with dental braces. *J. Contemp. Brachyther.* **2017**, *9*, 490–495.
53. Jaarsma-Coes, M.G.; Ferreira, T.A.G.; van Haren, G.R.; Marinkovic, M.; Beenakker, J.-W.M. MRI enables accurate diagnosis and follow-up in uveal melanoma patients after vitrectomy. *Melanoma Res.* **2019**, *29*, 655–659.
54. Van Rijn, G.A.; Mourik, J.E.M.; Teeuwisse, W.M.; Luyten, G.P.M.; Webb, A.G. Magnetic Resonance Compatibility of Intraocular Lenses Measured at 7 Tesla. *Investig. Ophthalmol. Vis. Sci.* **2012**, *53*, 3449–3453.
55. Islamaj, E.; Van Vught, L.; Jordaan-Kuip, C.P.; Vermeer, K.A.; Ferreira, T.A.; De Waard, P.W.T.; Lemij, H.G.; Beenakker, J.-W.M. Magnetic resonance imaging reveals possible cause of diplopia after Baerveldt glaucoma implantation. *PLoS ONE* **2022**, *17*, e0276527.
56. Foti, P.V.; Ini, C.; Broggi, G.; Farina, R.; Palmucci, S.; Spatola, C.; Liardo, R.L.E.; Milazzotto, R.; Raffaele, L.; Salamone, V.; et al. Histopathologic and MR Imaging Appearance of Spontaneous and Radiation-Induced Necrosis in Uveal Melanomas: Initial Results. *Cancers* **2022**, *14*, 215.
57. Choi, Y.J.; Kim, T.W.; Kim, S.; Choung, H.; Lee, M.J.; Kim, N.; Khwarg, S.I.; Yu, Y.S. Effects on Periocular Tissues after Proton Beam Radiation Therapy for Intraocular Tumors. *J. Korean Med. Sci.* **2018**, *33*, e120.
58. Chen, S.; Ji, X.; Liu, M.; Xia, Z.; Zheng, H.; Yin, Q.; Wang, H.; Li, Y. The value of MRI in evaluating the efficacy and complications with the treatment of intra-arterial chemotherapy for retinoblastoma. *Oncotarget* **2017**, *8*, 38413–38425.
59. Jeong, H.; Sa, H.-S. Uveal Melanoma with Massive Extraocular Extension through the Sclerocorneal Limbus. *Korean J. Ophthalmol.* **2015**, *29*, 280–281.
60. Houle, V.; Bélair, M.; Allaire, G.S. AIRP Best Cases in Radiologic-Pathologic Correlation: Choroidal Melanoma. *Radiographics* **2011**, *31*, 1231–1236.
61. Khetan, V.; Gupta, K.; Mohan, E.R.; Gopal, L. Uveal melanoma presenting as cataract and staphyloma. *Indian J. Ophthalmol.* **2009**, *57*, 223–225.
62. Rebolleda, G.; Suárez Figueroa, M.; Muñoz-Negrete, F.J.; Rocamora, A. Magnetic resonance imaging in cavitary choroidal melanoma. *Eur. J. Ophthalmol.* **2000**, *10*, 335–337.
63. Biswas, J.; Raghavendra, R.; Ratra, V.; Krishnakumar, S.; Gopal, L.; Shanmugam, M.P. Diffuse malignant melanoma of the choroid simulating metastatic tumour in the choroid. *Indian J. Ophthalmol.* **2000**, *48*, 137–140.
64. Nguyen, T.-N.; Edelstein, C.; Mansour, M.; Burnier, M.N. Primary choroidal melanoma masquerading as a hemorrhagic lesion in a patient with ocular trauma. *Can. J. Ophthalmol.* **2003**, *38*, 228–229.
65. Minija, C.; Shanmugam, M.P. Subretinal lipid exudation associated with untreated choroidal melanoma. *Indian J. Ophthalmol.* **2011**, *59*, 233–235.
66. Becerra, E.M.; Saornil, M.A.; Blanco, G.; Méndez, M.C.; Muiños, Y.; Esteban, M.R. Cavitary choroidal melanoma. *Can. J. Ophthalmol.* **2005**, *40*, 619–622.

67. Jiblawi, A.; Chanbour, H.; Tayba, A.; Khayat, H.; Jiblawi, K. Magnetic Resonance Imaging Diagnosis of Choroidal Melanoma. *Cureus* **2021**, *13*, e16628.
68. Koolstra, K.; Beenakker, J.M.; Koken, P.; Webb, A.; Börnert, P. Cartesian MR fingerprinting in the eye at 7T using compressed sensing and matrix completion-based reconstructions. *Magn. Reson. Med.* **2019**, *81*, 2551–2565.
69. Damento, G.M.; Koeller, K.K.; Salomão, D.R.; Pulido, J.S. T2 Fluid-Attenuated Inversion Recovery Imaging of Uveal Melanomas and Other Ocular Pathology. *Ocul. Oncol. Pathol.* **2016**, *2*, 251–261.
70. Hirunpat, P.; Sanghan, N.; Hirunpat, S. White matter: A good reference for the signal intensity evaluation in magnetic resonance imaging for the diagnosis of uveal melanoma. *Neuroradiol. J.* **2021**, *34*, 113–119.
71. Wei, W.; Jia, G.; von Tengg-Kobligk, H.; Heverhagen, J.T.; Abdel-Rahman, M.; Wei, L.; Christoforidis, J.B.; Davidorf, F.; Knopp, M.V. Dynamic Contrast-Enhanced Magnetic Resonance Imaging of Ocular Melanoma as a Tool to Predict Metastatic Potential. *J. Comput. Assist. Tomogr.* **2017**, *41*, 823–827.
72. Jaarsma-Coes, M.G.; Ferreira, T.A.; van Houdt, P.J.; van der Heide, U.A.; Luyten, G.P.M.; Beenakker, J.-W.M. Eye-specific quantitative dynamic contrast-enhanced MRI analysis for patients with intraocular masses. *Magn. Reson. Mater. Phys. Biol. Med.* **2022**, *35*, 311–323.
73. Su, Y.; Xu, X.; Wei, W.; Xian, J. Using a novel MR imaging sign to differentiate retinal pigment epithelium from uveal melanoma. *Neuroradiology* **2020**, *62*, 347–352.
74. Stroszczynski, C.; Hosten, N.; Bornfeld, N.; Wiegel, T.; Schueler, A.; Foerster, P.; Lemke, A.J.; Hoffmann, K.T.; Felix, R. Choroidal hemangioma: MR findings and differentiation from uveal melanoma. *AJNR Am. J. Neuroradiol.* **1998**, *19*, 1441–1447.
75. Lemke, A.-J.; Hosten, N.; Wiegel, T.; Prinz, R.D.; Richter, M.; Bechrakis, N.E.; Foerster, P.I.; Felix, R. Intraocular metastases: Differential diagnosis from uveal melanomas with high-resolution MRI using a surface coil. *Eur. Radiol.* **2001**, *11*, 2593–2601.
76. Nagesh, C.; Rao, R.; Hiremath, S.; Honavar, S. Magnetic resonance imaging of the orbit, Part 1: Basic principles and radiological approach. *Indian J. Ophthalmol.* **2021**, *69*, 2574.
77. Orman, G.; Huisman, T. A descriptive neuroimaging study of retinoblastoma in children: Magnetic resonance imaging features. *Pol. J. Radiol.* **2022**, *87*, 363–368.
78. De Graaf, P.; Barkhof, F.; Moll, A.C.; Imhof, S.M.; Knol, D.L.; van der Valk, P.; Castelijns, J.A. Retinoblastoma: MR imaging parameters in detection of tumor extent. *Radiology* **2005**, *235*, 197–207.
79. Nagesh, C.; Rao, R.; Hiremath, S.; Honavar, S. Magnetic resonance imaging of the orbit, Part 2: Characterization of orbital pathologies. *Indian J. Ophthalmol.* **2021**, *69*, 2585.
80. Damianidis, C.; Konstantinou, D.; Kyriakou, V.; Arvaniti, M.; Kotziamani, N.; Rodokalakis, G.; Agriou, A.; Emmanouilidou, M.; Tsitouridis, I. Magnetic Resonance Imaging and Ultrasonographic Evaluation of Retinal Detachment in Orbital Uveal Melanomas. *Neuroradiol. J.* **2010**, *23*, 329–338.
81. Via, R.; Pica, A.; Antonioli, L.; Paganelli, C.; Fattori, G.; Spaccapaniccia, C.; Lomax, A.; Weber, D.C.; Schalenbourg, A.; Baroni, G.; et al. MRI and FUNDUS image fusion for improved ocular biometry in Ocular Proton Therapy. *Radiother. Oncol.* **2022**, *174*, 16–22.
82. Li, Y.; Yang, X.; Huang, Y.; Hei, Y.; Wang, L.; Xiao, L. Orbital Extension of Uveal Melanoma: Treatment and Survival Analysis. *Int. Ophthalmol. Clin.* **2019**, *59*, 37–51.
83. Blanco, G. Diagnosis and treatment of orbital invasion in uveal melanoma. *Can. J. Ophthalmol.* **2004**, *39*, 388–396.
84. Fusetti, S.; Parrozzani, R.; Urban, F.; Gurabardhi, M.; Ferronato, G.; Midena, E. Modified Enucleation for Choroidal Melanoma with Large Extrascleral Extension. *Orbit* **2010**, *29*, 70–75.

85. Modarres, M.; Rezanejad, A.; Falavarjani, K.G. Recurrence and massive extraocular extension of choroidal malignant melanoma after vitrectomy and endoresection. *Indian J. Ophthalmol.* **2014**, *62*, 731–733.
86. Mittica, N.; Vemuganti, G.K.; Duffy, M.; Torczynski, E.; Edward, D.P. Late Orbital Recurrence of a Choroidal Melanoma Following Internal Resection: Report of a Case and Review of the Literature. *Surv. Ophthalmol.* **2003**, *48*, 181–190.
87. Kiratli, H.; Koç, I.; Tarlan, B. Orbital Extension of an Unsuspected Choroidal Melanoma Presumably through an Aqueous Tube Shunt. *Ocul. Oncol. Pathol.* **2016**, *2*, 144–147.
88. Sambuelli, R.; Luna, J.D.; Reviglio, V.E.; Aoki, A.; Juarez, C.P. Small choroidal melanoma with massive extraocular extension: Invasion through posterior scleral emissary channels. *Int. Ophthalmol.* **2001**, *24*, 213–218.
89. Jacobsen, B.H.; Ricks, C.; Harrie, R.P. Ocular ultrasound versus MRI in the detection of extrascleral extension in a patient with choroidal melanoma. *BMC Ophthalmol.* **2018**, *18*, 320.
90. Jacinto, F.A.; Margo, C.E. Neglected Choroidal Melanoma Tracking Along Optic Nerve to Brain. *Ophthalmology* **2016**, *123*, 2488.
91. Singh, A.D.; Platt, S.M.; Lystad, L.; Lowe, M.; Oh, S.; Jones, S.E.; Alzahrani, Y.; Plesec, T. Optic Nerve Assessment Using 7-Tesla Magnetic Resonance Imaging. *Ocul. Oncol. Pathol.* **2016**, *2*, 178–180.
92. Bradley, A.; Estes, A.; Ulrich, L.; Thomas, D.; Gay, D. Epibulbar Plasmacytoma Masquerading as Subconjunctival Hemorrhage in a Patient With Multiple Myeloma. *Cornea* **2017**, *36*, 249–251.
93. Maheshwari, A.; Finger, P.T. Cancers of the eye. *Cancer Metastasis Rev.* **2018**, *37*, 677–690.
94. Mahajan, A.; Crum, A.; Johnson, M.H.; Materin, M.A. Ocular Neoplastic Disease. *Semin. Ultrasound CT MRI* **2011**, *32*, 28–37.
95. Surukrattanaskul, S.; Keyurapan, B.; Wangtiraumnuay, N. Correlation between clinical presentations, radiological findings and high risk histopathological features of primary enucleated eyes with advanced retinoblastoma at Queen Sirikit National Institute of Child Health: 5 years result. *PLoS ONE* **2022**, *17*, e0270362.
96. Brisse, H.J.; on behalf of the European Retinoblastoma Imaging Collaboration (ERIC); de Graaf, P.; Galluzzi, P.; Cosker, K.; Maeder, P.; Göricke, S.; Rodjan, F.; de Jong, M.C.; Savignoni, A.; et al. Assessment of early-stage optic nerve invasion in retinoblastoma using high-resolution 1.5 Tesla MRI with surface coils: A multicentre, prospective accuracy study with histopathological correlation. *Eur. Radiol.* **2015**, *25*, 1443–1452.
97. Seibel, I.; Riechardt, A.I.; Erb-Eigner, K.; Böker, A.; Cordini, D.; Heufelder, J.; Jousen, A.M. Proton Beam Irradiation: A Safe Procedure in Postequatorial Extraocular Extension From Uveal Melanoma. *Am. J. Ophthalmol.* **2018**, *191*, 49–53.
98. Beenakker, J.-W.M.; Wezel, J.; Groen, J.; Webb, A.G.; Börnert, P. Silent volumetric multi-contrast 7 Tesla MRI of ocular tumors using Zero Echo Time imaging. *PLoS ONE* **2019**, *14*, e0222573.
99. Walter, U.; Niendorf, T.; Graessl, A.; Rieger, J.; Krüger, P.-C.; Langner, S.; Guthoff, R.F.; Stachs, O. Ultrahigh field magnetic resonance and colour Doppler real-time fusion imaging of the orbit—A hybrid tool for assessment of choroidal melanoma. *Eur. Radiol.* **2014**, *24*, 1112–1117.
100. Su, Y.; Xu, X.; Zuo, P.; Xia, Y.; Qu, X.; Chen, Q.; Guo, J.; Wei, W.; Xian, J. Value of MR-based radiomics in differentiating uveal melanoma from other intraocular masses in adults. *Eur. J. Radiol.* **2020**, *131*, 109268.
101. Tofts, P.S. T1-weighted DCE imaging concepts: Modelling, acquisition and analysis. *Signal* **2010**, *500*, 400.

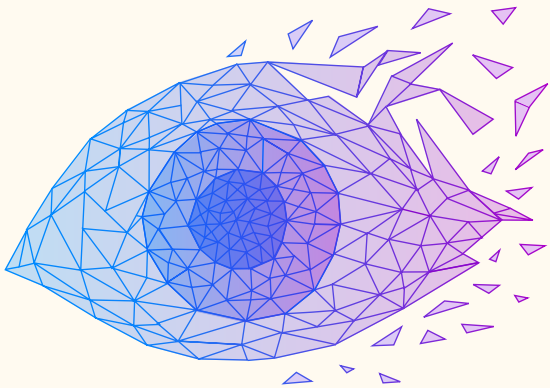
102. Xu, Q.-G.; Xian, J.-F. Role of Quantitative Magnetic Resonance Imaging Parameters in the Evaluation of Treatment Response in Malignant Tumors. *Chin. Med. J.* **2015**, *128*, 1128–1133.
103. Gumeler, E.; Parlak, S.; Yazici, G.; Karabulut, E.; Kiratli, H.; Oguz, K.K. Single shot echo planar imaging (ssEPI) vs single shot turbo spin echo (ssTSE) DWI of the orbit in patients with ocular melanoma. *Br. J. Radiol.* **2021**, *94*, 20200825.
104. Seeger, A.; Batra, M.; Süsskind, D.; Ernemann, U.; Hauser, T.-K. Assessment of uveal melanomas using advanced diffusion-weighted imaging techniques: Value of reduced field of view DWI ("zoomed DWI") and readout-segmented DWI (RESOLVE). *Acta Radiol.* **2019**, *60*, 977–984.
105. Paul, K.; Huelnhagen, T.; Oberacker, E.; Wenz, D.; Kuehne, A.; Waiczies, H.; Schmitter, S.; Stachs, O.; Niendorf, T. Multiband diffusion-weighted MRI of the eye and orbit free of geometric distortions using a RARE-EPI hybrid. *NMR Biomed.* **2018**, *31*, e3872.
106. Paul-Christian, K.; Graessl, A.; Rieger, J.; Lysiak, D.; Huelnhagen, T.; Winter, L.; Heidemann, R.; Lindner, T.; Hadlich, S.; Zimpfer, A.; et al. Diffusion-Sensitized Ophthalmic Magnetic Resonance Imaging Free of Geometric Distortion at 3.0 and 7.0 T. *Investig. Radiol.* **2015**, *50*, 309–321.
107. Shukla-Dave, A.; Obuchowski, N.A.; Chenevert, T.L.; Jambawalikar, S.; Schwartz, L.H.; Malyarenko, D.; Huang, W.; Noworolski, S.M.; Young, R.J.; Jackson, E.F.; et al. Quantitative imaging biomarkers alliance (QIBA) recommendations for improved precision of DWI and DCE-MRI derived biomarkers in multicenter oncology trials. *J. Magn. Reson. Imaging* **2019**, *49*, e101–e121.
108. Shields, C.L.; Furuta, M.; Berman, E.L.; Zahler, J.D.; Hoberman, D.M.; Dinh, D.H.; Mashayekhi, A.; Shields, J.A. Choroidal nevus transformation into melanoma: Analysis of 2514 consecutive cases. *Arch. Ophthalmol.* **2009**, *127*, 981–987.
109. Roelofs, K.A.; O'Day, R.; Al Harby, L.; Arora, A.K.; Cohen, V.M.; Sagoo, M.S.; Damato, B. The MOLES System for Planning Management of Melanocytic Choroidal Tumors: Is It Safe? *Cancers* **2020**, *12*, 1311.
110. Narang, S.; Pandey, A.K.; Giran, M.; Kaur, R. Plaque brachytherapy for choroidal melanoma with vitreous haemorrhage: A therapeutic challenge. *BMJ Case Rep.* **2021**, *14*, e240935.
111. Jager, M.J.; Shields, C.L.; Cebulla, C.M.; Abdel-Rahman, M.H.; Grossniklaus, H.E.; Stern, M.H.; Carvajal, R.D.; Belfort, R.N.; Jia, R.; Damato, B.E.; et al. Uveal melanoma. *Nat. Rev. Dis. Primers* **2020**, *6*, 24.
112. Altun, E.; Aribal, E.; Toker, E.; Öğüt, M.S. Anterior coloboma with macrophthalmos and cyst: MR findings. *Clin. Imaging* **2005**, *29*, 430–433.
113. Brennan, R.C.; Wilson, M.W.; Kaste, S.; Helton, K.J.; McCarville, M.B. US and MRI of pediatric ocular masses with histopathological correlation. *Pediatr. Radiol.* **2012**, *42*, 738–749.
114. Zhou, L.; Zhu, X.-H.; Zhang, K.; Hu, R.; Myers, F. Case Report: Adult Retinoblastoma Progression in 19 Months. *Optom. Vis. Sci.* **2020**, *97*, 1010–1016.
115. Mukhija, R.; Lomi, N.; Kumar, S.; Sen, S. Retinoblastoma in an adult: A diagnostic dilemma. *BMJ Case Rep.* **2019**, *12*, e230537.
116. Jansen, R.W.; de Bloeme, C.M.; Brisse, H.J.; Galluzzi, P.; Cardoen, L.; Göricke, S.; Maeder, P.; Cassoux, N.; Gauthier, A.; Schlueter, S.; et al. MR Imaging Features to Differentiate Retinoblastoma from Coats' Disease and Persistent Fetal Vasculature. *Cancers* **2020**, *12*, 3592.
117. Meltzer, D.E.; Garner, H.R.; Fazzone, H.E. Kikuchi-Fujimoto Disease with Bilateral Uveitis. *J. Radiol. Case Rep.* **2009**, *3*, 1–6.

118. Iturralde, J.C.; Bianciotto, C.; Lally, S.E.; Krasnow, M.; Shields, C.L. Massive choroidal effusion and painful secondary glaucoma from underlying uveal melanoma. *Graefe's Arch. Clin. Exp. Ophthalmol.* **2012**, *250*, 627–630.
119. Wei, W.-B.; Jie, Y.; Mo, J.; Li, B. Clinical characteristics and treatment of neurofibroma of the choroid. *Chin. Med. J.* **2012**, *125*, 1832–1835.
120. Singh, P.; Sen, S.; Banerjee, M.; Meel, R. Choroidal melanoma masquerading as orbital cellulitis. *BMJ Case Rep.* **2018**, *11*, e227486.
121. Kiratli, H. Persistent Intraschisis Hemorrhage Simulating Choroidal Melanoma. *Jpn. J. Ophthalmol.* **2002**, *46*, 222–225.
122. Shields, C.L.; Honavar, S.G.; Shields, J.A.; Cater, J.; Demirci, H. Circumscribed choroidal hemangioma: Clinical manifestations and factors predictive of visual outcome in 200 consecutive cases. *Ophthalmology* **2001**, *108*, 2237–2248.
123. Cho, Y.J.; Bin Won, J.; Byeon, S.H.; Yang, W.I.; Koh, H.J.; Kwon, O.W.; Lee, S.C. A Choroidal Schwannoma Confirmed by Surgical Excision. *Korean J. Ophthalmol.* **2009**, *23*, 49–52.
124. Xian, J.; Xu, X.; Wang, Z.; Yang, B.; Li, B.; Man, F.; Chen, Q.; Shi, J.; Zhang, Y. MR Imaging Findings of the Uveal Schwannoma. *AJNR Am. J. Neuroradiol.* **2009**, *30*, 769–773.
125. Demirci, H.; Shields, C.L.; Honavar, S.; Shields, J.A.; Bardenstein, D.S. Long-term Follow-up of Giant Nodular Posterior Scleritis Simulating Choroidal Melanoma. *Arch. Ophthalmol.* **2000**, *118*, 1290–1292.
126. Kraniias, G.; Tyradellis, C.; Krebs, T.; Augsburg, J. Bilateral atypical nodular posterior scleritis. *Eur. J. Ophthalmol.* **2006**, *16*, 614–617.
127. Branisteanu, D.C.; Bogdanici, C.M.; Branisteanu, D.E.; Maranduca, M.A.; Zemba, M.; Balta, F.; Branisteanu, C.I.; Moraru, A.D. Uveal melanoma diagnosis and current treatment options (Review). *Exp. Ther. Med.* **2021**, *22*, 1–8.
128. Markiewicz, A.; Donizy, P.; Nowak, M.; Krzyżiński, M.; Elas, M.; Płonka, P.M.; Orłowska-Heitzmann, J.; Biecek, P.; Hoang, M.P.; Romanowska-Dixon, B. Amelanotic Uveal Melanomas Evaluated by Indirect Ophthalmoscopy Reveal Better Long-Term Prognosis Than Pigmented Primary Tumours—A Single Centre Experience. *Cancers* **2022**, *14*, 2753.
129. Almarzooqi, S.; Reyes-Múgica, M.; Ali, B.R.; Habbal, A.; Asha, M.J.; AlShamsi, E.T. Congenital Teratocarcinoma with *CTNNB1* Gene Mutation Presenting as an Ocular Mass. *Pediatr. Dev. Pathol.* **2022**, *25*, 1093526622111127.
130. Hada, M.; Chawla, B.; Seth, R.; Khurana, S.; Kashyap, S. Primary intraocular malignant rhabdoid tumor presenting as orbital mass with intracranial extension in an adolescent. *Can. J. Ophthalmol.* **2017**, *52*, e3–e5.
131. Richter, M.N.; Bechrakis, N.E.; Stoltenburg-Didinger, G.; Foerster, M.H. Transscleral resection of a ciliary body leiomyoma in a child: Case report and review of the literature. *Graefe's Arch. Clin. Exp. Ophthalmol.* **2003**, *241*, 953–957.
132. Oh, K.J.; Kwon, B.J.; Han, M.H.; Hwang, P.G.; Kim, C.J.; Na, D.G.; Chang, K.-H. MR Imaging Findings of Uveal Leiomyoma: Three Cases. *AJNR Am. J. Neuroradiol.* **2005**, *26*, 100–103.
133. Küker, W.; Herrlinger, U.; Grönewäller, E.; Rohrbach, J.M.; Weller, M. Ocular manifestation of primary nervous system lymphoma: What can be expected from imaging? *J. Neurol.* **2002**, *249*, 1713–1716.
134. Jaarsma-Coes, M.G.; Ferreira, T.A.; Luyten, G.P.M.; Beenakker, J.W.M. Reaction on “Ocular ultrasound versus MRI in the detection of extrascleral extension in a patient with choroidal melanoma”. *BMC Ophthalmol.* **2019**, *19*, 193.
135. Fleury, E.; Trnkova, P.; Erdal, E.; Hassan, M.; Stoel, B.; Jaarsma-Coes, M.; Luyten, G.; Herault, J.; Webb, A.; Hoogeman, M.; et al. Three-dimensional MRI-based treatment planning approach for non-invasive ocular proton therapy. *Med. Phys.* **2021**, *48*, 1315–1326.

136. Nguyen, H.-G.; Sznitman, R.; Maeder, P.; Schalenbourg, A.; Peroni, M.; Hrbacek, J.; Weber, D.C.; Pica, A.; Cuadra, M.B. Personalized Anatomic Eye Model from T1-Weighted Volume Interpolated Gradient Echo Magnetic Resonance Imaging of Patients with Uveal Melanoma. *Int. J. Radiat. Oncol.* **2018**, *102*, 813–820.
137. Ciller, C.; De Zanet, S.; Kamnitsas, K.; Maeder, P.; Glocker, B.; Munier, F.L.; Rueckert, D.; Thiran, J.-P.; Cuadra, M.B.; Sznitman, R. Multi-channel MRI segmentation of eye structures and tumors using patient-specific features. *PLoS ONE* **2017**, *12*, e0173900.
138. Hassan, M.K.; Fleury, E.; Shamonin, D.; Fonk, L.G.; Marinkovic, M.; Jaarsma-Coes, M.G.; Luyten, G.P.; Webb, A.; Beenakker, J.-W.; Stoel, B. An Automatic Framework to Create Patient-specific Eye Models From 3D Magnetic Resonance Images for Treatment Selection in Patients with Uveal Melanoma. *Adv. Radiat. Oncol.* **2021**, *6*, 100697.
139. Hrbacek, J.; Mishra, K.K.; Kacperek, A.; Dendale, R.; Nauraye, C.; Auger, M.; Herault, J.; Daftari, I.K.; Trofimov, A.V.; Shih, H.A.; et al. Practice Patterns Analysis of Ocular Proton Therapy Centers: The International OPTIC Survey. *Int. J. Radiat. Oncol.* **2016**, *95*, 336–343.
140. Thomson, R.M.; Furutani, K.M.; Kaulich, T.W.; Mourtada, F.; Rivard, M.J.; Soares, C.G.; Vanneste, F.M.; Melhus, C.S. AAPM recommendations on medical physics practices for ocular plaque brachytherapy: Report of task group 221. *Med. Phys.* **2020**, *47*, e92–e124.
141. Ares, W.J.; Flickinger, J.C.; Lunsford, L.D. Leksell Radiosurgery for Orbital, Uveal, and Choroidal Tumors. *Prog. Neurol. Surg.* **2019**, *34*, 298–305.
142. Sarici, A.M.; Pazarli, H. Gamma-knife-based stereotactic radiosurgery for medium- and large-sized posterior uveal melanoma. *Graefes Arch. Clin. Exp. Ophthalmol.* **2013**, *251*, 285–294.
143. Miralbell, R.; Caro, M.; Weber, D.C.; Elizalde, J.; Perez-Ochoa, A.; Villà, S.; IgnacioToscas, J.; Martinez, P.; Linero, D.; Nouet, P.; et al. Stereotactic Radiotherapy for Ocular Melanoma: Initial Experience Using Closed Eyes for Ocular Target Immobilization. *Technol. Cancer Res. Treat.* **2007**, *6*, 413–417.
144. Zorlu, F.; Selek, U.; Kiratli, H. Initial results of fractionated CyberKnife radiosurgery for uveal melanoma. *J. Neuro-Oncol.* **2009**, *94*, 111–117.
145. Dieckmann, K.; Georg, D.; Zehetmayer, M.; Rottenfusser, A.; Pötter, R. Stereotactic Photon Beam Irradiation of Uveal Melanoma: Indications and Experience at the University of Vienna since 1997. *Strahlenther. Onkol.* **2007**, *183*, 11–13.
146. Schirmer, C.M.; Chan, M.; Mignano, J.; Duker, J.; Melhus, C.S.; Williams, L.B.; Wu, J.K.; Yao, K.C. Dose De-Escalation with Gamma Knife Radiosurgery in the Treatment of Choroidal Melanoma. *Int. J. Radiat. Oncol.* **2009**, *75*, 170–176.
147. Furdova, A.; Furda, R.; Sramka, M.; Chorvath, M.; Rybar, J.; Vesely, P.; Valaskova, J.; Siska, V. Stereotactic irradiation on linear accelerator—Ultrasound versus MRI in choroidal melanoma volume calculation. *BMC Ophthalmol.* **2022**, *22*, 1–10.
148. Schmelter, V.; Hofmann, T.; Schneider, F.; Weber, C.; Fuerweger, C.; Muacevic, A.; Priglinger, S.G.; Foerster, P.; Liegl, R. Robotic CyberKnife radiosurgery for small choroidal melanomas. *Melanoma Res.* **2022**, *32*, 192–199.
149. Via, R.; Hennings, F.; Pica, A.; Fattori, G.; Beer, J.; Peroni, M.; Baroni, G.; Lomax, A.; Weber, D.C.; Hrbacek, J. Potential and pitfalls of 1.5T MRI imaging for target volume definition in ocular proton therapy. *Radiother. Oncol.* **2021**, *154*, 53–59.
150. Daftari, I.; Aghaian, E.; O'Brien, J.M.; Dillon, W.; Phillips, T.L. 3D MRI-based tumor delineation of ocular melanoma and its comparison with conventional techniques. *Med. Phys.* **2005**, *32*, 3355–3362.
151. Marnitz, S.; Cordini, D.; Bendl, R.; Lemke, A.J.; Heufelder, J.; Simiantonakis, I.; Kluge, H.; Bechrakis, N.E.; Foerster, M.H.; Hinkelbein, W. Proton therapy of uveal melanomas: Intercomparison of MRI-based and conventional treatment planning. *Strahlenther. Onkol.* **2006**, *182*, 395–399.

152. Zoberi, J.E.; Garcia-Ramirez, J.; Hedrick, S.; Rodriguez, V.; Bertelsman, C.G.; Mackey, S.; Hu, Y.; Gach, H.M.; Rao, P.K.; Grigsby, P.W. MRI-based treatment planning and dose delivery verification for intraocular melanoma brachytherapy. *Brachytherapy* **2018**, *17*, 31–39.
153. Dobler, B.; Bendl, R. Precise modelling of the eye for proton therapy of intra-ocular tumours. *Phys. Med. Biol.* **2002**, *47*, 593–613.
154. Hennings, F.; Lomax, A.; Pica, A.; Weber, D.C.; Hrbacek, J. Automated Treatment Planning System for Uveal Melanomas Treated with Proton Therapy: A Proof-of-Concept Analysis. *Int. J. Radiat. Oncol.* **2018**, *101*, 724–731.
155. Wulff, J.; Koska, B.; Heufelder, J.; Janson, M.; Bäcker, C.M.; Siregar, H.; Behrends, C.; Bäumer, C.; Foerster, A.; Bechrakis, N.E.; et al. Commissioning and validation of a novel commercial TPS for ocular proton therapy. *Med. Phys.* **2022**, *50*, 365–379.
156. Astrahan, M.A. Improved treatment planning for COMS eye plaques. *Int. J. Radiat. Oncol. Biol. Phys.* **2005**, *61*, 1227–1242.
157. Jaarsma-Coes, M.G.; Marinkovic, M.; Astreinidou, E.; Schuurmans, M.S.; Peters, F.P.; Luyten, G.P.; Rasch, C.R.; Beenakker, J.-W.M. Measuring eye deformation between planning and proton beam therapy position using magnetic resonance imaging. *Phys. Imaging Radiat. Oncol.* **2020**, *16*, 33–36.
158. Detorakis, E.T.; Perisinakis, K.; Drakonaki, E.; Liakopoulos, D.; Tzedakis, A.; Papadaki, E.; Tsilimbaris, M.K. MRI and dual-energy CT fusion anatomic imaging in Ru-106 ophthalmic brachytherapy. *Brachytherapy* **2021**, *20*, 828–834.
159. Fionda, B.; Pagliara, M.M.; Lancellotta, V.; Caputo, C.G.; Casà, C.; Sammarco, M.G.; Placidi, E.; Cornacchione, P.; Boselli, F.; Iezzi, R.; et al. Radiological and clinical findings in uveal melanoma treated by plaque interventional radiotherapy (brachytherapy): Visual atlas and literature review on response assessment. *J. Contemp. Brachyther.* **2022**, *14*, 96–106.
160. Jampol, L.M.; Moy, C.S.; Murray, T.G.; Reynolds, S.M.; Albert, D.M.; Schachat, A.P.; Diddie, K.R.; E Engstrom, R.; Finger, P.T.; Hovland, K.R.; et al. The COMS randomized trial of iodine 125 brachytherapy for choroidal melanoma: IV. Local treatment failure and enucleation in the first 5 years after brachytherapy. COMS report no. 19. *Ophthalmology* **2002**, *109*, 2197–2206.
161. Maschi, C.; Thariat, J.; Herault, J.; Caujolle, J.P. Tumour Response in Uveal Melanomas Treated with Proton Beam Therapy. *Clin. Oncol.* **2015**, *28*, 198–203.
162. Kang, D.W.; Lee, S.C.; Park, Y.G.; Chang, J.H. Long-term results of Gamma Knife surgery for uveal melanomas. *J. Neurosurg.* **2012**, *117*, 108–114.
163. Bitencourt, F.B.C.S.N.; Bitencourt, A.G.V.; Chojniak, M.M.M.; Souza, J.O.; Castro, D.G.; Pellizzon, A.C.A.; Chojniak, R. Response Evaluation of Choroidal Melanoma After Brachytherapy Using Diffusion-Weighted Magnetic Resonance Imaging (DW-MRI): Preliminary Findings. *Front. Oncol.* **2020**, *10*, 825.
164. Toktas, Z.O.; Bicer, A.; Demirci, G.; Pazarli, H.; Abacioglu, U.; Peker, S.; Kilic, T. Gamma knife stereotactic radiosurgery yields good long-term outcomes for low-volume uveal melanomas without intraocular complications. *J. Clin. Neurosci.* **2010**, *17*, 441–445.
165. Kim, T.W.; Choi, E.; Park, J.; Shin, D.-H.; Jung, S.K.; Seok, S.; Cho, K.H.; Kim, J.-Y.; Kim, D.Y.; Suh, Y.K.; et al. Clinical Outcomes of Proton Beam Therapy for Choroidal Melanoma at a Single Institute in Korea. *Cancer Res. Treat.* **2018**, *50*, 335–344.
166. Mishra, K.K.; Daftari, I.K. Proton therapy for the management of uveal melanoma and other ocular tumors. *Chin. Clin. Oncol.* **2016**, *5*, 50.
167. Egger, E.; Schalenbourg, A.; Zografos, L.; Bercher, L.; Boehringer, T.; Chamot, L.; Goitein, G. Maximizing local tumor control and survival after proton beam radiotherapy of uveal melanoma. *Int. J. Radiat. Oncol.* **2001**, *51*, 138–147.

168. Knutsen, S.; Hafslund, R.; Monge, O.R.; Valen, H.; Muren, L.P.; Rekestad, B.L.; Krohn, J.; Dahl, O. Dosimetric verification of a dedicated 3D treatment planning system for episcleral plaque therapy. *Int. J. Radiat. Oncol.* **2001**, *51*, 1159–1166.
169. Results of a survey across 17 ocular proton therapy centers. Presented at the OPTIC subcommittee meeting at PTCOG 2022. Miami, FL, USA, 14 July 2022.
170. Najjar, Y.G.; Navrazhina, K.; Ding, F.; Bhatia, R.; Tsai, K.; Abbate, K.; Durden, B.; Eroglu, Z.; Bhatia, S.; Park, S.; et al. Ipilimumab plus nivolumab for patients with metastatic uveal melanoma: A multicenter, retrospective study. *J. Immunother. Cancer* **2020**, *8*, e000331
171. Nathan, P.; Hassel, J.C.; Rutkowski, P.; Baurain, J.-F.; Butler, M.O.; Schlaak, M.; Sullivan, R.J.; Ochseneither, S.; Dummer, R.; Kirkwood, J.M.; et al. Overall Survival Benefit with Tebentafusp in Metastatic Uveal Melanoma. *N. Engl. J. Med.* **2021**, *385*, 1196–1206
172. Grech Fonk, L.; Ferreira, T.A.; Webb, A.G.; Luyten, G.P.M.; Beenakker, J.M. The Economic Value of MR-Imaging for Uveal Melanoma. *Clin. Ophthalmol.* **2020**, *14*, 1135–1143.



Chapter 3

Geometrical accuracy of magnetic resonance imaging for ocular proton therapy planning

PhD project chapter

L. Klaassen, C. Haasjes, M. Hol, P. Cambraia Lopes
K. Spruijt, C. van de Steeg – Henzen, T.H.K. Vu, P.A.C. Bakker
C.R.N. Rasch, B.M. Verbist, J.W.M. Beenakker

Physics & Imaging in Radiation Oncology (2024). doi: 10.1016/j.phro.2024.100598

ABSTRACT

Background & purpose

Magnetic resonance imaging (MRI) is increasingly used in treatment preparation of ocular proton therapy, but its spatial accuracy might be limited by geometric distortions due to susceptibility artefacts. A correct geometry of the MR images is paramount since it defines where the dose will be delivered. In this study, we assessed the geometrical accuracy of ocular MRI.

Materials & methods

A dedicated ocular 3 T MRI protocol, with localized shimming and increased gradients, was compared to computed tomography (CT) and X-ray images in a phantom and in 15 uveal melanoma patients. The MRI protocol contained three-dimensional T2-weighted and T1-weighted sequences with an isotropic reconstruction resolution of 0.3–0.4 mm. Tantalum clips were identified by three observers and clip-clip distances were compared between T2-weighted and T1-weighted MRI, CT and X-ray images for the phantom and between MRI and X-ray images for the patients.

Results

Interobserver variability was below 0.35 mm for the phantom and 0.30(T1)/0.61(T2) mm in patients. Mean absolute differences between MRI and reference were below 0.27 ± 0.16 mm and 0.32 ± 0.23 mm for the phantom and in patients, respectively. In patients, clip-clip distances were slightly larger on MRI than on X-ray images (mean difference T1: 0.11 ± 0.38 mm, T2: 0.10 ± 0.44 mm). Differences did not increase at larger distances and did not correlate to interobserver variability.

Conclusions

A dedicated ocular MRI protocol can produce images of the eye with a geometrical accuracy below half the MRI acquisition voxel (<0.4 mm). Therefore, these images can be used for ocular proton therapy planning, both in the current model-based workflow and in proposed three-dimensional MR-based workflows.

INTRODUCTION

Ocular proton therapy (OPT) results in high local control rates and is therefore one of the primary treatments for uveal melanoma [1], [2], [3]. Treatment planning in ocular proton therapy is generally based on a geometrical model which is rigidly rescaled to patient-specific eye dimensions. Therefore, definition of the target and organs at risk (OAR) conventionally relies on several ophthalmological modalities, such as ocular ultrasound and fundoscopic imaging, and the surgical placement of tantalum clips, which can be identified in the eye treatment room with X-ray imaging [4].

Ocular Magnetic Resonance Imaging (MRI) offers three-dimensional imaging with soft tissue contrast that is superior to other imaging modalities, such as ultrasound and Computed Tomography (CT) [5], [6]. Therefore, it is increasingly used in ocular oncology for diagnosis, treatment decision making and treatment preparation [7], [8], [9], [10]. In the context of ocular proton therapy planning, MR-based measurements such as tumour dimensions and clip-tumour distances have been proposed to improve the accuracy of the current, model-based, treatment planning [4], [11]. Furthermore, several centres are exploring the possibility of moving towards three-dimensional (3D) MR-based ocular proton therapy [12], [13], [14], [15].

In MR-guided radiotherapy, susceptibility artefacts caused by the boundaries between air and different tissues can limit the spatial accuracy of MR images [16]. In ocular MRI, such geometric distortions may be caused by the nasal and oral cavities and orbital bone. At the eyelids, a wet gauze has been proposed to mitigate these artefacts [10], [17], [18]. Although in other tumour sites acceptance criteria for geometric distortions up to 1–2 mm have been described [19], for the eye sub-millimetre differences can already have direct clinical implications, the most important being underdosage of the tumour [11], [20], [21]. In general, geometric distortions caused by magnetic field inhomogeneities scale with measured distance, suggesting that their extent will be limited in a small organ such as the eye.

A complicating factor in the use of MRI for OPT planning is the use of tantalum fiducial clips, which are sutured onto the sclera and are used for treatment planning and daily position verification. Although the MR-safety of these clips has been shown, they can result in signal void artefacts [22]. Several strategies have been proposed to mitigate these artefacts, such as the use of a spin echo sequence, localized shimming and increased gradient strengths (>22 mT/m) [11]. Several studies suggest that, when such a dedicated ocular MRI protocol is used, potential geometric distortions on the MR images are limited, as there is a high level of agreement between MRI and other

modalities, such as the optics-based eye length measurements [23], [24]. However, moving towards 3D MR-based OPT, the geometrical accuracy of the used MR images becomes increasingly relevant, as possible distortions may result in an incorrect target definition, possibly leading to a tumour underdosage or an increase in OAR toxicity.

Although the use of MRI has advantages in terms of 3D imaging and soft tissue contrast, possible geometrical distortions would contribute to treatment uncertainties. Therefore, the aim of this study was to assess the geometrical accuracy of a dedicated ocular MRI protocol for ocular proton therapy planning. To this end, clip-clip and landmark-landmark distances were assessed on the proposed MRI protocol and on X-ray and CT images in a phantom and in patients.

METHODS

The geometric accuracy of the ocular MRI protocol currently used clinically for proton therapy planning at the Leiden UMC and HollandPTC (proton therapy centre) was assessed in a phantom and in patients.

The phantom (Fig. 1A–C) consisted of a cellulose acetate butyrate head-shaped shell (Phantom Laboratory LiquiPhil Head, Salem, New York, United States) filled with a saline solution, two 3D-printed polyamide grids as geometric reference and several air-filled tubes, mimicking the oral and nasal cavities (Fig. 1A–B). To one of the grids, five tantalum clips (Altomed Limited, Boldon, England), with a diameter of 2.5 mm and a thickness of 0.17 mm, were glued (Fig. 1C–D). Furthermore, nine intersections of the grid served as landmarks (Fig. 1E). These were chosen to have a landmark-landmark distance representative for the field of view of the scans.

For the *in vivo* evaluation, data of 15 consecutive uveal melanoma patients, referred to HollandPTC by the Leiden UMC, were retrospectively analysed after approval of the local ethics committee and having obtained written informed consent. All patients underwent clinical MRI scans to prepare for proton therapy. Patients had a median tumour prominence (including sclera) of 8.3 mm (range 2.4–11.4 mm) and a median largest basal diameter of 14.2 mm (range 7.9–17.6 mm), with 6/15 tumours being located in the left eye. Most tumours had a central localization (10/15), with 3/15 tumours located mid-peripherally and 2/15 peripherally. The clips were placed by an ocular oncologist, adjacent to the tumour.

Imaging

The evaluated MRI scans are part of a protocol that was described earlier [11] and were obtained at two 3 T scanners (phantom: Ingenia, patients: Ingenia Elition, Philips Healthcare, the Netherlands) with a 4.7 cm surface receive coil (Philips Healthcare), placed on the affected eye [25]. The scan parameters from this MRI protocol differ from earlier described diagnostic protocols [7], [25] as it includes localized first-order shimming, increased gradient strengths and resulting minimal water-fat shift, spin echo (SE) sequences and higher refocussing angles to minimize tantalum clip induced artefacts. These modifications of the acquisition parameters result in higher geometrical accuracy at the cost of signal-to-noise. From the complete protocol, the 3D T2-weighted and T1-weighted SE sequences were assessed, as these are suitable for image-based radiotherapy planning. All MR scans had an isotropic reconstruction resolution of 0.3–0.4 mm (Table 1). In accordance with local clinical protocol, all sequences were performed without fat suppression to improve clip visibility. A shim volume of $65 \times 60 \times 55 \text{ mm}^3$ was placed around the eye. For the patients, the T1-weighted scan was obtained after administration of 0.1 mmol/kg of gadoterate meglumine (DOTAREM, Guerbet, Roissy CdG Cedex, France) [11]. Patients were supported by a head rest (Fig. 2I) and were asked to keep their eyes closed during the exam, without specific gazing angle instructions.

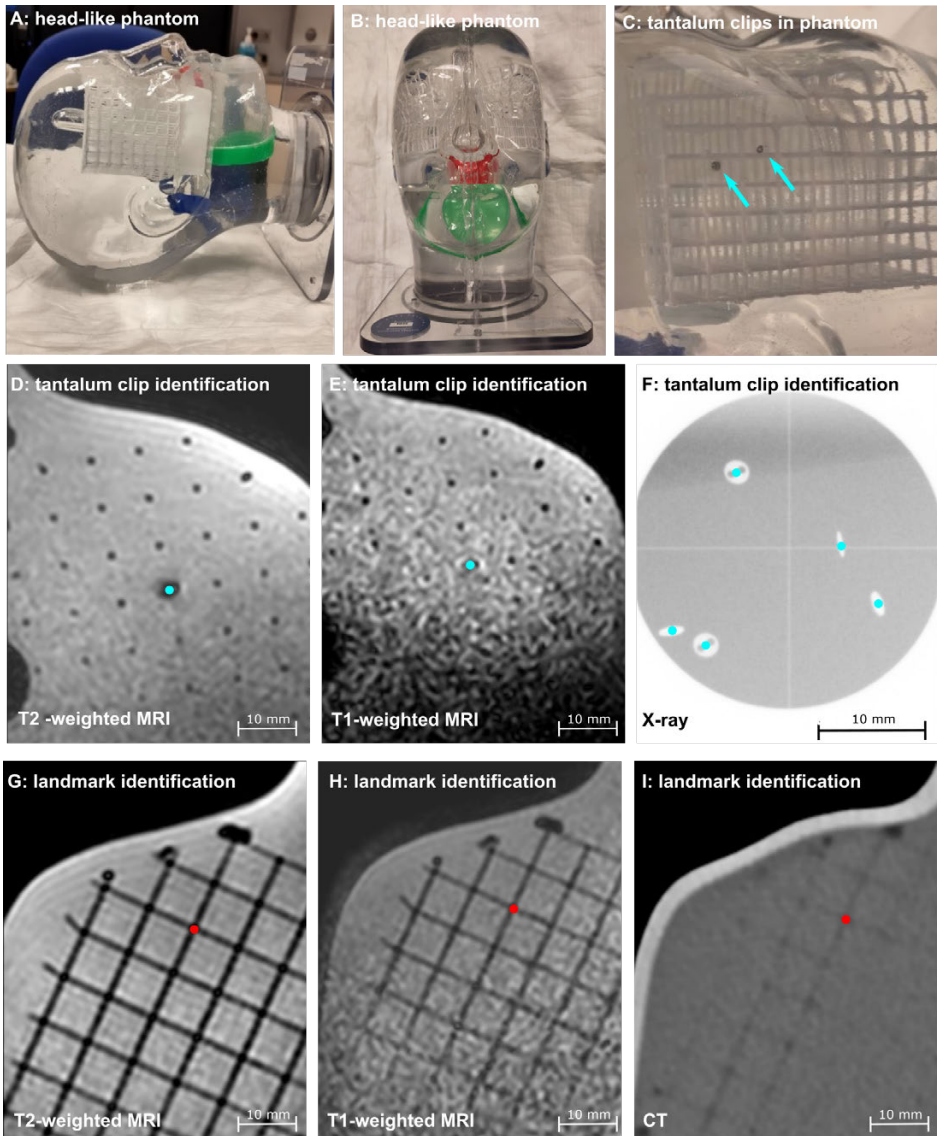


Figure 1. Phantom set-up. (A,B) The head-like phantom, (C) Five tantalum clips were glued onto one of the polyamide grids. These tantalum clips (D-F) and nine grid intersection landmarks (G-I) were identified by three observers in a 3D viewer on T2-weighted MRI (D,G), T1-weighted MRI (E,H), X-ray (F) and CT images (I).

Table 1.

	MRI		CT		X-ray images
	T1-weighted	T2-weighted	120 kV	140 kV	
Acquisition resolution	$0.8 \times 0.8 \times 0.8 \text{ mm}^3$	$0.8 \times 0.8 \times 0.8 \text{ mm}^3$	$0.3 \times 0.3 \times 0.5 \text{ mm}^3$	$0.3 \times 0.3 \times 0.5 \text{ mm}^3$	LR: $0.08 \times 0.08 \text{ mm}^2$
Reconstruction resolution	$0.4 \times 0.4 \times 0.4 \text{ mm}^3$	$0.3 \times 0.3 \times 0.4 \text{ mm}^3$			AP: $0.10 \times 0.10 \text{ mm}^2$
TE [ms] / TR [ms] / Flip or Refocusing Angle [°] / Echo train length	26/400/90/20	305/2500/35/117	-	-	-
Bandwidth [Hz]	758	943	-	-	-
Scan time [mm:ss]	02:07	02:58	-	-	-
Remarks	Patients: contrast-enhanced	-	Without metal artefact reduction	With metal artefact reduction	From eye treatment room
Evaluation	Phantom & patients	Phantom & patients	Phantom (landmark side)	Comparison to X-ray	Phantom & patients

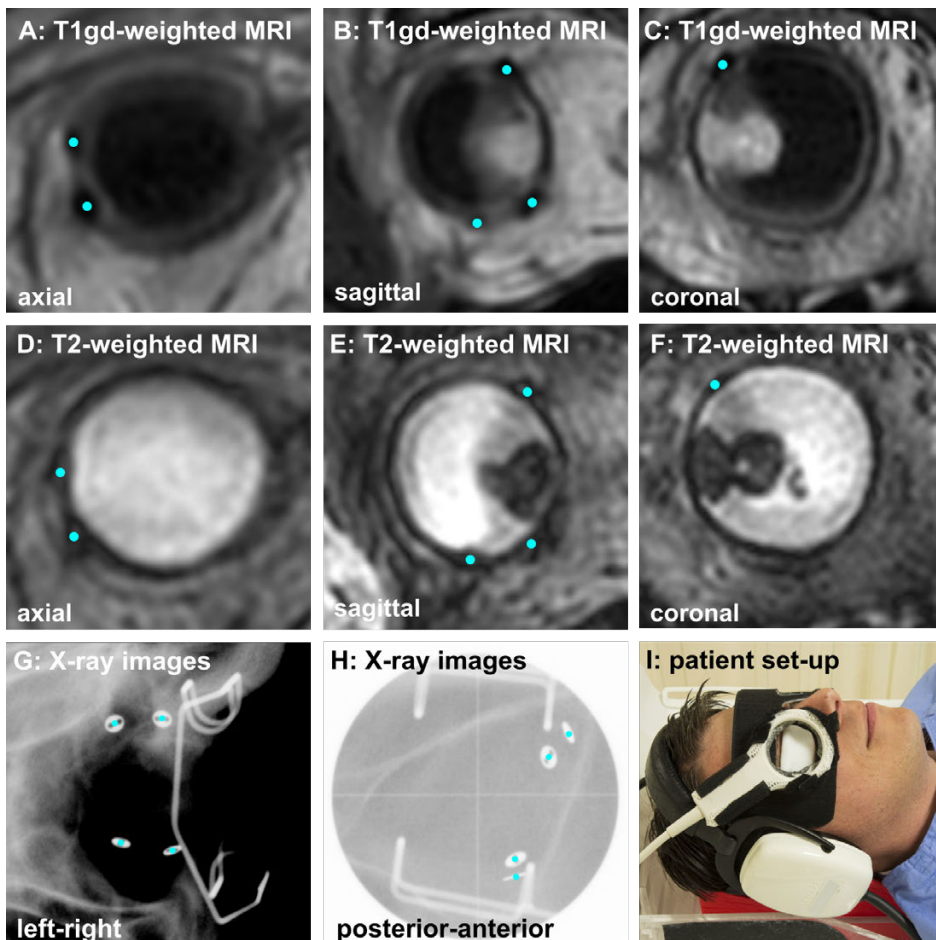


Figure 2. Images used in the patients: 3D contrast-enhanced T1-weighted (T1gd) MRI (A-C), 3D T2-weighted MRI (D-F), and X-ray images (G,H) and the patient set-up (I). Tantalum clips were identified on MRI and X-ray images by three observers.

As a ground-truth reference for the tantalum clip position both in the phantom and in patients, X-ray images from the eye treatment room (ETR) were used. For the grid intersection landmarks in the phantom, CT scans (SOMATOM Definition Edge, Siemens Healthineers, Erlangen, Germany) were used as a reference, as these were not visible on the X-ray images. The X-ray images consisted of one anteroposterior image (resolution $0.10 \times 0.10 \text{ mm}^2$) and one lateral image ($0.08 \times 0.08 \text{ mm}^2$) in the treatment gazing direction, fixated by a LED and verified with an in-room camera. As the feet-head coordinate of the clips was represented in both the anteroposterior and lateral images, the average position was used for comparison with the MR images.

The CT scans had an in-plane resolution of $0.3 \times 0.3 \text{ mm}^2$, with a slice thickness of 0.5 mm and were obtained at 120 kV. To compare the tantalum clips positions on CT scans to the X-ray images, an additional CT scan was obtained at 140 kV with a metal artefact reduction protocol (Supplementary Fig. 1). More details about the imaging protocol are listed in Table 1.

Analysis

For both the phantom and patient data, the tantalum clips were manually identified by three observers (LK, MH, JWB) in a 3D viewer in MeVisLab (MeVis Medical Solutions AG, Bremen, Germany) (Fig. 1, Fig. 2). Similarly, for the phantom, nine grid intersection landmarks were identified. Clip-clip distances were compared between MRI and X-ray images, and landmark-landmark distances were compared between MRI and CT.

To assess possible systematic displacement of the centre of the clip-induced susceptibility artefacts with respect to the anatomy, four additional grid intersection landmarks were identified at the clip side of the phantom (Supplementary Fig. 2). With these additional landmarks, four clip-landmark distances were measured. Differences between CT and T1-weighted and T2-weighted MRI were assessed in the left–right, anteroposterior and craniocaudal direction. Furthermore, to assess how accurate clip locations on MRI can be translated to location in the eye treatment room, rigid iterative closest point registration was performed between the T1-weighted MRI and X-ray clip locations per patient [26]. Means and standard deviations of the residual errors were reported.

Finally, the largest diameter of the clip artefact was measured in a 3D viewer using a multiplanar reconstruction on all MRI sequences and on CT.

Statistical analyses

Interobserver variability for clip/landmark identification was determined by calculating the average distance to the average clip or landmark position for all three modalities. Furthermore, interobserver variability for clip-clip and/or landmark-landmark distances was expressed as the standard deviation from the mean clip-clip distance between the three observers.

Mean differences and mean absolute differences between the clip-clip distances on MRI and the reference modality were assessed. Furthermore, to assess the effect of possible magnetic field inhomogeneities, the correlation between landmark-landmark or clip-clip distance and difference between MRI and the reference was assessed using either Pearson's r for normally distributed data or Kendall's tau for non-normally

distributed data, depending on the results of the Shapiro-Wilks test for normality. Furthermore, the correlation between CT/X-ray-MRI differences and interobserver variability was assessed in the same way.

RESULTS

Interobserver variability

Observers agreed well on clip and landmark positions in the phantom: mean distances to mean clip or landmark position were below the acquisition voxel size for all sequences and imaging modalities, except for the T2-weighted MRI in patients (range 0.04 mm – 0.61 mm, Table 2). In patients, the mean distance to mean clip location for three observers was 0.05 mm, with standard deviations between clip-clip distances of 0.03 mm. For the contrast-enhanced T1-weighted MRI scans, the mean distance to mean clip location for three observers was 0.30 mm, a similar interobserver variation as in the phantom (Table 2). Similar interobserver variabilities were observed for clip-clip and landmark-landmark distances, with all mean SDs below 0.28 mm (Supplementary Table 1).

Table 2. Interobserver variability between 3 observers for clip and landmark identification on MRI and CT in a phantom and in patients.

	Inter-observer variability: Mean distance to mean clip or landmark position [mm]		
	Phantom		Patients (n = 15)
	Clips (n = 5)	Landmarks (n = 9)	Clips (n = 59)
T1-weighted MRI	0.35 ± 0.11	0.08 ± 0.03	0.30 ± 0.09
T2-weighted MRI	0.13 ± 0.04	0.11 ± 0.02	0.61 ± 0.19
CT	0.15 ± 0.05	0.21 ± 0.05	–
X-ray	0.04 ± 0.02	–	0.05 ± 0.01

Differences in clip-clip and landmark-landmark distances

For the phantom, mean absolute differences between MRI and the reference were below 0.27 ± 0.16 mm for the clips and 0.20 ± 0.14 mm for the landmarks, for distances up to 37 mm (Fig. 3, Supplementary Fig. 3). In patients, clip-clip distances were slightly larger on MR than on X-ray images, with a mean difference of 0.11 mm ± 0.38 mm for T1 and 0.10 ± 0.44 mm for T2 (Fig. 3). This effect was not observed in the phantom, with mean differences of 0.03 ± 0.31 mm and -0.04 ± 0.16 mm for T1 and T2, respectively.

Differences between MR and X-ray images were not correlated to the clip-clip distance for the phantom (Supplementary Fig. 3, Pearson's $r = -0.01$, $p = 0.87$) or in patients (Fig. 4A, Pearson's $r = 0.17$, $p = 0.12$), suggesting that geometrical distortions due to magnetic field inhomogeneity were minor or absent. In some patients with clips located close to the tumour edge, a local distortion of the tumour contour was observed on the MR images due to the clip's signal void artefact (Fig. 4B). MRI-reference differences did not correlate with interobserver variation on MRI for both the phantom and patients (Supplementary Fig. 3).

Other analyses

Largest diameters of the tantalum marker signal void in the phantom were, on average, 4.7 mm for T2-weighted MRI, 4.6 mm for T1-weighted MRI and 18.7 mm for CT.

In the phantom, the mean absolute difference of the clip-clip distances between CT and X-ray was 0.16 ± 0.06 mm.

In the assessment of systematic clip displacement in the phantom with respect to the landmarks, differences between CT and T1-weighted MRI were 0.29 ± 0.30 mm, 0.25 ± 0.29 mm and -0.36 ± 0.44 mm in the left–right, anteroposterior and craniocaudal directions, respectively. For T2-weighted MRI, differences were 0.43 ± 0.43 mm, 0.22 ± 0.33 mm and 0.04 ± 0.33 mm, respectively.

After registration of the clips on the contrast-enhanced T1-weighted MRI to the clip location on X-ray images, mean differences below 10⁻⁶ mm and standard deviations of 0.17, 0.25 and 0.16 mm for the left–right, anteroposterior and craniocaudal directions were observed. Differences between directions were not significant ($p = 1.00$).

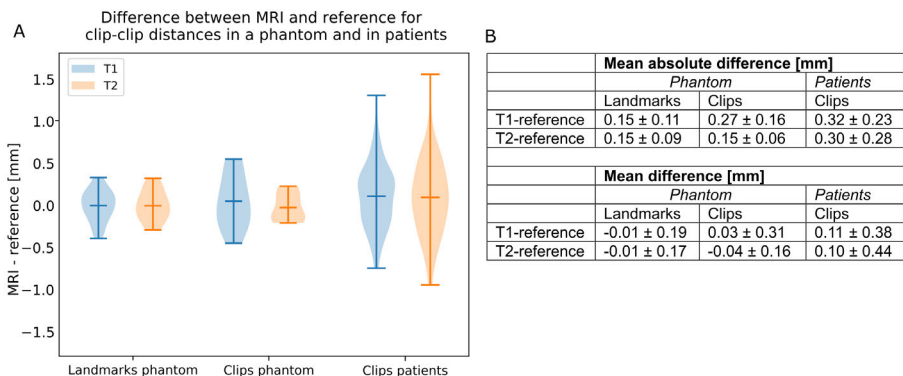


Figure 3. (A) Difference in clip-clip and landmark-landmark distances between MRI and the reference (X-ray for the clips and CT for the landmarks) in a phantom and in patients. (B)

Mean absolute differences ($\pm SD$) and mean differences ($\pm SD$) were below half the acquisition voxel size for all sequences.

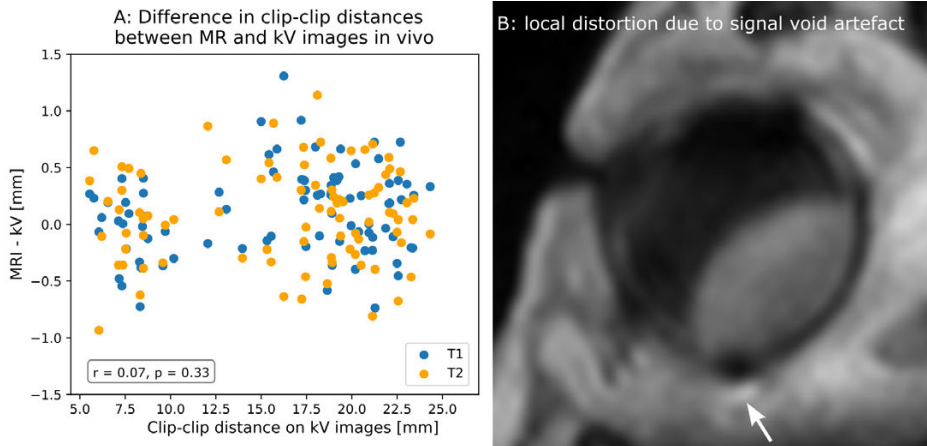


Figure 4. Difference between X-ray and MR images for clip-clip distances in patients. (A) Mean clip-clip distances were on average 0.1 ± 0.4 mm larger on MRI. Differences were not larger at larger distances (Pearson's $r = 0.07$, $p = 0.33$). (B) For some clips located close to the tumour, a local distortion of the tumour shape was observed. Below the clip a local increase in signal is observed, due to the local inhomogeneous magnetic field.

DISCUSSION

In this paper, the geometrical accuracy of a clinically used ocular MRI protocol was assessed. Both in the phantom and in patients, differences between MRI and the reference (CT or X-ray images) were smaller than half the MRI acquisition voxel (<0.4 mm). These differences were observed over distances up to 37 mm, which is more than the typical diameter of the eye (approximately 24 mm), and therefore larger than the dimensions relevant for ocular proton therapy. Results were similar between T1-weighted and T2-weighted sequences, but in patients, larger interobserver variation was observed for clip identification on the T2-weighted scans. This larger interobserver variation may be caused by the difficulty of finding the clip centre due to the longer echo train of the T2-weighted scan (Table 1). As differences between MRI and the reference did not increase at larger distances, we can conclude that magnetic field inhomogeneities are limited in this specific MRI protocol. In patients, clip-clip distances on MRI were on average 0.1 mm larger than on the X-ray images. This is likely related to the fact that the clip-induced signal void and the sclera are both hypo-intense on all MR-sequences, making the centre of the clip appear slightly more

outward of the eye. We explored whether automatic clip detection, as for example proposed for prostate radiotherapy [27], [28], [29], was feasible for this protocol, but this generally resulted in larger errors between MRI and X-ray images (Appendix A). Possible displacements of the tantalum clip artefact centre with respect to grid intersection landmarks were assessed in the phantom, resulting in mean differences in clip-reference distances between MRI and CT below half an MRI acquisition voxel, which can likely be attributed to large clip-related artefacts on CT (Supplementary Fig. 1).

The results from this study correspond well to the literature on geometric accuracy of MRI for radiotherapy planning in other tumour sites: in patients with prostate cancer, mean differences below 1 mm were reported [30]. Comparable results were found in geometrical accuracy of MRI for neurological tumours, with differences up to 0.6 mm and 1.3 mm reported in different studies [31], [32]. In a phantom study, mean differences of 0.2 mm between clip location on MRI and true clip locations were described [33]. Furthermore, another phantom study evaluated several MRI protocols with thicker slices of 1 mm at 1.5 and 3.0 T and found mean distortions of 0.5 to 0.8 mm [34].

Uncertainties regarding MRI imaging are below half an acquisition voxel and are smaller than some uncertainties in the current target definition, such as the interobserver variability of 0.6 mm in tumour thickness measurements on ultrasound [35], errors larger than 1 mm in surgical measurement of clip-tumour distances [11] and the even larger discrepancies in the registration of fundoscopic imaging data [36]. As this MRI protocol provides geometrically accurate visualisation of the tumour and surrounding structures, it might contribute to a decrease of the current uncertainties in target definition, although further studies are required on the accurate GTV determination of ocular tumours on MRI [7], [9], [21], [37]. In this context, particularly fundoscopy will be valuable in the identification of the macula position and possible flat tumour extensions.

A limitation of the phantom analysis is that the phantom lacked fatty tissue around the eye, which is present in patients. This resulted in a lower contrast-to-noise ratio between the clip and surrounding anatomy in the phantom compared to in patients (Fig. 1E and 2A), especially for the 3D T1-weighted spin echo sequence. Correspondingly, the phantom interobserver variability for this sequence is poorer than the interobserver variability in patients.

In this study, spatially localized MRI artefacts, such as signal build-up or the signal void artefact itself, were not considered. These local effects might affect MR-based tumour definition, especially when clips are located very close to the tumour (Fig. 4B). However, clip artefacts are significantly larger on CT than on MRI, with an average CT artefact of more than 7 times the tantalum clip diameter [22], whereas the artefact on MRI extends about one mm around the clip itself. Therefore, image distortions further away from the clip are unlikely.

The results obtained in this study depend strongly on the used MRI protocol and are therefore not directly applicable to all ocular MR images. To limit the extent of susceptibility induced artefacts, the protocol utilized a spin echo sequence, localized shimming, and increased gradient strengths. Scans with less dedicated settings, or sequences which are more affected by magnetic field inhomogeneities such as the constructive interference in steady state (CISS) or volumetric interpolated breath-hold examination (VIBE) sequence [21], [22], [38], [39], [40], will likely have larger geometric distortions. Similarly, protocols which scan both orbits and/or the entire head are expected to provide a less accurate visualisation, as the possibility of using shimming to correct for magnetic field inhomogeneities will be limited, due to the nasal cavity which is present in the middle of the field of view.

The protocol described in this study is currently used clinically for treatment planning at HollandPTC. Several measures were taken to minimize geometric distortions, which also result in a lower signal-to-noise ratio (SNR) compared to the diagnostic protocols. Therefore, more subtle anatomical features, which aid the differential diagnosis, may not be visible in these scans. However, as a study on interobserver variability with a previous version of this protocol showed the largest variation in the decision to include or exclude areas [37], and tumour borders were easily distinguishable in this study (Fig. 2, Fig. 4), the impact of the lower SNR on contouring accuracy will likely be limited.

In conclusion, a dedicated ocular MRI protocol can provide geometrically accurate images of the eye since differences between MRI and the reference were well below the voxel size and did not depend on distances. As these discrepancies did not increase with distance, magnetic field inhomogeneities do not limit the geometrical accuracy of ocular MRI. Therefore, these images can be used for ocular proton therapy planning, both in the current model-based workflow and future 3D MR-only workflows.

REFERENCES

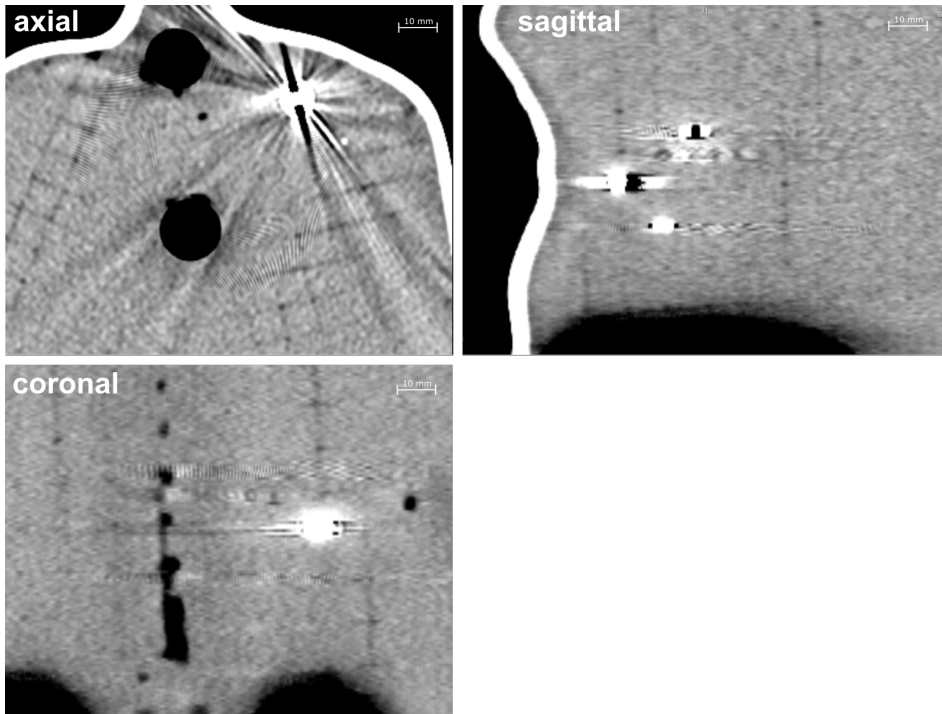
1. Dendale R., Lumbroso-Le Rouic L., Noel G., Feuvret L., Levy C., Delacroix S., et al. Proton beam radiotherapy for uveal melanoma: results of Curie Institut-Orsay proton therapy center (ICPO) *Int J Radiat Oncol Biol Phys.* 2006;65:780–787. doi: 10.1016/j.ijrobp.2006.01.020.
2. Marinkovic M., Pors L.J., van den Berg V., Peters F.P., Schalenbourg A., Zografos L., et al. Clinical Outcomes after International Referral of Uveal Melanoma Patients for Proton Therapy. *Cancers (Basel)* 2021;13. doi: 10.3390/cancers13246241.
3. Mishra K.K., Daftari I.K. Proton therapy for the management of uveal melanoma and other ocular tumors. *Chin Clin Oncol.* 2016;5:50. doi: 10.21037/cco.2016.07.06.
4. Hrbacek J., Mishra K.K., Kacperek A., Dendale R., Nauraye C., Auger M., et al. Practice Patterns Analysis of Ocular Proton Therapy Centers: The International OPTIC Survey. *Int J Radiat Oncol Biol Phys.* 2016;95:336–343. doi: 10.1016/j.ijrobp.2016.01.040.
5. Jaarsma-Coes M.G., Klaassen L., Marinkovic M., Luyten G.P.M., Vu T.H.K., Ferreira T.A., et al. Magnetic Resonance Imaging in the Clinical Care for Uveal Melanoma Patients-A Systematic Review from an Ophthalmic Perspective. *Cancers (Basel)* 2023;15. doi: 10.3390/cancers15112995
6. Niendorf T., Beenakker J.M., Langner S., Erb-Eigner K., Bach Cuadra M., Beller E., et al. Ophthalmic Magnetic Resonance Imaging: Where Are We (Heading To)? *Curr Eye Res.* 2021;46:1251–1270. doi: 10.1080/02713683.2021.1874021.
7. Ferreira T.A., Jaarsma-Coes M.G., Marinkovic M., Verbist B., Verdijk R.M., Jager M.J., et al. MR imaging characteristics of uveal melanoma with histopathological validation. *Neuroradiology.* 2022;64:171–184. doi: 10.1007/s00234-021-02825-5.
8. Foti P.V., Travali M., Farina R., Palmucci S., Spatola C., Raffaele L., et al. Diagnostic methods and therapeutic options of uveal melanoma with emphasis on MR imaging-Part I: MR imaging with pathologic correlation and technical considerations. *Insights Imaging.* 2021;12:66. doi: 10.1186/s13244-021-01000-x.
9. Klaassen L., Jaarsma-Coes M.G., Verbist B.M., Vu T.H.K., Marinkovic M., Rasch C.R.N., et al. Automatic Three-Dimensional Magnetic Resonance-based measurements of tumour prominence and basal diameter for treatment planning of uveal melanoma. *Phys Imaging Radiat Oncol.* 2022;24:102–110. doi: 10.1016/j.phro.2022.11.001.
10. Beenakker J.W., van Rijn G.A., Luyten G.P., Webb A.G. High-resolution MRI of uveal melanoma using a microcoil phased array at 7 T. *NMR Biomed.* 2013;26:1864–1869. doi: 10.1002/nbm.3041.
11. Jaarsma-Coes M.G., Ferreira T.A., Marinkovic M., Vu T.H.K., van Vught L., van Haren G.R., et al. Comparison of Magnetic Resonance Imaging-Based and Conventional Measurements for Proton Beam Therapy of Uveal Melanoma. *Ophthalmol Retina.* 2023;7:178–188. doi: 10.1016/j.oret.2022.06.019.
12. Fleury E., Trnkova P., Erdal E., Hassan M., Stoel B., Jaarma-Coes M., et al. Three-dimensional MRI-based treatment planning approach for non-invasive ocular proton therapy. *Med Phys.* 2021;48:1315–1326. doi: 10.1002/mp.14665.
13. Via R., Pica A., Antonioli L., Paganelli C., Fattori G., Spaccapaniccia C., et al. MRI and FUNDUS image fusion for improved ocular biometry in Ocular Proton Therapy. *Radiother Oncol.* 2022;174:16–22. doi: 10.1016/j.radonc.2022.06.021.
14. Wulff J., Koska B., Heufelder J., Janson M., Backer C.M., Siregar H., et al. Commissioning and validation of a novel commercial TPS for ocular proton therapy. *Med Phys.* 2023;50:365–379. doi: 10.1002/mp.16006.

15. Wulff J., Koska B., Janson M., Baumer C., Denker A., Geismar D., et al. Technical note: Impact of beam properties for uveal melanoma proton therapy-An in silico planning study. *Med Phys.* 2022;49:3481–3488. doi: 10.1002/mp.15573.
16. Weygand J., Fuller C.D., Ibbott G.S., Mohamed A.S., Ding Y., Yang J., et al. Spatial Precision in Magnetic Resonance Imaging-Guided Radiation Therapy: The Role of Geometric Distortion. *Int J Radiat Oncol Biol Phys.* 2016;95:1304–1316. doi: 10.1016/j.ijrobp.2016.02.059.
17. Bert R.J., Patz S., Ossiani M., Caruthers S.D., Jara H., Krejza J., et al. High-resolution MR imaging of the human eye 2005. *Acad Radiol.* 2006;13:368–378. doi: 10.1016/j.acra.2005.10.023.
18. Berkowitz B.A., McDonald C., Ito Y., Tofts P.S., Latif Z., Gross J. Measuring the human retinal oxygenation response to a hyperoxic challenge using MRI: eliminating blinking artifacts and demonstrating proof of concept. *Magn Reson Med.* 2001;46:412–416. doi: 10.1002/mrm.1206.
19. Kavaluus H., Nousiainen K., Kajjaluo S., Seppala T., Saarilahti K., Tenhunen M. Determination of acceptance criteria for geometric accuracy of magnetic resonance imaging scanners used in radiotherapy planning. *Phys Imaging Radiat Oncol.* 2021;17:58–64. doi: 10.1016/j.phro.2021.01.003.
20. Beenakker J.W., Ferreira T.A., Soemarwoto K.P., Genders S.W., Teeuwisse W.M., Webb A.G., et al. Clinical evaluation of ultra-high-field MRI for three-dimensional visualisation of tumour size in uveal melanoma patients, with direct relevance to treatment planning. *MAGMA.* 2016;29:571–577. doi: 10.1007/s10334-016-0529-4.
21. Via R., Hennings F., Pica A., Fattori G., Beer J., Peroni M., et al. Potential and pitfalls of 1.5T MRI imaging for target volume definition in ocular proton therapy. *Radiother Oncol.* 2021;154:53–59. doi: 10.1016/j.radonc.2020.08.023.
22. Oberacker E., Paul K., Huelnhagen T., Oezerdem C., Winter L., Pohlmann A., et al. Magnetic resonance safety and compatibility of tantalum markers used in proton beam therapy for intraocular tumors: A 7.0 Tesla study. *Magn Reson Med.* 2017;78:1533–1546. doi: 10.1002/mrm.26534.
23. Wiseman S.J., Tatham A.J., Meijboom R., Terrera G.M., Hamid C., Doubal F.N., et al. Measuring axial length of the eye from magnetic resonance brain imaging. *BMC Ophthalmol.* 2022;22:54. doi: 10.1186/s12886-022-02289-y.
24. van Vught L., Shamonin D.P., Luyten G.P.M., Stoel B.C., Beenakker J.M. MRI-based 3D retinal shape determination. *BMJ Open Ophthalmol.* 2021;6:e000855. doi: 10.1136/bmjophth-2021-000855.
25. Ferreira T.A., Grech Fonk L., Jaarsma-Coes M.G., van Haren G.G.R., Marinkovic M., Beenakker J.M. MRI of Uveal Melanoma. *Cancers (Basel)* 2019;11. doi: 10.3390/cancers11030377.
26. Flannigan C. icp. Commit 167cc4a ed2017.
27. Galassi F., Brujic D., Rea M., Lambert N., Desouza N., Ristic M. Fast and accurate localization of multiple RF markers for tracking in MRI-guided interventions. *MAGMA.* 2015;28:33–48. doi: 10.1007/s10334-014-0446-3.
28. Gustafsson C., Korhonen J., Persson E., Gunnlaugsson A., Nyholm T., Olsson L.E. Registration free automatic identification of gold fiducial markers in MRI target delineation images for prostate radiotherapy. *Med Phys.* 2017;44:5563–5574. doi: 10.1002/mp.12516.
29. Gustafsson C.J., Sward J., Adalbjornsson S.I., Jakobsson A., Olsson L.E. Development and evaluation of a deep learning based artificial intelligence for automatic identification of gold fiducial markers in an MRI-only prostate radiotherapy workflow. *Phys Med Biol.* 2020;65 doi: 10.1088/1361-6560/abb0f9.

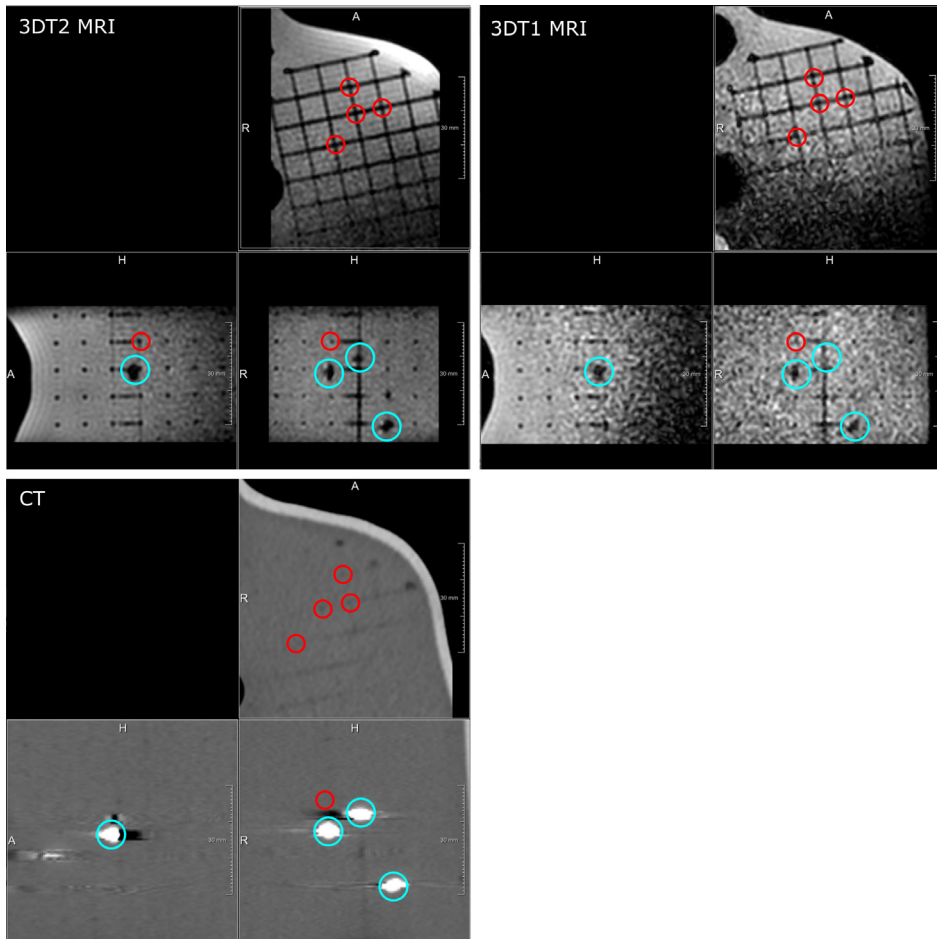
30. Jonsson J.H., Garpebring A., Karlsson M.G., Nyholm T. Internal fiducial markers and susceptibility effects in MRI-simulation and measurement of spatial accuracy. *Int J Radiat Oncol Biol Phys.* 2012;82:1612–1618. doi: 10.1016/j.ijrobp.2011.01.046.
31. Karaïskos P., Moutsatsos A., Pappas E., Georgiou E., Roussakis A., Torrens M., et al. A simple and efficient methodology to improve geometric accuracy in gamma knife radiation surgery: implementation in multiple brain metastases. *Int J Radiat Oncol Biol Phys.* 2014;90:1234–1241. doi: 10.1016/j.ijrobp.2014.08.349.
32. Zhang B., MacFadden D., Damyanovich A.Z., Rieker M., Stainsby J., Bernstein M., et al. Development of a geometrically accurate imaging protocol at 3 Tesla MRI for stereotactic radiosurgery treatment planning. *Phys Med Biol.* 2010;55:6601–6615. doi: 10.1088/0031-9155/55/22/002.
33. Nousiainen K., Makela T. Measuring geometric accuracy in magnetic resonance imaging with 3D-printed phantom and nonrigid image registration. *MAGMA.* 2020;33:401–410. doi: 10.1007/s10334-019-00788-6.
34. Pappas E.P., Alshantay M., Moutsatsos A., Lababidi H., Alsafi K., Georgiou K., et al. MRI-Related Geometric Distortions in Stereotactic Radiotherapy Treatment Planning: Evaluation and Dosimetric Impact. *Technol Cancer Res Treat.* 2017;16:1120–1129. doi: 10.1177/1533034617735454.
35. Char D.H., Kroll S., Stone R.D., Harrie R., Kerman B. Ultrasonographic measurement of uveal melanoma thickness: interobserver variability. *Br J Ophthalmol.* 1990;74:183–185. doi: 10.1136/bjo.74.3.183.
36. Wulff J., Koska B., Ahmad Khalil D., Richter R., Maximilian Backer C., Baumer C., et al. Uncertainties in ocular proton planning and their impact on required margins. *Phys Med.* 2024;121 doi: 10.1016/j.ejmp.2024.103358.
37. Jaarsma-Coes M.G., Klaassen L., Verbist B.M., Vu T.H.K., Klaver Y.L.B., Rodrigues M.F., et al. Inter-Observer Variability in MR-Based Target Volume Delineation of Uveal Melanoma. *Adv Radiat Oncol.* 2023;8 doi: 10.1016/j.adro.2022.101149.
38. Guberina M., Sokolenko E., Guberina N., Dalbah S., Pottgen C., Lubcke W., et al. Feasibility, Method and Early Outcome of Image-Guided Volumetric Modulated Arc Radiosurgery Followed by Resection for AJCC Stage IIA-III B High-Risk Large Intraocular Melanoma. *Cancers (Basel)* 2022;14. doi: 10.3390/cancers14194729.
39. Danieli L., Riccitelli G.C., Distefano D., Prodi E., Ventura E., Cianfoni A., et al. Brain Tumor-Enhancement Visualization and Morphometric Assessment: A Comparison of MPRAGE, SPACE, and VIBE MRI Techniques. *AJNR Am J Neuroradiol.* 2019;40:1140–1148. doi: 10.3174/ajnr.A6096.
40. de Graaf P., Goricke S., Rodjan F., Galluzzi P., Maeder P., Castelijns J.A., et al. Guidelines for imaging retinoblastoma: imaging principles and MRI standardization. *Pediatr Radiol.* 2012;42:2–14. doi: 10.1007/s00247-011-2201-5.

SUPPLEMENTARY DATA**Supplementary Table 1:** *Interobserver variability of clip-clip and landmark-landmark distances in the phantom*

Inter-observer variability: SD for clip-clip and landmark-landmark distances [mm]		
<i>Phantom</i>		
	Clips	Landmarks
T1-weighted SE MRI	0.28	0.06
T2-weighted SE MRI	0.08	0.06
CT	0.10	0.13
X-ray	0.04	
<i>Patients</i>		
	Clips	
Contrast-enhanced T1-weighted SE MRI	0.20	
T2-weighted SE MRI	0.50	
X-ray	0.03	

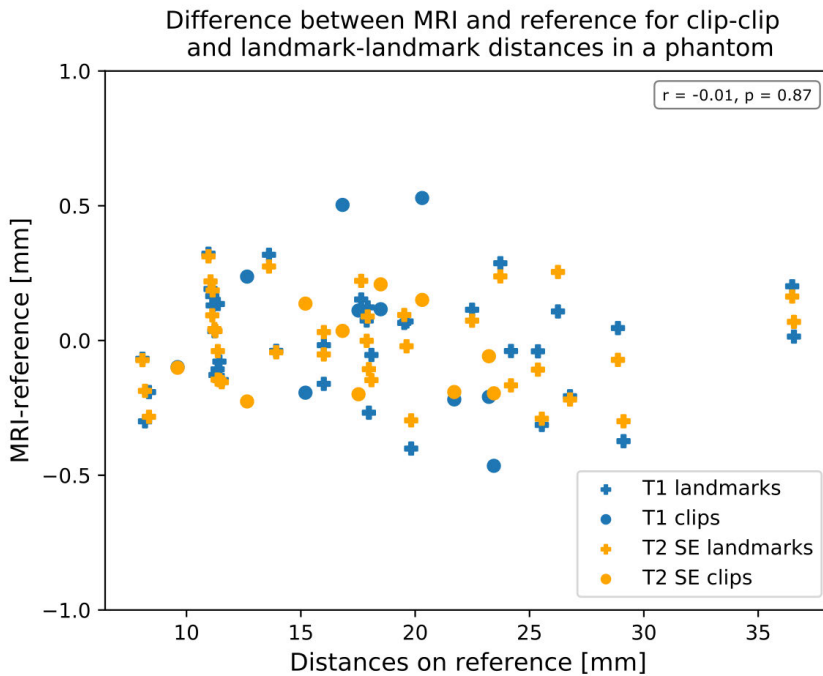


Supplementary Figure 1: Clip identification on CT

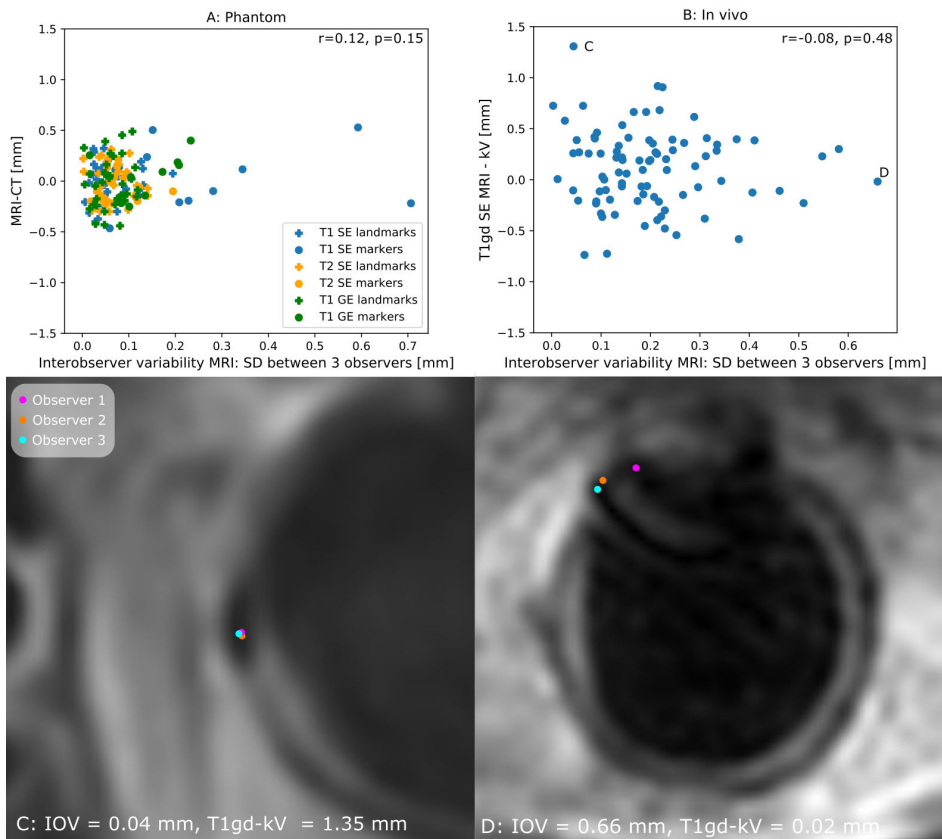


Supplementary Figure 2: Relative displacement analysis

Supplementary Figure 2: to assess possible systematic displacement of the centre of the clip-induced susceptibility artefacts with respect to the anatomy, four additional grid intersection landmarks (red) were identified at the clip side of the phantom. Distances between the clips (blue) and the grid intersection landmarks were determined.



Supplementary Figure 3: Difference in clip-clip (circle) and landmark-landmark (cross) distances between T1-weighted and T2-weighted MRI and the reference (X-ray for the clips and CT for the landmarks) in a phantom. Differences do not increase at larger clip-clip distances (Pearson's $r=-0.01$, $p=0.87$).



Supplementary Figure 4: Differences between MRI and X-ray/CT measurements did not depend on inter-observer variability. (A) Phantom. (B) In patients. (C) An example of a clip in a patient with a low interobserver variability, but a higher difference between X-ray and MRI. (D) An example of a clip in a patient that was difficult to identify on MR, but still resulted in a small difference between the mean location on MR and X-ray images.

APPENDIX A: SEMIAUTOMATIC DETECTION OF TANTALUM CLIP LOCATIONS IN OCULAR MAGNETIC RESONANCE IMAGING SCANS

Automatic fiducial clip detection has proven to reduce the interobserver variation of clip location other tumour sites. Therefore, a semi-automatic segmentation pipeline to detect tantalum clip locations in ocular MRI scans was developed and evaluated. The method was developed and evaluated on contrast-enhanced 3D T1-weighted images (main text: Table 1) of the 15 uveal melanoma patients in this study.

Methods

Approximate clip locations were manually annotated in MeVisLab (MeVis Medical Solutions, Bremen, Germany) (Figure A). A small region of interest ($5 \times 5 \times 5 \text{ mm}^3$) is extracted around the initial annotation, which is subsequently upsampled 5 times to allow for sub-voxel evaluation (Figure B). Using binary thresholding, the clip signal void is segmented (Figure C). The threshold is based on the signal intensity around the initial annotation. After thresholding, the Euclidean distance transform is applied, followed by Gaussian smoothing (sigma 0.3 mm, Figure D). The clip centre is defined as the local maximum closest to the initial annotation.

Evaluation

The manually determined clip locations were used as initial annotations for the segmentation pipeline. Clip-clip distances were calculated for the semiautomatically determined clip locations, and compared with the clip-clip distances on X-ray images.

The semiautomatic clip detection pipeline reduced the median interobserver variability from 0.25 mm to 0.04 mm, reducing the interobserver variability for 47/59 clips (Figure 2). However, the resulting clip-clip distances were less in agreement with the ground truth X-ray images than the manual annotations (mean absolute difference 0.32 mm vs 0.82 mm, Figure 3).

Incorrect clip locations from the semi-automatic method appeared to be caused by the similar signal intensities of the clip signal void, the sclera and the vitreous, which resulted in the inclusion of part of the vitreous in threshold image (Figure 4). In the future, this might be solved by including a segmentation of the sclera in the algorithm.

Conclusion

The developed semiautomatic pipeline reduced the interobserver variability, but at the cost of a strongly reduced accuracy and precision of the clip locations. Consequently, the smallest uncertainties are obtained by manual determination of the clip locations.

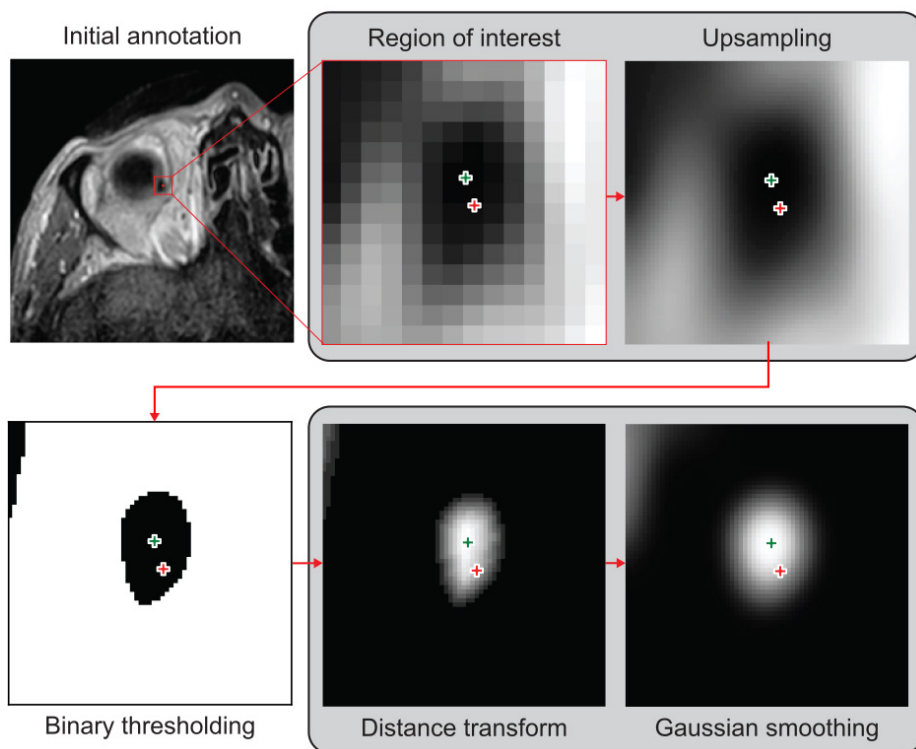


Figure 1: Semiautomatic detection method with initial annotation (red clip) and final result (green clip). Manually, the approximate clip location is identified. A 5x5x5 mm³ region of interest is selected around the initial annotation and upsampled 5 times. Euclidean distance transform is then applied to the thresholded ROI. After Gaussian smoothing with a kernel size of 0.3 mm, the clip location is defined as the maximum of the distance transform.

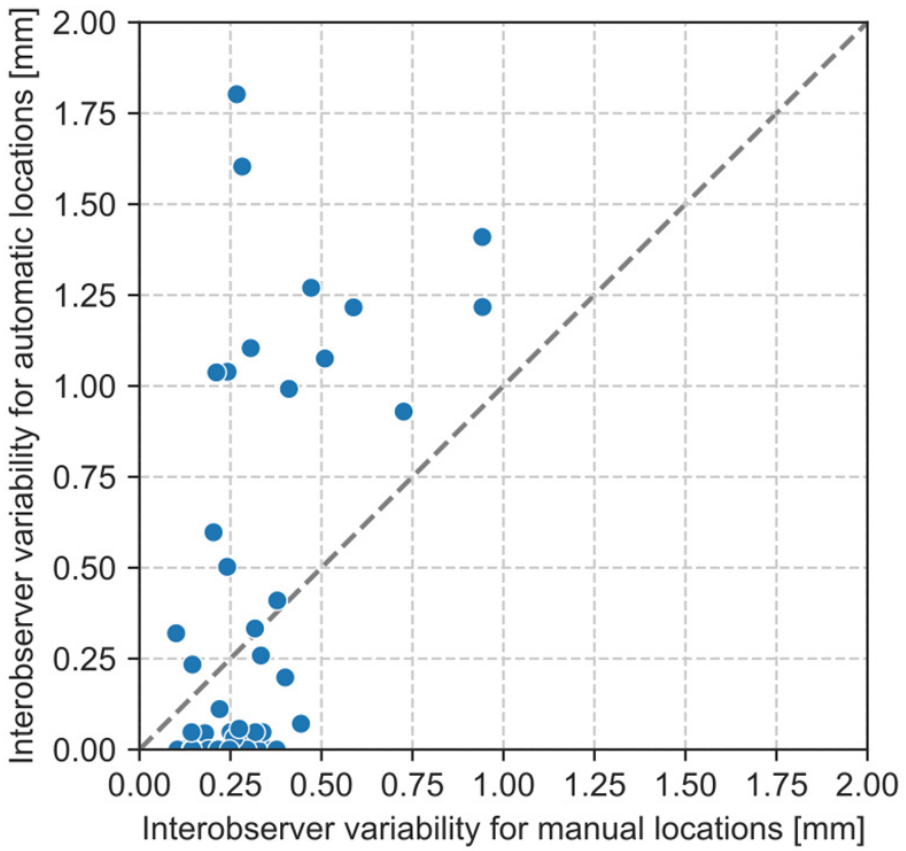


Figure 2: Semiautomatic detection reduced the median interobserver variability from 0.25 mm to 0.04 mm.

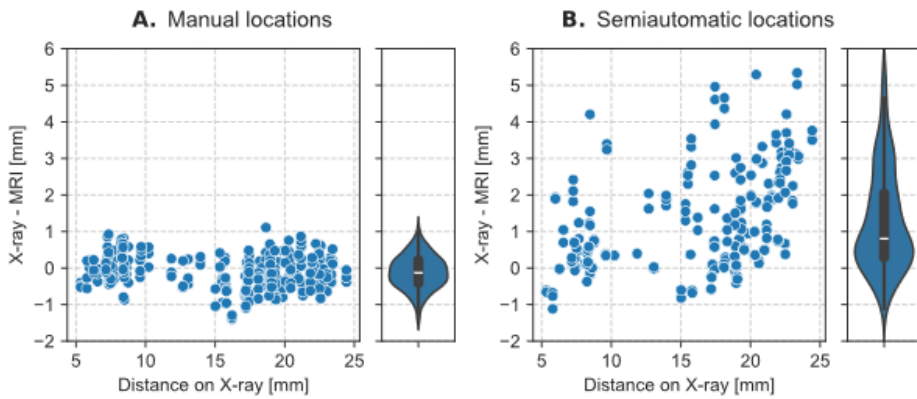


Figure 3: Comparison between manually determined clip locations (A) and clip locations determined with the semiautomatic pipeline (B). The semiautomatically determined clip locations show a larger median error and variability.

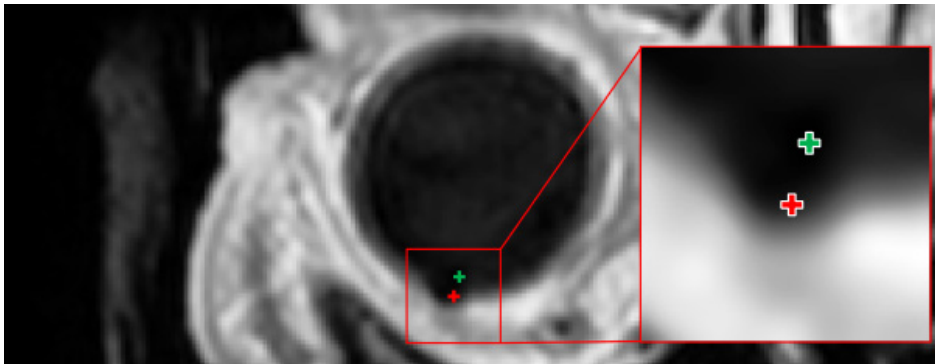
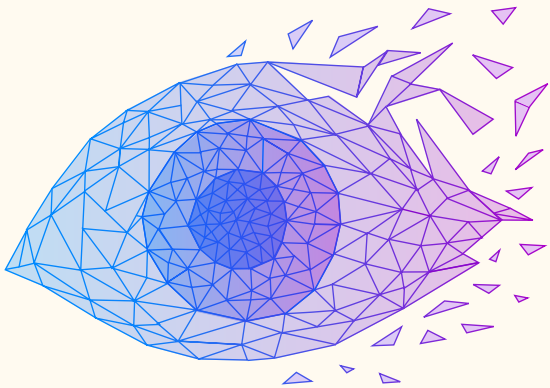


Figure 4: Due to the absence of a clear boundary between the signal void and the vitreous body, the clip detection pipeline locates the clip centre in the vitreous. The inset image shows the upsampled region of interest used to determine the clip location (Figure B). Red: initial annotation. Green: semiautomatic location.



Chapter 4

Automatic three-dimensional magnetic resonance-based measurements of tumour prominence and basal diameter for treatment planning of uveal melanoma

PhD project chapter

L. Klaassen, M.G. Jaarsma-Coes, B.M. Verbist, T.H.K. Vu, M. Marinkovic
C.R.N. Rasch, G.P.M. Luyten, J.W.M. Beenakker

Physics & Imaging in Radiation Oncology (2022). doi: 10.1016/j.phro.2022.11.001

ABSTRACT

Background and Purpose

Three-dimensional (3D) Magnetic Resonance Imaging (MRI) is increasingly used to complement conventional two-dimensional ultrasound in the assessment of tumour dimension measurement of uveal melanoma. However, the lack of definitions of the 3D measurements of these tumour dimensions hinders further adaptation of MRI in ocular radiotherapy planning. In this study, we composed 3D MR-based definitions of tumour prominence and basal diameter and compared them to conventional ultrasound.

Materials and methods

Tumours were delineated on 3DT2 and contrast-enhanced 3DT1 (T1gd) MRI for 25 patients. 3D definitions of tumour prominence and diameter were composed and evaluated automatically on the T1gd and T2 contours. Automatic T1gd measurements were compared to manual MRI measurements, to automatic T2 measurements and to manual ultrasound measurements.

Results

Prominence measurements were similar for all modalities (median absolute difference 0.3 mm). Automatic T1gd diameter measurements were generally larger than manual MRI, automatic T2 and manual ultrasound measurements (median absolute differences of 0.5, 1.6 and 1.1 mm respectively), mainly due to difficulty defining the axis of the largest diameter. Largest differences between ultrasound and MRI for both prominence and diameter were found in anteriorly located tumours (up to 1.6 and 4.5 mm respectively), for which the tumour extent could not entirely be visualized with ultrasound.

Conclusions

The proposed 3D definitions for tumour prominence and diameter agreed well with ultrasound measurements for tumours for which the extent was visible on ultrasound. 3D MRI measurements generally provided larger diameter measurements than ultrasound. In anteriorly located tumours, the MRI measurements were considered more accurate than conventional ultrasound.

INTRODUCTION

Uveal melanoma (UM) is the most frequently occurring primary intraocular malignancy [1]. For UM, tumour location and dimensions are major factors in treatment decision making, as only tumours up to a certain size can be treated with brachytherapy [1], [2], [3], whereas larger and juxtapapillary UM are preferably treated with external beam radiotherapy, such as proton beam therapy (PBT) or Cyber Knife [4], [5], [6]. Furthermore, tumour prominence and diameter measurements are of importance for radiotherapy planning: in brachytherapy, prominence and largest basal diameter (LBD) determine the application time and applicator size, while for PBT, these two-dimensional (2D) tumour measurements, together with the second basal diameter (SBD) are important factors in the definition of three-dimensional (3D) clinical target volume [2], [7]. Additionally, prominence, LBD and SBD are used in tumour staging, prognosis and follow-up [8], [9], [10], [11], [12].

Conventionally, tumour prominence and diameters are determined using 2D B-scan ultrasound [1]. For a correct prominence measurement, the transducer has to be positioned perpendicular to the tumour base, as oblique cuts through the tumour can result in overestimation of the true tumour prominence [13]. For anterior tumours, correct transducer placement might be hindered due to anatomical structures around the eye [14]. Additionally, to correctly determine the LBD, the longest tumour axis has to be identified, which can be difficult as no 3D visualization is available.

Magnetic resonance imaging (MRI) is increasingly used for the diagnosis, therapy planning and follow-up of UM [7], [15], [16], [17], [18], [19], [20]. Various studies suggest that MRI's 3D tumour visualisation and better tissue contrast might be beneficial in determining UM tumour dimensions compared to conventional 2D ultrasound, corresponding to findings in other malignancies [16], [17], [18], [19], [20], [21], [22], [23], [24]. Nevertheless, several uncertainties in MR-based dimensions measurements for ocular tumours remain that hinder broader application of MRI in ocular radiotherapy planning, for example regarding the optimal method to measure in 3D and the differences related to the various MRI contrasts.

Although the 3D visualisation of the tumour of MRI allows for a more comprehensive assessment of tumour geometry [18], tumour dimension measurements can be performed in different planes, resulting in different possible prominence and diameter measurements, especially for complexly shaped tumours (Fig. 1) [19], [25]. Additionally, manual measurement of prominence and LBD on MRI is reported to be difficult and time-consuming [26]. Therefore, the current clinical practice might

benefit from automated tumour prominence and diameter measurements, using an unambiguous geometrical definition. Furthermore, studies showed an 11–44 % larger tumour volume on contrast-enhanced T1-weighted images (T1gd) compared to T2-weighted images [21], [27]. Although such a difference between MRI sequences is not uncommon [28], [29], these differences should be kept in mind when defining optimal measurements.

In this study, we aimed to compose and evaluate a geometrical 3D definition of prominence and diameters.

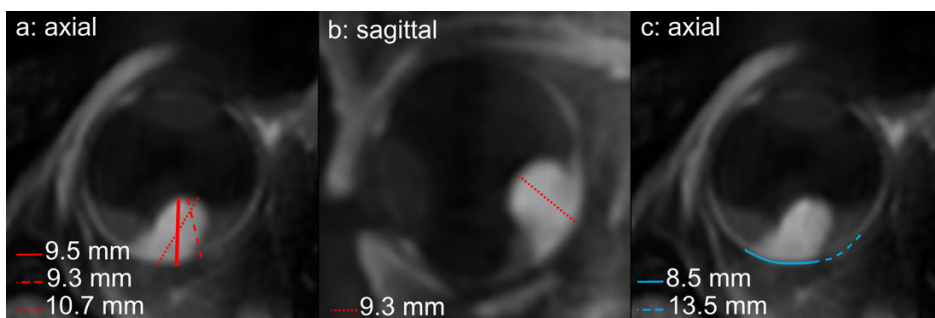


Figure 1. Several measuring planes on T1gd-weighted MRI for a mushroom shaped UM. (a) Three possible prominence measurements in the axial plane for a complexly shaped tumour: starting with the point closest to the centre of the eye (solid, the definition used in this study), parallel with the main tumour axis (dotted) and including the overhanging part of the tumour (dashed). (b) An evaluation of the same tumour in the sagittal plane resulted in a different measurement. (c) For obliquely oriented tumours, several base definitions are possible depending on whether the overhanging part is included as tumour base.

MATERIALS AND METHODS

Data of 25 patients, who received an MRI as part of clinical care ($n = 17$) or in the context of a scientific study ($n = 8$), were analysed retrospectively after approval of the local ethics committee, in accordance with the Declaration of Helsinki. Patients were diagnosed by an ocular oncologist based on fundus photography, ocular ultrasound and fluorescein angiography. The patients were selected to provide a clinically representative range in tumour size, shape and location. Patients were 62 ± 10 years old and 57 % were male. A wide range of tumour sizes was present, ranging from The American Joint Committee on Cancer (AJCC, 8th edition) stage T1 up to T4, with most patients in stages T2 (40 %) and T3 (40 %) [30]. 28 % of patients had an anteriorly

located tumour and most tumours were dome-shaped (68 %), followed by mushroom-shaped (16 %) and flat (16 %). Patients were treated with either 106-Ruthenium brachytherapy (32 %) or PBT (68 %). The average time between ultrasound and MRI was 14 ± 11 days.

Image acquisition

3DT1gd and 3DT2-weighted images, both with acquisition voxel size of $0.8 \times 0.8 \times 0.8$ mm³, were acquired to an earlier described protocol [15], [16]. Ultrasound images were obtained by an ocular oncologist [25]. Details on image acquisition are further described in the Supplementary Materials.

Tumour delineation

Delineations were performed semi-automatically on the 3D T1gd and T2-weighted images using an in-house developed analysis pipeline in MeVisLab (MeVis Medical Solutions, Bremen, Germany) using a subdivision surface fit [26], [31] (Fig. 1a-b). Areas which were hypointense compared to the vitreous on T2 and enhancing on T1gd compared to the native T1 were considered tumour.

The globe, defined as a combination of the vitreous, lens and tumour, was delineated in a similar fashion (Fig. 2a-b, yellow contour). Since clinical ultrasound measurements include the sclera, the outer sclera boundary at the tumour base was delineated as well (Fig. 2c). Based on the clinical evaluation of the MR-images by a neuro-radiologist with 20 years of experience (BV), an ophthalmic MRI expert with 9 years of experience (JWB) verified, and if necessary corrected, all contours.

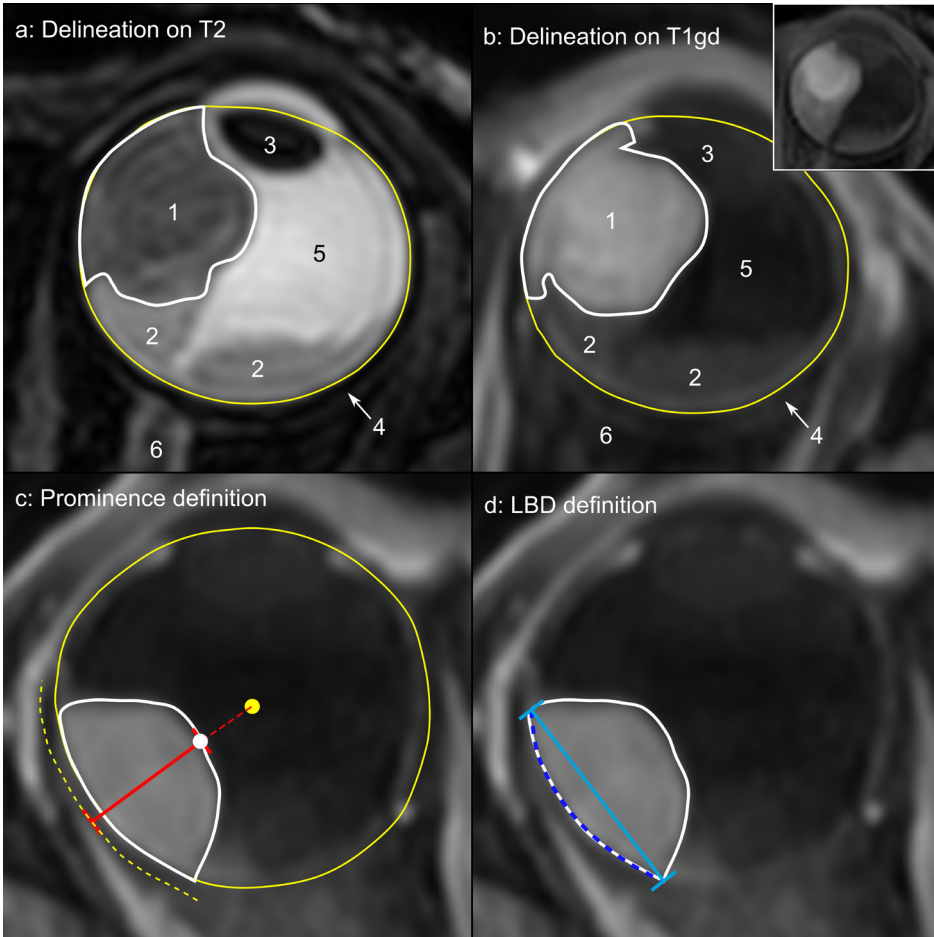


Figure 2. Tumour (white contour) and globe (defined as combination of vitreous, lens and tumour, yellow contour) were delineated on T2-weighted (a) and contrast-enhanced T1-weighted (T1gd) (b) images, with the native T1-weighted image used as a reference (inset). Anatomical structures are marked as follows: (1) tumour, (2) retinal detachment, (3) lens, (4) sclera (hypointense layer), (5) vitreous, (6) optic nerve. Tumour prominence (c, red line) and largest basal diameter (d, blue line) were automatically determined. (c) Tumour prominence was measured from the tumour apex (white dot) to the sclera (dashed yellow line) (centre-based definition, Appendix A). (d) LBD was the largest Euclidean distance between two points in the tumour base (base: dashed line, measurement: solid line). In this image, the axial plane was shown as an example, whereas the tumour delineation was evaluated in the axial, sagittal and coronal plane.

Automatic 3D MRI measurements

In a pilot study, further described in the Supplementary Materials, we developed 3D definitions of tumour prominence and base. In short, three different 3D definitions of the tumour prominence and three different LBD definitions were evaluated in a multidisciplinary tumour board, consisting of ocular oncologists, radiation oncologists, clinical physicists and radiologists (BV, TV, MM, GL, CR, JWB). As these definitions were based on the 3D tumour contours, the resulting dimensions were not restricted to an individual slice of the MR-images. These definitions provided different approaches on how to define the tumour base and apex, e.g. point closest to the eye centre or point most distant from the sclera. The evaluation of these definitions in 25 patients showed comparable measurements for patients with rotational-symmetric tumours. However, in the asymmetric tumours, some of the definitions resulted in measurement which did not conform the current clinical consensus. For example, defining the apex as the point most distant from the sclera resulted in an oblique prominence measurement which could not be used for radiotherapy planning purposes (Supplementary Fig. 1). The multidisciplinary evaluation of the definitions resulted in one prominence and one tumour base definition which provided visually acceptable measurements in all patients.

Based on the results of this pilot study, the tumour apex was defined as the point of the tumour contour closest to the centre of the globe (Fig. 2c). The prominence was measured along the line between the centre of the globe and the tumour apex (Fig. 1a, solid red line) and included the sclera to match the clinical convention at our centre.

LBD was defined as the largest Euclidean distance between two points in the tumour base (Fig. 2d, base: dashed line, LBD: solid line), which was defined as all points of the tumour contour less than 2 mm distant from the inner sclera contour, in order to create a robust tumour base. SBD was the largest distance between two points in the tumour base, perpendicular to the LBD.

For all patients the prominence, LBD and SBD were automatically determined using the T1gd- and T2-based 3D contours in Python (version 3.7.6). This code is available on GitHub via https://github.com/MREYE-LUMC/OPT_tumourmodels.

Manual MRI measurements

In order to assess how these automatic 3D measurements relate to the currently used manual assessments, the prominence and LBD were measured manually on the T1gd-weighted images. For the prominence, the clinical measurement was used, measured

perpendicular to the sclera [25]. For the LBD, the measurements were repeated on the delineated tumour contour, to avoid the confounding effect of a different tumour boundary interpretation [27]. For each patient, the angle between the lines of manual and the automatic measurement was determined.

Statistical analysis

Automatic T1gd prominence and LBD measurements were compared to manual MRI measurements. Additionally, automatic prominence and LBD were compared between T1gd and T2. Furthermore, the automatic T1gd and clinical ultrasound measurements were compared for prominence, LBD and SBD. For the prominence, differences > 0.5 mm and for the diameters, differences > 1.0 mm were considered clinically significant [25]. Medians and 25th–75th percentiles of the automatic-manual, T1gd-T2 and T1gd-ultrasound differences were assessed, as non-normality was demonstrated with a Shapiro-Wilk test (e.g. $p = 0.0003$ for the ultrasound-T1gd prominence comparison). Results for anterior tumours, defined as having a centre of mass in the anterior 50 % of the globe, were assessed separately. Additionally, tumours where the full extent could not be accurately determined on MRI or ultrasound, e.g. due to a flat tumour or a limited penetration depth or limited field of view (FOV) of the ultrasound transducer, were marked (Supplementary Fig. 2) [25].

RESULTS

Representative examples of automatic prominence and LBD measurements on T2 and T1gd, and the corresponding ultrasound measurements, are shown in Fig. 3, with an overview of the primary outcomes. All comparisons and individual measurements for all patients can be found in the Supplementary Materials.

On T1gd, manual and automatic prominence measurements were comparable (median absolute difference 0.3 mm, Fig. 4a), with differences > 0.5 mm for 8/25 patients. The median absolute difference between automatic and manual LBD measurements was 0.5 mm, with differences > 1.0 mm for 14/25 patients (Fig. 4b). Larger differences were found in patients where the manual measurement was performed in a different plane than the automatic measurement (Fig. 4c). The mean angle between the manual and automatic measurement was 26 degrees (Fig. 4c, Supplementary Fig. 3).

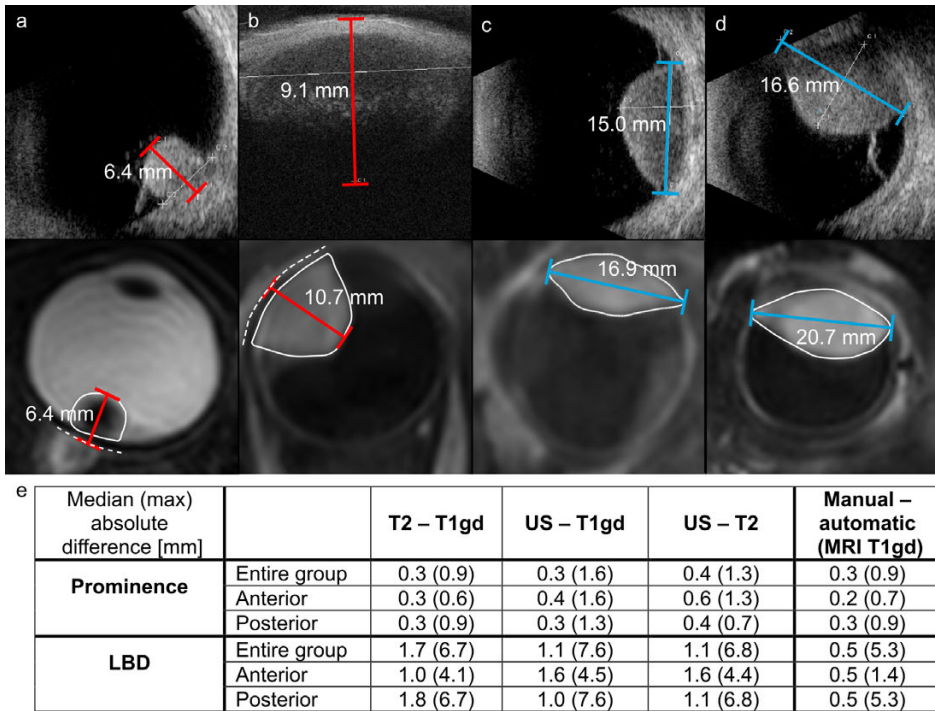


Figure 3. Four typical examples of ultrasound (upper images) and MRI measurements (lower images) from four different patients and an overview of the main comparisons. (a) T2 and ultrasound measurements were similar. (b) T1gd prominence was larger for an anteriorly located tumour for which the extent was not entirely visible on UBM. (c) T1gd LBD was larger than on ultrasound for a tumour whose extent was visible on both modalities. (d) T1gd LBD was larger than on ultrasound and extent was not entirely visible on ultrasound. (e) Overview of the main comparisons performed in this study: automatic T2 - automatic T1gd, ultrasound (US) - automatic T1gd, ultrasound - automatic T2, manual T1gd - automatic T1gd.

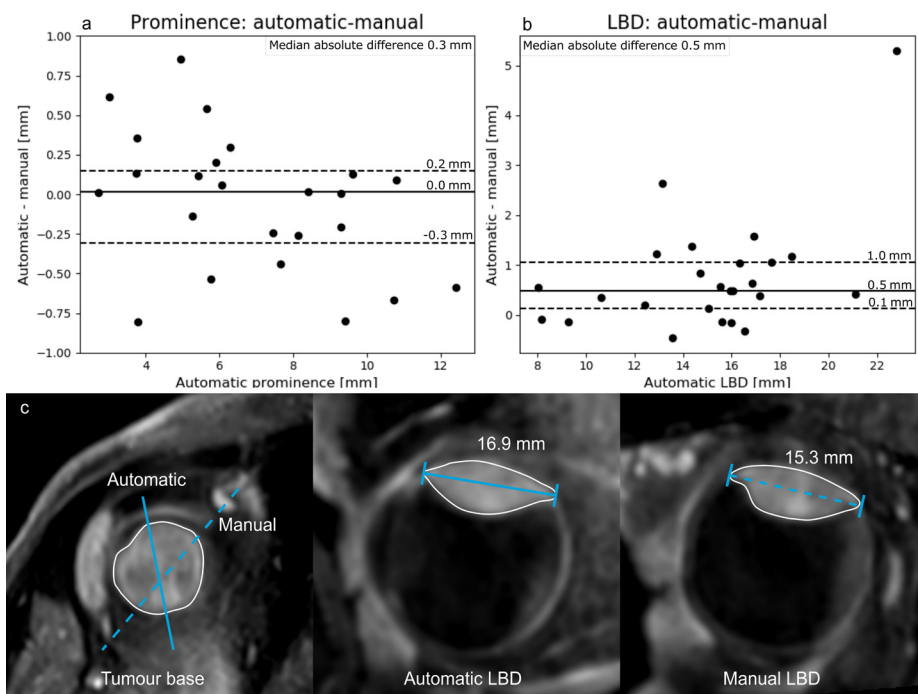


Figure 4. (a) Differences between automatic and manual prominence measurements. (b) Differences between automatic and manual LBD measurements. (c) Manually determining the plane of the largest basal diameter proved to be difficult due to the curved tumour base. As a result, manual measurements generally underestimated the LBD.

Due to a limited penetration depth of the UBM transducer, the tumour apex was not visible in 2/25 patients, both of which had an anteriorly located tumour (Supplementary Fig. 2a). The full extent of the tumour base did not fit within the ultrasound's field of view for 9/25 patients, of which 7 had an anteriorly located tumour (Supplementary Fig. 2b). In 3/4 patients with an ultrasound prominence < 4 mm, the extent of the tumour base was difficult to assess on MRI.

The difference between ultrasound- and automatic T1gd-based prominence was > 0.5 mm in 6/25 patients, with a median absolute difference of 0.4 and 0.3 mm for anterior and posterior tumours, respectively (Fig. 5a). A retrospective re-evaluation of the ultrasound and fundus images of the patient with the largest difference (1.3 mm), showed that a haemorrhage at the tumour apex was erroneously included as tumour on ultrasound (Supplementary Fig. 4). For the remaining patients the largest absolute difference of 0.9 mm was found in a patient with an anteriorly located tumour, for which the apex was visible on ultrasound, with a prominence of 13.3

mm on ultrasound and 12.4 mm on MRI. Differences between T1gd- and T2-based prominence were small: for 6/25 patients, the difference was > 0.5 mm, with a median absolute difference of 0.3 mm and a maximum of 0.9 mm (Fig. 5b).

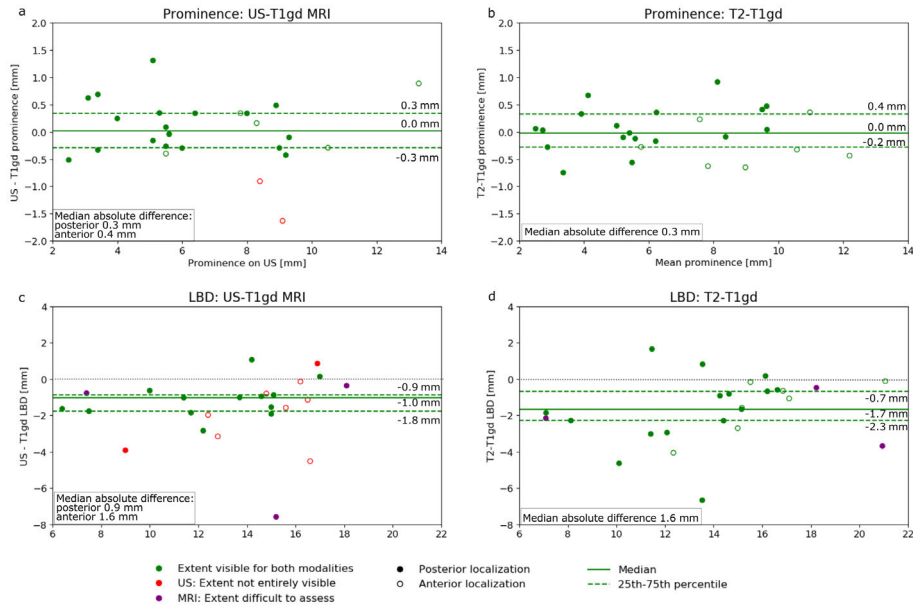


Figure 5. Comparison of prominence and LBD between ultrasound and MRI. (a) For the prominence, ultrasound-T1gd differences were largest in anteriorly located tumours that were not fully visible on ultrasound. The largest prominence difference of 1.3 mm was caused by the erroneous inclusion of haemorrhage in the tumour prominence on ultrasound (Supplementary Figure 3). (b) Absolute differences between T1gd and T2 prominence measurements were < 0.5 mm in 19/25 patients. (c) Comparing ultrasound and T1gd MRI, LBD was larger on T1gd MRI in 22/25 patients. (d) Comparing LBD between T2 and T1gd, LBD was larger on T1gd in 22/25 patients.

Compared to ultrasound, 16/25 of LBD measurements were > 1.0 mm larger on the automatic T1gd measurement (Fig. 3c). Median absolute differences between ultrasound and T1gd (Fig. 5c) were 0.9 mm for posteriorly located tumours and 1.6 mm for anteriorly located tumours. Slightly larger differences were found for the SBD, which resulted in a median absolute difference of 1.3 mm (maximum 4.6 mm, Supplementary Fig. 5).

Differences between automatic T2 and automatic T1gd LBD were > 1.0 mm in 15/25 patients, with 13/15 being larger on T1gd. A median absolute difference of 1.6

mm was found between the two sequences (Fig. 5d). Often, peritumoral choroidal enhancement was visible on T1gd, which consequently was included as tumour, while this was not considered tumour on T2 and ultrasound (Fig. 6b-c). T2-based LBD measurements were more in agreement with ultrasound (median absolute difference 0.4 mm), compared to T1gd-based measurements (Supplementary Fig. 6). These smaller diameters on T2 were also reflected in the tumour volumes: tumour volume was larger on T1gd for 20/25 patients (average volume difference 18 %).

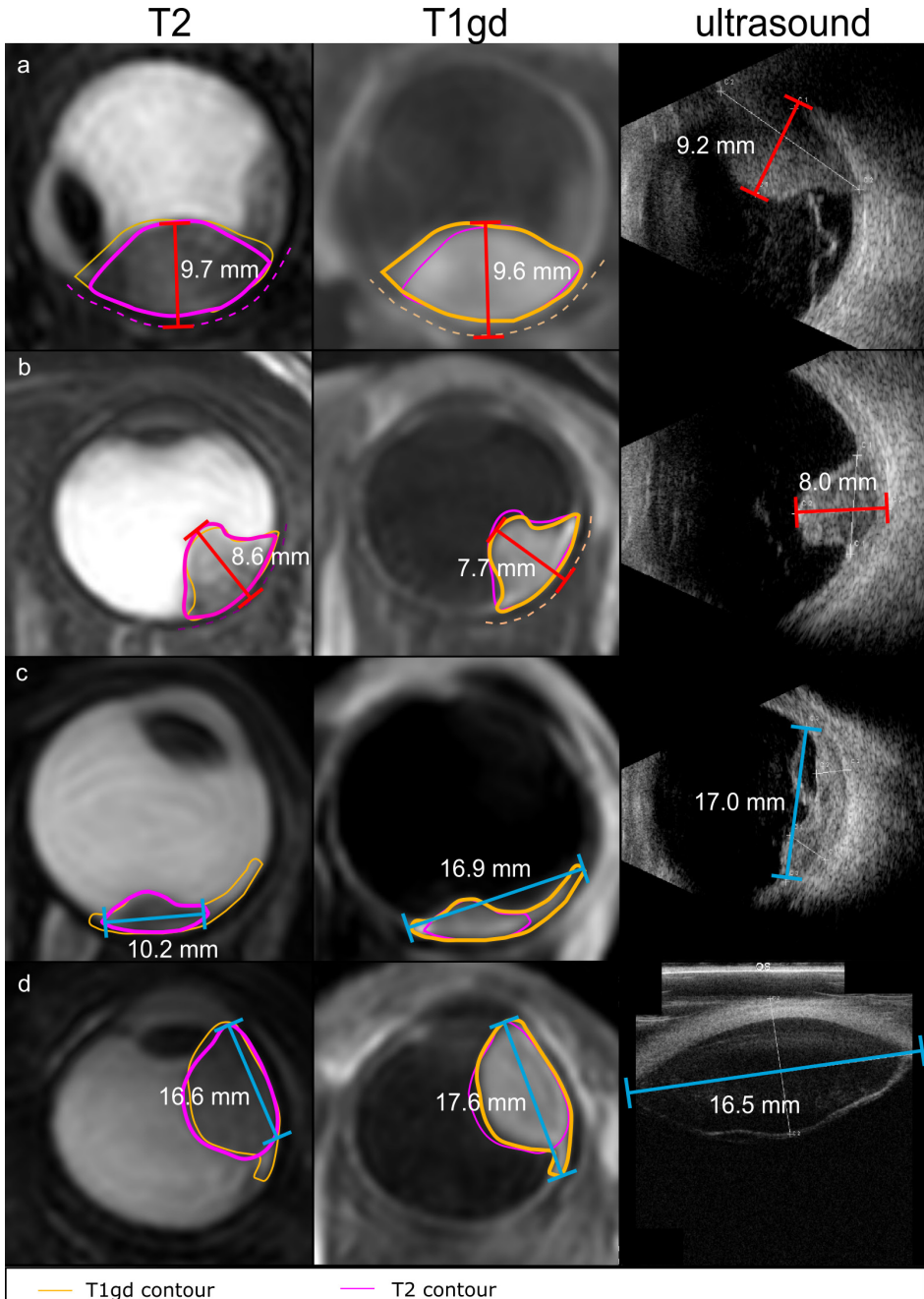


Figure 6. Prominence and LBD measurement on T2-weighted MRI (left column), T1gd-weighted MRI (middle column) and US (right column). (a) Prominence was generally similar on T1gd and T2. (b) The largest difference between T2 and T1gd prominence was 0.9 mm. (c,d) LBD was generally larger on T1gd.

DISCUSSION

With this study, we proposed an unambiguous 3D-imaging based prominence and base definition for treatment planning of uveal melanoma, which takes the requirements for brachytherapy and PBT planning into account [25], [32], [33], and which poses an extension of an earlier study [34], which assumed a dome shaped tumour with a circular base.

The proposed prominence and base definitions were considered appropriate by the multidisciplinary tumour board in our cohort of 25 patients. Although the cohort contained a variety of tumour sizes and shapes, we noted that in none of the obliquely oriented tumours, the LBD contained the overhanging part. As a result, the effects from overhanging parts were not reflected in the LBD assessments. Accurately incorporating overhanging parts in directions other than the LBD measurement axis, will however be beneficial for PBT, where similar discrepancies have been reported describing the tumour-marker relation [25]. We anticipate that the proposed definition may result in erroneous measurements for very prominent UM, with the centre of the eye within the mass. Nonetheless, the proposed prominence definition proved to be robust for variations in the location of the centre of the eye (Supplementary Fig. 7).

As the proposed automatic measurement methods are independent of field strength they are also applicable for patients scanned at lower field strengths than 3 T. In this study, subjects were scanned with closed eyes, as a previous comparison between different protocols showed that, while the use of a cued blinking protocol [35] results in less motion artefacts in some patients, not all patients are able to adhere to such a protocol, resulting in overall degraded image quality [36].

As part of the data was acquired as part of regular clinical care, the MRI and ultrasound were not acquired on the same day for most patients. However, we expect the impact of this delay to be limited, as UM are known to be slow growing tumours [37], [38], which is confirmed by the accordance in prominence measurements between both modalities.

In general, tumour prominence measurements agreed well across modalities if tumour extent was entirely visible, with all interquartile ranges within half the MRI acquisition voxel size. This corresponds to the recently reported interobserver delineation variation of 0.4 mm of ocular MRI [27] and is smaller than the reproducibility of B-mode ultrasound of 0.6 mm [13], [14]. In our study, the largest prominence

differences were found in patients for whom the tumour apex was not visible on ultrasound. This particularly occurred in patients with anteriorly located tumours imaged with a UBM probe, which has a limited penetration depth due to its higher frequency (50 MHz). For these patients, MRI was considered to be more accurate. Previous studies by Ferreira and Schueller [16], [39] reported similar prominence measurements, although measurement methods differed.

Automatic LBD measurements were generally larger than manual MRI measurements, which were often performed in a plane not containing the largest diameter. Since the LBD can, by definition, not be overestimated, the automatic measurement was considered more accurate. However, since 68 % of the differences were < 1 mm, manual measurements are generally sufficient, especially given the known interobserver variability of the tumour-choroid interface on MRI of 0.6 mm [27]. On T1gd, peritumoral enhancement was included, which was invisible on T2, resulting in larger measurements on T1gd (median absolute difference 1.7 mm). Although the enhancement could be inflammatory of origin, it could also correspond to a small flat tumour extension. We therefore recommend to include these areas as tumour, until histopathology proves otherwise.

Generally, we found larger LBDs on T1gd than on ultrasound, with differences largest in anteriorly located tumours, especially when the full tumour extent was not visible on ultrasound. These differences can partly be explained by manual definition of the plane of the LBD of the ultrasound exam, which similar to the manual MRI measurements, might miss the actual largest diameter, with the added difficulty that no 3D visualisation can be made with ultrasound. In some patients the peritumoral choroidal enhancement observed on T1gd was included on ultrasound (Fig. 6c), while in other patients it was not (Fig. 6d). This inconsistency leads to uncertainties in the LBD measurement of flat UM as well, with differences between T1gd and ultrasound up to 7.6 mm. In 3/4 patients with flat UM, the MRI-report explicitly mentioned that the tumour extent was difficult to assess, confirming previous findings that MRI of flat melanoma can be difficult [16], [25], [34], [40], [41]. However, on ultrasound, the extent of these flat tumours is also not clearly visible. Therefore, optical validation of the flat tumour extent, which can be measured on some fundus and OCT imaging modalities [10], or increased margins, is necessary. For the SBD larger discrepancies with ultrasound were observed than for the LBD, however, the resulting ellipsoid model is more accurate than a circular model based on the LBD alone [8], [9], [42], [43], [44], [45].

The clinical impact of the observed differences between ultrasound and MRI will depend on the application, and therefore an MRI-scan will not be needed for all patients. In general, we recommend to perform an MRI when the tumour extent is not fully visible on ultrasound, which was most often seen in anteriorly located tumours. For treatment selection, the effect of incorporating the MRI-based measurements proposed in this study will depend on the type of treatments that are available. When a 0.5 mm change in prominence or 1 mm change in LBD can result in a shift of optimal treatment modality [19], [46], we advise to perform an MRI with automatic T1gd measurements to confirm the ultrasound measurements. Although the benefit of including MRI in radiotherapy planning requires further study, we expect less benefit for patients treated with brachytherapy, due to the limited degrees of freedom with the currently available applicators. For PBT, however, the currently relatively large margins of up to 3 mm are in part needed for the uncertainties introduced by the ultrasound measurements [47], [48], [49]. Given the earlier reported benefits of including MRI for ocular PBT planning, we would recommend to perform an MRI for these patients and use the proposed 3D prominence and basal diameter definitions to resolve the discrepancies observed for complexly shaped tumours between MRI and ultrasound [25], especially until fully image-based 3D treatment planning systems for UM are clinically available [21], [50], [51], [52].

In conclusion, 3D MRI-based tumour measurements were comparable to 2D ultrasound-based measurements. For anteriorly located tumours, MRI was more accurate. Furthermore, the methods proposed in this paper can contribute to a more personalized, image-based, radiotherapy planning for ocular oncology patients.

REFERENCES

1. Jager M.J., Shields C.L., Cebulla C.M., Abdel-Rahman M.H., Grossniklaus H.E., Stern M.H., et al. Uveal melanoma. *Nat Rev Dis Primers*. 2020;6:24. doi: 10.1038/s41572-020-0158-0.
2. Yang J., Manson D.K., Marr B.P., Carvajal R.D. Treatment of uveal melanoma: where are we now? *Ther Adv Med Oncol*. 2018 doi: 10.1177/1758834018757175.
3. Kaliki S., Shields C.L. Uveal melanoma: relatively rare but deadly cancer. *Eye*. 2017;31:241–257. doi: 10.1038/eye.2016.275.
4. Mishra K.K., Daftari I.K. Proton therapy for the management of uveal melanoma and other ocular tumors. *Chin Clin Oncol*. 2016;5:50. doi: 10.21037/cco.2016.07.06
5. Mor J.M., Semrau R., Baus W., Koch K.R., Schaub F., Cursiefen C., et al. CyberKnife(R): new treatment option for uveal melanoma. *Ophthalmologe*. 2018;115:302–308. doi: 10.1007/s00347-017-0560-5.
6. Parker T., Rigney G., Kallos J., Stefko S.T., Kano H., Niranjana A., et al. Gamma knife radiosurgery for uveal melanomas and metastases: a systematic review and meta-analysis. *Lancet Oncol*. 2020;21:1526–1536. doi: 10.1016/S1470-2045(20)30459-9.
7. Hrbacek J., Mishra K.K., Kacperek A., Dendale R., Nauraye C., Auger M., et al. Practice patterns analysis of ocular proton therapy centers: The International OPTIC Survey. *Int J Radiat Oncol Biol Phys*. 2016;95:336–343. doi: 10.1016/j.ijrobp.2016.01.040.
8. Furdova A., Babal P., Kobzova D., Zahorjanova P., Kapitanova K., Sramka M., et al. Uveal melanoma survival rates after single dose stereotactic radiosurgery. *Neoplasma*. 2018;65:965–971. doi: 10.4149/neo_2018_171209N808.
9. Gass J.D. Comparison of uveal melanoma growth rates with mitotic index and mortality. *Arch Ophthalmol*. 1985;103:924–931. doi: 10.1001/archophth.1985.01050070050028.
10. Solnik M., Padaszyska N., Czarnecka A.M., Synoradzki K.J., Yousef Y.A., Choragiewicz T., et al. Imaging of uveal melanoma-current standard and methods in development. *Cancers*. 2022;14 doi: 10.3390/cancers14133147.
11. Amin F.E.S., Greene F. Eighth edition. Springer; New York: 2017. *AJCC Cancer Staging Manual*.
12. Kaliki S., Shields C.L., Shields J.A. Uveal melanoma: estimating prognosis. *Indian J Ophthalmol*. 2015;63:93–102. doi: 10.4103/0301-4738.154367.
13. Char D.H., Kroll S., Stone R.D., Harrie R., Kerman B. Ultrasonographic measurement of uveal melanoma thickness: interobserver variability. *Br J Ophthalmol*. 1990;74:183–185. doi: 10.1136/bjo.74.3.183.
14. Haritoglou C., Neubauer A.S., Herzum H., Freeman W.R., Mueller A.J. Interobserver and intraobserver variability of measurements of uveal melanomas using standardised echography. *Br J Ophthalmol*. 2002;86:1390–1394. doi: 10.1136/bjo.86.12.1390.
15. Kamrava M., Sepahdari A.R., Leu K., Wang P.C., Roberts K., Demanes D.J., et al. Quantitative multiparametric MRI in uveal melanoma: increased tumor permeability may predict monosomy 3. *Neuroradiology*. 2015;57:833–840. doi: 10.1007/s00234-015-1546-0.
16. Ferreira T.A., Jaarsma-Coes M.G., Marinkovic M., Verbist B., Verdijk R.M., Jager M.J., et al. MR imaging characteristics of uveal melanoma with histopathological validation. *Neuroradiology*. 2022;64:171–184. doi: 10.1007/s00234-021-02825-5.
17. Foti P.V., Travali M., Farina R., Palmucci S., Spatola C., Raffaele L., et al. Diagnostic methods and therapeutic options of uveal melanoma with emphasis on MR imaging-Part I: MR imaging with pathologic correlation and technical considerations. *Insights Imaging*. 2021;12:66. doi: 10.1186/s13244-021-01000-x.

18. Niendorf T., Beenakker J.M., Langner S., Erb-Eigner K., Bach Cuadra M., Beller E., et al. Ophthalmic magnetic resonance imaging: where are we (heading to)? *Curr Eye Res.* 2021;46:1251–1270. doi: 10.1080/02713683.2021.1874021.
19. Beenakker J.W., Ferreira T.A., Soemarwoto K.P., Genders S.W., Teeuwisse W.M., Webb A.G., et al. Clinical evaluation of ultra-high-field MRI for three-dimensional visualisation of tumour size in uveal melanoma patients, with direct relevance to treatment planning. *MAGMA.* 2016;29:571–577. doi: 10.1007/s10334-016-0529-4.
20. Ferreira T.A., Grech Fonk L., Jaarsma-Coes M.G., van Haren G.G.R., Marinkovic M., Beenakker J.M. MRI of uveal melanoma. *Cancers.* 2019;11 doi: 10.3390/cancers11030377.
21. Marnitz S., Cordini D., Bendl R., Lemke A.J., Heufelder J., Simiantonakis I., et al. Proton therapy of uveal melanomas: intercomparison of MRI-based and conventional treatment planning. *Strahlenther Onkol.* 2006;182:395–399. doi: 10.1007/s00066-006-1512-1.
22. Cuesta Cuesta A.B., Martin Rios M.D., Noguero Meseguer M.R., Garcia Velasco J.A., de Matias M.M., Bartolome Sotillos S., et al. Accuracy of tumor size measurements performed by magnetic resonance, ultrasound and mammography, and their correlation with pathological size in primary breast cancer. *Cir Esp (Engl Ed)* 2019;97:391–396. doi: 10.1016/j.ciresp.2019.04.017.
23. Taydas O., Durhan G., Akpınar M.G., Demirkazık F.B. Comparison of MRI and US in tumor size evaluation of breast cancer patients receiving neoadjuvant chemotherapy. *Eur J Breast Health.* 2019;15:119–124. doi: 10.5152/ejbh.2019.4547.
24. Cha M.J., Lee M.W., Cha D.I., Kim J.H., Rhim H., Cho Y.K., et al. Size discrepancy between sonographic and computed tomographic/magnetic resonance imaging measurement of hepatocellular carcinoma: the necessity of tumor size measurement standardization. *J Ultrasound Med.* 2013;32:1703–1709. doi: 10.7863/ultra.32.10.1703.
25. Jaarsma-Coes M.G., Ferreira T.A., Marinkovic M., Vu T.H.K., van Vught L., van Haren G.R., et al. Comparison of MRI-based and conventional measurements for proton beam therapy of uveal melanoma. *Ophthalmol Retina.* 2022 doi: 10.1016/j.oret.2022.06.019.
26. Hassan M.K., Fleury E., Shamonin D., Fonk L.G., Marinkovic M., Jaarsma-Coes M.G., et al. An automatic framework to create patient-specific eye models from 3D magnetic resonance images for treatment selection in patients with uveal melanoma. *Adv Radiat Oncol.* 2021;6:100697. doi: 10.1016/j.adro.2021.100697.
27. Jaarsma-Coes M, Klaassen L, Verbist BM, Vu THK, Klaver YLB, et al. Inter-Observer variability in MR-based target volume delineation of uveal melanoma. submitted. 2022.
28. Kumar S., Holloway L., Boxer M., Yap M.L., Chlap P., Moses D., et al. Variability of gross tumour volume delineation: MRI and CT based tumour and lymph node delineation for lung radiotherapy. *Radiother Oncol.* 2021;167:292–299. doi: 10.1016/j.radonc.2021.11.036.
29. Song Y., Erickson B., Chen X., Li G., Wu G., Paulson E., et al. Appropriate magnetic resonance imaging techniques for gross tumor volume delineation in external beam radiation therapy of locally advanced cervical cancer. *Oncotarget.* 2018;9:10100–10109. doi: 10.18632/oncotarget.24071.
30. Kivelä T.S., Grossniklaus H.E., et al. *AJCC cancer staging manual.* 8th edition. Springer; New York (NY): 2016. Uveal melanoma; p. p. 805:17.
31. Kitslaar Pieter H, Staring M, Lelieveldt BPF, van der Geest RJ. Segmentation of branching vascular structures using adaptive subdivision surface fitting. *Proceedings Volume 9413, Medical Imaging 2015: Image Processing; 94133Z* 2015. <https://doi.org/10.1117/12.2082222>.

32. Collaborative Ocular Melanoma Study G. Comparison of clinical, echographic, and histopathological measurements from eyes with medium-sized choroidal melanoma in the collaborative ocular melanoma study: COMS report no. 21. *Arch Ophthalmol* 2003;121:1163-71. <https://doi.org/10.1001/archopht.121.8.1163>.
33. Varian Medical Systems. Planning Reference Guide for Eclipse Ocular Proton Planning. 2007; 1-286.
34. Via R., Hennings F., Pica A., Fattori G., Beer J., Peroni M., et al. Potential and pitfalls of 1.5T MRI imaging for target volume definition in ocular proton therapy. *Radiother Oncol*. 2021;154:53-59. doi: 10.1016/j.radonc.2020.08.023.
35. Beenakker J.W.M., van Rijn G.A., Luyten G.P.M., Webb A.G. High-resolution MRI of uveal melanoma using a microcoil phased array at 7 T. *NMR Biomed*. 2013;26:1864-1869. doi: 10.1002/nbm.3041.
36. Tang M.C.Y., Jaarsma-Coes M.G., Ferreira T.A., Zwirs-Grech Fonk L., Marinkovic M., Luyten G.P.M., et al. A comparison of 3 T and 7 T MRI for the clinical evaluation of uveal melanoma. *J Magn Reson Imaging*. 2022;55:1504-1515. doi: 10.1002/jmri.27939.
37. Augsburger J.J., Gonder J.R., Amsel J., Shields J.A., Donoso L.A. Growth rates and doubling times of posterior uveal melanomas. *Ophthalmology*. 1984;91:1709-1715. doi: 10.1016/s0161-6420(84)34088-x.
38. Char D.H., Kroll S., Phillips T.L. Uveal melanoma. Growth rate and prognosis. *Arch Ophthalmol*. 1997;115:1014-1018. doi: 10.1001/archopht.1997.01100160184007.
39. Schueller P., Dogan A., Panke J.E., Micke O., Willich N. Does the imaging method have an influence on the measured tumor height in ruthenium plaque therapy of uveal melanoma? *Strahlenther Onkol*. 2005;181:320-325. doi: 10.1007/s00066-005-1342-6.
40. Beenakker JM, Rasch CRN. Letter to the Editor of Radiotherapy and Oncology regarding the paper titled "MRI and FUNDUS image fusion for improved ocular biometry in Ocular Proton Therapy" by Via et al. *Radiother Oncol* 2022. <https://doi.org/10.1016/j.radonc.2022.08.018>.
41. Via R., Pica A., Antonioli L., Paganelli C., Fattori G., Spaccapaniccia C., et al. MRI and FUNDUS image fusion for improved ocular biometry in Ocular Proton Therapy. *Radiother Oncol*. 2022;174:16-22. doi: 10.1016/j.radonc.2022.06.021.
42. Heilemann G., Fetty L., Dulovits M., Blaickner M., Nesvacil N., Georg D., et al. Treatment plan optimization and robustness of (106)Ru eye plaque brachytherapy using a novel software tool. *Radiother Oncol*. 2017;123:119-124. doi: 10.1016/j.radonc.2017.01.010.
43. Studenski M.T., Patel N.V., Markoe A., Harbour J.W., Samuels S.E. Influence of tumor shape and location in eye plaque brachytherapy dosimetry. *Brachytherapy*. 2020;19:249-254. doi: 10.1016/j.brachy.2020.01.001.
44. Tien C.J., Astrahan M.A., Kim J.M., Materin M., Chen Z., Nath R., et al. Incorporating patient-specific CT-based ophthalmic anatomy in modeling iodine-125 eye plaque brachytherapy dose distributions. *Brachytherapy*. 2017;16:1057-1064. doi: 10.1016/j.brachy.2017.06.014.
45. Daftari I., Aghaian E., O'Brien J.M., Dillon W., Phillips T.L. 3D MRI-based tumor delineation of ocular melanoma and its comparison with conventional techniques. *Med Phys*. 2005;32:3355-3362. doi: 10.1118/1.2068927.
46. Grech Fonk L., Ferreira T.A., Webb A.G., Luyten G.P.M., Beenakker J.M. The economic value of MR-imaging for uveal melanoma. *Clin Ophthalmol*. 2020;14:1135-1143. doi: 10.2147/OPHT.S238405.
47. Damato B., Kacperek A., Errington D., Heimann H. Proton beam radiotherapy of uveal melanoma. *Saudi J Ophthalmol*. 2013;27:151-157. doi: 10.1016/j.sjopt.2013.06.014.

48. Jung S.K., Park Y.H., Shin D.H., Kim H.S., Jung J.H., Kim T.H., et al. Visual outcomes of proton beam therapy for choroidal melanoma at a single institute in the Republic of Korea. *PLoS One*. 2020;15:e0242966. doi: 10.1371/journal.pone.0242966.
49. Marinkovic M., Pors L.J., van den Berg V., Peters F.P., Schalenbourg A., Zografos L., et al. Clinical outcomes after international referral of uveal melanoma patients for proton therapy. *Cancers*. 2021;13. doi: 10.3390/cancers13246241.
50. Fleury E., Trnkova P., Erdal E., Hassan M., Stoel B., Jaarma-Coes M., et al. Three-dimensional MRI-based treatment planning approach for non-invasive ocular proton therapy. *Med Phys*. 2021;48:1315–1326. doi: 10.1002/mp.14665.
51. Pfeiffer K., Dobler B., Rethfeldt C., Schlegel W., Bendl R. OCTOPUS: a planning tool for proton therapy of eye tumours. *Phys Med*. 2001;17:59–62.
52. Wulff J., Koska B., Janson M., Baumer C., Denker A., Geismar D., et al. Technical note: Impact of beam properties for uveal melanoma proton therapy-An in silico planning study. *Med Phys*. 2022;49:3481–3488. doi: 10.1002/mp.15573.

APPENDIX A: EVALUATION OF 3D PROMINENCE AND TUMOUR BASE DEFINITIONS IN UVEAL MELANOMA – A PILOT STUDY

Introduction

The aim of this pilot study was to determine a 3D prominence and basal diameter definition suitable for brachytherapy and proton beam therapy planning and evaluate these, based on 3D MRI tumour contours.

Methods

In a multidisciplinary tumour board, consisting of ocular oncologists, radiation oncologists, clinical physicists and radiologists, three prominence and three base definitions were devised.

Tumour contours on T1gd-weighted MRI were used to evaluate these prominence (Figure 1) and base (Figure 2) definitions:

- Hausdorff distance: Hausdorff distance between tumour top and base. This determines the largest distance within the tumour, i.e. the largest distance that the beta particles will have to travel in case of ruthenium brachytherapy.
- Sclera-based definition: largest distance between tumour top and base, perpendicular to the sclera. This definition is based on description of B-mode ultrasound measurements as performed by ocular oncologists in the case of an idealized spherical eye.
- Centre-based definition: distance between tumour apex and base, measured along the line between centre of the globe and tumour apex, where tumour apex is defined as the point of the tumour closest to the centre of the globe. This definition is based on the current ocular radiotherapy planning methods, where the tumour apex is used to define the clinical target volume.

The LBD was the largest distance between two points in the tumour base, with the base defined as follows:

- Non-projected: The tumour base defined as the cross-section between tumour and choroid. However, this definition may result in an underestimation of overhanging tumours (Main text figure 1).
- Projected base: Non projected base, extended by the projection of the tumour on the sclera from the centre of the eye. This definition was added to accommodate for a better description of overhanging tumours.

- Parallel projected base: Non projected base, extended by the projection of the tumour on the sclera, parallel to centre-based prominence definition. This definition was added to accommodate for a better description of overhanging tumours and is an alternative to the projected base mentioned before.

Results were evaluated in a multidisciplinary tumour board, consisting of ocular oncologists, radiation oncologists, clinical physicists and radiologists. Assessment criteria were (a) the measurement had to be similar to the clinical ultrasound measurement, e.g. perpendicular to the sclera, and (b) had to be suited to use in both brachytherapy planning and proton beam therapy planning.

Results

For the prominence, differences between all definitions were <0.5 mm for 13/25 patients. For 9/25 patients, the Hausdorff distance and the centre-based definition were similar, but the sclera-based definition resulted in an oblique measurement (Figure 3a). For 3/25 patients, the Hausdorff distance resulted in a measurement on the edge of the tumour (Figure 3b), which was judged to not represent the current ultrasonic prominence measurements. The centre-based definition gave consistent results for all patients, and yielded a visually similar measurement as obtained clinically on ultrasound.

For the LBD, the projected base overestimated the tumour base in non-overhanging tumours (Figure 4a). The parallel projected base offered an adequate description of overhanging tumours and non-overhanging tumours (Figure 4b). The non-projected base gives an adequate description of non-overhanging tumours, but lacks in the representation of overhanging tumours. However, this definition corresponds most to the current ultrasound measurements.

Conclusion

The Hausdorff distance and the sclera-based definition resulted in oblique measurements or measurements at the side of the tumour, whereas the centre-based definition yielded a visually similar measurement as obtained clinically on ultrasound and also matched the desired radiotherapy definition for ocular PBT and brachytherapy.

The parallel projected base offered the most adequate description of both non-overhanging and overhanging tumours, however the non-projected base is more comparable to the current measurement methods. Therefore, in this study, for the comparisons between modalities, the non-projected base will be used. For future research, the use of a projected base for measurement of the LBD might be considered.

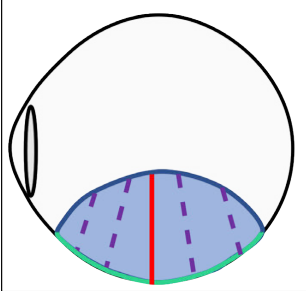
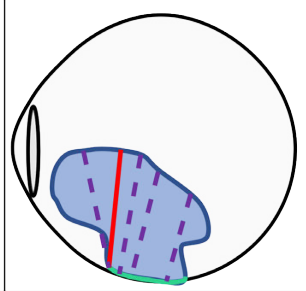
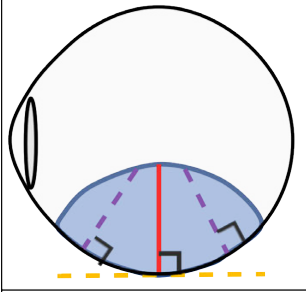
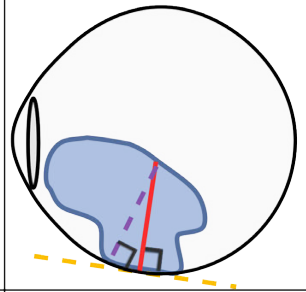
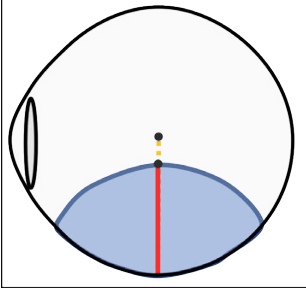
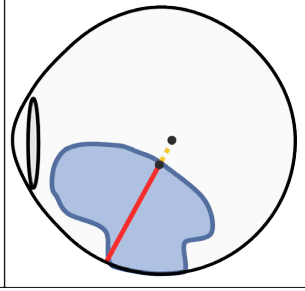
Prominence definitions		
		Hausdorff distance Maximum of all minimum distances between all points in tumour base (green) and top.
		Sclera-based definition Largest distance between tumour top and base, perpendicular to the sclera.
		Centre-based definition Distance between tumour apex and base, measured along the line between vitreous' centre of mass and tumour apex, where tumour apex is defined as the point of the tumour closest to the centre of the vitreous.

Figure 1: Schematic view of the three prominence definitions that were evaluated.

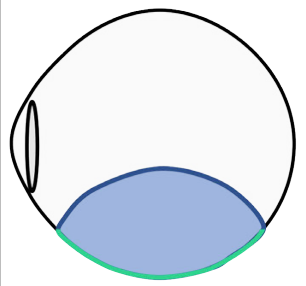
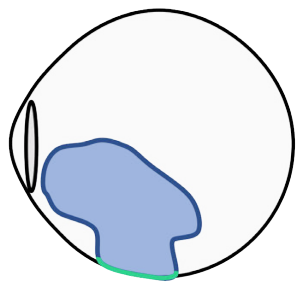
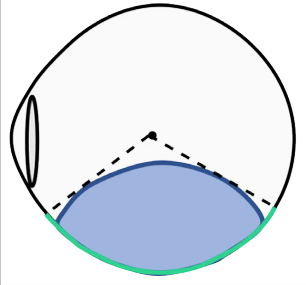
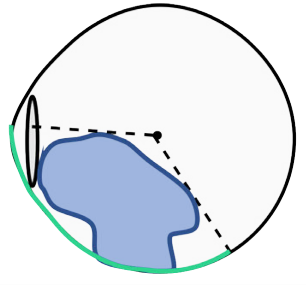
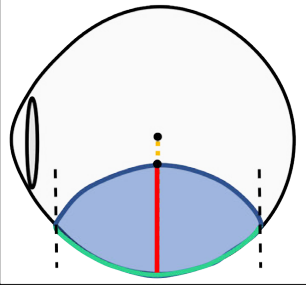
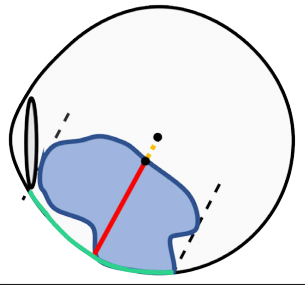
Base definitions		
		Non-projected base Cross-section between tumour and choroid.
		Projected base Non-projected base, extended by the projection of the tumour on the sclera from the centre of the vitreous-lens complex.
		Parallel projected base Non-projected base, extended by the projection of the tumour on the sclera, parallel to the centre-based prominence definition.

Figure 2: Schematic view of the three evaluated base definitions.

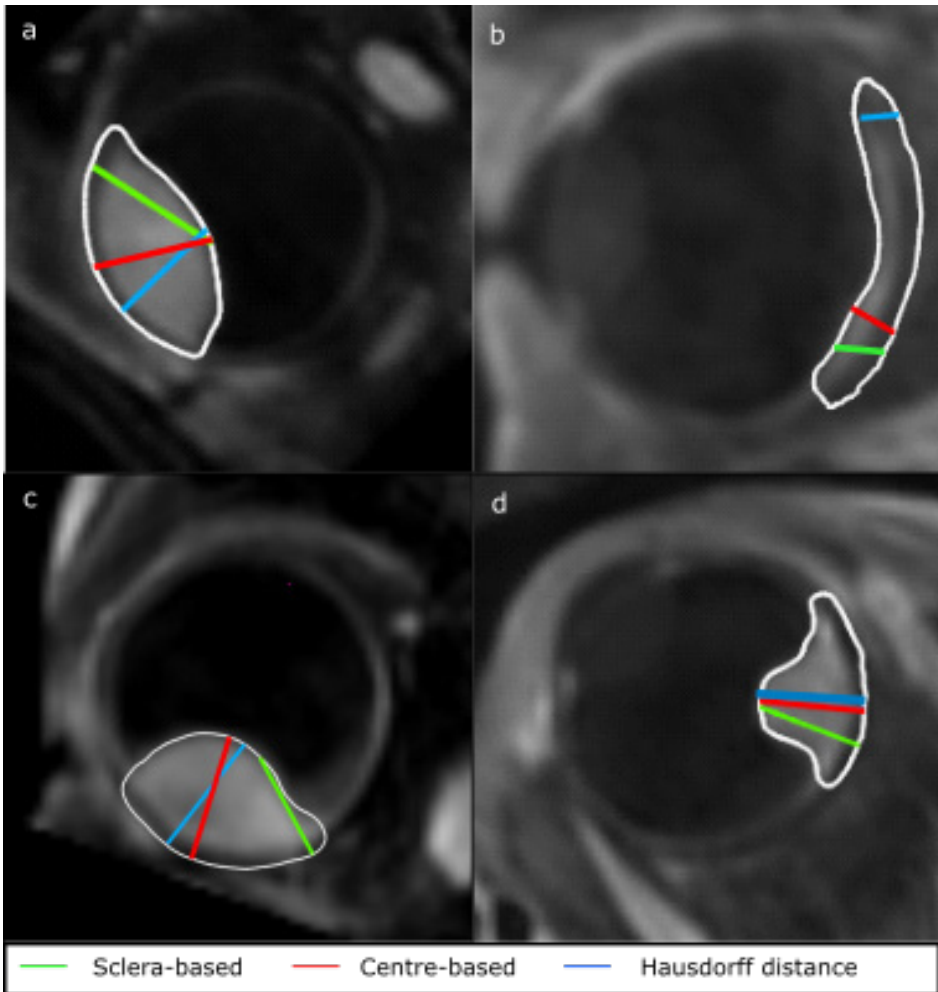


Figure 3: (a,c,d) The sclera-based definition gave oblique measurements in 9/25 patients, (b) the Hausdorff distance gave measurements on the side of the tumour in 3/25 patients. In all cases, the centre-based definition gave acceptable results.

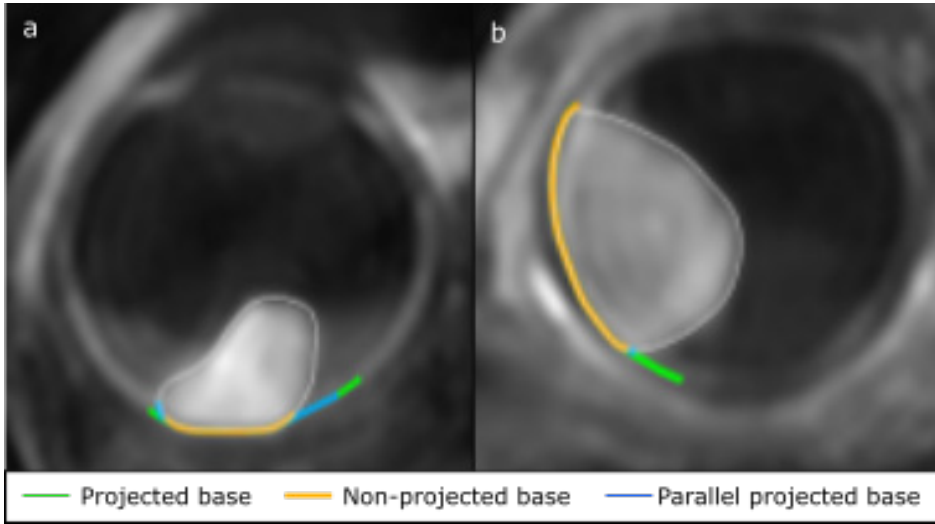


Figure 4: (a) The parallel projection of the base (blue) gave an adequate description of both overhanging and non-overhanging tumours, (b) the projection of the base (green) overestimated the base in non-overhanging tumours.

Appendix B: Overview of prominence, LBD and SBD for all patients and measurement methods

Patient	Tumour location	AJCC classification	Prominence										LBD				SBD		Volume						
			US [mm]	MRI manual [mm]	MRI auto T2 [mm]	MRI auto T1gd [mm]	Remarks	US [mm]	MRI manual T1gd [mm]	MRI auto T2 [mm]	MRI auto T1gd [mm]	Angle between manual & automatic [deg]	Remarks	US [mm]	MRI auto T1gd [mm]	Remarks	US [mm]	MRI auto T1gd [mm]		Remarks					
																					Treatment	T4	T3	T2	T1
Pt001	Posterior	T4	PBT	3.1	No clinical prominence measurement due to flatness	2.5	2.5	2.5	2.5	18.1	17.3	18.0	18.5	31	MRI: extent difficult to assess due to flatness	17.1	13.0	US: entire base not in FOV	294	205					
Pt002	Anterior	T3	PBT	8.4	9.3	8.7	9.3	9.3	15.6	16.8	16.5	17.2	2	US: top not in FOV	15.6	16.8	16.5	17.2	2	US: entire base not in FOV	13.6	14.0	US: entire base not in FOV	841	699
Pt003	Anterior	T3	PBT	9.1	11.4	10.4	10.7	10.7	14.8	15.7	15.4	15.6	3	US: top not in FOV	14.8	15.7	15.4	15.6	3	US: entire base not in FOV	13.7	14.3	US: entire base not in FOV	898	827
Pt004	Posterior	T3	PBT	9.0	9.5	9.7	9.3	9.3	15.1	16.1	14.3	16.0	2		15.1	16.1	14.3	16.0	2		12.7	13.8		816	778
Pt005	Posterior	T1	PBT	3.4	3.6	3.0	3.7	3.7	7.5	9.4	7.0	9.3	8		7.5	9.4	7.0	9.3	8		6.7	8.9		838	49
Pt006	Anterior	T4	PBT	10.5	10.7	11.1	10.8	10.8	16.6	20.7	21.0	21.1	10		16.6	20.7	21.0	21.1	10	US: entire base not in FOV	15.5	15.4	US: entire base not in FOV	1499	1431
Pt007	Posterior	T2	PBT	2.5	2.4	2.7	3.0	3.0	15.2	17.5	19.1	22.8	63		15.2	17.5	19.1	22.8	63	MRI: extent difficult to assess	14.9	20.1	MRI: extent difficult to assess	433	194

Appendix B Continued

Patient	AJCC Tumour location	AJCC classification	Treatment	Prominence						LBD				SBD		Volume		
				US		MRI auto		MRI manual		MRI auto		MRI manual		US			MRI auto	
				mm	mm	mm	mm	mm	mm	mm	mm	mm	mm	mm	mm		mm	mm
Pt008	Posterior	T2	PBT	8.0	8.1	8.6	7.7	11.7	14.0	10.6	13.6	3	8.9	10.6	280	306		
Pt009	Posterior	T3	PBT	8.9	8.4	8.3	8.4	15.0	15.3	16.3	16.9	83	14.8	15.0	747	720		
Pt010	Anterior	T3	PBT	7.8	7.7	7.7	7.5	16.5	16.6	16.6	17.6	59	16.2	16.5	683	617		
Pt011	Posterior	T3	PBT	9.3	10.2	9.9	9.4	14.2	10.5	14.0	13.1	28	8.3	9.0	410	486		
Pt012	Anterior	T3	PBT	13.3	13.0	12.0	12.4	12.8	15.5	14.4	16.0	23	10.2	14.9	1097	976		
Pt013	Anterior	T3	PBT	8.3	8.4	7.5	8.1	16.2	15.3	13.6	16.3	41	14.7	15.2	726	506		
Pt014	Posterior	T3	PBT	9.2	9.5	9.7	9.6	16.9	15.6	16.2	16.0	23	14.1	13.8	769	822		
Pt015	Posterior	T2	PBT	5.1	4.6	4.5	3.8	11.4	12.2	7.8	12.4	1	9.6	7.8	77	85		
Pt016	Posterior	T2	PBT	6.4	6.0	6.4	6.1	6.4	7.5	6.2	8.0	36	5.8	7.7	163	112		

US: haemorrhage included in tumour measurement

US: entire base not in FOV

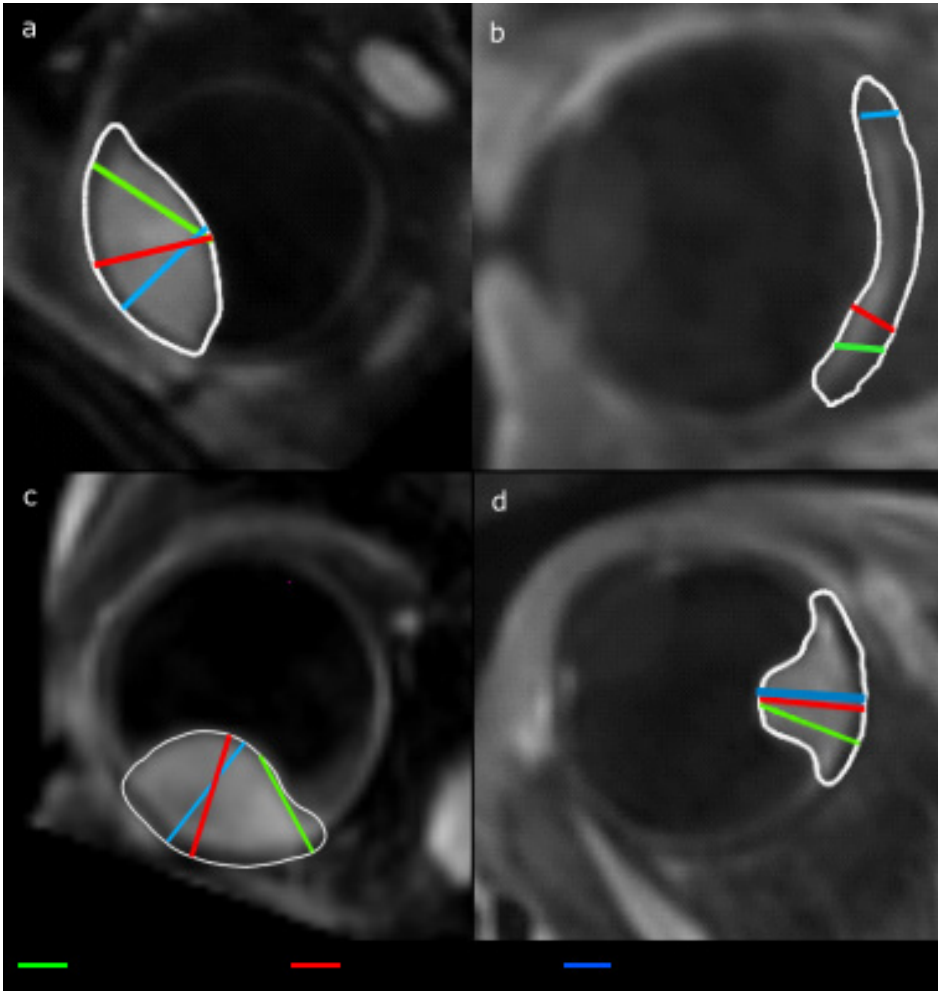
US: entire base not in FOV

US: entire base not in FOV

US: entire base not in FOV

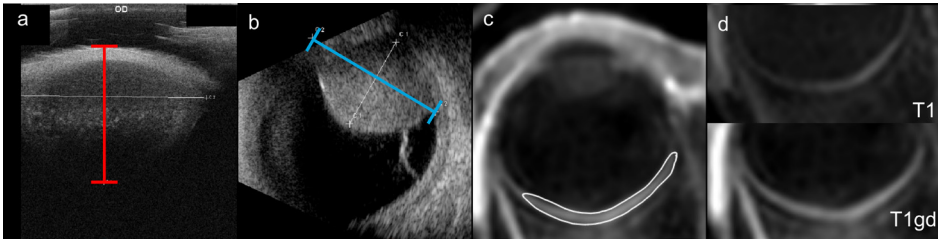
Supplementary Table 1: Overview of all comparisons performed.

		US - MRI manual	US - T1gd automatic	US - T2 automatic	MRI manual - T1gd automatic	MRI manual - T2 automatic	T2 automatic - T1gd automatic
Prominence	Entire group	0.4 (2.3)	0.3 (1.6)	0.4 (1.3)	0.3 (0.9)	0.4 (1.1)	0.3 (0.9)
Median (max) absolute difference [mm]	Anterior location	0.2 (2.3)	0.4 (1.6)	0.6 (1.3)	0.2 (0.7)	0.6 (1.0)	0.3 (0.6)
	Posterior location	0.5 (1.2)	0.3 (1.3)	0.4 (0.7)	0.3 (0.9)	0.3 (1.1)	0.3 (0.9)
LBD	Entire group	1.0 (4.1)	1.1 (7.6)	1.1 (6.8)	0.5 (5.3)	1.6 (6.0)	1.7 (6.7)
Median (max) absolute difference [mm]	Anterior location	0.9 (4.1)	1.6 (4.5)	1.6 (4.4)	0.5 (1.4)	0.3 (2.7)	1.0 (4.1)
	Posterior location	1.1 (3.7)	1.0 (7.6)	1.1 (6.8)	0.5 (5.3)	1.8 (6.0)	1.8 (6.7)
SBD	Entire group	N.A.	1.1 (5.2)	N.A.	N.A.	N.A.	N.A.
Median (max) absolute difference [mm]	Anterior location	N.A.	0.4 (4.7)	N.A.	N.A.	N.A.	N.A.
	Posterior location	N.A.	1.8 (5.2)	N.A.	N.A.	N.A.	N.A.
Volume	Entire group	N.A.	N.A.	N.A.	N.A.	N.A.	66 (789)
Median (max) absolute difference [mm ³]							



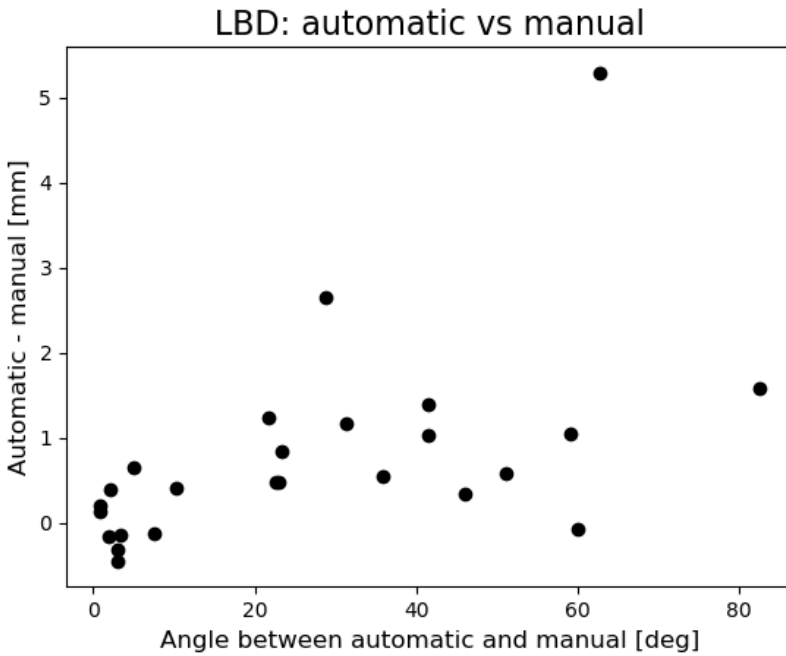
Supplementary Figure 1: Overview of prominence definitions

Supplementary Figure 1: (a,c,d) The sclera-based definition gave oblique measurements in 9/25 patients, (b) the Hausdorff distance gave measurements on the side of the tumour in 3/25 patients. In all cases, the centre-based definition gave acceptable results.



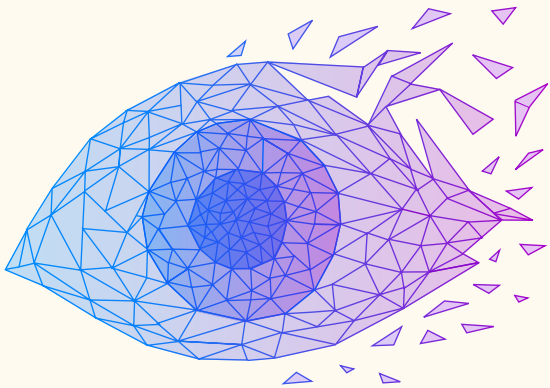
Supplementary Figure 2: Tumours marked separately

Supplementary Figure 2: Tumours with incomplete visualization of the tumour extent were marked separately. On ultrasound, this was due to either (a) limited penetration depth or (b) limited field of view of the ultrasound transducer. In some flat UM the extent of flat tumour components was difficult to assess on MRI (c,d). (d): the area that was thickened and enhanced compared to the native T1-weighted scan was considered tumour.



Supplementary Figure 3: Angle between automatic and manual LBD measurement

Supplementary Figure 3: Relationship between angle between automatic and manual LBD measurement and difference between the two methods.



Chapter 5

Comparing model-based and delineation-based target volume definition for ocular proton beam therapy planning

PhD project chapter

L. Klaassen, C.R.N. Rasch. J.W.M. Beenakker

Submitted to Physica Medica.

ABSTRACT

Background

In recent years, eye-specific, high-resolution MRI protocols have become available for ocular tumours, enabling 3D tumour delineation. Despite these advances, ocular proton therapy typically still relies on model-based target volume definition. Therefore, the aim of this research was to compare model-based and delineation-based target volume definition for ocular tumours.

Methods

Tumours were delineated for 70 uveal melanoma patients. From the delineated tumour base, polynomial models of different degrees were generated. Additionally, model variations with expanded base and added thickness were generated. Models were considered acceptable at a coverage level of 98% or a maximum underestimation of 0.4 mm. The best model for each patient was defined as the acceptable model with the smallest volume.

Results

For 69/70 patients, an acceptable tumour model could be generated, out of whom 12/69 needed an expansion of the tumour base or added tumour thickness to produce at least one acceptable model. At a coverage level of 98%, tumours were overestimated with 20.5% (5th-95th percentile: 5.7%-59.7%), corresponding to a median absolute surface distance of 0.42 mm. Irregularly shaped tumours showed larger overestimations than dome-shaped tumours (16.4% vs 36.6%, $p < 0.001$).

Conclusion

Tumour models as used in ocular proton therapy treatment planning systems can achieve acceptable tumour coverage. However, to achieve this coverage, the tumour models overestimated the delineated tumour volume.

INTRODUCTION

Ocular proton therapy (PT) is one of the main treatment options for intra-ocular tumours such as uveal melanoma, especially for larger lesions or those located near the optic nerve [1-3]. In ocular proton therapy, most treatment planning systems, such as EyePlan, Eclipse Ocular Proton Planning (EOPP), RayOcular and Octopus use a model-based approach for definition of the eye and the tumour [3-8]. In this approach, the user defines a tumour base on the fundus view (a map-like representation of the inside of the eye) and annotates the location of the tumour apex. Subsequently, a polynomial function is then used to model the three-dimensional tumour-vitreous interface. The degree of the polynomial is manually selected by the user to achieve the best possible correspondence to the observed tumour shape.

However, several imaging modalities, such as B-scan ultrasound and magnetic resonance imaging (MRI), reveal that up to 30% of ocular tumours can occur in complex shapes that are not easily captured by mathematical models [9]. For example, mushroom-shaped, multilobular, asymmetrical, and overhanging tumours have been described [2, 10-12].

In many other tumour sites, tumour delineation based on 3D imaging has long been the standard of care. In recent years, eye-specific, high-resolution MRI protocols have become available for ocular tumours as well [10, 13, 14], enabling geometrically accurate tumour delineation with sub-millimetre interobserver variation [15, 16]. Despite these advances, many treatment planning systems for ocular PT continue to rely on geometrical models for target volume definition. Therefore, the aim of this research was to compare model-based and delineation-based target volume definition for ocular tumours.

METHODS

Patients

For this study, data from two existing cohorts were analysed retrospectively. The first cohort consisted of 56 uveal melanoma patients who received an MRI as part of clinical care or a scientific study between May 2019 and March 2021, receiving either brachytherapy, proton therapy or enucleation. The second cohort consisted of 14 patients who underwent MRI scans before proton therapy in the context of a prospective scientific study between November 2022 and February 2024, resulting in a total of 70 included patients. Both cohorts are described in more detail in a

previous paper [9] and both studies were conducted after approval of the local ethics committee (METC Leiden-Den Haag-Delft, NL73433.058.20 and NL57130.058.16).

MRI acquisition and analysis

Tumours were delineated on the 3D contrast-enhanced T1-weighted scans (Figure 1A), with the 3D non-contrast-enhanced T1-weighted scan and 3D T2-weighted scans used as a reference to distinguish the tumour from surrounding structures. These MRI scans were acquired with a 3 tesla MRI scanner (Ingenia Elition, Philips Healthcare, the Netherlands) with a 4.7 cm surface receive coil (Philips Healthcare), using an earlier described protocol [13, 14]. The MRI scans had an acquisition voxel size of $0.8 \times 0.8 \times 0.8 \text{ mm}^3$, a reconstruction voxel size of $0.4 \times 0.4 \times 0.4 \text{ mm}^3$ and the contrast-enhanced T1-weighted scan was acquired in 2 minutes and 7 seconds.

Tumour delineation was performed by one observer (LK) and the contours were verified and, if necessary, corrected by an ophthalmic MRI expert (JWB) with 12+ years of experience. For overhanging tumours, the projection of the tumour top on the retina was also included, similar to the clinical workflow.

Tumour thickness and largest basal diameter were computed automatically based on the 3D tumour delineations according to a previously published method [17].

Tumour models

Tumour models were generated using Python (version 3.12.7). The tumour thickness was determined automatically [17] and the tumour base was extracted from the delineated tumour (Figure 1B). For each point on the tumour base, the height of the model was calculated by taking into account the tumour thickness, the distance from that point to the edge of the base and a shape factor. That shape factor defined the degree of the polynomial used to model the tumour's vertical profile, where a value of 1 resulted in a pyramidal shape and a value of 10 approximated a cylindrical shape (Figure 1C). The calculated heights were then projected from the corresponding points in the base, parallel with the vector of the tumour thickness, resulting in a three-dimensional reconstruction of the tumour geometry (Figure 1D).

We expect that some tumours, for example asymmetrical or overhanging tumours, may be more accurately described with a larger base or a larger thickness. Therefore, for each patient, variations of the standard model were created: one with 0.5 mm added thickness, one with an expansion of the base contour of 1.0 mm, and a combination of both.

For all four tumour variations, models were created with shape factors ranging from 1 to 10 in increments of 0.1. The code to generate these tumour models is available on GitHub: github.com/MREYE-LUMC/OPT_tumourmodels.

Model evaluation

All models were compared to the tumour delineation and evaluated based on volume and surface distance metrics.

Volume and surface distance metrics

Tumour coverage and volumes of overestimation and underestimation, relative to the delineated tumour volume, were determined. Additionally, signed surface distances were determined between the top of the delineated tumour and the top of each model, as at the tumour base both contours were identical by definition. Here, negative distances corresponded to model contours that were inside the delineated tumour contour and vice versa. Minimum and median surface distance, as well as the 5th and 95th percentiles, were determined. Additionally, the median absolute surface distance was determined to quantify overall deviation regardless of direction.

Selection of best models

Models were considered acceptable if they either had a coverage larger than 98% or a minimum surface distance of greater than -0.4 mm, meaning the model contour was allowed to lie at most 0.4 mm inside of the delineated contour, corresponding to the MRI reconstruction voxel size and the size of the dose grid used in the treatment planning system at our centre. The best model was then selected from all acceptable models and was defined as the model with the lowest volume.

Sensitivity to varying thresholds and shape factors

The sensitivity of the results for different acceptance thresholds was investigated: in addition to the previously mentioned threshold of 98% coverage *or* a maximum underestimation of 0.4 mm, three other thresholds were evaluated: (1) a more lenient threshold with a coverage of 95% *or* a maximum underestimation of 0.4 mm; (2) a threshold of the coverage of 95% *and* a maximum underestimation of 0.4 mm; and (3) a stricter threshold with a coverage of 98% *or* a maximum surface distance of 0.2 mm.

Furthermore, as the optimal shape factor was selected with a precision of one decimal, a level of accuracy that may be challenging to achieve in clinical practice, the sensitivity of the results to variations in the shape factor was evaluated. For each overall best model (i.e. one per patient), the analysis was repeated using three alternative shape factor values: the shape factor rounded down, rounded up, and rounded up plus one.

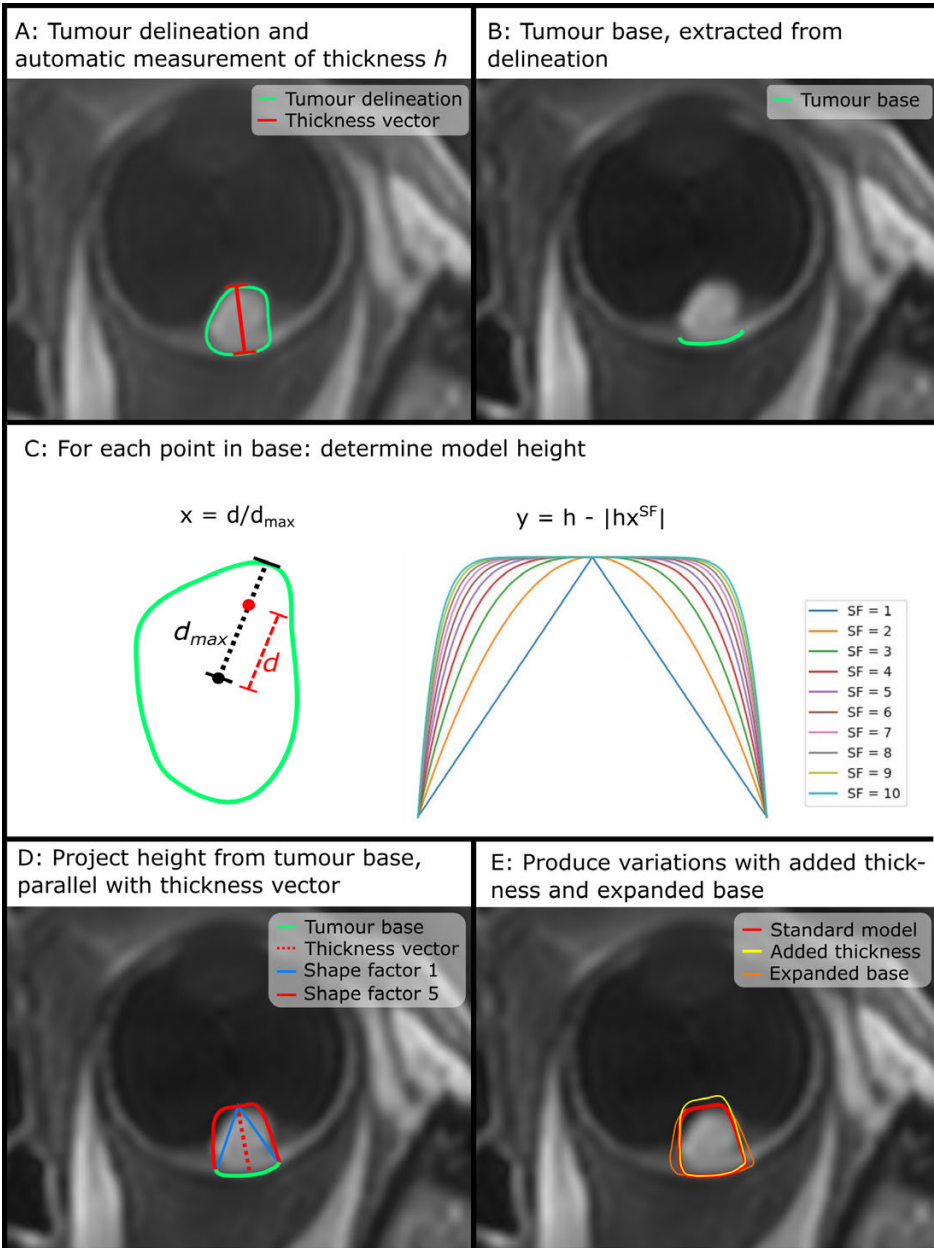
Statistics

For each variation, the number of patients with an acceptable model was reported. Median and 5th and 9th percentiles of all volume and surface distance metrics were calculated for all best models.

Additionally, tumour shape was classified as regular (dome-shaped or flat lesions) or irregular (mushroom-shaped, bilobular or other asymmetrical shapes) [9]. Differences in tumour overestimation, 95th percentile surface distance and shape factor between regularly and irregularly shaped tumours were evaluated with an unpaired t-test or Mann-Whitney U test, depending on the results of the Shapiro-Wilk test for normality.

Figure 1: Generation of a geometric tumour model from a delineated tumour. (A) Tumours were delineated (green contour) and the thickness (red line) was determined automatically; (B) the tumour base (green line) was extracted from delineation; (C) for each point in the tumour base, model height was determined based on distance d from base centre to the point, distance d_{max} from base centre to outer contour in the same direction, thickness h and shape factor SF ; (D) model height was projected from tumour base (green line), parallel to the thickness vector (dashed red line); (E) variations of the standard tumour model (red line) with added thickness (yellow line) and expanded tumour base (orange line) were produced as well.





RESULTS

Average tumour thickness and largest basal diameter were 6.4 ± 3.0 mm (range 1.3–12.9 mm) and 15.0 ± 3.7 mm (range 7.2–22.4 mm). AJCC 8th edition TNM staging [18] was as follows: T1: 13%, T2: 14%, T3: 50%, T4: 23%. 50/70 tumours had a regular shape and 20/70 had an irregular shape.

For 69/70 patients, an acceptable tumour model could be produced with either the standard model or one of the expanded variations, out of whom 12/69 needed one of the variations to produce at least one acceptable model (Table 1). However, for an additional 25 patients, one of the expanded variations produced a model with a smaller overestimation than the standard model, due to a lower shape factor that resulted in an acceptable model.

For one patient, no acceptable tumour model could be produced with the threshold of coverage of 98% or maximum underestimation of 0.4 mm. This patient had a very flat tumour with a large diameter and acceptable models could only be produced with the more lenient threshold of 95% coverage.

With the best models, an average coverage of 98.1% was achieved (5th-95th percentile: 94.2% – 98.7%), corresponding to a relative overestimation of 20.5% (5th-95th percentile: 5.7% – 59.9%, Table 1, Figure 2). For the entire group, the median 5th percentile surface distance was -0.23 mm, with the lowest values observed in the largest tumours (Figure 2C). Similarly, median 95th percentile surface distance was 1.10 mm, with larger tumours exhibiting higher values (Figure 2D). This effect likely occurred because the models, despite larger surface distances, still adhered to the 98% coverage threshold, due to their large volume. Examples of patients with relatively high underestimation or overestimation are shown in Figure 3.

In irregularly shaped tumours a larger amount of overestimation of the tumour was required for an acceptable model: medians for relative overestimation were 16.4% and 36.6% (<0.001), with 95th percentile surface distances of 0.99 mm and 2.08mm for regularly shaped and irregularly shaped tumours, respectively (Fig 4A,B). Differences in shape factor between regularly and irregularly shaped tumours were not significant (2.3 for regular shape and 2.2 for irregular shape, $p=0.66$). However, variations to make the tumour model larger were used more often in irregularly shaped tumours (41% of regularly shaped tumours and 85% of irregularly shaped tumours, Fig 4C,D).

At the more lenient threshold of 95% coverage, all patients had an acceptable tumour

model, with a median overestimation of 10.6%. The stricter thresholds resulted in a decreasing number of patients meeting the requirements ($n=61$ for the 95% coverage *and* maximum underestimation of 0.4 mm threshold) or an increasing overestimation (22.2% for the maximum underestimation of 0.2 mm). All results for the different thresholds are shown in Supplementary Table 2-5.

In the analysis for robustness to variation in shape factors, each step of 1.0 in shape factor corresponded to an increase of overestimation of approximately 15 percentage points and approximately 0.3 mm in the 5th percentile surface distance (Supplementary Table 6). Rounding down to the nearest shape factor resulted in a decrease in coverage to a median of 94.9%, corresponding to a 5th percentile surface distance of -0.44 mm.

Table 1: Volume and distance metrics for all variations of tumour models. Median and 5th-95th percentiles are shown. The overall best model was the model with the lowest overestimation.

	Standard model	With added thickness	With expanded base	With added thickness and expanded base	Overall best model
Number of patients with acceptable model	57	58	68	69	699
Median shape factor	2.5 (1.8 – 4.7)	2.2 (1.7 – 4.6)	1.8 (1.1 – 4.3)	1.4(1.1 – 3.3)	2.3 (1.2 – 4.3)
Volume metrics					
Coverage [%]	98.1 (94.4 – 98.4)	98.1 (92.8 – 98.6)	98.3 (94.5 – 99.1)	98.5 (98.0 – 99.2)	98.1 (94.2 – 98.7)
Overestimation [%]	17.5 (5.5 – 51.5)	20.1 (7.7 – 51.7)	28.8 (14.0 – 84.6)	30.9 (12.6 – 63.3)	20.5 (5.7 – 59.9)
Distance metrics [mm]					
5th percentile surface distance	-0.23 (-0.38 – 0.10)	-0.21 (-0.46 – 0.20)	-0.17 (-0.44 – 0.31)	-0.22 (-0.39 – 0.14)	-0.23 (-0.46 – 0.06)
Median surface distance	0.45 (0.18 – 1.14)	0.56 (0.25 – 1.10)	0.44 (0.15 – 1.53)	0.42 (0.12 – 1.09)	0.41 (0.14 – 0.87)
95th percentile surface distance	1.31 (0.53 – 3.00)	1.35 (0.61 – 2.90)	1.22 (0.58 – 3.57)	1.08 (0.54 – 3.16)	1.10 (0.53 – 2.74)
Median absolute surface distance	0.45 (0.19 – 1.14)	0.56 (0.26 – 1.10)	0.47 (0.19 – 1.53)	0.42 (0.15 – 1.09)	0.42 (0.18 – 0.88)

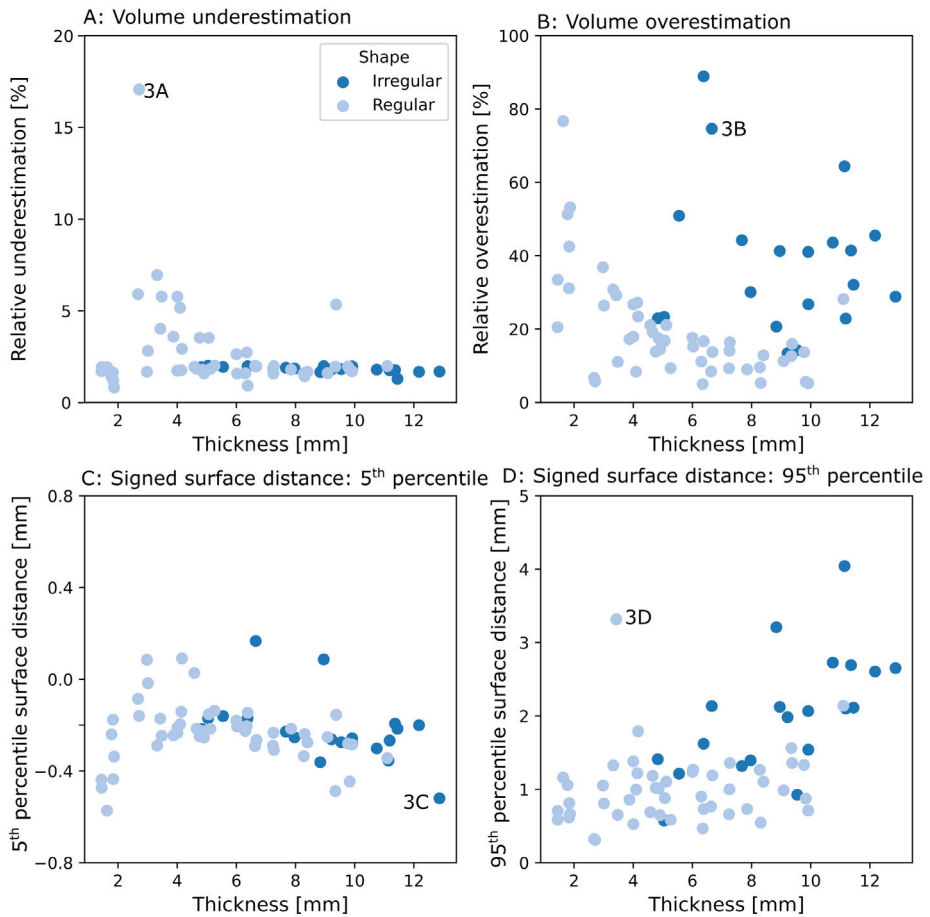


Figure 2: Relationship between model performance and tumour thickness: (A) underestimation, (B) volume overestimation, (C) 5th percentile of signed surface distance, (D) 95th percentile of signed surface distance. Negative signed surface distance corresponds to a that model contour is inside the delineated tumour contour. Regularly shaped tumours are shown in light blue, irregularly shaped tumours in dark blue. Annotated points are shown in detail in Figure 3.

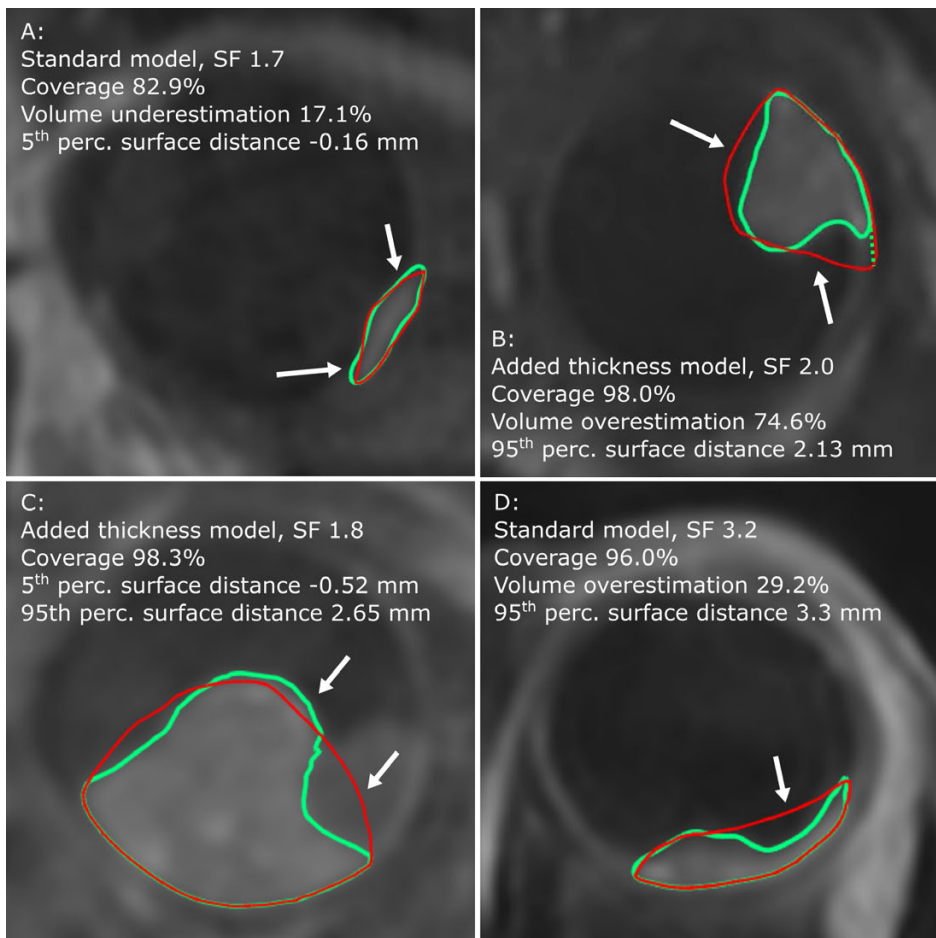


Figure 3: Examples of delineated tumours (green) with their best-performing tumour model (red). **(A)** Small tumour with a relatively large volume underestimation of 17% (arrows). This model was accepted because the maximum underestimation was still within 0.4 mm. **(B)** Asymmetrical (overhanging) tumour that required a manual expansion of the tumour base (dashed green line) to achieve an acceptable coverage, resulting in a large overestimation of 74.6%. The area at the white arrow was not covered by the standard model. **(C)** Large mushroom-shaped shaped tumour with relatively large areas of over- and underestimation (white arrows) but with a coverage of over 98%. **(D)** Dome-shaped tumour with flat extension (white arrow), which is overestimated by the tumour model, resulting in a relatively large large 95th percentile surface distance of 3.3 mm.

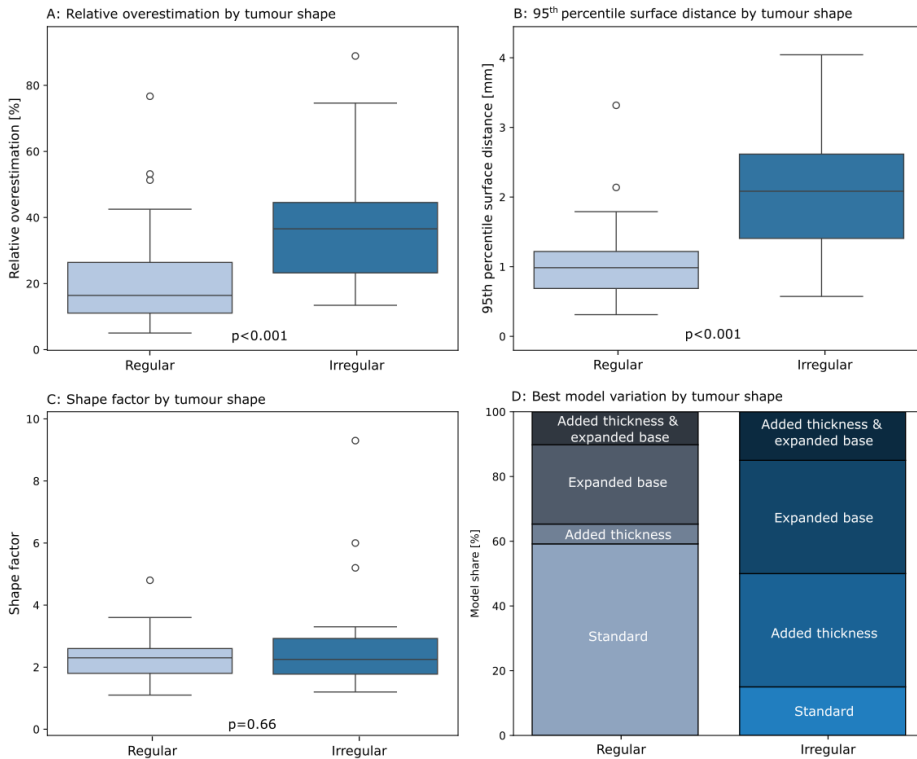


Figure 4: The influence of tumour shape (regular shape: $n = 50$, irregular shape: $n=20$) on model performance. **(A)** Irregular tumours show a larger relative overestimation; **(B)** and a larger 95th percentile surface distance; **(C)**. Shape factors did not differ significantly; **(D)** Irregular tumours needed an expansion of the standard model more often.

DISCUSSION

This study compared geometric tumour models used in treatment planning systems for ocular PT to delineated ocular tumours. The results show that acceptable tumour models could be generated for almost all patients, although especially irregularly shaped tumours often needed expansion of the tumour base, extra thickness, or both. Furthermore, at this coverage level, tumours were overestimated by approximately 20%.

Most of the overestimation occurred at the vitreous body, however, if a base expansion was required to adequately cover the tumour, the overestimation also occurred along the retina and choroid. Both coverage and overestimation of the tumour depended on

the shape factor of the tumour model: with shape factors rounded down, coverage decreased to about 95%. However, depending on the tumour shape and location, the effect on the collimator size and therefore irradiated volume is likely smaller.

Few papers have addressed margin calculation in ocular PT. In the studies by Wulff et al. [19] and Björkman et al. [20], the tumour model itself is not considered. Our results show that an increase or decrease of 1 in shape factor resulted in about a 0.3 mm difference in the 5th percentile surface distance, i.e. a possible underestimation or overestimation of the tumour contour. It may be advisable to incorporate this variation in the margin recipe. Nevertheless, the margin of 2.5 mm has been widely used in clinical practice across multiple centres, resulting in high local control rates [21-25]. This suggests that the tumour models used in clinical practice provide sufficient coverage with the current radiation technique. It is likely that either the user already expands the tumour base during model creation - similar to the approach in this study - or that the single beam dose delivery used in ocular PT, inherently irradiates regions potentially uncovered by the tumour model.

The workflow in this paper uses the same tumour base for the ground-truth delineation and the tumour model, eliminating any effects from the base delineation typically performed in the fundus view in clinical practice. In practice, the difference between base delineation in a 3D imaging viewer and the fundus view, based on clip-tumour distances and tumour diameters, might be larger than the differences between model-based and delineation-based target volume delineation as described in this study. This is especially relevant because differences of about 1 mm in clip-tumour distances between different measurement modalities are not uncommon [12]. In this context, MRI-based delineation fused with fundus imaging [26, 27] may improve the accuracy of base delineation.

Furthermore, various projection methods are possible to generate the tumour top from the delineated tumour base. In this paper, we applied a curved projection where the height was projected relative to each point of the tumour base. An alternative method would project relative to plane perpendicular to the eye at the apex location. We compared these approaches for the standard, unexpanded, model and found that they resulted in tumour models with similar performance (Supplementary Figure 1 and Supplementary Table 7).

In this study, the impact of the differences between model-based and delineation-based target volume definition on irradiated volume was not assessed. In most centres offering ocular PT, a single passive scattering beam with a patient-specific collimator

is used, with patients gazing at a LED at a predefined gazing angle [3]. This workflow, which deviates from conventional external radiotherapy practices, results in an irradiated volume that is inherently significantly larger than the delineated volume. It is therefore possible that under- and overestimations observed in this study have a limited effect on irradiated volume. Moreover, in the case of overestimation, the effect on organs at risk might be limited, as overestimation primarily involves the vitreous body.

The acceptance threshold of a coverage of 98% and a maximum underestimation of the tumour contour of 0.4 mm is somewhat arbitrary. The 98% threshold was chosen since it is a commonly used metric in the evaluation of radiotherapy plans, while the 0.4 mm corresponds with the size of the dose grid used in the treatment planning system at our centre. To assess the robustness of these thresholds, we also evaluated both more lenient and stricter thresholds. Our results showed that overestimation decreased with the more lenient thresholds, whereas a stricter threshold led to fewer patients meeting the criteria for an acceptable model.

Conclusion

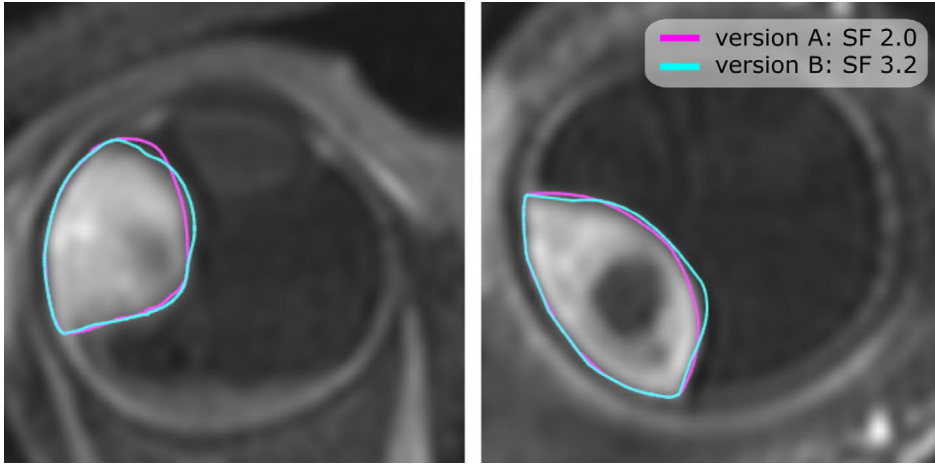
All tumour models as used in ocular proton therapy treatment planning systems can achieve acceptable tumour coverage. However, to achieve this coverage, the tumour models overestimated the delineated tumour volume.

REFERENCES

1. Jager MJ, Shields CL, Cebulla CM, Abdel-Rahman MH, Grossniklaus HE, Stern MH, et al. Uveal melanoma. *Nat Rev Dis Primers*. 2020;6:24. doi: 10.1038/s41572-020-0158-0.
2. Kaliki S, Shields CL. Uveal melanoma: relatively rare but deadly cancer. *Eye (Lond)*. 2017;31:241-57. doi: 10.1038/eye.2016.275.
3. Hrbacek J, Kacperek A, Beenakker JM, Mortimer L, Denker A, Mazal A, et al. PTCOG Ocular Statement: Expert Summary of Current Practices and Future Developments in Ocular Proton Therapy. *Int J Radiat Oncol Biol Phys*. 2024;120:1307-25. doi: 10.1016/j.ijrobp.2024.06.017.
4. Daftari I, Aghaian E, O'Brien JM, Dillon W, Phillips TL. 3D MRI-based tumor delineation of ocular melanoma and its comparison with conventional techniques. *Med Phys*. 2005;32:3355-62. doi: 10.1118/1.2068927.
5. Daftari IK, Mishra KK, O'Brien JM, Tsai T, Park SS, Sheen M, et al. Fundus image fusion in EYEPLAN software: an evaluation of a novel technique for ocular melanoma radiation treatment planning. *Med Phys*. 2010;37:5199-207. doi: 10.1118/1.3488891.
6. Dobler B, Bendl R. Precise modelling of the eye for proton therapy of intra-ocular tumours. *Phys Med Biol*. 2002;47:593-613. doi: 10.1088/0031-9155/47/4/304.
7. Varian Medical Systems. Planning Reference Guide for Eclipse Ocular Proton Planning. 2007.
8. Wulff J, Koska B, Heufelder J, Janson M, Backer CM, Siregar H, et al. Commissioning and validation of a novel commercial TPS for ocular proton therapy. *Med Phys*. 2023;50:365-79. doi: 10.1002/mp.16006.
9. Klaassen L, Ferreira TA, Luyten G, Beenakker JM. Estimating uveal melanoma volume with ellipsoid tumour models. *Acta Ophthalmol*. 2025. doi: 10.1111/aos.17492.
10. Foti PV, Travali M, Farina R, Palmucci S, Spatola C, Raffaele L, et al. Diagnostic methods and therapeutic options of uveal melanoma with emphasis on MR imaging-Part I: MR imaging with pathologic correlation and technical considerations. *Insights Imaging*. 2021;12:66. doi: 10.1186/s13244-021-01000-x.
11. Ramos-Davila EM, Dalvin LA. Clinical Implications of Ultrasound-Based Morphology in Choroidal Melanoma. *Ophthalmol Retina*. 2025;9:263-71. doi: 10.1016/j.oret.2024.09.010.
12. Jaarsma-Coes MG, Ferreira TA, Marinkovic M, Vu THK, van Vught L, van Haren GR, et al. Comparison of Magnetic Resonance Imaging-Based and Conventional Measurements for Proton Beam Therapy of Uveal Melanoma. *Ophthalmol Retina*. 2023;7:178-88. doi: 10.1016/j.oret.2022.06.019.
13. Ferreira TA, Grech Fonk L, Jaarsma-Coes MG, van Haren GGR, Marinkovic M, Beenakker JM. MRI of Uveal Melanoma. *Cancers (Basel)*. 2019;11. doi: 10.3390/cancers11030377.
14. Ferreira TA, Jaarsma-Coes MG, Marinkovic M, Verbist B, Verdijk RM, Jager MJ, et al. MR imaging characteristics of uveal melanoma with histopathological validation. *Neuroradiology*. 2022;64:171-84. doi: 10.1007/s00234-021-02825-5.
15. Jaarsma-Coes MG, Klaassen L, Verbist BM, Vu THK, Klaver YLB, Rodrigues MF, et al. Inter-Observer Variability in MR-Based Target Volume Delineation of Uveal Melanoma. *Adv Radiat Oncol*. 2023;8:101149. doi: 10.1016/j.adro.2022.101149.
16. Klaassen L, Haasjes C, Hol M, Cambraia Lopes P, Spruijt K, van de Steeg-Henzen C, et al. Geometrical accuracy of magnetic resonance imaging for ocular proton therapy planning. *Phys Imaging Radiat Oncol*. 2024;31:100598. doi: 10.1016/j.phro.2024.100598.
17. Klaassen L, Jaarsma-Coes MG, Verbist BM, Vu THK, Marinkovic M, Rasch CRN, et al. Automatic Three-Dimensional Magnetic Resonance-based measurements of tumour prominence and basal diameter for treatment planning of uveal melanoma. *Phys Imaging Radiat Oncol*. 2022;24:102-10. doi: 10.1016/j.phro.2022.11.001.

18. Kivelä T SR, Grossniklaus HE, et al. Uveal melanoma. AJCC Cancer Staging Manual. 8th edition. New York: Springer; 2016. p. 805-17.
19. Wulff J, Koska B, Ahmad Khalil D, Richter R, Maximilian Backer C, Baumer C, et al. Uncertainties in ocular proton planning and their impact on required margins. *Phys Med*. 2024;121:103358. doi: 10.1016/j.ejmp.2024.103358.
20. Bjorkman D, Via R, Lomax A, De Prado M, Baroni G, Weber DC, et al. The effect of intra- and inter-fractional motion on target coverage and margins in proton therapy for uveal melanoma. *Phys Med Biol*. 2024;69. doi: 10.1088/1361-6560/ad8297.
21. Egger E, Schalenbourg A, Zografos L, Bercher L, Boehringer T, Chamot L, et al. Maximizing local tumor control and survival after proton beam radiotherapy of uveal melanoma. *Int J Radiat Oncol Biol Phys*. 2001;51:138-47. doi: 10.1016/s0360-3016(01)01560-7.
22. Marinkovic M, Pors LJ, van den Berg V, Peters FP, Schalenbourg A, Zografos L, et al. Clinical Outcomes after International Referral of Uveal Melanoma Patients for Proton Therapy. *Cancers (Basel)*. 2021;13. doi: 10.3390/cancers13246241.
23. Bensoussan E, Thariat J, Maschi C, Delas J, Schouver ED, Herault J, et al. Outcomes After Proton Beam Therapy for Large Choroidal Melanomas in 492 Patients. *Am J Ophthalmol*. 2016;165:78-87. doi: 10.1016/j.ajo.2016.02.027.
24. Hussain RN, Chiu A, Pittam B, Taktak A, Damato BE, Kacperek A, et al. Proton beam radiotherapy for choroidal and ciliary body melanoma in the UK-national audit of referral patterns of 1084 cases. *Eye (Lond)*. 2023;37:1033-6. doi: 10.1038/s41433-022-02178-0.
25. Papakostas TD, Lane AM, Morrison M, Gragoudas ES, Kim IK. Long-term Outcomes After Proton Beam Irradiation in Patients With Large Choroidal Melanomas. *JAMA Ophthalmol*. 2017;135:1191-6. doi: 10.1001/jamaophthalmol.2017.3805.
26. Haasjes C, Vu THK, Beenakker JWM. Patient-specific mapping of fundus photographs to three-dimensional ocular imaging. *Medical Physics*. 2025;52:2330-9. doi: 10.1002/mp.17576.
27. Via R, Pica A, Antonioli L, Paganelli C, Fattori G, Spaccapaniccia C, et al. MRI and FUNDUS image fusion for improved ocular biometry in Ocular Proton Therapy. *Radiother Oncol*. 2022;174:16-22. doi: 10.1016/j.radonc.2022.06.021.

SUPPLEMENTARY MATERIALS



Supplementary Figure 1: Comparison of different methods for projection of model height. Supplementary Figure 1: model heights projected from the curved tumour base (pink) and from a plane perpendicular to the thickness vector (blue), resulting in very similar tumour models.

Supplementary Table 2: Comparisons between model and tumour with different thresholds for acceptance.

	>95% OR > -0.4 mm	>95% AND > -0.4 mm	>98% OR > -0.4 mm	>98% OR > -0.2 mm
Number of patients with acceptable model	70	61	69	69
Median shape factor	2.0 (1.2 – 4.2)	2.6 (1.4 – 6.8)	2.3 (1.2 – 4.3)	2.2
Used model (standard / added thickness / expanded base / both)	43/12/11/4	31/10/12/8	32/10/19/8	27/11/20/11
Volume metrics				
Coverage [%]	95.4 (94.9 – 96.3)	98.8 (95.5 – 99.8)	98.1 (94.2 – 98.7)	98.2 (98.0 – 98.7)
Overestimation [%]	10.6 (2.3 – 33.3)	22.1 (10.1 – 86.9)	20.5 (5.7 – 59.9)	22.2 (8.6 – 59.9)
Distance metrics [mm]				
5th percentile surface distance	-0.43 (-0.79 – -0.17)	-0.07 (-0.23 – 0.33)	-0.23 (-0.46 – 0.06)	-0.22 (-0.4 – 0.09)
Median surface distance	0.19 (-0.12 – 0.49)	0.57 (0.21 – 1.57)	0.41 (0.14 – 0.87)	0.41 (0.19 – 0.87)
95th percentile surface distance	0.79 (0.31 – 2.46)	1.38 (0.59 – 3.70)	1.10 (0.53 – 2.71)	1.14 (0.56 – 2.71)
Median absolute surface distance	0.29 (0.14 – 0.57)	0.57 (0.22 – 1.57)	0.42 (0.18 – 0.88)	0.43 (0.21 – 0.88)

Bold: threshold that was used throughout the paper (coverage >98% or minimum of surface distances >-0.4).

Supplementary Tables 3-5: All model variations for the different thresholds

	Standard model	With added thickness	With expanded base	With added thickness and expanded base	Overall best model
Number of patients with acceptable model	64	65	69	70	70
Median shape factor	2.1 (1.5 – 7.0)	1.9 (1.3 – 5.9)	1.5 (1.0 – 2.9)	1.2 (1.0 – 1.9)	2.0 (1.2 – 4.2)
Volume metrics					
Coverage [%]	95.4 (94.5 – 96.4)	95.4 (93.5 – 96.3)	95.8 (95.1 – 97.9)	96.2 (95.1 – 99.1)	95.4 (94.9 – 96.3)
Overestimation [%]	9.5 (2.2 – 35.4)	14.5 (3.3 – 39.9)	23.6 (7.4 – 54.3)	24.9 (7.9 – 55.1)	10.6 (2.3 – 33.3)
Distance metrics [mm]					
5th percentile surface distance	-0.43 (-0.81 – -0.16)	-0.41 (-0.76 – -0.10)	-0.43 (-0.68 – 0.09)	-0.43 (-0.73 – 0.13)	-0.43 (-0.79 – -0.17)
Median surface distance	0.20 (-0.13 – 0.57)	0.28 (-0.07 – 0.67)	0.29 (0.12 – 0.89)	0.28 (0.11 – 0.81)	0.19 (-0.12 – 0.49)
95th percentile surface distance	0.88 (0.30 – 2.49)	0.96 (0.46 – 2.58)	0.89 (0.46 – 2.92)	0.90 (0.48 – 2.89)	0.79 (0.31 – 2.46)
Median absolute surface distance	0.31 (0.14 – 0.62)	0.37 (0.14 – 0.74)	0.33 (0.15 – 0.96)	0.35 (0.14 – 0.88)	0.30 (0.14 – 0.57)

Supplementary Table 3: Threshold >95% coverage OR minimum surface distance >-0.4 mm). Median and 5th-95th percentiles are shown. The overall best model was the model with the lowest overestimation.

Supplementary Table 4

	Standard model	With added thickness	With expanded base	With added thickness and expanded base	Overall best model
Number of patients with acceptable model	48	51	57	61	61
Median shape factor	2.8 (2.1 – 4.7)	2.5 (1.8 – 4.8)	2.0 (1.3 – 4.6)	1.7 (1.1 – 5.9)	2.6 (1.4 – 6.8)
Volume metrics					
Coverage [%]	98.3 (95.3 – 99.7)	98.3 (95.7 – 99.6)	99.1 (96.0 – 99.7)	99.5 (98.2 – 99.9)	98.8 (95.5 – 99.8)
Overestimation [%]	20.7 (10.4 – 59.9)	26.2 (10.7 – 69.6)	30.6 (17.9 – 87.4)	35.1 (17.4 – 91.0)	22.1 (10.1 – 86.6)
Distance metrics [mm]					
5th percentile surface distance	-0.11 (-0.22 – 0.27)	-0.07 (-0.21 – 0.38)	0.13 (-0.17 – 0.41)	0.14 (-0.18 – 0.43)	-0.07 (-0.23 – 0.33)
Median surface distance	0.54 (0.24 – 1.51)	0.70 (0.32 – 1.71)	0.69 (0.28 – 1.60)	0.73 (0.31 – 1.76)	0.57 (0.21 – 1.57)
95th percentile surface distance	1.39 (0.66 – 3.18)	1.52 (0.77 – 3.56)	1.36 (0.67 – 3.30)	1.43 (0.68 – 3.88)	1.38 (0.59 – 3.70)
Median absolute surface distance	0.54 (0.25 – 1.51)	0.70 (0.33 – 1.71)	0.69 (0.29 – 1.60)	0.73 (0.31 – 1.76)	0.57 (0.22 – 1.57)

Supplementary Table 4: Threshold >95% coverage AND minimum surface distance >0.4 mm. Median and 5th-95th percentiles are shown. The overall best model was the model with the lowest overestimation.

Supplementary Table 5

	Standard model	With added thickness	With expanded base	With added thickness and expanded base	Overall best model
Number of patients with acceptable model	57	58	68	69	69
Median shape factor	2.7 (1.8 – 6.2)	2.3 (1.7 – 5.3)	1.9 (1.1 – 5.1)	1.5 (1.1-3.3)	2.2 (1.2 – 4.4)
Volume metrics					
Coverage [%]	98.1 (97.1 – 98.5)	98.1 (96.2– 98.6)	98.5 (97.6 – 98.4)	98.5 (98.0 – 99.4)	98.2 (98.0 – 98.7)
Overestimation [%]	22.1 (7.6 – 68.7)	24.7 (8.8 – 70.6)	30.9 (14. – 58.2)	31.0 (12.6 – 63.3)	22.2 (8.6 – 59.9)
Distance metrics [mm]					
5th percentile surface distance	-0.22 (-0.38 – 0.19)	-0.20 (-0.46 – 0.25)	-0.17 (-0.44 – -0.38)	-0.21 (-0.39 – 0.22)	-0.22 (-0.46 – 0.09)
Median surface distance	0.55 (0.22 – 1.27)	0.60 (0.27 – 1.11)	0.45 (0.16=7 – 1.58)	0.42 (0.12 – 1.09)	0.41 (0.19 – 0.87)
95th percentile surface distance	1.36 (0.58 – 3.24)	1.40 (0.66 – 2.90)	1.22 (0.59 – 3.57)	1.10 (0.57 – 3.16)	1.14 (0.56 – 2.71)
Median absolute surface distance	0.55 (0.28 – 1.27)	0.60 (0.32 – 1.11)	0.48 (0.19 – 1.58)	0.42 (0.15 –1.09)	0.43 (0.21 – 0.88)

Supplementary Table 5: Threshold >98% coverage OR minimum surface distance >-0.2 mm. Median and 5th-95th percentiles are shown. The overall best model was the model with the lowest overestimation.

Supplementary Table 6: Sensitivity of the outcome metrics for varying shape factors.

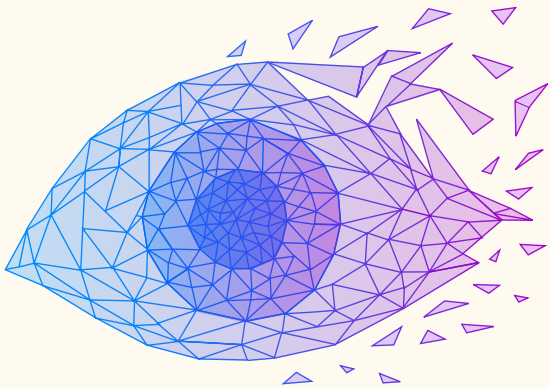
	Overall best model	Rounded down	Rounded up	Rounded up + 1
Median shape factor	2.3	2.0	3.0	4.0
Volume metrics				
Coverage [%]	98.1 (94.2 – 98.7)	94.9 (80.4 – 98.0)	98.5 (92.8 – 99.7)	99.0 (95.8 – 99.8)
Overestimation [%]	20.5 (5.7 – 59.9)	11.6 (1.9 – 51.2)	30.3 (12.8 – 64.1)	43.4 (26.9 – 84.8)
Distance metrics [mm]				
5th percentile surface distance	-0.23 (-0.46 – 0.06)	-0.44 (-1.70 – -0.20)	-0.08 (-0.51 – 0.31)	0.16 (-0.53 – 0.71)
Median surface distance	0.41 (0.14 – 0.87)	0.17 (-0.62 – 0.76)	0.65 (0.15 – 1.20)	0.97 (0.27 – 1.60)
95th percentile surface distance	1.10 (0.53 – 2.71)	0.88 (0.23 – 2.38)	1.47 (0.71 – 2.95)	1.84 (0.78 – 3.45)
Median absolute surface distance	0.42 (0.18 – 0.88)	0.34 (0.16 – 0.98)	0.65 (0.22 – 1.21)	0.97 (0.40 – 1.60)

Supplementary Table 6: Volume and distance metrics for three variations of shape factor from the overall best tumour models were calculated: rounded down, rounded up and rounded up plus one. Median and 5th-95th percentiles are shown.

Supplementary Table 7: Comparison of curved and plane projection

	Plane projection	Curved projection
Median shape factor	4.8 (2.8 – 8.2)	2.3 (1.8 – 3.5)
Volume metrics		
Coverage [%]	98.0 (93.7 – 98.5)	98.1 (94.6 – 98.4)
Overestimation [%]	20.5 (12.2 – 40.6)	14.8 (5.3 – 52.7)
Distance metrics [mm]		
5th percentile surface distance	-0.19 (-0.32 – -0.02)	-0.23 (-0.38 – -0.05)
Median surface distance	0.57 (0.34 – 1.02)	0.41 (0.17 – 0.97)
95th percentile surface distance	1.58 (0.93 – 2.62)	1.24 (0.53 – 2.73)
Median absolute surface distance	0.57 (0.35 – 1.02)	0.42 (0.19 – 1.00)

Median and 5th-95th percentile volume and distance metrics for the best standard models for patients who had both an acceptable model in the curved and plane projection. Performance metrics for the two projections were similar, but the required shape factor differed. The curved projection was used throughout this paper.



Chapter 6

Estimating uveal melanoma volume with ellipsoid tumour models

PhD project chapter

L. Klaassen, T.A. Ferreira, G.P.M. Luyten, J.W.M. Beenakker

Acta Ophthalmologica (2024). doi: 10.1111/aos.17492

ABSTRACT

Purpose: Ellipsoid tumour models are used to approximate the tumour volume of uveal melanomas, as the conventionally used ultrasound does not provide a three-dimensional visualisation of the tumour. However, these models are a simplification of the actual tumour geometry. The aim of this study was to determine to what extent several of these frequently used ellipsoid tumour models accurately describe uveal melanoma volume.

Methods: Tumours were delineated on contrast-enhanced T1-weighted MRI for 70 uveal melanoma patients. The MRI-delineated volume was compared to three ellipsoid models, which used two-dimensional measurements such as thickness and basal diameters as an input: half ellipsoids with round ($V_{\text{roundbase}}$) or oval base (V_{ovalbase}) and a paraboloid consisting of two parts, also incorporating the curvature of the eye wall (V_{twoparts}).

Results: Statistically significant relative differences between MRI-delineated and model volume of $53\pm 32\%$ ($V_{\text{roundbase}}$), $26\pm 24\%$ (V_{ovalbase}) and $15\pm 24\%$ (V_{twoparts}) were observed ($P < 0.001$). Tumour volume and shape did not influence the difference between the model volumes and MRI-delineated tumour volume.

Conclusion: All tumour models result in considerable systematic overestimations of tumour volume, with large variations in overestimation between patients. Adding the perpendicular basal diameter to the model decreases this variation. Although ellipsoid tumour models have shown to be valuable on a group level, they should be used with caution for individual patients.

INTRODUCTION

Uveal melanoma, although the most frequently occurring primary ocular malignancy in adults, is a rare disease with an incidence of about 2-10 per million per year, varying per region [1-3]. Despite the high local control after treatment of the primary tumour [4-6], 5-year survival is still relatively poor at 25% to 97% [7], depending on clinical, histopathological and genetic factors. As prognosis is important for patient counselling, several methods have been described to non-invasively estimate prognosis or metastatic risk, including tumour size [8]. Shields et al. [9] described a 5% increase in the 10-year risk of metastasis at each millimetre increase of tumour thickness. In another study, increasing basal diameter was associated with lower survival [10]. These two tumour measurements are complemented with factors such as ciliary body involvement in the frequently used AJCC TNM staging system [7, 11]. Furthermore, tumour volume has been described to be a better prognostic factor [12-17].

However, with conventional ophthalmic imaging methods, such as ultrasound, funduscopy or optical coherence tomography, tumour volume cannot be measured [18]. Several studies therefore propose tumour models using two-dimensional measurements, such as thickness and diameter, to estimate tumour volume. For example, Richtig et al. [12] proposed a half ellipsoid model in which the tumour thickness and largest basal diameter are used. Later studies added more measurements to further personalize these tumour models, such as the perpendicular basal diameter [14, 15] or eye diameter [16].

These studies assume that uveal melanomas can be described as a regularly shaped ellipsoid. However, several studies show that uveal melanomas not only appear in the common dome shape, but also in bilobated, overhanging or mushroom configurations [19-21]. Therefore, the aforementioned ellipsoid tumour models are a simplification of tumour geometry and may therefore not be accurate, influencing prognosis estimation.

With the introduction of ocular MRI in the clinical care of uveal melanoma patients, a non-invasive method of three-dimensional tumour imaging has become available [18, 21, 22]. High-resolution sequences enable more accurate methods for measuring tumour thickness, diameters, and clip-tumour distances than conventional ophthalmic imaging has been able to [19, 20, 23, 24]. Furthermore, isotropic sequences enable three-dimensional (3D) tumour delineations [25, 26].

The aim of this study was to determine to what extent several frequently used ellipsoid tumour models can approximate uveal melanoma volume measured on MRI.

METHODS

Patient population

For this study, data from two existing cohorts was analysed retrospectively.

For the first cohort, all UM patients who received an MRI between May 2019 and March 2021 as part of clinical care or in the context of a scientific study were evaluated retrospectively. Patients in this cohort with tumours with a thickness below 7 mm were generally treated with ^{106}Ru brachytherapy (apex dose 130 GyE), whereas larger tumours and juxtapapillary tumours were treated with proton beam therapy (tumour dose 60 GyE) or enucleation [4, 27]. Patients from this cohort were included if they had a primary tumour without extrascleral extension. Patients for whom the tumour extent could not be assessed accurately on MRI, according to the report of a neuroradiologist with over 20 years of experience, were excluded. Furthermore, for patients who underwent tumour endoresection after primary treatment, the scan after treatment was excluded.

The second cohort consisted of 14 patients who underwent MRI-scans before proton beam therapy in the context of a separate prospective scientific study between November 2022 and February 2024.

Both studies were conducted after approval of the local ethics committee (METC Leiden-Den Haag-Delft, NL73433.058.20 and NL57130.058.16), in accordance with the Declaration of Helsinki.

MRI acquisition and analysis

Tumours were delineated on the 3D contrast-enhanced T1-weighted scans (Figure 1), with the 3D non-contrast-enhanced T1-weighted scan and 3D T2-weighted scans used as a reference to distinguish tumour from surrounding structures. These MRI-scans were acquired with a 3 tesla MRI scanner (Ingenia Elition, Philips Healthcare, the Netherlands) with a 4.7 cm surface receive coil (Philips Healthcare), using an earlier described protocol [19, 23]. The MRI-scans had an acquisition voxel size of $0.8 \times 0.8 \times 0.8 \text{ mm}^3$, a reconstruction voxel size of $0.4 \times 0.4 \times 0.4 \text{ mm}^3$ and the contrast-enhanced T1-weighted scan were acquired in 2 minutes and 7 seconds.

Tumour delineation was performed by one observer (LK) and the contours were verified, and if necessary corrected, by an ophthalmic MRI expert (JWB) with 10+ years of experience, based on the clinical evaluation by a neuroradiologist with over 20 years of experience.

Tumour thickness, largest basal diameter (LBD) and perpendicular basal diameter (PBD) were computed automatically based on the 3D tumour contours according to a previously published method [24]. These MRI measurements were used as inputs for the tumour models.

Tumour shape was assessed visually and classified as regular (dome-shaped or flat lesions) or irregular (mushroom-shaped or bilobated lesions). In general, tumour shape was taken from the radiology report. Tumours for which the shape was not mentioned in the radiology report were independently assessed by two observers (LK and JWB), and disagreements were discussed in a consensus meeting.

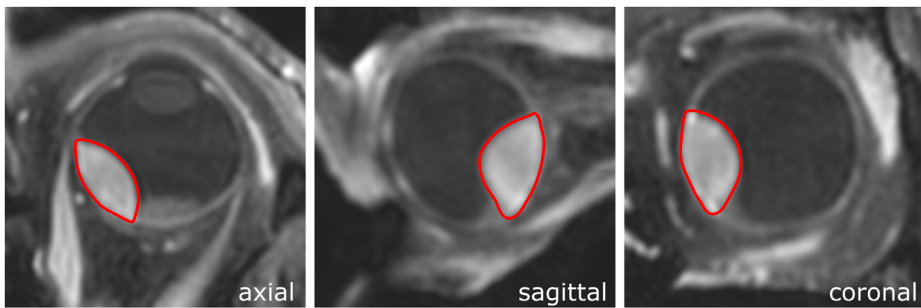


Figure 1: Tumour delineation (red contour) was performed on 3D contrast-enhanced T1-weighted MRI.

Tumour models

The volume of the delineated tumours was compared to the volume calculated with three frequently used tumour models, based on the thickness and basal diameters of the MRI delineation (Figure 2). The most straightforward model, the half ellipsoid with round base ($V_{\text{roundbase}}$), uses tumour thickness and largest basal diameter to approximate tumour volume. First described by Richtig et al. [12], this model is used for prognosis, growth rate estimation and treatment response assessment [28-31].

Other studies propose a half ellipsoid with oval base (V_{ovalbase}). This model uses both the largest basal diameter and the perpendicular basal diameter and is used for prognosis and treatment planning comparisons [14, 15, 32-35].

The most extensive model compared in this study is the paraboloid with two parts (V_{twoparts}). This model assumes the tumour consists of a paraboloid, comparable to the half ellipsoid in the previously mentioned formulas, and a spherical cap approximating the curvature of the eye. Variations of this model are applied in the context of

comparison to new treatment planning and diagnostic techniques [25, 36] and prognosis [16]. The model compared in this study was proposed by Caminal et al. [36]. In this study, the radius of the eye was assumed to be 12 mm [37].

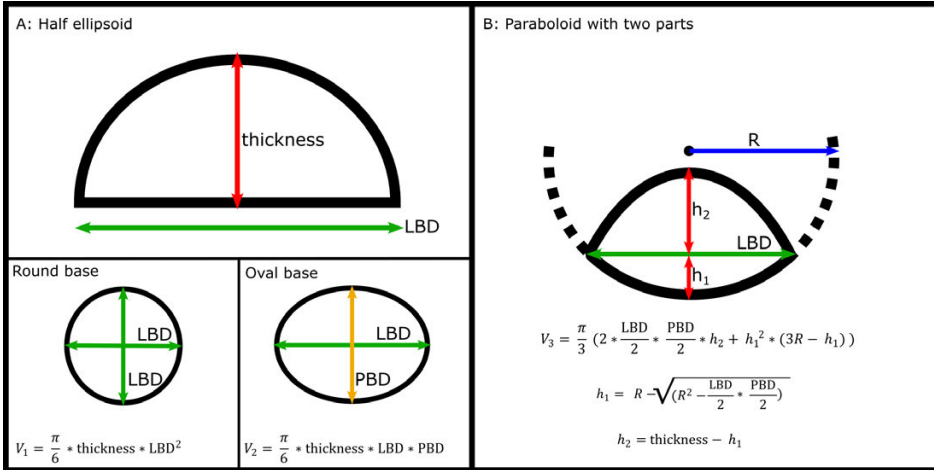


Figure 2: Models for calculation of uveal melanoma tumour volume. Thickness, LBD and PBD are determined automatically based on the MRI contours. (A) The two ellipsoid tumour models with their respective interpretations of the tumour base. (B) The paraboloid model with two parts R: eye radius, assumed to be 12 mm [37]; $h_1 = \sqrt{R^2 - LBD/2 * SBD/2}$; $h_2 = thickness - h_1$.

Statistics

All three tumour models were compared to the MRI-delineated tumour volume. Mean differences and mean absolute differences were determined. Model volumes were compared to the MRI-delineated tumour volume using two-tailed paired t-tests or Wilcoxon signed rank tests, depending on the results of the Shapiro-Wilks test for normality. This analysis was repeated for all three models and for the group before treatment, the group after treatment and the entire cohort, resulting in 9 comparisons. Therefore, the significance level was adjusted using a Bonferroni correction, resulting in a significance level of $P < 0.0056$.

To assess whether tumour shape influenced the difference between the MRI-delineated and estimated tumour volume, the difference between the regular and irregular tumour shapes was determined in a multiple linear regression, also taking tumour volume into account.

RESULTS

From the retrospective cohort, 60 patients were assessed for the inclusion and exclusion criteria. 4 patients were excluded: 1 had extrascleral extensions and

3 were evaluated to assess possible tumour recurrences. One patient underwent endoresection in between the pre-treatment and post-treatment scan, and therefore the post-treatment scan was excluded from this study.

Including 14 patients of the prospective cohort, in total 70 patients were included in this study. For 35/70 patients, both pre-treatment and post-treatment scans were available, resulting in 105 scans. The majority received proton beam therapy (64%), while 23% received brachytherapy and 11% underwent enucleation.

Before treatment

Average (\pm standard deviation) tumour volume on MRI before treatment was 567 ± 415 mm³ (range 33-1663 mm³). Average thickness, LBD and PBD were 6.4 ± 3.0 mm (range 1.3-12.9 mm), 15.0 ± 3.7 mm (range 7.2-22.4 mm) and 12.5 ± 3.1 mm (range 6.0-20.9 mm), respectively. AJCC TNM [11] was as follows: T1: 13%, T2: 14%, T3: 50%, T4: 23%.

On average, all tumour models resulted in a significant overestimation of the tumour volume (Wilcoxon signed rank tests, all $P < 0.001$): the model volume was larger than the MRI-delineated volume in 97%, 89% and 84%, for $V_{\text{roundbase}}$, V_{ovalbase} and V_{twoparts} , respectively. Mean differences between the model and the MRI volume were smallest for the paraboloid model with two parts, which resulted in an average overestimation of 16 ± 23 % (V_{twoparts} , Table 1). This model also resulted in the smallest variation in overestimation between patients. Between the two ellipsoid models, the model that incorporated the PBD (V_{ovalbase}) performed best, with an overestimation of 282 ± 22 %. The largest differences between the model and the MRI tumour volume were observed for the ellipsoid with the round base ($V_{\text{roundbase}}$), with an average overestimation of 53 ± 30 %, corresponding to the largest variation between patients. All differences between the tumour models and the MRI tumour volume are shown in Table 1 and Figure 3. An example of all three tumour models and the MRI delineation for tumours with a regular (dome) shape and an irregular (mushroom) shape are shown in Figure 4.

After treatment

For the 35 patients with scans before and after treatment, average tumour volume did not change after treatment (511 ± 354 mm³ versus 456 ± 409 mm³, $P = 0.07$). Tumour model performance was similar to the pre-treatment group (Table 1).

Effect of tumour volume and shape

In a multiple linear regression, tumour volume and tumour shape did not have a statistically significant effect on the relative difference between the model volumes and MRI-delineated tumour volume for all tumour models (Supplementary Table 1).

Table 1: Mean difference between tumour models and MRI volume.

	Mean difference between tumour models and MRI-delineated volume \pm SD (range)								
	Before treatment (n=70)		After treatment (n=35)		Entire cohort (n=105)				
	Volume [mm ³]	Relative [%]	p-value	Volume [mm ³]	Relative [%]	p-value			
V _{roundbase}	303 \pm 254 (-52 - 975)	53 \pm 30 (-18 - 129)	<0.001	265 \pm 258 (-19 - 1070)	54 \pm 35 (-28 - 133)	<0.001	291 \pm 256 (-53 - 1070)	53 \pm 32 (-29 - 133)	<0.001
V _{ovalbase}	163 \pm 151 (-128 - 651)	28 \pm 22 (-44 - 78)	<0.001	123 \pm 124 (-27 - 433)	23 \pm 29 (-45 - 108)	<0.001	150 \pm 144 (-128 - 651)	26 \pm 24 (-45 - 108)	<0.001
V _{twoparts}	101 \pm 128 (-252 - 550)	16 \pm 23 (-69 - 69)	<0.001	79 \pm 99 (-41 - 351)	12 \pm 27 (-50 - 92)	<0.001	94 \pm 120 (-252 - 550)	15 \pm 24 (-69 - 92)	<0.001

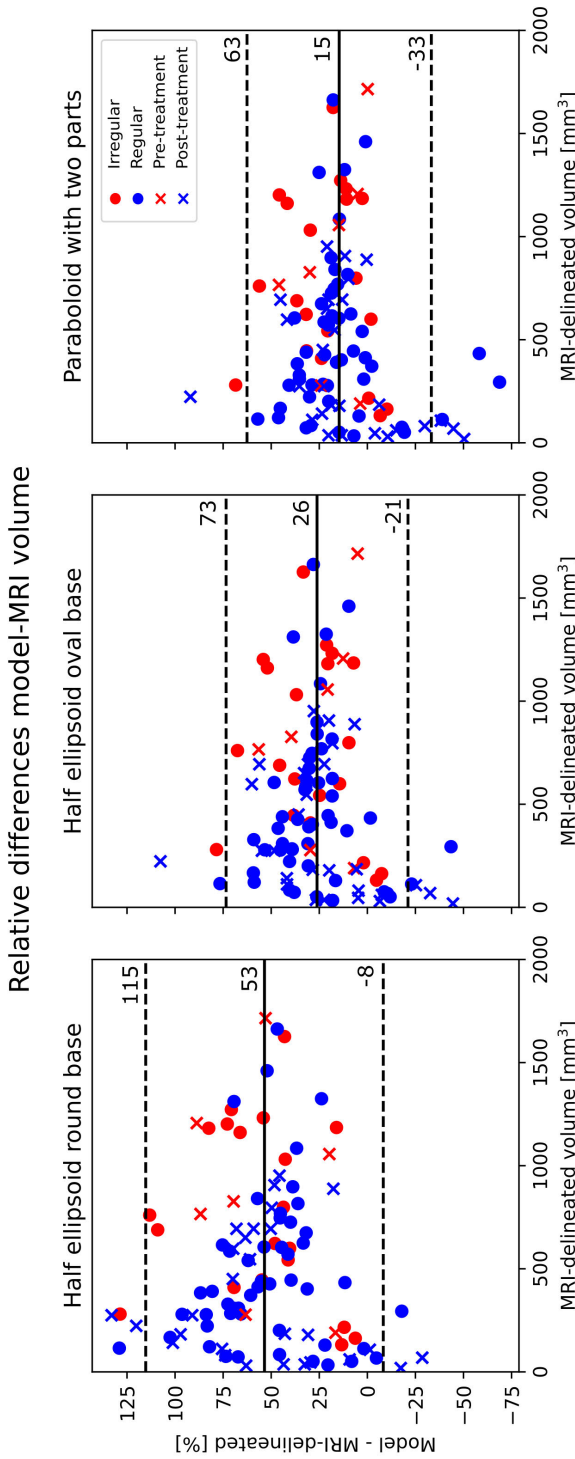


Figure 3: Differences between the calculated tumour volume with 3 tumour models and the MRI-delineated tumour volume. Mean (solid line) and confidence intervals (dashed line) are shown for the entire cohort.

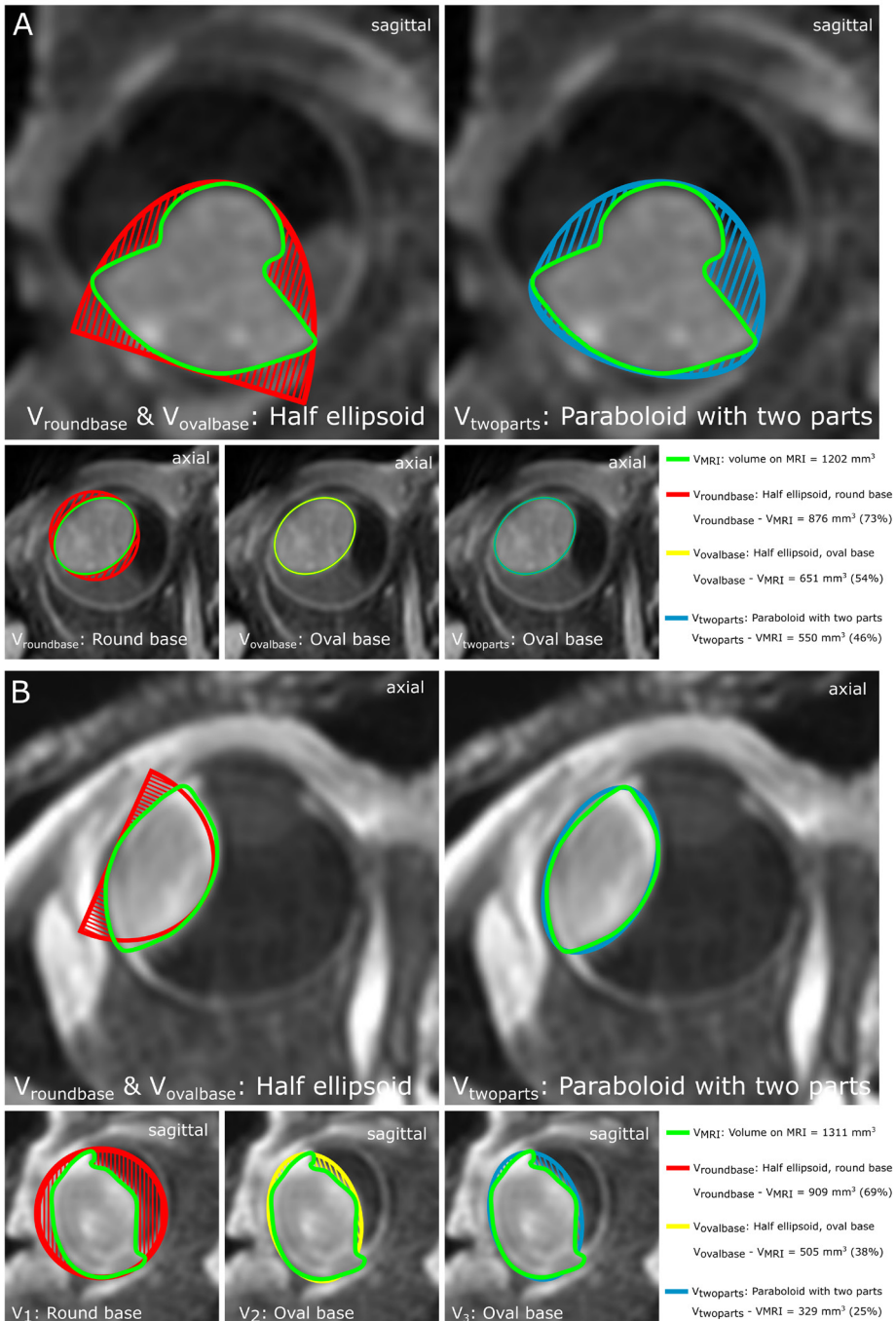


Figure 4: Two examples of the three tumour models and the MRI contours for patients with an irregular (mushroom) shape (A) and with a regular (dome) shape (B). Green: MRI tumour

contours, red: half ellipsoid with round base, yellow: half ellipsoid with oval base, blue: paraboloid with two parts.

DISCUSSION

Ellipsoid tumour models are used to determine uveal melanoma volume to estimate prognosis, to compare tumour volumes to other modalities and to perform treatment planning comparisons. In this study, we show that frequently used methods result in considerable systematic overestimations of the MRI-delineated tumour volume and large variation in overestimation between patients.

All tumour models resulted in systematic overestimations of the MRI-delineated tumour volume, which was smallest in the paraboloid with two parts (15%). This model also had the smallest variation between patients (SD: 24%), although comparable to the ellipsoid with oval base (SD: 24%), for which a larger mean overestimation was observed.

The paraboloid with two parts may be further improved by measuring the radius of the eye instead of taking a population average, as was done in this study. However, decreasing or increasing the radius by 1 mm [38] resulted in a volume change of 0.5%, suggesting this improvement would have limited effect. Furthermore, using a population average, this method can be used by only measuring the thickness and two basal diameters, making it easily applicable in routine clinical care and in retrospective studies. The half ellipsoid with round base ($V_{\text{roundbase}}$) resulted in the largest overestimation and largest variation in overestimation within the cohort. An improvement of this model was proposed by Stalhammar et al. [13], adjusting the perpendicular diameter to 85% of the largest basal diameter. Although in our cohort this proportion between largest and perpendicular diameter was similar, this adjustment does not decrease the large variation between patients.

Although dome-shaped tumours are the most frequently occurring tumour shape, uveal melanoma may appear in several shapes, especially after breaking through Bruch's membrane [19, 21]. Although not significant, the effect of tumour shape was largest in the half ellipsoid with round base and smallest in the paraboloid with two parts. Arnljots et al. used the second theorem of Pappus to estimate tumour volume by determining the surface area of two halves of enucleated tumours on histology slices [39], which might result in a more accurate volume estimation in enucleated eyes than the ellipsoid tumour models in this paper, especially for tumours with an irregular shape.

One previous study compared the MRI tumour volume with the half ellipsoid with oval base [35]. However, this study aimed to compare MRI and ultrasound tumour volume and therefore used the ultrasound measurements for the model, making it difficult to directly compare the results. However, in both this study and in our cohort, the model volume was larger than the MRI tumour volume. Although previous studies show that on average ultrasound measurements agree with MRI measurements, the latter are more accurate in anteriorly located tumours, especially if not the entire tumour extent is visible in the ultrasound images [22]. Therefore, using ultrasound measurements for tumour volume estimation would result in even more patient-specific variation.

More accurate estimation of tumour volume may contribute to improved prediction of metastasis and survival. Despite it being an important factor, frequently used models result in an overestimation of the tumour volume and the amount of overestimation significantly between patients. Here, systematic overestimations will likely not affect the accuracy of prognosis estimation, since patients with similarly sized tumours will remain equally sized. However, the large variation between patients will likely heavily influence the results. For example, two tumours from our cohort with a comparable volume on MRI of 1181 and 1185 mm³ had model volumes of 2156 and 1375 mm³ ($V_{\text{roundbase}}$). According to Stalhammar et al., who adjusted the ellipsoid with round base by a factor of 0.85, these two tumours would be categorized as V3 and V4, corresponding to an increase in hazard ratio of 2.32 for metastatic death [13]. Similarly, the AJCC classification, which uses thickness and largest diameter to estimate prognosis [7, 11], might not be an optimal representation of tumour load. All in all, this shows that models using two or three tumour dimension measurements might offer valuable estimations on a group level, but on an individual level, and that therefore a more accurate determination of tumour volume might improve prognosis estimation.

Beside prognosis, ellipsoid tumour models are also used in treatment response assessment of uveal melanoma. In this study, we show that model performance is similar before and after treatment, although tumour volume often has not decreased in size at the time of the first follow-up MRI scan [40].

This study shows that using the best-performing tumour model decreases systematic errors in tumour volume estimation and halves the variation between patients. In the future, three-dimensional imaging may become more widely available, for example due to the increase in image-guided ocular radiotherapy [41, 42], resulting in precise measurements of tumour volume instead of estimations. We hypothesize that using delineated tumour volume as a prognostic tool may improve prognosis estimation,

similar to other tumour sites [43-45]. However, future analyses using survival data in larger cohorts should be performed.

Limitations

Due to the retrospective design of this study, a bias might exist towards larger tumours, as in our centre these patients undergo standard MR exams to prepare for proton therapy, whereas patients with smaller tumours do not. Therefore, the number of patients receiving proton beam therapy in this cohort is larger than on average in our centre.

In this study, we assessed how well ellipsoid models can describe volume for uveal melanomas, which typically not all have an ellipsoidal configuration. In this context we used a three-dimensional delineation of the tumour, based on MR-images, as ground truth volume. We acknowledge that this method has its limitations, as flat extensions might be missed [21, 22]. Nevertheless, earlier studies showed that MRI provides a geometrically accurate representation of the tumour [46], and that MR-based prominence and basal diameter measures typically correspond well with ultrasound measurements [22, 24], upon which most current staging methods, such as the AJCC classification, are mostly based [47]. Future improvements in MRI delineations may be achieved by combining MRI with optical methods such as fundoscopy [48], which may aid in accurately including thin lesions and flat tumour extensions. This is particularly relevant for 9 out of 70 patients in this study with a flat lesion of which the tumour extent was more difficult to assess on MRI. However, as the tumour model was based on the dimensions of the MRI delineation, slight inaccuracies in delineation would influence both the MRI-delineated volume and the tumour model in the same way and therefore not impact the reported differences.

Conclusion

All ellipsoid tumour models result in considerable systematic overestimations of tumour volume, with large variations in overestimation between patients. Adding the perpendicular basal diameter to the model decreases the variation between patients. Although ellipsoid tumour models have shown to be valuable on a group level, they should be used with caution on an individual level.

Supplementary Table 1: Effect of true volume and tumour shape on difference between model volume and true volume

	Regression coefficient \pm SD (P-value)		
	$V_{\text{roundbase}}$	V_{ovalbase}	V_{twoparts}
Intercept	57.9 \pm 7.5	27.3 \pm 5.7	19.1 \pm 5.8
MRI volume [mm ³]	P<0.001	P<0.001	P=0.001
Shape (1: regular, 0: irregular)	-0.03 \pm 0.11	-0.01 \pm 0.08	-0.03 \pm 0.08
	P=0.74	P=0.89	P=0.70
	-3.5 \pm 7.3	-2.4 \pm 5.6	-8.3 \pm 5.63
	P=0.63	P=0.68	P=0.14

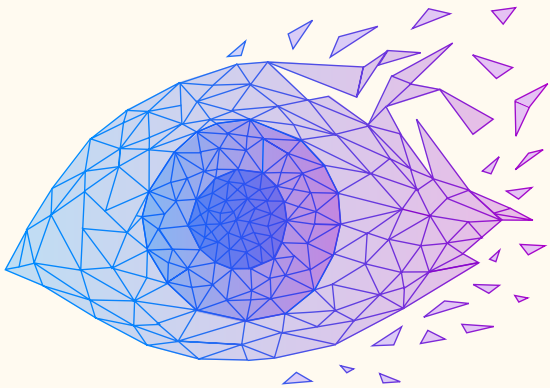
Supplementary Table 1: Multiple linear regression for the difference between model volume and true tumour volume for all patients and all timepoints. Tumour volume and shape do not have a significant effect on the difference between model volume and true tumour volume.

REFERENCES

1. Jager MJ, Shields CL, Cebulla CM, Abdel-Rahman MH, Grossniklaus HE, Stern MH, et al. Uveal melanoma. *Nat Rev Dis Primers*. 2020;6:24. doi: 10.1038/s41572-020-0158-0.
2. Hou X, Rokohl AC, Li X, Guo Y, Ju X, Fan W, et al. Global incidence and prevalence in uveal melanoma. *Adv Ophthalmol Pract Res*. 2024;4:226-32. doi: 10.1016/j.aopr.2024.10.001.
3. Wu M, Yavuziyigitoglu S, Brosens E, Ramdas WD, Kilic E, Rotterdam Ocular Melanoma Study G. Worldwide Incidence of Ocular Melanoma and Correlation With Pigmentation-Related Risk Factors. *Invest Ophthalmol Vis Sci*. 2023;64:45. doi: 10.1167/iovs.64.13.45.
4. Marinkovic M, Pors LJ, van den Berg V, Peters FP, Schalenbourg A, Zografos L, et al. Clinical Outcomes after International Referral of Uveal Melanoma Patients for Proton Therapy. *Cancers (Basel)*. 2021;13. doi: 10.3390/cancers13246241.
5. Mishra KK, Daftari IK. Proton therapy for the management of uveal melanoma and other ocular tumors. *Chin Clin Oncol*. 2016;5:50. doi: 10.21037/cco.2016.07.06.
6. Buonanno F, Conson M, de Almeida Ribeiro C, Oliviero C, Itta F, Liuzzi R, et al. Local tumor control and treatment related toxicity after plaque brachytherapy for uveal melanoma: A systematic review and a data pooled analysis. *Radiother Oncol*. 2022;166:15-25. doi: 10.1016/j.radonc.2021.11.007.
7. Force AOOT. International Validation of the American Joint Committee on Cancer's 7th Edition Classification of Uveal Melanoma. *JAMA Ophthalmol*. 2015;133:376-83. doi: 10.1001/jamaophthalmol.2014.5395.
8. Kaliki S, Shields CL, Shields JA. Uveal melanoma: estimating prognosis. *Indian J Ophthalmol*. 2015;63:93-102. doi: 10.4103/0301-4738.154367.
9. Shields CL, Furuta M, Thangappan A, Nagori S, Mashayekhi A, Lally DR, et al. Metastasis of uveal melanoma millimeter-by-millimeter in 8033 consecutive eyes. *Arch Ophthalmol*. 2009;127:989-98. doi: 10.1001/archophthalmol.2009.208.
10. Kujala E, Makitie T, Kivela T. Very long-term prognosis of patients with malignant uveal melanoma. *Invest Ophthalmol Vis Sci*. 2003;44:4651-9. doi: 10.1167/iovs.03-0538.
11. Kivelä T, Simpson RE, Grossniklaus HE, al. Uveal melanoma. *AJCC Cancer Staging Manual* 8th ed. 8th edition. New York, NY: Springer; 2016. p. 805-17.
12. Richtig E, Langmann G, Mullner K, Richtig G, Smolle J. Calculated tumour volume as a prognostic parameter for survival in choroidal melanomas. *Eye (Lond)*. 2004;18:619-23. doi: 10.1038/sj.eye.6700720.
13. Stalhammar G, Coupland SE, Ewens KG, Ganguly A, Heimann H, Shields CL, et al. Improved Staging of Ciliary Body and Choroidal Melanomas Based on Estimation of Tumor Volume and Competing Risk Analyses. *Ophthalmology*. 2024;131:478-91. doi: 10.1016/j.ophtha.2023.10.026.
14. Gass JD. Comparison of prognosis after enucleation vs cobalt 60 irradiation of melanomas. *Arch Ophthalmol*. 1985;103:916-23. doi:
15. Char DH, Kroll S, Phillips TL. Uveal melanoma. Growth rate and prognosis. *Arch Ophthalmol*. 1997;115:1014-8. doi: 10.1001/archophth.1997.01100160184007.
16. Li W, Gragoudas ES, Egan KM. Tumor basal area and metastatic death after proton beam irradiation for choroidal melanoma. *Arch Ophthalmol*. 2003;121:68-72. doi: 10.1001/archophth.121.1.68.
17. Hagstrom A, Witzzenhausen H, Stalhammar G. Tailoring surveillance imaging in uveal melanoma based on individual metastatic risk. *Can J Ophthalmol*. 2024. doi: 10.1016/j.jcjo.2024.07.014.
18. Solnik M, Padaszynska N, Czarnecka AM, Synoradzki KJ, Yousef YA, Choragiewicz T, et al. Imaging of Uveal Melanoma-Current Standard and Methods in Development. *Cancers (Basel)*. 2022;14. doi: 10.3390/cancers14133147.

19. Ferreira TA, Jaarsma-Coes MG, Marinkovic M, Verbist B, Verdijk RM, Jager MJ, et al. MR imaging characteristics of uveal melanoma with histopathological validation. *Neuroradiology*. 2022;64:171-84. doi: 10.1007/s00234-021-02825-5.
20. Jaarsma-Coes MG, Ferreira TA, Marinkovic M, Vu THK, van Vught L, van Haren GR, et al. Comparison of Magnetic Resonance Imaging-Based and Conventional Measurements for Proton Beam Therapy of Uveal Melanoma. *Ophthalmol Retina*. 2023;7:178-88. doi: 10.1016/j.oret.2022.06.019.
21. Foti PV, Travali M, Farina R, Palmucci S, Spatola C, Raffaele L, et al. Diagnostic methods and therapeutic options of uveal melanoma with emphasis on MR imaging-Part I: MR imaging with pathologic correlation and technical considerations. *Insights Imaging*. 2021;12:66. doi: 10.1186/s13244-021-01000-x.
22. Jaarsma-Coes MG, Klaassen L, Marinkovic M, Luyten GPM, Vu THK, Ferreira TA, et al. Magnetic Resonance Imaging in the Clinical Care for Uveal Melanoma Patients-A Systematic Review from an Ophthalmic Perspective. *Cancers (Basel)*. 2023;15. doi: 10.3390/cancers15112995.
23. Ferreira TA, Grech Fonk L, Jaarsma-Coes MG, van Haren GGR, Marinkovic M, Beenakker JM. MRI of Uveal Melanoma. *Cancers (Basel)*. 2019;11. doi: 10.3390/cancers11030377.
24. Klaassen L, Jaarsma-Coes MG, Verbist BM, Vu THK, Marinkovic M, Rasch CRN, et al. Automatic Three-Dimensional Magnetic Resonance-based measurements of tumour prominence and basal diameter for treatment planning of uveal melanoma. *Phys Imaging Radiat Oncol*. 2022;24:102-10. doi: 10.1016/j.phro.2022.11.001.
25. Daftari I, Aghaian E, O'Brien JM, Dillon W, Phillips TL. 3D MRI-based tumor delineation of ocular melanoma and its comparison with conventional techniques. *Med Phys*. 2005;32:3355-62. doi: 10.1118/1.2068927.
26. Jaarsma-Coes MG, Klaassen L, Verbist BM, Vu THK, Klaver YLB, Rodrigues MF, et al. Inter-Observer Variability in MR-Based Target Volume Delineation of Uveal Melanoma. *Adv Radiat Oncol*. 2023;8:101149. doi: 10.1016/j.adro.2022.101149.
27. Marinkovic M, Horeweg N, Fiocco M, Peters FP, Sommers LW, Laman MS, et al. Ruthenium-106 brachytherapy for choroidal melanoma without transpupillary thermotherapy: Similar efficacy with improved visual outcome. *Eur J Cancer*. 2016;68:106-13. doi: 10.1016/j.ejca.2016.09.009.
28. Gillam M, Fenech GA, Chadwick O, Nairn J, Chadha V, Connolly J, et al. When Is the Optimum Radiological Response to Proton Beam Therapy in Uveal Melanoma? *Ocul Oncol Pathol*. 2023;9:130-7. doi: 10.1159/000533308.
29. Uner OE, See TRO, Szalai E, Grossniklaus HE, Stalhammar G. Estimation of the timing of BAP1 mutation in uveal melanoma progression. *Sci Rep*. 2021;11:8923. doi: 10.1038/s41598-021-88390-6.
30. Augsburger JJ, Gonder JR, Amsel J, Shields JA, Donoso LA. Growth rates and doubling times of posterior uveal melanomas. *Ophthalmology*. 1984;91:1709-15. doi: 10.1016/s0161-6420(84)34088-x.
31. Singh AD. Uveal melanoma: implications of tumor doubling time. *Ophthalmology*. 2001;108:829-31. doi: 10.1016/s0161-6420(00)00607-2.
32. Furdova A, Babal P, Kobzova D, Zahorjanova P, Kapitanova K, Sramka M, et al. Uveal melanoma survival rates after single dose stereotactic radiosurgery. *Neoplasma*. 2018;65:965-71. doi: 10.4149/neo_2018_171209N808.
33. Studenski MT, Patel NV, Markoe A, Harbour JW, Samuels SE. Influence of tumor shape and location in eye plaque brachytherapy dosimetry. *Brachytherapy*. 2020;19:249-54. doi: 10.1016/j.brachy.2020.01.001.

34. Tien CJ, Astrahan MA, Kim JM, Materin M, Chen Z, Nath R, et al. Incorporating patient-specific CT-based ophthalmic anatomy in modeling iodine-125 eye plaque brachytherapy dose distributions. *Brachytherapy*. 2017;16:1057-64. doi: 10.1016/j.brachy.2017.06.014.
35. Furdova A, Furda R, Sramka M, Chorvath M, Rybar J, Vesely P, et al. Stereotactic irradiation on linear accelerator - ultrasound versus MRI in choroidal melanoma volume calculation. *BMC Ophthalmol*. 2022;22:333. doi: 10.1186/s12886-022-02558-w.
36. Caminal JM, Mejia K, Arias L, Masuet-Aumatell C, Larrucea-Maseda J, Modolell I, et al. Tumor Volumes in Choroidal Melanoma: Agreement Between Three-Dimensional Ultrasound and Two Mathematical Models. *Am J Ophthalmol*. 2016;166:181-8. doi: 10.1016/j.ajo.2016.03.046.
37. Escudero-Sanz I, Navarro R. Off-axis aberrations of a wide-angle schematic eye model. *J Opt Soc Am A Opt Image Sci Vis*. 1999;16:1881-91. doi: 10.1364/josaa.16.001881.
38. van Vught L, Shamonin DP, Luyten GPM, Stoel BC, Beenakker JM. MRI-based 3D retinal shape determination. *BMJ Open Ophthalmol*. 2021;6:e000855. doi: 10.1136/bmjophth-2021-000855.
39. Arnljots TS, Al-Sharbaty Z, Lardner E, All-Eriksson C, Seregard S, Stalhammar G. Tumour thickness, diameter, area or volume? The prognostic significance of conventional versus digital image analysis-based size estimation methods in uveal melanoma. *Acta Ophthalmol*. 2018;96:510-8. doi: 10.1111/aos.13668.
40. Tang MCY, Ferreira TA, Marinkovic M, Jaarsma-Coes MG, Klaassen L, Vu THK, et al. MR-based follow-up after brachytherapy and proton beam therapy in uveal melanoma. *Neuroradiology*. 2023;65:1271-85. doi: 10.1007/s00234-023-03166-1.
41. Hrbacek J, Kacperek A, Beenaker JM, Mortimer L, Denker A, Mazal A, et al. PTCOG Ocular Statement: Expert Summary of Current Practices and Future Developments in Ocular Proton Therapy. *Int J Radiat Oncol Biol Phys*. 2024. doi: 10.1016/j.ijrobp.2024.06.017.
42. Hrbacek J, Mishra KK, Kacperek A, Dendale R, Nauraye C, Auger M, et al. Practice Patterns Analysis of Ocular Proton Therapy Centers: The International OPTIC Survey. *Int J Radiat Oncol Biol Phys*. 2016;95:336-43. doi: 10.1016/j.ijrobp.2016.01.040.
43. Duran AO, Inanc M, Bozkurt O, Ozaslan E, Ozkan M. Tumor Volume Is a Better Prognostic Factor than Greatest Tumor Diameter in Operated Stage I-III Non-Small-Cell Lung Cancer. *Clin Lung Cancer*. 2023;24:252-9. doi: 10.1016/j.clcc.2023.02.009.
44. Studer G, Lutolf UM, El-Bassiouni M, Rousson V, Glanzmann C. Volumetric staging (VS) is superior to TNM and AJCC staging in predicting outcome of head and neck cancer treated with IMRT. *Acta Oncol*. 2007;46:386-94. doi: 10.1080/02841860600815407.
45. Thoenissen P, Engelmann T, Heselich A, Winkelmann R, Burck I, Sader R, et al. MRI tumour volumetry as a new staging tool in diagnosis and therapy of oral cancer. *J Craniomaxillofac Surg*. 2024;52:1140-7. doi: 10.1016/j.jcms.2024.03.012.
46. Klaassen L, Haasjes C, Hol M, Cambraia Lopes P, Spruijt K, van de Steeg-Henzen C, et al. Geometrical accuracy of magnetic resonance imaging for ocular proton therapy planning. *Phys Imaging Radiat Oncol*. 2024;31:100598. doi: 10.1016/j.phro.2024.100598.
47. Shields CL, Kaliki S, Furuta M, Fulco E, Alarcon C, Shields JA. American Joint Committee on Cancer Classification of Uveal Melanoma (Anatomic Stage) Predicts Prognosis in 7,731 Patients: The 2013 Zimmerman Lecture. *Ophthalmology*. 2015;122:1180-6. doi: 10.1016/j.ophtha.2015.01.026.
48. Haasjes C, Vu THK, Beenakker JM. Patient-specific mapping of fundus photographs to three-dimensional ocular imaging. *Med Phys*. 2024. doi: 10.1002/mp.17576.



Chapter 7

Quantitative Perfusion-Weighted Magnetic Resonance Imaging in Uveal Melanoma

PhD project chapter

L. Klaassen, M.G. Jaarsma-Coes, M. Marinkovic, G.P.M. Luyten
C.R.N. Rasch, T.A. Ferreira, J.W.M. Beenakker

Investigative Ophthalmology & Visual Science (2024). doi: 10.1167/iovs.65.11.17.

ABSTRACT

Purpose

Perfusion-weighted imaging (PWI; magnetic resonance imaging [MRI]) has been shown to provide valuable biological tumor information in uveal melanoma (UM). Clinically used semiquantitative methods do not account for tumor pigmentation and eye movement. We hypothesize that a quantitative PWI method that incorporates these, provides a more accurate description of tumor perfusion than the current clinical method. The aim of this study was to test this in patients with UM before and after radiotherapy.

Methods

Perfusion-weighted 3T MRIs were retrospectively analyzed in 47 patients with UM before and after radiotherapy. Tofts pharmacokinetic modeling was performed to determine vascular permeability (K^{trans}), extracellular extravascular space (v_e), and reflux rate (k_{ep}). These were compared with semiquantitative clinical parameters including peak intensity and outflow percentage.

Results

The effect of tumor pigmentation on peak intensity and outflow percentage was statistically significant ($P < 0.01$) and relative peak intensity was significantly different between melanotic and amelanotic tumors (1.5 vs. 1.9, $P < 0.01$). Before radiotherapy, median tumor K^{trans} was 0.63 min^{-1} (range = $0.06\text{--}1.42 \text{ min}^{-1}$), median v_e was 0.23 (range = $0.09\text{--}0.63$), and median k_{ep} was 2.3 min^{-1} (range = $0.6\text{--}5.0 \text{ min}^{-1}$). After radiotherapy, 85% showed a decrease in K^{trans} and k_{ep} ($P < 0.01$). Changes in tumor pigmentation before and after radiotherapy were small and not significant (median increase in T1 of 33 ms, $P = 0.55$).

Conclusions

Quantitative PWI parameters decreased significantly after radiotherapy and can therefore serve as an early biomarker for treatment response assessment. However, due to the nonsignificant changes in tumor pigmentation before and after radiotherapy, the current semiquantitative method appears to be sufficiently sensitive for detection of changes in tumor perfusion.

INTRODUCTION

Uveal melanoma (UM) is the most frequently occurring primary intraocular malignancy in adults [1]. In the clinical care for UM patients, magnetic resonance imaging (MRI) is increasingly being used [2, 3]. In addition to three-dimensional high-resolution anatomical images, dedicated functional sequences can provide tumor biomarkers for differential diagnosis and response assessment [4-6]. In this context, perfusion-weighted MRI (PWI) is a technique that can obtain information on the tumor perfusion by administering an intravenous contrast agent while continuously imaging the eye, to visualize the arrival, uptake and outflow of the contrast agent (Figure 1).

In clinical practice a semi-quantitative PWI analysis is generally performed [7], in which a representative region of interest (ROI) is drawn in one or several of the slices. By showing the average signal intensities of the ROI on each of the time points, a time intensity curve (TIC) is obtained. From this time-intensity curve, tumor parameters such as shape of the curve (e.g. a wash-out curve), relative peak intensity and outflow percentage can be derived. These semi-quantitative parameters have shown to be valuable for differential diagnosis [7, 8], prognosis [9] and early response assessment [10] of UM.

For other tumor sites, the more quantitative pharmacokinetic modeling (PKM) has shown to provide a more accurate description of the tumor's perfusion characteristics, as the exchange of contrast agent from the blood to the tissue's extracellular extravascular space is quantified [11-15]. The Tofts model is one of the most commonly used methods to perform PKM of MRI perfusion data [16, 17] [18, 19]. In this model, the transfer rate of gadolinium from blood plasma to (tumor) tissue is modelled by K^{trans} , which depends on the vascular permeability, while v_e describes the fraction of extracellular extravascular space. For each voxel these quantities can be obtained. From these quantitative parameters, k_{ep} , the reflux rate at which the gadolinium is transferred back into the vasculature, can be derived.

Recently, Jaarsma et al. [18] adapted this quantitative PWI analysis method for intra-ocular malignancies, showing that PKM can potentially provide more accurate biomarkers of the lesion's vasculature as it corrects for both eye motion and the tumor pigmentation. In particular the confounding effect of varying melanin content of UM, could overshadow the differences in tumor vasculature as it has a strong effect on the observed signal enhancement due to its effect on longitudinal relaxation time (T1) [7, 18].

We hypothesize that for UM, the quantitative PWI method, which corrects for tumor pigmentation, is more accurate and will provide significantly different results than the current clinical method. The aim of this study was to test this hypothesis in a cohort of UM patients before and after treatment.

METHODS

Patient population

All UM patients who received an MRI between May 2019 and March 2021 as part of clinical care or in the context of a scientific study were evaluated. Only patients with a tumor prominence larger than 2.5 mm (excluding sclera) on MRI were included, as the proposed PWI method is less reliable for thinner tumors due to partial volume effects[18]. Data were analyzed retrospectively after approval of the local ethics committee, in accordance with the Declaration of Helsinki. For all patients, pre-treatment MRIs were available, and post-treatment scans, acquired approximately one to three months after treatment, were available for 26/47 patients. Tumors with a prominence below 7 mm were generally treated with ^{106}Ru brachytherapy (apex dose 130 Gy [20]), whereas larger tumors and juxtapapillary tumors were treated with proton beam therapy (tumor dose 60 GyRBE [21]) or enucleation.

Image acquisition

Patients were scanned on a 3 tesla MRI scanner (Ingenia Elition, Philips Healthcare, the Netherlands) with a 4.7 cm surface receive coil (Philips Healthcare) according to the protocol by Ferreira et al [4, 7]. Scans used in this study included fat-suppressed contrast-enhanced 3D T1-weighted images, a variable flip angle series used for T1-mapping, a DREAM series for $B1^+$ -mapping [22], and a dynamic contrast-enhanced time series with a temporal resolution of 1.9 seconds per dynamic. The dynamic time series was acquired with a spatial resolution of $1.25 \times 1.25 \times 1.5 \text{ mm}^3$ using the TWIST method [18, 23]. The dynamic time series were acquired using a bolus of 0.1 mmol/kg gadoterate meglumine (DOTAREM; Guerbet, Roissy CdG Cedex, France), administered 6 seconds after the start of the scan, using a power injector with an injection rate of 2 ml/s [18]. More scan parameters can be found in Table 1.

Table 1: Scan parameters.

	T1-mapping	B1+-mapping	DCE-MRI	3D T1
Acquisition voxel size [mm ³]	1.25×1.25×1.5	2.0×2.0×2.0	1.25×1.25×1.5	0.8×0.8×0.8
TE/TE2/TR [ms]	3.1/-/7.0	2.3/3.6/7.1	2.3/-/4.5	31/-/400
Flip angle [deg]	2/5/9/15	10	13	90
Fat suppression	Proset 11	SPIR	Proset 11	SPIR
Scan time [mm:ss]	4 x 00:07	00:14	04:00	02:07
Remarks		DREAM sequence	Temporal resolution 1.9s/dynamic, TWIST	Contrast- enhanced

DCE: dynamic contrast-enhanced, TE: echo time, TR: repetition time, SPIR: spectral presaturation with inversion recovery, DREAM: dual refocusing echo acquisition mode [22], TWIST: time-resolved angiography with stochastic trajectories sequence [23].

Quantitative analysis

Tumors were semi-automatically delineated on the contrast enhanced 3D T1-images in MeVisLab (MeVis Medical Solutions, Bremen, Germany) using a subdivision surface fit [24] and manual correction by an ophthalmic MRI-expert with 10 years of experience based on the clinical evaluation of the images by a neuroradiologist with at least 20 years of experience. Tumor prominence was computed automatically based on the 3D tumor contours according to a previously published method [25].

The quantitative eye-specific PWI analysis was performed in Matlab 2019b (MathWorks, Natick, Massachusetts, USA) based on the method described by Jaarsma et al [18]. First, the variable flip angle series, B1⁺-mapping scans and all separate timepoints of the DCE-MRI were rigidly registered to the contrast-enhanced 3D T1-weighted scan using Elastix 4.9.0 [26] in two steps: first unmasked, then using an eye mask to correct for eye motion. Then, a T1-map was calculated using the variable flip angle series and the B1⁺-map [18]. The tumor contours were eroded by two reconstruction voxels (total 0.6 mm) to eliminate any effects of partial voluming and sub-voxel eye motion after registration. Subsequently, voxel-wise pharmacokinetic modelling (PKM) was performed according to the formulas of Tofts [19] for the first 90 timepoints (172 seconds), resulting in a K^{trans} , v_e and k_{ep} value per voxel for all tumors, with k_{ep} defined as the ratio between K^{trans} and v_e . An overview of the methods is shown in Figure 1.

Clinical parameters

Relative peak intensity and outflow percentage, the most commonly used clinical PWI parameters [7], were determined. Relative peak intensity was defined as the ratio

between signal intensity of the highest peak within the first 90 seconds and mean signal intensity of the second through fourth time point. Outflow percentage was defined as the difference between the intensity 120 seconds after the peak and the peak intensity, divided by the peak intensity. Based on outflow percentage, tumors were assigned a TIC type, with outflow percentages of -5% or lower corresponding to wash-out curves, between -5% and 5% to plateau curves, and higher than 5% corresponding to progressive curves, respectively.

Statistics

Medians and 25-75th percentiles were determined for $B1^+$, T1, K^{trans} , v_e and k_{ep} , relative peak intensity and outflow percentage before and after treatment. The difference in K^{trans} and relative peak intensity between melanotic and amelanotic tumors was determined using an unpaired t-test or Mann-Whitney test. Tumors were considered amelanotic if they had a median T1 larger than 1000 ms, based on a previous study in which all amelanotic tumors had a T1 above 1000 ms [18]. Additionally, the significance of the difference in K^{trans} , v_e and k_{ep} between the two timepoints was determined using a paired T-test or Wilcoxon signed rank test. As tumor pigmentation affects longitudinal relaxation time (T1) and therefore the amount of apparent enhancement [7, 18], tumor T1 was compared before and after treatment in the same way.

To test if the quantitative PWI method was significantly different from the current clinical method the following comparisons were performed: First, multiple linear regression was performed with K^{trans} and T1 for relative peak intensity, as T1 has been proposed to be a confounding factor in the analysis of tumor vascularity. Similarly, the multiple linear regression was performed with k_{ep} and T1 for outflow percentage. Furthermore, to test if the quantitative PWI method was different from the current clinical method for the follow-up after treatment, Pearson's or Kendall's correlation coefficient was determined for the change in K^{trans} and change in relative peak intensity, and for the change in k_{ep} and the change in outflow percentage.

Additionally, since tumor prominence is an important prognostic factor [27], Pearson's or Kendall's correlation coefficient was determined for tumor prominence and PWI characteristics such as peak intensity and outflow percentage, for tumor prominence and median tumor T1, and for tumor prominence and PWI parameters such as K^{trans} , v_e and k_{ep} .

For all statistical analyses, p-values lower than 0.05 were considered statistically significant and the choice between parametric and non-parametric testing depended on the result of the Shapiro-Wilks test for normality.

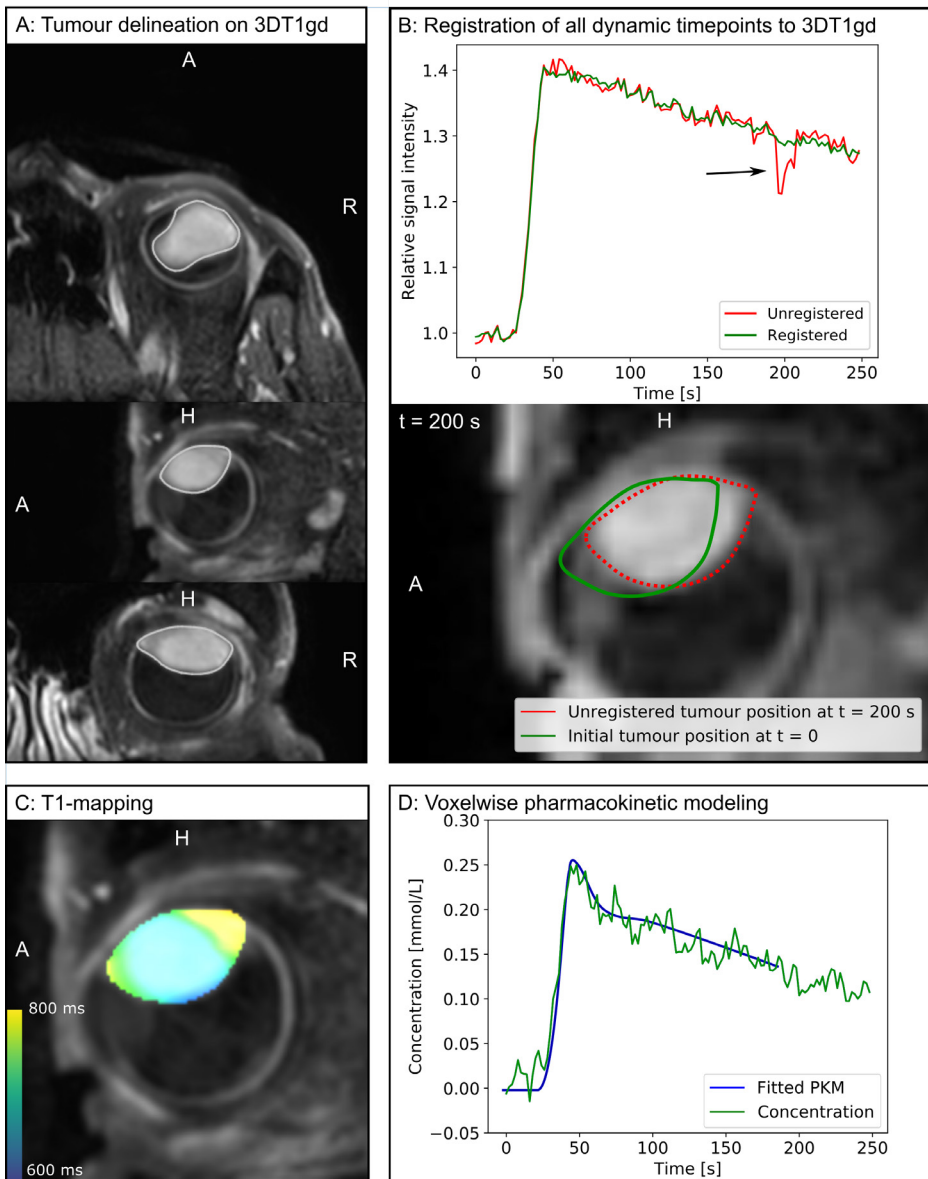


Figure 1: Overview of methods. Additional diagnostic sequences for this patient can be found in Supplementary Figure 1. (A) Tumors were delineated on the contrast-enhanced 3D T1-weighted image (3DT1gd). (B) All timepoints of the dynamic scan, the flip angle series and the B1-map were registered to contrast-enhanced 3D T1-weighted scan. In this figure, a mean time intensity curve is shown before and after registration, with the expected and actual tumor position at $t=200$ s shown. (C) A T1-map was made for each tumor using the flip angle series and B1-map. (D) Voxel-wise pharmacokinetic (PKM) modelling was performed using the T1-map, B1-map, and time-concentration curve. PKM was performed up to $t=180$ s.

RESULTS

47 patients were included, of whom 26 underwent an MRI-scan both before and after treatment. Median tumor prominence excluding sclera was 6.6 mm (range 2.7-13.8 mm). 53% of all patients were treated with proton beam therapy, whereas 30% received ^{106}Ru brachytherapy and 17% of patients underwent enucleation. Median tumor B1^+ was 91% (range 78-103%) and median tumor T1 was 920 ms (range 460-1500 ms). For the subgroup of 26 patients who underwent scans before and after treatment, the majority underwent proton beam therapy (24/26, 92%), while 2 patients (8%) received brachytherapy. Median relative peak intensity and outflow percentage before treatment were 1.63 (range 1.19-2.66) and -8% (range -24% - 3%), respectively. Relative peak intensity was significantly higher for patients with a higher T1: median relative peak intensities for melanotic and amelanotic tumors were 1.5 (range 1.2-1.9) and 1.9 (range 1.3-2.6), respectively ($p < 0.01$). Pre-treatment, 68% of tumors had a wash-out type curve and the remaining 32% had a plateau type curve.

Before treatment, median tumor K^{trans} , v_e and k_{ep} were 0.63 min^{-1} (range 0.06-1.42 min^{-1}), 0.23 (range 0.09-0.63) and 2.3 min^{-1} (range 0.6-5.0 min^{-1}), respectively (Figure 2a). Time-intensity curves of two representative patients, one with a highly enhancing wash-out curve and one with a plateau curve showing less enhancement, are shown in Figure 2b. Results for all patients can be found in Supplementary Table 1. The eye-specific quantitative PWI analysis used in this paper corrects for T1, resulting in a smaller, although still significant, difference in K^{trans} between melanotic and amelanotic tumors (median 0.47 min^{-1} vs 0.67 min^{-1} , $p = 0.03$, Figure 4). Amelanotic tumors had a smaller tumor prominence than melanotic tumors (5.9 mm vs 7.7 mm, $p = 0.03$). Correlations between prominence and PWI parameters before treatment were weak and not significant (Supplementary Figure 2).

Quantitative PWI measures compared to semi-quantitative clinical parameters

Generally, tumors with high K^{trans} values (Figure 2b, green curve) had a higher peak intensity than tumors with lower K^{trans} values (Figure 2b, blue curve), which was also reflected in regression coefficient of 0.84 (Figure 3a, both K^{trans} and T1 $p < 0.01$). Due to the significant effect of tumor pigmentation, different patients with similar K^{trans} values showed larger differences in relative peak intensity (Figure 3a). Furthermore, both k_{ep} and T1 were significant factors for the outflow percentage ($p < 0.001$), with a regression coefficient of 0.80 ($p < 0.001$).

Follow-up

The median time between treatment and the post-treatment MRI-scan was 69 days (range 26-112 days). 85% showed a decrease in K^{trans} and k_{ep} after treatment, with the median K^{trans} for all patients decreasing from 0.62 min^{-1} before treatment to 0.41 min^{-1} after treatment ($p < 0.01$) and median k_{ep} from 2.5 before treatment to 1.8 after treatment ($p < 0.01$) (Figure 5). No significant difference was observed for v_e , with median values of 0.23 and 0.24 before and after treatment, respectively ($p = 0.95$). Although K^{trans} and k_{ep} decreased for the majority of patients, two patients showed an increase in K^{trans} (Figure 5c), and one patient showed an increase in k_{ep} (Figure 5c-d). For these patients, the TIC remained the wash-out type and for the patients with increasing K^{trans} , the peak intensity was higher after treatment than before treatment. Change in K^{trans} correlated significantly with change in relative peak intensity (Pearson's $r = 0.72$, $p < 0.01$, Supplementary Figure 3a) and change in k_{ep} correlated significantly with change in outflow percentage (Pearson's $r = -0.83$, $p < 0.01$, Supplementary Figure 3b). Differences in T1 between the timepoints were small and not significant (median increase of 33 ms, $p = 0.55$, Supplementary Figure 4).

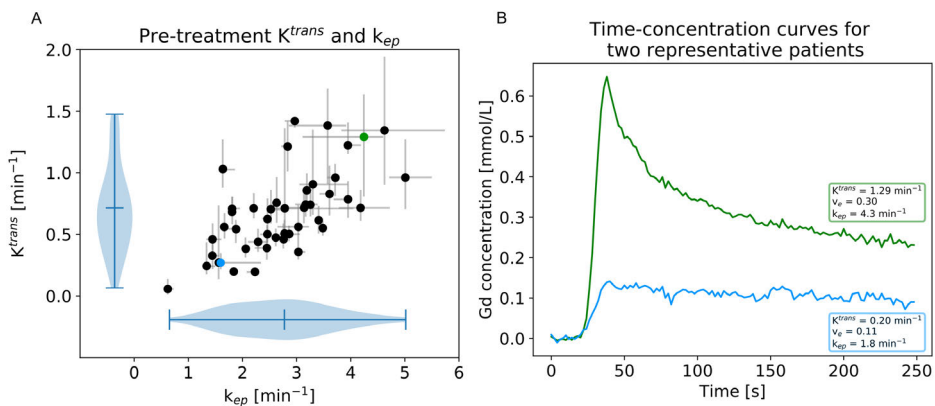


Figure 2: (A) Median with IQR of K^{trans} and k_{ep} for each tumor before treatment. (B) Examples of time-concentration curves for patients with low and high K^{trans} and k_{ep} values. Mean time-concentration curves of the entire tumor are shown.

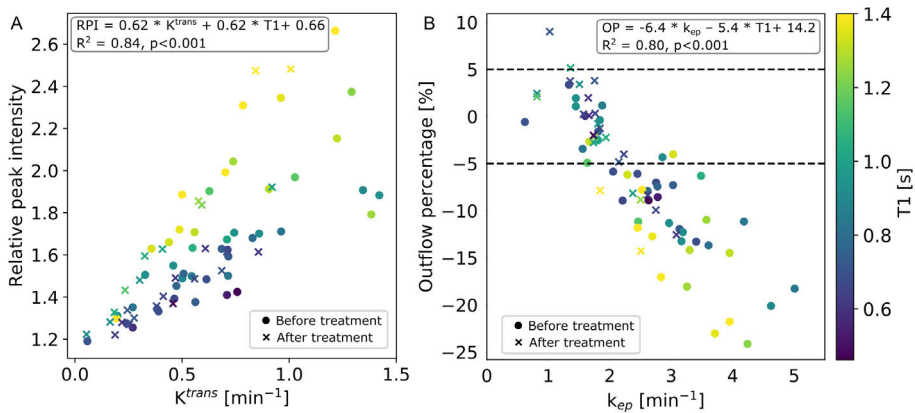


Figure 3: Comparison between quantitative and semi-quantitative PWI parameters. RPI: relative peak intensity, OP: outflow percentage. For the regression analysis, T1 was measured in seconds. **(A)** The regression coefficient between K^{trans} , T1 and relative peak intensity was significant. The importance of correcting for T1 can be observed here: patients with similar K^{trans} values have varying peak intensities. **(B)** The regression coefficients between k_{ep} , T1 and outflow percentage was significant. Values with similar k_{ep} values correspond to varying outflow percentages.

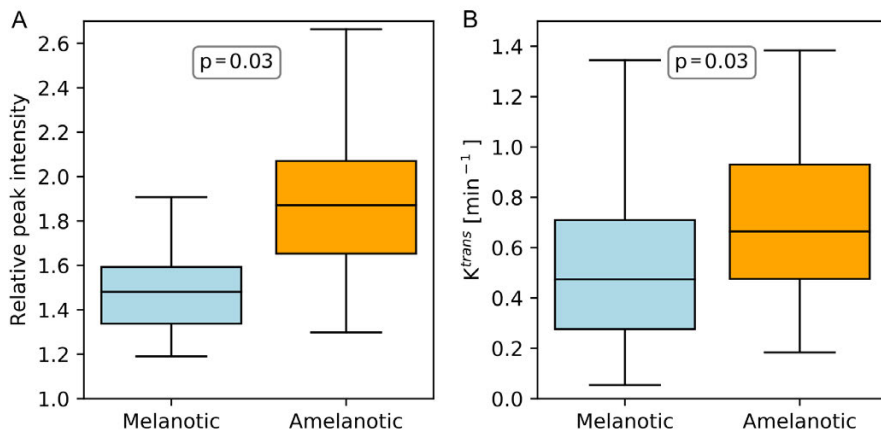


Figure 4: Relative peak intensity (semi-quantitative clinical parameter) and K^{trans} (quantitative PWI analysis) for melanotic and amelanotic tumors. Large differences exist between relative peak intensity (left) due to the confounding effect of the difference in native T1, which is corrected in the calculation of K^{trans} (right), although differences between melanotic and amelanotic tumors remain. Tumors were considered amelanotic if they had a median tumor T1 higher than 1000 ms.

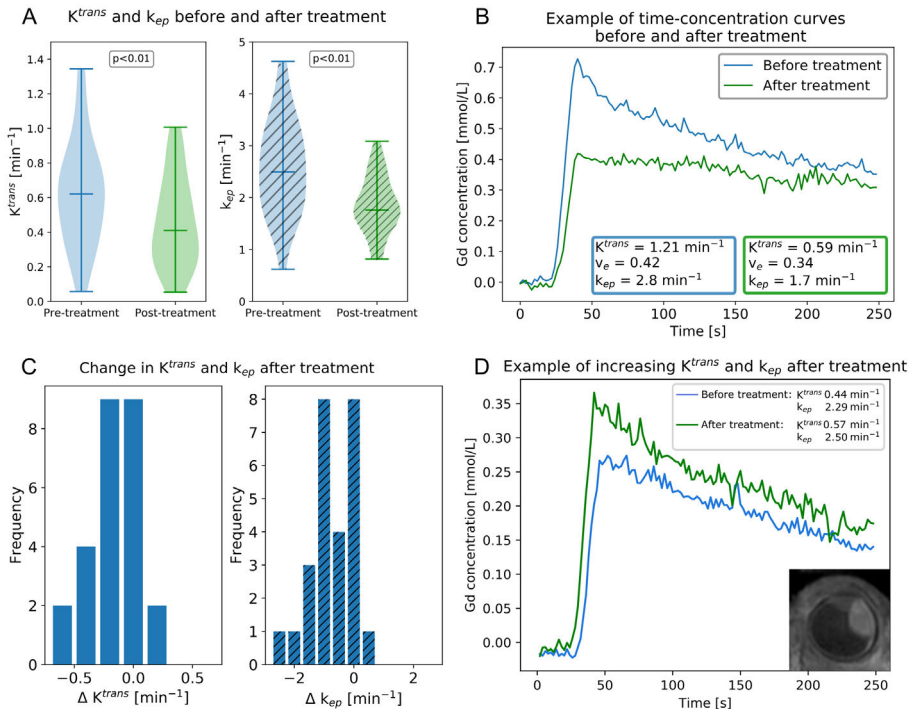


Figure 5: Both K^{trans} and k_{ep} decrease after treatment. **(A)** Violin plots of K^{trans} and k_{ep} values before and after treatment, **(B)** examples of time-concentration curves with corresponding PWI parameters for one patient, **(C)** changes in K^{trans} and k_{ep} after treatment, **(D)** patient with increase in K^{trans} and k_{ep} after treatment.

DISCUSSION

In this paper, an eye-specific quantitative PWI analysis, which incorporates the confounding effect of tumor pigmentation, was compared to current clinical method for uveal melanoma patients before and after treatment. In addition, this is the first description of pharmacokinetic parameters of a large cohort of uveal melanoma patients.

Overall, the values of the quantitative PWI parameters found in this cohort correspond well to an earlier study with the same method, but a different cohort [18], as well as to another study from a different center [28]. The study of Kamrava et al. [29], however, reported a lower transfer constant from blood to tissue (K^{trans}) which could be caused by partial voluming, due to their relatively poor slice thickness of 3 mm,

but could also be the result of a different contrast agent. These differences accentuate that the reference values proposed in this paper are specific to the used acquisition and analysis methods. Furthermore, the clinically used, semi-quantitative, parameters (relative peak intensity, outflow percentage and TIC type) observed in this cohort were comparable to prior UM studies [7, 8, 30], with wash-out curves being the most prevalent and plateau curves occurring in approximately one third of the patients. No progressive curves were observed before treatment, a finding consistent with the literature [2].

Previous research has shown that semi-quantitative PWI parameters can serve as an early biomarker for treatment response [10]. Here, we show that these early changes are also reflected in the tumor's pharmacokinetic parameters as both K^{trans} and k_{ep} decreased significantly after treatment. A decrease in K^{trans} after treatment corresponds to decreased tumor perfusion, which is also reflected by the lower relative peak intensities after treatment. Similarly, the decrease in k_{ep} corresponds to less reflux back into the blood vessels, which is qualitatively reflected in lower washout after the initial enhanced after contrast administration.

A similar post-treatment decrease of quantitative PWI parameters has been reported in other tumor sites, such as breast, head-and-neck, and rectal cancer [12, 13, 15, 31]. However, for patients with small changes in PWI parameters, it is difficult to determine whether this is truly due to the absence of biological changes, as no research has been performed on the reproducibility of this eye-specific quantitative PWI analysis.

Comparison with semi-quantitative clinical evaluation and added value

Although several differences exist between the proposed quantitative PWI method and the clinically used semi-quantitative method, significant regression coefficients were observed between K^{trans} and peak intensity, and k_{ep} and outflow percentage. The main difference between the two approaches is that in the quantitative method the actual gadolinium concentration is calculated, while the semi-quantitative method evaluates relative signal intensities, a metric which is partly determined by the tumor T1. The implications of this confounding effect are shown, as patients with different peak intensities can have the same K^{trans} . Incorporating these differences in tumor T1 results in a more accurate comparison of lesions, which is especially relevant in UM, as this T1 differs between melanotic and amelanotic UM. Interestingly, with the quantitative method still a difference in K^{trans} between melanotic and amelanotic tumors was observed, which might be related to the difference in tumor size or other differences between the two groups, as pigmentation appears to be related to genetic status and prognosis [1, 32].

For treatment response assessment, incorporating this confounding effect of pigmentation appears to be less relevant, as minimal changes in tumor T1 before and after treatment were observed, suggesting that the semi-quantitative method is sufficient to assess whether changes associated with treatment response are present.

Although the correlation between the quantitative PWI method and current clinical method was significant, relative peak intensity differed significantly between the melanotic and amelanotic subgroups. Therefore, the more advanced quantitative method may be valuable for differential diagnosis of intraocular lesions, as, conversely to UM, these are generally non-pigmented (except melanocytoma). For orbital lesions, the pharmacokinetic parameters have already been described by Xu et al. [33] and Ro et al. [34], who found larger K^{trans} and k_{ep} values for malignant orbital masses compared to benign lesions. However, studies describing intraocular masses in terms of quantitative PWI parameters are sparse [35, 36]. In clinical practice, we therefore advise to use separate reference values for pigmented and unpigmented UM when comparing the TIC-related metrics, such as peak enhancement, between lesions.

Furthermore, although on a group level a correlation between the clinical and quantitative methods was observed, on a patient level the lack of motion correction in the clinical method might be a limitation. Due to the registration, the proposed quantitative method might be more robust to slow gaze drifts, which can be missed during the clinical evaluation [10]. However, as this eye-specific registration is not available in clinically used software packages and is therefore time intensive, the current clinical practice of mitigating movement artefacts by the manual selection of a suitable neighboring timepoint is likely sufficient for most cases.

Similarly, the fully quantitative method is a voxel-wise analysis, in contrast to the clinical method, where an averaged representative 2D ROI is evaluated. This voxel-wise analysis allows for a more detailed evaluation of the mass, which might be valuable for heterogeneous tumors [7, 37, 38]. Clinically, it is proposed to obtain several ROIs to correctly evaluate these masses [7, 10], but this is only feasible to a certain extent. Although the proposed quantitative PWI method provides quantifiable insights into tumor heterogeneity, the clinical value of this heterogeneity is currently unknown.

MRI is gaining a more prominent place in the clinical care of uveal melanoma patients: it is for example now routinely used in the proton therapy planning [39-41], as it provides a geometrically accurate three dimensional visualization of the tumor and surrounding structures [42]. With these developments, various MR-biomarkers have

become accessible in routine clinical care. Diffusion Weighted Imaging, for example, can aid in the differential diagnosis [2, 7] and reportedly holds promise in prognosis determination [43]. Similar applications, including treatment response assessment have been reported of PWI [2, 7, 10, 29]. In this context, the quantitative analysis as proposed by Tofts et al [19] has been validated in phantom studies [44-46] and was adapted for eye-specific applications by Jaarsma et al [18], correcting for confounding factors such as tumor pigmentation and eye movement. However, this method requires several calibration scans and post-processing steps. As the semi-quantitative analysis is more accessible, it is used clinically, and in this paper we show that these semi-quantitative parameters strongly correlate to the validated Tofts method and are therefore sufficiently accurate for early treatment response assessment [10]. Furthermore, reference values are given for melanotic and amelanotic UM, simplifying the use of the semi-quantitative method in the differential diagnosis of amelanotic intraocular masses. Future research will have to show whether semi-quantitative PWI is of added value for estimation of prognosis [29], as the differences in perfusion between several risk profiles might be smaller.

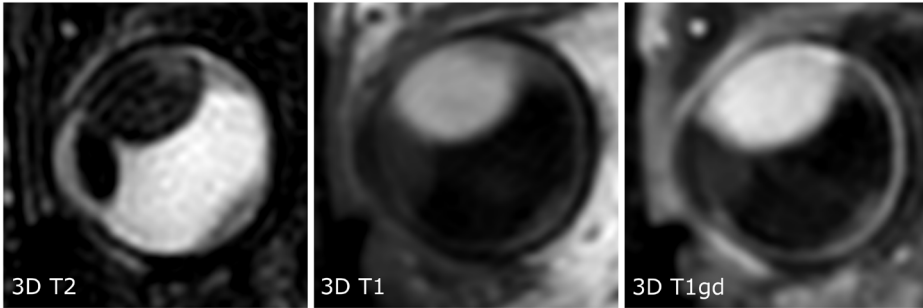
Limitations

The proposed method corrects for tumor pigmentation and eye motion. However, due to the limited field of view, no personal AIF could be determined. Although population-based AIFs are widely used [47, 48], especially K^{trans} estimations may be less accurate on the patient level, especially for subjects with an impaired cardiac output. Here, an overestimation of the AIF would result in an underestimation of K^{trans} [49]. However, in this context, it is important to realize that UM patients are not predisposed to cardiovascular abnormalities. Furthermore, adding a personal AIF to this method would require enlarging the field of view, resulting in a decrease in either spatial or temporal resolution, which might be unfavorable, especially in small UM.

Conclusions

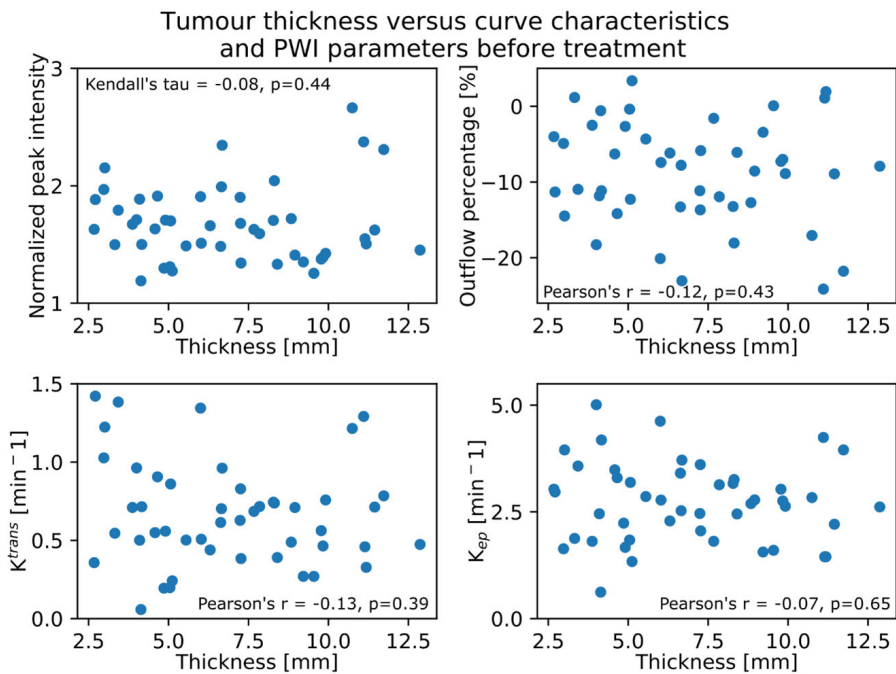
In this paper, we show that a quantitative PWI method that corrects for tumor pigmentation can serve as an early biomarker for treatment response assessment, as both K^{trans} and k_{ep} decreased significantly after radiotherapy. However, due to the non-significant changes in tumor pigmentation before and after treatment, the current clinical semi-quantitative method appears to be sufficient as a biomarker for changes after ocular radiotherapy. For differential diagnosis, the quantitative PWI method may be preferred, although studies on quantitative PWI for intraocular masses are sparse. In clinical practice, we therefore advise to use separate reference values for pigmented and unpigmented intra-ocular masses when interpreting semi-quantitative parameters such as peak enhancement.

Supplementary Figure 1



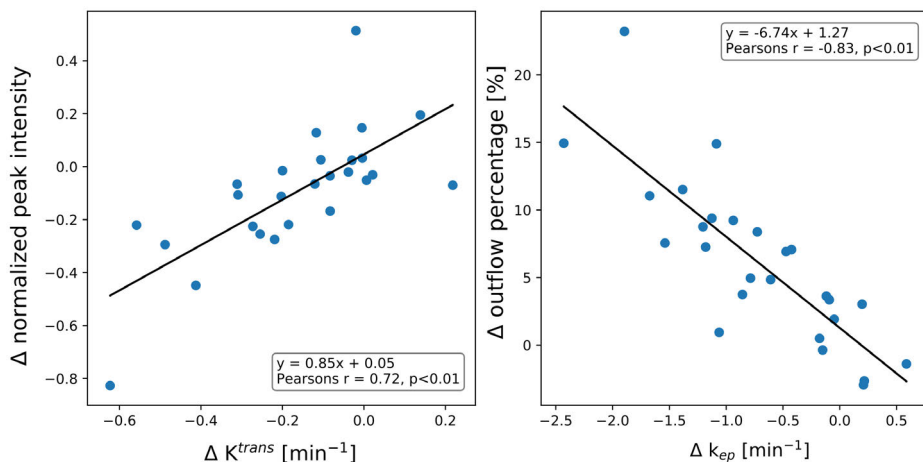
Supplementary Figure 1: Additional diagnostic sequences for the patient shown in Figure 1. The tumor is located superiorly, with retinal detachment visible both around the tumor and inferior.

Supplementary Figure 2



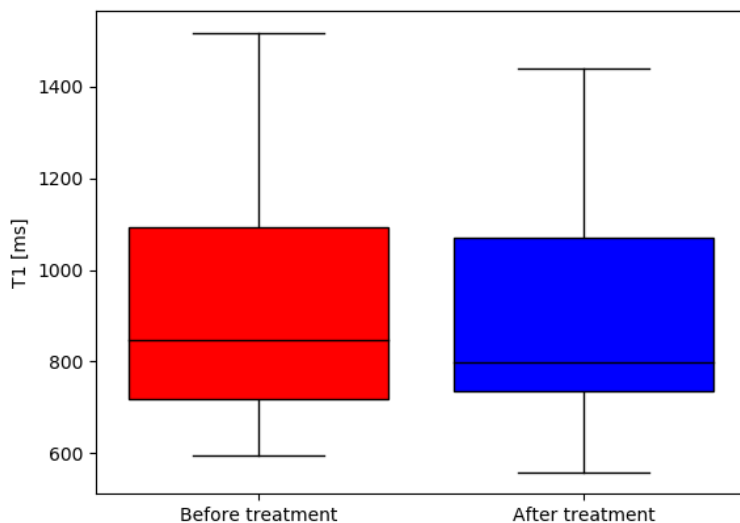
Supplementary Figure 2: Tumor prominence compared to curve characteristics and PWI parameters before treatment. Correlations between prominence and the curve characteristics and PWI parameters were weak and not significant.

Supplementary Figure 3



Supplementary Figure 3: Change in K^{trans} correlated with change in relative peak intensity (Pearson's $r = 0.72$, $p < 0.01$, Supplementary Figure 2a) and change in k_{ep} correlated with change in outflow percentage (Pearson's $r = 0.86$, $p < 0.01$, Supplementary Figure 2b).

Supplementary Figure 4



Supplementary Figure 4: Differences in T1 between the timepoints were small and not significant (median increase of 33 ms, $p = 0.55$).

Supplementary Table 1: Results per patient

Patient	Timepoint	Treatment	Volume [mm ³]	Prominence [mm]	Median T1 [ms]	Median B1 [%]	Median K ^{trans} [min ⁻¹]	Median V _e	Median k _{ep} [min ⁻¹]	TIC type	TIC	
											relative peak intensity [%]	TIC outflow percentage
Patient 1	Pre-treatment	Enucleation	791	11.7	1758	80	0.78	0.20	3.95	washout	2.31	-21.8
Patient 2	Pre-treatment	Enucleation	1626	8.8	1369	100	0.49	0.18	2.69	washout	1.72	-12.7
Patient 3	Pre-treatment	Enucleation	412	4.0	831	93	0.96	0.19	5.01	washout	1.71	-18.3
Patient 4	Pre-treatment	Enucleation	606	7.8	734	94	0.72	0.23	3.13	washout	1.59	-11.9
Patient 5	Pre-treatment	Enucleation	1202	12.9	776	85	0.47	0.18	2.62	washout	1.45	-7.9
Patient 6	Pre-treatment	Brachytherapy	115	3.0	1315	100	1.22	0.31	3.95	washout	2.15	-14.5
Patient 7	Pre-treatment	Brachytherapy	167	3.9	1009	92	0.71	0.39	1.81	plateau	1.67	-2.5
Patient 8	Pre-treatment	PBT	841	8.4	685	90	0.39	0.16	2.45	washout	1.33	-6.1
	Post-treatment	PBT	906	8.7	722	88	0.19	0.10	1.84	plateau	1.22	-1.2
Patient 9	Pre-treatment	Enucleation	1663	11.1	1229	99	1.29	0.30	4.24	washout	2.37	-24.1
Patient 10	Pre-treatment	Brachytherapy	281	5.1	684	94	0.24	0.18	1.34	plateau	1.27	3.4
Patient 11	Pre-treatment	Enucleation	84	2.7	938	95	1.42	0.48	2.97	washout	1.88	-11.3
	Pre-treatment	PBT	1460	9.8	664	92	0.46	0.17	2.75	washout	1.39	-7.0
Patient 12	Post-treatment	PBT	1715	13.3	744	89	0.38	0.24	1.57	plateau	1.36	0.3
Patient 13	Pre-treatment	PBT	280	6.7	1428	85	0.70	0.28	2.53	washout	1.99	-7.8
	Post-treatment	PBT	223	5.5	1055	96	0.92	0.39	2.38	washout	1.92	-8.2
Patient 14	Pre-treatment	PBT	747	7.2	1146	100	0.63	0.25	2.46	washout	1.90	-11.1
	Post-treatment	PBT	694	7.4	1045	91	0.41	0.24	1.74	plateau	1.63	-2.8
Patient 15	Pre-treatment	PBT	410	7.7	741	94	0.68	0.38	1.81	plateau	1.63	-1.6
	Post-treatment	PBT	278	6.4	737	88	0.41	0.23	1.76	plateau	1.40	0.3

Supplementary Table 1 Continued

Patient	Timepoint	Treatment	Volume [mm ³]	Prominence [mm]	Median T1 [ms]	Median B1 [%]	Median K ^{trans} [min ⁻¹]		Median V _e	Median k _{ep} [min ⁻¹]	TIC type	TIC peak intensity	TIC relative peak intensity [%]
							Median K ^{trans} [min ⁻¹]	Median V _e					
Patient 16	Pre-treatment	PBT	726	7.3	686	89	0.38	0.19	2.06	2.06	washout	1.34	-5.9
	Post-treatment	PBT	694	7.4	1079	97	0.18	0.09	1.94	1.94	plateau	1.33	-2.2
Patient 17	Pre-treatment	PBT	769	8.3	933	89	0.74	0.23	3.17	3.17	washout	1.71	-13.2
	Post-treatment	PBT	796	8.1	738	90	0.56	0.25	2.23	2.23	plateau	1.49	-4.0
Patient 18	Pre-treatment	PBT	163	5.0	930	88	0.20	0.11	1.84	1.84	plateau	1.31	-0.4
	Post-treatment	PBT	190	5.8	674	90	0.22	0.13	1.66	1.66	plateau	1.28	0.1
Patient 19	Pre-treatment	PBT	760	9.5	595	88	0.27	0.17	1.60	1.60	plateau	1.25	0.1
	Post-treatment	PBT	766	9.3	971	89	0.16	0.11	1.51	1.51	plateau	1.28	3.4
Patient 20	Pre-treatment	PBT	1232	10.7	1517	89	1.21	0.43	2.83	2.83	washout	2.66	-17.1
	Post-treatment	PBT	614	6.1	1222	91	0.59	0.34	1.75	1.75	plateau	1.84	-2.2
Patient 21	Pre-treatment	PBT	309	3.0	1160	78	1.03	0.63	1.63	1.63	plateau	1.97	-4.9
	Post-treatment	PBT	275	3.4	1409	96	1.01	0.55	1.84	1.84	washout	2.48	-7.9
Patient 22	Pre-treatment	Brachytherapy	689	9.0	533	101	0.71	0.26	2.78	2.78	washout	1.41	-8.6
Patient 23	Pre-treatment	Enucleation	1325	9.9	462	95	0.76	0.29	2.63	2.63	washout	1.42	-8.9
Patient 24	Pre-treatment	PBT	132	5.5	912	87	0.50	0.18	2.86	2.86	plateau	1.49	-4.3
Patient 25	Pre-treatment	PBT	439	6.0	768	92	0.51	0.18	2.78	2.78	washout	1.51	-7.4
	Post-treatment	PBT	450	5.7	698	90	0.47	0.28	1.65	1.65	plateau	1.49	2.0
Patient 26	Pre-treatment	Enucleation	1272	11.1	940	91	0.46	0.32	1.45	1.45	plateau	1.55	1.1
Patient 27	Pre-treatment	PBT	586	7.3	797	88	0.83	0.23	3.61	3.61	washout	1.68	-13.7
	Post-treatment	PBT	651	6.9	758	90	0.71	0.26	2.75	2.75	washout	1.61	-9.9

Patient	Timepoint	Treatment	Volume [mm ³]	Prominence [mm]	Median T1 [ms]	Median B1 [%]	Median		TIC type	TIC relative peak intensity	TIC outflow percentage	
							K ^{trans} [min ⁻¹]	V _e				
Patient 28	Pre-treatment	PBT	625	6.7	1366	98	0.96	0.26	3.71	washout	2.35	-23.0
	Post-treatment	PBT	546	5.6	1440	95	0.84	0.34	2.51	washout	2.47	-14.3
Patient 29	Pre-treatment	PBT	328	4.1	712	85	0.06	0.09	0.62	plateau	1.19	-0.6
	Post-treatment	PBT	275	4.1	962	83	0.05	0.07	0.82	plateau	1.22	2.4
Patient 30	Pre-treatment	Brachytherapy	540	4.9	1468	81	0.19	0.09	2.24	plateau	1.30	
Patient 31	Pre-treatment	Brachytherapy	445	4.9	1313	89	0.56	0.33	1.67	plateau	1.71	-2.7
Patient 32	Pre-treatment	Brachytherapy	278	3.4	1264	97	1.38	0.39	3.57	washout	1.79	-11.0
Patient 33	Pre-treatment	Brachytherapy	223	4.6	1057	92	0.55	0.16	3.49	washout	1.63	-6.3
Patient 34	Pre-treatment	Brachytherapy	279	5.1	919	89	0.86	0.27	3.19	washout	1.70	-12.3
	Post-treatment	Brachytherapy	111	2.9	991	90	0.30	0.17	1.81	plateau	1.48	-0.8
Patient 35	Pre-treatment	Brachytherapy	372	4.2	838	92	0.71	0.17	4.18	washout	1.50	-11.1
	Post-treatment	Brachytherapy	141	2.8	794	90	0.69	0.39	1.75	plateau	1.53	3.8
Patient 36	Pre-treatment	Brachytherapy	130	2.7	1341	103	0.36	0.12	3.03	plateau	1.63	-4.0
Patient 37	Pre-treatment	PBT	309	6.0	903	96	1.34	0.29	4.62	washout	1.91	-20.1
	Post-treatment	PBT	179	4.9	693	91	0.86	0.28	3.08	washout	1.61	-12.6
Patient 38	Pre-treatment	Brachytherapy	284	4.1	1495	105	0.50	0.20	2.46	washout	1.89	-11.8
Patient 39	Pre-treatment	Brachytherapy	402	4.7	1303	98	0.91	0.27	3.30	washout	1.91	-14.2
Patient 40	Pre-treatment	PBT	898	9.8	745	91	0.56	0.19	3.03	washout	1.38	-7.3
	Post-treatment	PBT	952	10.5	742	90	0.25	0.19	1.36	plateau	1.27	3.8

Supplementary Table 1 *Continued*

Patient	Timepoint	Treatment	Volume [mm ³]	Prominence [mm]	Median T1 [ms]	Median		TIC type	TIC relative peak intensity [%]	TIC outflow percentage [%]		
						Median B1 [%]	Median K ^{trans} [min ⁻¹]					
Patient 41	Pre-treatment	PBT	816	8.3	1269	103	0.74	0.23	3.26	washout	2.04	-18.1
	Post-treatment	PBT	888	8.9	1082	102	0.33	0.24	1.36	progressive	1.59	5.2
Patient 42	Pre-treatment	PBT	616	6.3	1335	72	0.44	0.19	2.29	washout	1.66	-6.2
	Post-treatment	PBT	597	6.4	1264	83	0.58	0.23	2.50	washout	1.86	-8.8
Patient 43	Pre-treatment	PBT	604	6.6	689	91	0.61	0.18	3.41	washout	1.48	-13.3
	Post-treatment	PBT	694	8.7	709	103	0.61	0.23	2.62	washout	1.63	-8.3
Patient 44	Pre-treatment	PBT	1182	9.2	829	91	0.27	0.17	1.56	plateau	1.35	-3.4
	Post-treatment	PBT	1207	9.9	801	88	0.28	0.13	2.15	plateau	1.30	-4.8
Patient 45	Pre-treatment	PBT	1161	11.2	938	98	0.33	0.23	1.45	plateau	1.51	1.9
	Post-treatment	PBT	827	9.0	791	89	0.24	0.24	1.02	progressive	1.34	9.0
Patient 46	Pre-treatment	PBT	1031	11.4	660	102	0.71	0.32	2.21	washout	1.62	-8.9
	Post-treatment	PBT	1056	11.3	559	96	0.46	0.26	1.74	plateau	1.37	-2.0
Patient 47	Pre-treatment	PBT	73	3.3	856	85	0.55	0.29	1.88	plateau	1.50	1.2
	Post-treatment	PBT	182	3.9	1174	84	0.23	0.29	0.82	plateau	1.43	2.1

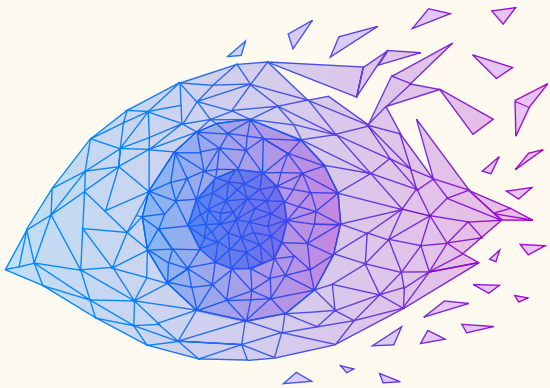
REFERENCES

1. Jager MJ, Shields CL, Cebulla CM, Abdel-Rahman MH, Grossniklaus HE, Stern MH, et al. Uveal melanoma. *Nat Rev Dis Primers*. 2020;6:24. doi: 10.1038/s41572-020-0158-0.
2. Jaarsma-Coes MG, Klaassen L, Marinkovic M, Luyten GPM, Vu THK, Ferreira TA, et al. Magnetic Resonance Imaging in the Clinical Care for Uveal Melanoma Patients-A Systematic Review from an Ophthalmic Perspective. *Cancers (Basel)*. 2023;15. doi: 10.3390/cancers15112995.
3. Solnik M, Padaszynska N, Czarnecka AM, Synoradzki KJ, Yousef YA, Choragiewicz T, et al. Imaging of Uveal Melanoma-Current Standard and Methods in Development. *Cancers (Basel)*. 2022;14. doi: 10.3390/cancers14133147.
4. Ferreira TA, Grech Fonk L, Jaarsma-Coes MG, van Haren GGR, Marinkovic M, Beenakker JM. MRI of Uveal Melanoma. *Cancers (Basel)*. 2019;11. doi: 10.3390/cancers11030377.
5. Foti PV, Travali M, Farina R, Palmucci S, Spatola C, Raffaele L, et al. Diagnostic methods and therapeutic options of uveal melanoma with emphasis on MR imaging-Part I: MR imaging with pathologic correlation and technical considerations. *Insights Imaging*. 2021;12:66. doi: 10.1186/s13244-021-01000-x.
6. Niendorf T, Beenakker JM, Langner S, Erb-Eigner K, Bach Cuadra M, Beller E, et al. Ophthalmic Magnetic Resonance Imaging: Where Are We (Heading To)? *Curr Eye Res*. 2021;46:1251-70. doi: 10.1080/02713683.2021.1874021.
7. Ferreira TA, Jaarsma-Coes MG, Marinkovic M, Verbist B, Verdijk RM, Jager MJ, et al. MR imaging characteristics of uveal melanoma with histopathological validation. *Neuroradiology*. 2022;64:171-84. doi: 10.1007/s00234-021-02825-5.
8. Yuan Y, Kuai XP, Chen XS, Tao XF. Assessment of dynamic contrast-enhanced magnetic resonance imaging in the differentiation of malignant from benign orbital masses. *Eur J Radiol*. 2013;82:1506-11. doi: 10.1016/j.ejrad.2013.03.001.
9. Jiang X, Asbach P, Willerding G, Dulce M, Xu K, Taupitz M, et al. Dynamic contrast-enhanced MRI of ocular melanoma. *Melanoma Res*. 2015;25:149-56. doi: 10.1097/CMR.000000000000142.
10. Tang MCY, Ferreira TA, Marinkovic M, Jaarsma-Coes MG, Klaassen L, Vu THK, et al. MR-based follow-up after brachytherapy and proton beam therapy in uveal melanoma. *Neuroradiology*. 2023;65:1271-85. doi: 10.1007/s00234-023-03166-1.
11. Berman RM, Brown AM, Chang SD, Sankineni S, Kadakia M, Wood BJ, et al. DCE MRI of prostate cancer. *Abdom Radiol (NY)*. 2016;41:844-53. doi: 10.1007/s00261-015-0589-3.
12. Dijkhoff RAP, Beets-Tan RGH, Lambregts DMJ, Beets GL, Maas M. Value of DCE-MRI for staging and response evaluation in rectal cancer: A systematic review. *Eur J Radiol*. 2017;95:155-68. doi: 10.1016/j.ejrad.2017.08.009.
13. Guo W, Zhang Y, Luo D, Yuan H. Dynamic contrast-enhanced magnetic resonance imaging (DCE-MRI) for pretreatment prediction of neoadjuvant chemotherapy response in locally advanced hypopharyngeal cancer. *Br J Radiol*. 2020;93:20200751. doi: 10.1259/bjr.20200751.
14. Ma XZ, Lv K, Sheng JL, Yu YX, Pang PP, Xu MS, et al. Application evaluation of DCE-MRI combined with quantitative analysis of DWI for the diagnosis of prostate cancer. *Oncol Lett*. 2019;17:3077-84. doi: 10.3892/ol.2019.9988.
15. Sharma A, Sharma S, Sood S, Seam RK, Sharma M, Fotedar V. DCE-MRI and parametric imaging in monitoring response to neoadjuvant chemotherapy in breast carcinoma: a preliminary report. *Pol J Radiol*. 2018;83:e220-e8. doi: 10.5114/pjr.2018.76271.

16. Barboriak DP, MacFall JR, Viglianti BL, Dewhirst Dvm MW. Comparison of three physiologically-based pharmacokinetic models for the prediction of contrast agent distribution measured by dynamic MR imaging. *J Magn Reson Imaging*. 2008;27:1388-98. doi: 10.1002/jmri.21344.
17. Khalifa F, Soliman A, El-Baz A, Abou El-Ghar M, El-Diasty T, Gimel'farb G, et al. Models and methods for analyzing DCE-MRI: a review. *Med Phys*. 2014;41:124301. doi: 10.1118/1.4898202.
18. Jaarsma-Coes MG, Ferreira TA, van Houdt PJ, van der Heide UA, Luyten GPM, Beenakker JM. Eye-specific quantitative dynamic contrast-enhanced MRI analysis for patients with intraocular masses. *Magma*. 2022;35:311-23. doi: 10.1007/s10334-021-00961-w.
19. Tofts PS. Modeling tracer kinetics in dynamic Gd-DTPA MR imaging. *J Magn Reson Imaging*. 1997;7:91-101. doi: 10.1002/jmri.1880070113.
20. Marinkovic M, Horeweg N, Fiocco M, Peters FP, Sommers LW, Laman MS, et al. Ruthenium-106 brachytherapy for choroidal melanoma without transpupillary thermotherapy: Similar efficacy with improved visual outcome. *Eur J Cancer*. 2016;68:106-13. doi: 10.1016/j.ejca.2016.09.009.
21. Fleury E, Trnkova P, Spruijt K, Herault J, Lebbink F, Heufelder J, et al. Characterization of the HollandPTC proton therapy beamline dedicated to uveal melanoma treatment and an interinstitutional comparison. *Med Phys*. 2021;48:4506-22. doi: 10.1002/mp.15024.
22. Nehrke K, Bornert P. DREAM--a novel approach for robust, ultrafast, multislice B(1) mapping. *Magn Reson Med*. 2012;68:1517-26. doi: 10.1002/mrm.24158.
23. Tudorica LA, Oh KY, Roy N, Kettler MD, Chen Y, Hemmingson SL, et al. A feasible high spatiotemporal resolution breast DCE-MRI protocol for clinical settings. *Magn Reson Imaging*. 2012;30:1257-67. doi: 10.1016/j.mri.2012.04.009.
24. Hassan MK, Fleury E, Shamonin D, Fonk LG, Marinkovic M, Jaarsma-Coes MG, et al. An Automatic Framework to Create Patient-specific Eye Models From 3D Magnetic Resonance Images for Treatment Selection in Patients With Uveal Melanoma. *Adv Radiat Oncol*. 2021;6:100697. doi: 10.1016/j.adro.2021.100697.
25. Klaassen L, Jaarsma-Coes MG, Verbist BM, Vu THK, Marinkovic M, Rasch CRN, et al. Automatic Three-Dimensional Magnetic Resonance-based measurements of tumour prominence and basal diameter for treatment planning of uveal melanoma. *Phys Imaging Radiat Oncol*. 2022;24:102-10. doi: 10.1016/j.phro.2022.11.001.
26. Klein S, Staring M, Murphy K, Viergever MA, Pluim JP. elastix: a toolbox for intensity-based medical image registration. *IEEE Trans Med Imaging*. 2010;29:196-205. doi: 10.1109/TMI.2009.2035616.
27. Kaliki S, Shields CL, Shields JA. Uveal melanoma: estimating prognosis. *Indian J Ophthalmol*. 2015;63:93-102. doi: 10.4103/0301-4738.154367.
28. Wei W, Jia G, von Tengg-Kobligk H, Heverhagen JT, Abdel-Rahman M, Wei L, et al. Dynamic Contrast-Enhanced Magnetic Resonance Imaging of Ocular Melanoma as a Tool to Predict Metastatic Potential. *J Comput Assist Tomogr*. 2017;41:823-7. doi: 10.1097/RCT.0000000000000598.
29. Kamrava M, Sepahdari AR, Leu K, Wang PC, Roberts K, Demanes DJ, et al. Quantitative multiparametric MRI in uveal melanoma: increased tumor permeability may predict monosomy 3. *Neuroradiology*. 2015;57:833-40. doi: 10.1007/s00234-015-1546-0.
30. Buerk BM, Pulido JS, Chiong I, Folberg R, Edward DP, Duffy MT, et al. Vascular perfusion of choroidal melanoma by 3.0 tesla magnetic resonance imaging. *Trans Am Ophthalmol Soc*. 2004;102:209-15; discussion 15-7. doi: 10.4103/0366-6999.155127.
31. Xu QG, Xian JF. Role of quantitative magnetic resonance imaging parameters in the evaluation of treatment response in malignant tumors. *Chin Med J (Engl)*. 2015;128:1128-33. doi: 10.4103/0366-6999.155127.

32. Gelmi MC, Wierenga APA, Kroes WGM, van Duinen SG, Karuntu JS, Marinkovic M, et al. Increased Histological Tumor Pigmentation in Uveal Melanoma Is Related to Eye Color and Loss of Chromosome 3/BAP1. *Ophthalmol Sci*. 2023;3:100297. doi: 10.1016/j.xops.2023.100297.
33. Xu XQ, Qian W, Ma G, Hu H, Su GY, Liu H, et al. Combined diffusion-weighted imaging and dynamic contrast-enhanced MRI for differentiating radiologically indeterminate malignant from benign orbital masses. *Clin Radiol*. 2017;72:903 e9- e15. doi: 10.1016/j.crad.2017.04.007.
34. Ro SR, Asbach P, Siebert E, Bertelmann E, Hamm B, Erb-Eigner K. Characterization of orbital masses by multiparametric MRI. *Eur J Radiol*. 2016;85:324-36. doi: 10.1016/j.ejrad.2015.11.041.
35. Stroszczynski C, Hosten N, Bornfeld N, Wiegel T, Schueler A, Foerster P, et al. Choroidal hemangioma: MR findings and differentiation from uveal melanoma. *AJNR Am J Neuroradiol*. 1998;19:1441-7. doi:
36. Rodjan F, de Graaf P, van der Valk P, Moll AC, Kuijer JP, Knol DL, et al. Retinoblastoma: value of dynamic contrast-enhanced MR imaging and correlation with tumor angiogenesis. *AJNR Am J Neuroradiol*. 2012;33:2129-35. doi: 10.3174/ajnr.A3119.
37. Mensink HW, Vaarwater J, Kilic E, Naus NC, Mooy N, Luyten G, et al. Chromosome 3 intratumor heterogeneity in uveal melanoma. *Invest Ophthalmol Vis Sci*. 2009;50:500-4. doi: 10.1167/iovs.08-2279.
38. Stalhammar G, Grossniklaus HE. Intratumor Heterogeneity in Uveal Melanoma BAP-1 Expression. *Cancers (Basel)*. 2021;13. doi: 10.3390/cancers13051143.
39. Hrbacek J, Kacperek A, Beenaker JM, Mortimer L, Denker A, Mazal A, et al. PTCOG Ocular Statement: Expert Summary of Current Practices and Future Developments in Ocular Proton Therapy. *Int J Radiat Oncol Biol Phys*. 2024. doi: 10.1016/j.ijrobp.2024.06.017.
40. Jaarsma-Coes MG, Ferreira TA, Marinkovic M, Vu THK, van Vught L, van Haren GR, et al. Comparison of MRI-based and conventional measurements for proton beam therapy of uveal melanoma. *Ophthalmol Retina*. 2022. doi: 10.1016/j.oret.2022.06.019.
41. Wulff J, Koska B, Ahmad Khalil D, Richter R, Maximilian Backer C, Baumer C, et al. Uncertainties in ocular proton planning and their impact on required margins. *Phys Med*. 2024;121:103358. doi: 10.1016/j.ejmp.2024.103358.
42. Klaassen L, Haasjes C, Hol M, Cambraia Lopes P, Spruijt K, van de Steeg-Henzen C, et al. Geometrical accuracy of magnetic resonance imaging for ocular proton therapy planning. *Phys Imaging Radiat Oncol*. 2024;31:100598. doi: 10.1016/j.phro.2024.100598.
43. Zheng Y, Tang Y, Yao Y, Ge T, Pan H, Cui J, et al. Correlation Analysis of Apparent Diffusion Coefficient Histogram Parameters and Clinicopathologic Features for Prognosis Prediction in Uveal Melanoma. *Invest Ophthalmol Vis Sci*. 2024;65:3. doi: 10.1167/iovs.65.8.3.
44. Chao SL, Metens T, Lemort M. TumourMetrics: a comprehensive clinical solution for the standardization of DCE-MRI analysis in research and routine use. *Quant Imaging Med Surg*. 2017;7:496-510. doi: 10.21037/qims.2017.09.02.
45. Foltz W, Driscoll B, Laurence Lee S, Nayak K, Nallapareddy N, Fatemi A, et al. Phantom Validation of DCE-MRI Magnitude and Phase-Based Vascular Input Function Measurements. *Tomography*. 2019;5:77-89. doi: 10.18383/j.tom.2019.00001.
46. Kim H, Mousa M, Schexnailder P, Hergenrother R, Bolding M, Ntsikoussalabongui B, et al. Portable perfusion phantom for quantitative DCE-MRI of the abdomen. *Med Phys*. 2017;44:5198-209. doi: 10.1002/mp.12466.

47. Parker GJ, Roberts C, Macdonald A, Buonaccorsi GA, Cheung S, Buckley DL, et al. Experimentally-derived functional form for a population-averaged high-temporal-resolution arterial input function for dynamic contrast-enhanced MRI. *Magn Reson Med*. 2006;56:993-1000. doi: 10.1002/mrm.21066.
48. Fedorov A, Fluckiger J, Ayers GD, Li X, Gupta SN, Tempany C, et al. A comparison of two methods for estimating DCE-MRI parameters via individual and cohort based AIFs in prostate cancer: a step towards practical implementation. *Magn Reson Imaging*. 2014;32:321-9. doi: 10.1016/j.mri.2014.01.004.
49. Ziayee F, Muller-Lutz A, Gross J, Quentin M, Ullrich T, Heusch P, et al. Influence of arterial input function (AIF) on quantitative prostate dynamic contrast-enhanced (DCE) MRI and zonal prostate anatomy. *Magn Reson Imaging*. 2018;53:28-33. doi: 10.1016/j.mri.2018.06.004.



Chapter 8

Reproducibility of perfusion-weighted and diffusion-weighted MRI in uveal melanoma

Collaboration chapter

P.A.M. Janssen, T.A. Ferreiram T.H.K. Vu,
J.W.M. Beenakker, L. Klaassen

Submitted to Ocular Oncology & Pathology.

ABSTRACT

Introduction

Diffusion-weighted (DWI) and perfusion-weighted MRI (PWI) can assess biological tumour characteristics of uveal melanoma (UM), the most common primary intraocular malignant tumour in adults. Recent studies propose that these techniques can aid in the differential diagnosis, provide prognostic information, and enable early assessment of treatment response following radiation therapy. However, it is important to determine the extent to which any observed differences can be attributable to true biological changes in the tumour rather than day-to-day physiological or measurement variations. Therefore, this study aims to assess the reproducibility of ocular DWI and PWI measurements between two centres.

Methods

In this prospective study, 15 patients with UM were included. Each patient underwent two MRIs at two different centres with a mean interval of 28 days (range: 12-43 days). Apparent diffusion coefficient (ADC), relative peak intensity and outflow percentage of the tumour were compared between the two timepoints. Mean absolute differences between the two timepoints were calculated.

Results

Mean absolute differences between the two timepoints were $0.07 \times 10^{-3} \text{ mm}^2/\text{s}$ (95% CI, 0.04-0.11) for ADC, 0.11 (95% CI, 0.04-0.18) for relative peak intensity and 6 (95% CI, 3-10) percentage points for outflow percentage.

Conclusion

This study shows that DWI and PWI parameters demonstrate reproducibility in UM patients between two different centres, with variabilities smaller than differences typically observed in differential diagnosis or treatment response assessments.

INTRODUCTION

Uveal melanoma (UM) is the most common primary intraocular malignancy in adults, with an incidence of approximately six cases per one million individuals [1]. Conventional imaging modalities for diagnosis and follow-up include ultrasound, fundoscopy, and fluorescein angiography [2]. Treatment options range from enucleation to eye- and vision-preserving therapies, such as episcleral brachytherapy and proton beam therapy (PBT) [1].

In the last decade, the use of magnetic resonance imaging (MRI) in ocular oncology has increased, enabling three-dimensional tumour visualisation [3–7] and non-invasive assessment of tumour biology with functional imaging techniques such as diffusion-weighted imaging (DWI) and perfusion-weighted imaging (PWI) [2,8,9]. With DWI the apparent tissue's diffusion coefficient (ADC) can be assessed, which is a quantitative biomarker of water mobility based on the tissue microenvironment. PWI uses an intravenous contrast agent to assess tumour perfusion, with analysis focussing on the type of time-intensity curve (TIC), as well as TIC-derived measurements such as peak intensity and outflow percentage [10,11].

Different clinical applications of these functional imaging techniques have been proposed, often complementing the conventional ophthalmic imaging modalities. For example, PWI and DWI allow further characterization of UM, which may aid in differential diagnosis [8,10,12]. In PWI, UM often shows a wash-out TIC, whereas progressive TICs, which are more prevalent in benign lesions, have not been reported [8].

Furthermore, Tang et al [11] highlighted the role of PWI in response assessment, with favourable PWI changes observed after radiotherapy, before changes in size were apparent. In a study by Foti et al [13], a significant increase in ADC was shown after radiotherapy. Additionally, quantitative analysis of PWI has been proposed to potentially differentiate between high- and low-risk genetic sub-classes of UM, potentially providing a biopsy-less prognostication [8,14–16].

However, before these quantitative metrics can be used to further guide clinical decision-making, it is essential to determine whether the observed differences reflect true biological changes or merely normal day-to-day variability or inter-scanner differences [17]. Currently, the reproducibility of functional MRI for ocular tumours remains unknown. Therefore, in this study, we aim to assess the reproducibility of perfusion-weighted and diffusion-weighted MRI in patients with uveal melanoma.

METHODS

Study design

In this study, patients with UM and eligible for PBT underwent two MRI-scans, including PWI and DWI sequences, from which the functional parameters were compared and the reproducibility was determined.

This prospective study was conducted in accordance with the principles of the Declaration of Helsinki and was approved by the local ethics committee (registration number NL7343305820). Written informed consent was obtained from all participants.

Patients

Between October 2022 and February 2024, 15 patients diagnosed with UM who were treated with PBT were included in this study at the Leiden University Medical Center (LUMC). Patients were referred to HollandPTC for PBT, where they received four fractions of 15 GyE on four consecutive days [18].

Each patient underwent two MRI scans, including DWI and PWI sequences. These scans were performed over a period of two to six weeks. The first MRI was conducted before clip placement surgery at LUMC and was part of regular clinical care. The second MRI was performed at the first appointment at HollandPTC, at least 7 days after clip placement surgery.

MRI protocol

All MRIs were acquired using a dedicated 3-tesla ocular MRI protocol with a 4.7 cm surface receive coil (Philips Healthcare, Best, the Netherlands). At the LUMC, a 3 T Ingenia Elition MRI was used while at HollandPTC scans were performed with a 3 T Ingenia MRI (both software version 5.6, Philips Healthcare, Best, the Netherlands). The entire scan protocol contained anatomical scans, a dynamic contrast-enhanced scan and the diffusion-weighted scan and was previously described in more detail by Ferreira et al. Scans were optimized to limit the effect of potential eye movement [10,14]. Characteristics of the DWI and PWI scans analysed in this study are summarised in Table 1. The protocols at the two centres differed slightly due to differences in gradient performance and availability of specific software options (Table 1). The angulation of the DWI scans at the second timepoint were chosen such that they matched those of the first timepoint. For PWI, a bolus of 0.1 mmol/kg bodyweight of gadoterate meglumine (LUMC: Clariscan®, GE Healthcare, IL, USA and HollandPTC: Dotarem®, Guerbet Diagnostic Imaging, Villepinte, France) was administered using a power injector with an injection rate of 2 mL/second.

Image analysis

The DWI analysis was performed using Sectra IDS7 (Sectra AB, Linköping, Sweden, version 25.2), with the ADC map as provided by the scanner software. The PWI analysis was performed with Vitrea (Vital Images, Minnetonka, USA, version 7.16.0.703).

For both DWI and PWI, a single-slice oval range of interest (ROI) was manually drawn within the tumour by one observer (PJ) and were reviewed and if necessary adjusted by an ocular MRI expert with over 12 years of experience (JWB). This was done on the tumour slice with the largest lesion. ROI placement was guided by corresponding T1- and T2-weighted imaging to differentiate the tumour from retinal detachment, necrosis, and inflammation (10,14,19,20). For tumours with multiple components the most malignant measurement was chosen (e.g. lowest ADC value for DWI, and highest outflow and/or enhancement for PWI). The same size ROI was placed on the same location across both MRIs for each patient.

For PWI, the tumour was semi-quantitatively assessed by relative peak signal intensity and outflow percentage (Figure 1). The relative peak signal intensity was calculated by dividing the peak signal by the baseline signal averaged over the first 20 seconds (Figure 1). Outflow percentage was defined as the relative difference between peak intensity and the intensity two minutes post-peak (Figure 1). At all timepoints ROI placement was verified to be fully in the tumour, and adjusted if necessary to account for eye motion.

Statistical analysis

The primary aim was to assess functional MRI reproducibility by comparing ADC values, relative peak intensity, and outflow percentages between both timepoints per patient. Mean absolute differences were calculated, and Bland–Altman plots were used for comparison. Furthermore, the reproducibility coefficient (RDC) was calculated for the ADC and relative peak intensity, by using the within-subject coefficient of variation (wCV), following the recommendations of the Quantitative Imaging Biomarkers Alliance (QIBA) [17].

Table 1. PWI and DWI scan parameters.

Scan Name	Voxel size		FOV	Echo train		TE (ms) / TR (ms)		Scan time (mm:ss)	Fat supr.	Additional Parameters
	(mm ³)			length / FA (deg)		(ms)				
DWI (centre 1)	0.63 x 0.63 x 2.4	100 x 100 x 22	100 x 100 x 22	88/90	50/1555	01:33	SPIR	B= 0, 800 s/ mm ² , spin echo		
DWI (centre 2)	0.63 x 0.63 x 2.4	100 x 100 x 22	100 x 100 x 22	88/90	47/1802	01:48	SPIR	B= 0, 800 s/ mm ² , spin echo		
PWI (centre 1)	1 x 1 x 1.62	80 x 80 x 32	80 x 80 x 32	1 / 13	2.3/4.5	03:59	Proset	2 sec/dynamic, TWIST scan acceleration		
PWI (centre 2)	1 x 1 x 1.52	80 x 80 x 32	80 x 80 x 32	1 / 13	2.3/4.5	04:55	Proset	3.8 sec/dynamic		

FOV: field of view, FA: flip angle, TE: echo time, TR: repetition time, SPIR: spectral presaturation with inversion recovery, TWIST: Time-resolved angiography with stochastic trajectories sequence [25].

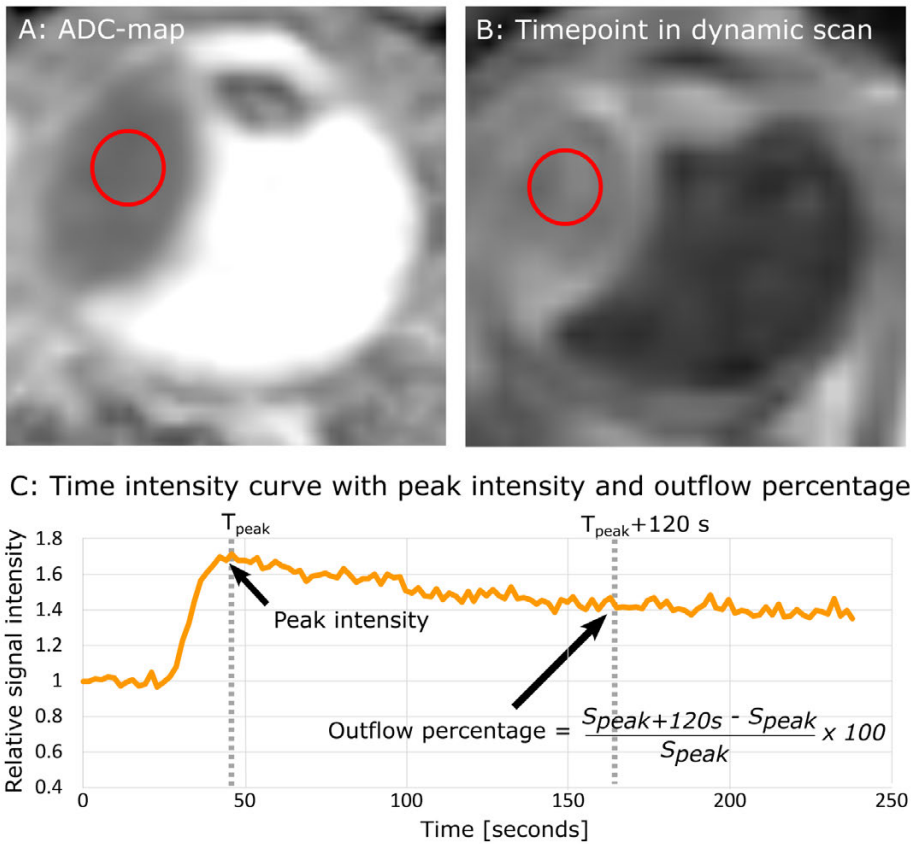


Figure 1. Determination of DWI and PWI parameters. (A) ADC-map with ROI (red circle). (B) One of the timepoints of the dynamic scan with ROI (red circle). (C) Time intensity curve with relative peak intensity and outflow percentage.

RESULTS

Fifteen patients were included in this study, all of whom underwent two MRI scans. One patient was excluded for both the PWI and DWI analysis due to a haemorrhage within the tumour between both time points. Furthermore, two patients did not complete the PWI scan at the second timepoint due to patient preferences or difficulty gaining access to the blood vessel and were therefore excluded for the PWI analysis.

Consequently, a total of 14 patients were included in the DWI analysis, and 12 patients in the PWI analysis, with a mean interval between both scans of 28 ± 8.8 (range: 12-43) days. Patient and tumour characteristics are summarised in Table 2.

Mean ADC values were $1.00 \pm 0.12 \times 10^{-3} \text{ mm}^2/\text{s}$ for the first timepoint and $1.03 \pm 0.08 \times 10^{-3} \text{ mm}^2/\text{s}$ for the second timepoint, with a mean absolute difference between both time points of $0.07 \pm 0.06 \times 10^{-3} \text{ mm}^2/\text{s}$ (95% CI: 0.04-0.11 mm^2/s) (Figure 2). The wCV was 0.066 mm^2/s , corresponding to a reproducibility coefficient of 18.4%.

Mean relative peak intensity values were 1.92 and 2.00, for the first and second timepoint respectively, with a mean absolute difference of 0.11 ± 0.10 (95% CI: 0.04-0.18) (Figure 2). The wCV was 0.046, corresponding to a reproducibility coefficient of 12.7%. For the outflow percentage, mean values were -18% at the first timepoint and -17% at the second timepoint, with a mean absolute difference of 6 ± 6 (95% CI: 3-10) percentage points (Figure 2).

Examples of two patients at both timepoints are shown in Figure 3.

Table 2. Baseline Characteristics of The Subjects

Characteristics	Patients (n = 14)
Age (years)	57 ± 14 (range: 25-72)
Sex – Male	57%
Eye – OD	50%
AJCC Classification: T1 / T2 / T3 / T4*	0 (0%) / 3 (21%) / 10 (71%) / 1 (7%)
Shape: Mushroom / Dome	3 (21%) / 11 (79%)
Prominence at baseline (mm)	7.1 ± 2.6 (range: 3.5-12)
Change in prominence between timepoints (mm)	0.4 ± 0.8 (range -0.5 – 3.0)

Data are presented as percentage (%) for categorical variables and as mean \pm SD for continuous variables. *According to the 8th American Joint Committee on Cancer (AJCC) edition [26].

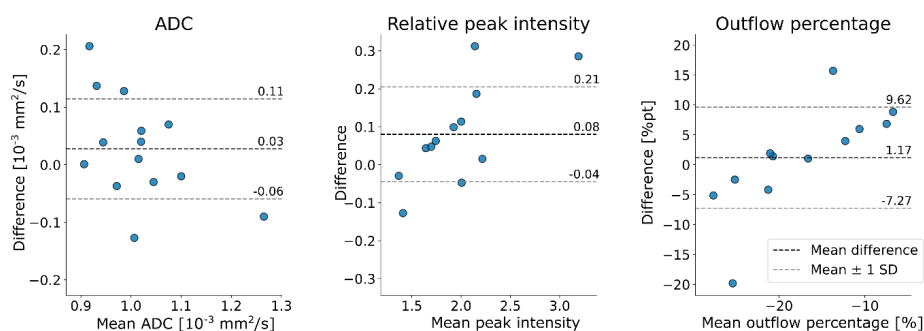


Figure 2. Bland-Altman plots for ADC, relative peak intensity and outflow percentage. Difference is the difference between timepoint 2 and timepoint 1.

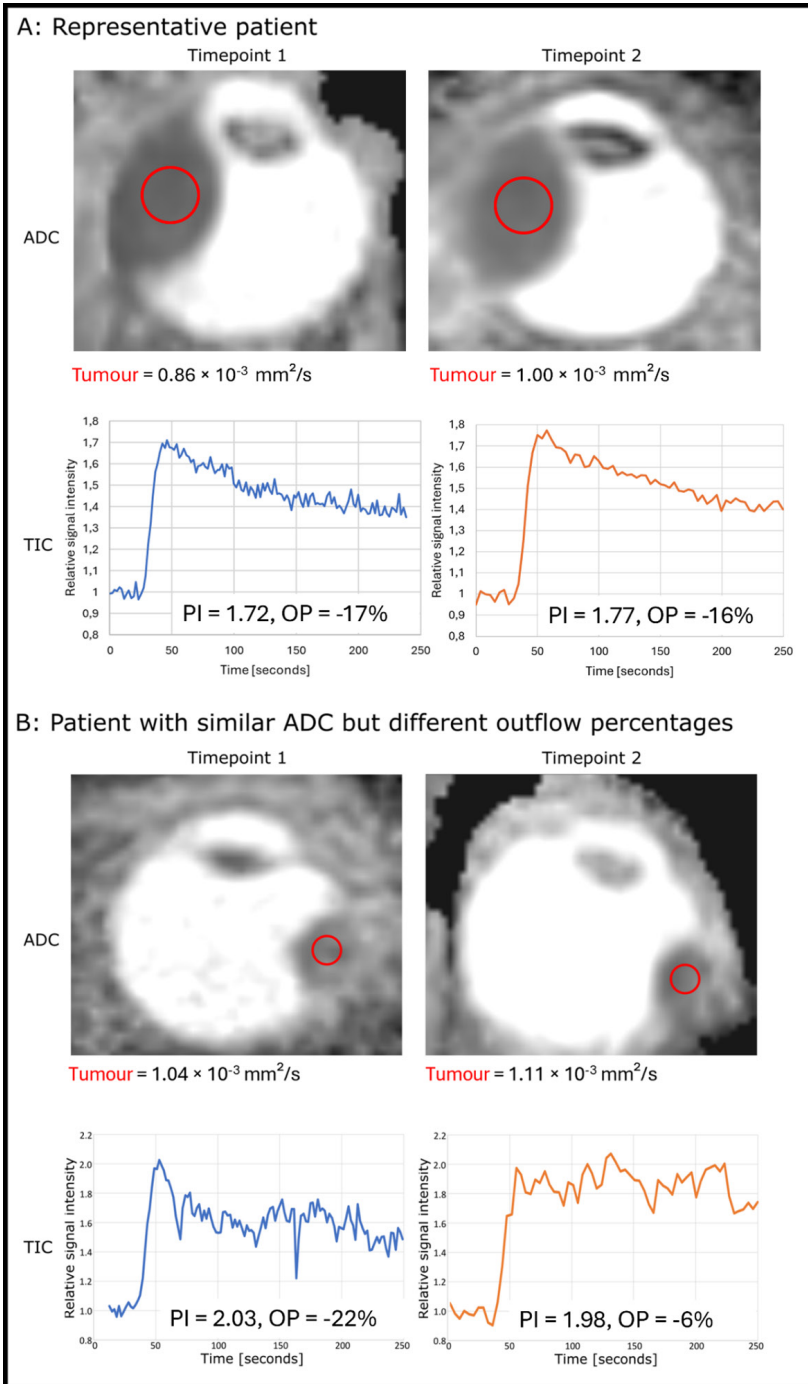


Figure 3. ADC-map and TIC for a representative patient (A) and a patient with large differences in outflow percentage (B).

DISCUSSION

This study evaluated the reproducibility of DWI and PWI for patients with UM. The ADC values observed in this study align with previously findings for UM (4,10,13,15,21). The PWI peak enhancement of our cohort are slightly higher than those reported by Ferreira et al. and Buerk et al (10,22), likely due to the studied patient population, which included patients treated with proton beam therapy, which are typically patients with a larger or juxtapapillary tumour not suitable for brachytherapy.

In the context of differential diagnosis, the reproducibility observed of $0.07 \times 10^{-3} \text{ mm}^2/\text{s}$ for ADC, 0.11 for relative peak intensity, and 6 percentage points for outflow percentage are substantially smaller than the differences reported between UM and benign lesions. For instance, Buerk et al. (24) observed a 0.4 lower peak intensity in benign choroidal lesions, and the review by Jaarsma et al. (20) highlighted larger differences in ADC values between benign and malignant entities, for example $1.11 \times 10^{-3} \text{ mm}^2/\text{s}$ for UM, compared to values of around $1.4 \times 10^{-3} \text{ mm}^2/\text{s}$ for inflammatory lesions and around $1.6 \times 10^{-3} \text{ mm}^2/\text{s}$ for other benign orbital lesions. This supports the clinical relevance of functional MRI metrics and their potential utility in distinguishing tumour types.

Similarly, studies evaluating treatment response with DWI or PWI reported larger differences after treatment than the observed reproducibility, except for smaller differences in outflow percentage observed early after proton beam therapy. For example, Foti et al. (13) noted substantial changes in ADC values after PBT, for example from 1.03 to $1.26 \times 10^{-3} \text{ mm}^2/\text{s}$ at one month post treatment, a change threefold larger than the reproducibility. Furthermore, Tang et al. (11) described an average absolute decrease of more than 0.5 in relative peak intensity, which is five times larger than the method's reproducibility. The same study used a threshold of 5% for a visually distinguishable difference in outflow percentage after treatment, which corresponds to the reproducibility found in this study. Therefore, differences larger than 5% can most likely be attributed to true biological changes and not just day-to-day physiological or measurement variations. All in all, this shows that the reproducibility observed in this paper is sufficient for differential diagnosis and treatment response assessment.

In this study, we focused on reproducibility under the premise of realistic clinical patient re-evaluation in a multi-centre setting, i.e., patients returning for a follow-up scan. Hence possible differences in patient, equipment and eye position are expected. A reliable MRI biomarker needs to be robust to such deviations. Therefore, a reproducibility analysis was chosen instead of a repeatability analysis.

There are multiple factors that could affect the reproducibility. An important one is the consistency in the identification of the ROI between the different MRI scans. Uveal melanomas can be heterogeneous [10], resulting in different values based on the placement of the ROI. In this study the ROIs were drawn manually by one person, as in clinical practise. Even though all ROIs used in this study were checked by an expert with 10+ years of experience in ocular MRI, we can expect that the ROI placements will not be perfectly consistent between time points. However, a perfect match of manually defined ROIs also cannot be expected in clinical practice. Therefore, it is useful to incorporate potential inconsistencies in region definition into account in assessing these scans in clinical practice. In this context, 3D ROI determination could improve reproducibility, but might not be an accurate representation of the current clinical workflow. One patient showed a visible increase in tumour volume between the two timepoints, most likely due to rupture of Bruch's membrane. Although differences in PWI and DWI parameters for the tumour were small, an additional analysis in the vitreous humour was performed to verify these results (Supplementary Figure 1).

Furthermore, the two MRI-scans compared were performed at two different centres with MR-scanners from the same vendor and with comparable scan protocols. On average, both the DWI and PWI measurements were slightly larger at the second centre. Differences between the scan protocols included different temporal resolutions for the PWI scans and the use of TWIST scan acceleration in centre 1, which was not available at centre 2. Both these factors may have an effect on, for example, peak intensity. Therefore, reproducibility within the exact same scanner might be higher than the reproducibility in this study. However, the reproducibility between different centres with scanners from different vendors might be lower.

Limitations

One of the main limitations of the study is the possible effect of the clip placement surgery, which was performed between both timepoints. Additionally, the relatively long interval between scans, on average 28 days, may have allowed for biological changes. Although UM is considered a slow growing tumour [23,24], some patients did show an increase in tumour prominence. These factors could lead to an overestimation of the variability and thus affect the assessment of reproducibility. Nonetheless, the observed reproducibility remains more than sufficient for current clinical applications, such as differential diagnosis and treatment response assessment.

Another limitation of this study is the small sample size, which reduced statistical power and prevented subgroup analyses, such as assessing reproducibility across

tumour sizes. Furthermore, the cohort consisted exclusively of patients referred for PBT. Future studies with larger and more diverse populations could validate these findings and examine reproducibility across different clinical subgroups.

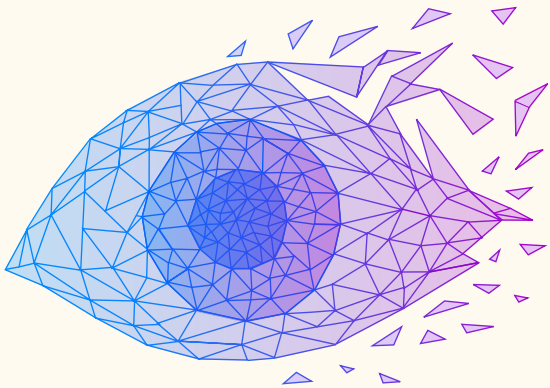
Conclusion

This study shows that DWI and PWI parameters demonstrate good reproducibility in uveal melanoma patients between two different centres, with variability smaller than differences typically observed in differential diagnosis or treatment response assessment. These findings support the use of functional MRI parameters as imaging biomarkers for these purposes in both clinical practice and research.

REFERENCES

1. Jager MJ, Shields CL, Cebulla CM, et al. Uveal melanoma. *Nat Rev Dis Primers*. 2020 Apr 9;6(1):24.
2. Solnik M, Padaszyńska N, Czarnecka AM, et al. Imaging of Uveal Melanoma—Current Standard and Methods in Development. *Cancers (Basel)*. 2022 Jun 27;14(13):3147.
3. Niendorf T, Beenakker JWM, Langner S, et al. Ophthalmic Magnetic Resonance Imaging: Where Are We (Heading To)? *Curr Eye Res*. 2021 Sep;46(9):1251–70.
4. Erb-Eigner K, Willerding G, Taupitz M, Hamm B, Asbach P. Diffusion-Weighted Imaging of Ocular Melanoma. *Investigative Radiology*. 2013 Oct;48(10):702.
5. Graaf P de, Pouwels PJW, Rodjan F, et al. Single-Shot Turbo Spin-Echo Diffusion-Weighted Imaging for Retinoblastoma: Initial Experience. *American Journal of Neuroradiology*. 2012 Jan 1;33(1):110–8.
6. Sepahdari AR, Aakalu VK, Setabutr P, Shiehorteza M, Naheedy JH, Mafee MF. Indeterminate Orbital Masses: Restricted Diffusion at MR Imaging with Echo-planar Diffusion-weighted Imaging Predicts Malignancy. *Radiology*. 2010 Aug;256(2):554–64.
7. Li DJ, Yang WL, Wang ZY, et al. [Comparative analysis on the significances of contrast-enhanced ultrasound and dynamic contrast-enhanced magnetic resonance imaging in uveal melanoma diagnosis]. *Zhonghua Yan Ke Za Zhi*. 2018 Mar 1;54(3):194–8.
8. Jaarsma-Coes MG, Klaassen L, Marinkovic M, et al. Magnetic Resonance Imaging in the Clinical Care for Uveal Melanoma Patients-A Systematic Review from an Ophthalmic Perspective. *Cancers (Basel)*. 2023 May 30;15(11):2995.
9. Foti PV, Travali M, Farina R, et al. Diagnostic methods and therapeutic options of uveal melanoma with emphasis on MR imaging—Part I: MR imaging with pathologic correlation and technical considerations. *Insights into Imaging*. 2021 Jun 3;12(1):66.
10. Ferreira TA, Jaarsma-Coes MG, Marinkovic M, et al. MR imaging characteristics of uveal melanoma with histopathological validation. *Neuroradiology*. 2022 Jan;64(1):171–84.
11. Tang MCY, Ferreira TA, Marinkovic M, et al. MR-based follow-up after brachytherapy and proton beam therapy in uveal melanoma. *Neuroradiology*. 2023 Aug 1;65(8):1271–85.
12. Yuan Y, Kuai XP, Chen XS, Tao XF. Assessment of dynamic contrast-enhanced magnetic resonance imaging in the differentiation of malignant from benign orbital masses. *European Journal of Radiology*. 2013 Sep 1;82(9):1506–11.
13. Foti PV, Longo A, Reibaldi M, et al. Uveal melanoma: quantitative evaluation of diffusion-weighted MR imaging in the response assessment after proton-beam therapy, long-term follow-up. *Radiol med*. 2017 Feb 1;122(2):131–9.
14. Ferreira TA, Grech Fonk L, Jaarsma-Coes MG, van Haren GGR, Marinkovic M, Beenakker JWM. MRI of Uveal Melanoma. *Cancers*. 2019 Mar;11(3):377.
15. Kamrava M, Sepahdari AR, Leu K, et al. Quantitative multiparametric MRI in uveal melanoma: increased tumor permeability may predict monosomy 3. *Neuroradiology*. 2015 Aug;57(8):833–40.
16. Wei W, Jia G, von Tengg-Kobligh H, et al. Dynamic Contrast-Enhanced Magnetic Resonance Imaging of Ocular Melanoma as a Tool to Predict Metastatic Potential. *J Comput Assist Tomogr*. 2017;41(5):823–7.
17. Shukla-Dave A, Obuchowski NA, Chenevert TL, et al. Quantitative Imaging Biomarkers Alliance (QIBA) Recommendations for Improved Precision of DWI and DCE-MRI Derived Biomarkers in Multicenter Oncology Trials. *J Magn Reson Imaging*. 2019 Jun;49(7):e101–21.
18. Rasch C, Bakker P, Rodrigues M, et al. PO-1587 two years of ocular proton therapy in The Netherlands, clinical results. *Radiotherapy and Oncology*. 2023 May 1;182:S1288–9.

19. Jaarsma-Coes MG, Klaassen L, Marinkovic M, et al. Magnetic Resonance Imaging in the Clinical Care for Uveal Melanoma Patients—A Systematic Review from an Ophthalmic Perspective. *Cancers*. 2023 Jan;15(11):2995.
20. Foti PV, Inì C, Broggi G, et al. Histopathologic and MR Imaging Appearance of Spontaneous and Radiation-Induced Necrosis in Uveal Melanomas: Initial Results. *Cancers (Basel)*. 2022 Jan 2;14(1):215.
21. Sepahdari AR, Politi LS, Aakalu VK, Kim HJ, Razek AAKA. Diffusion-weighted imaging of orbital masses: multi-institutional data support a 2-ADC threshold model to categorize lesions as benign, malignant, or indeterminate. *AJNR Am J Neuroradiol*. 2014 Jan;35(1):170–5.
22. Buerk BM, Pulido JS, Chiong I, et al. VASCULAR PERFUSION OF CHOROIDAL MELANOMA BY 3.0 TESLA MAGNETIC RESONANCE IMAGING. *Trans Am Ophthalmol Soc*. 2004 Dec;102:209–18.
23. Char DH, Kroll S, Phillips TL. Uveal melanoma. Growth rate and prognosis. *Arch Ophthalmol*. 1997 Aug;115(8):1014–8.
24. Augsburger JJ, Gonder JR, Amsel J, Shields JA, Donoso LA. Growth rates and doubling times of posterior uveal melanomas. *Ophthalmology*. 1984 Dec;91(12):1709–15.
25. Tudorica LA, Oh KY, Roy N, et al. A feasible high spatiotemporal resolution breast DCE-MRI protocol for clinical settings. *Magnetic Resonance Imaging*. 2012 Nov 1;30(9):1257–67.
26. AJCC Ophthalmic Oncology Task Force. International Validation of the American Joint Committee on Cancer's 7th Edition Classification of Uveal Melanoma. *JAMA Ophthalmol*. 2015 Apr;133(4):376–83.



Chapter 9

Discussion

The work in this thesis was conducted as part of the clipless ocular proton beam therapy project, a multidisciplinary, multi-centre project aimed at developing an ocular proton therapy workflow without surgical placement of tantalum clips. In particular, my contribution focused on further incorporation of magnetic resonance imaging and how it could aid in the treatment planning and follow-up of uveal melanoma patients treated with proton therapy.

Fortunately, local control after ocular proton beam therapy is high. However, up to 70% of uveal melanoma patients treated with proton beam therapy will be severely visually impaired 5 years after therapy [1]. Furthermore, around half of patients will die from metastases within 15 years [2]. Research on improving therapy for the primary tumour should therefore aim to preserve or approximate current local control, while improving quality of life, which needs to be a recurrent theme throughout the entire process: for example, during treatment, quality of life can be improved by making the treatment less invasive: with a clipless approach, eliminating the need for surgery prior to radiotherapy. Treatment itself should focus on preserving local control while minimizing vision loss. After treatment, patients are often anxious about the effectiveness of treatment and the development of metastases. In this context, reassurance could potentially be provided through earlier information on tumour response. This chapter focuses on an image-based clipless workflow, which could contribute to improvement in several areas. Furthermore, I will explore alternative approaches which could be used to improve visual acuity after proton beam therapy.

9.1 IMAGE-BASED CLIPLESS OCULAR PROTON THERAPY: WORKFLOW CONSIDERATIONS

Currently, tantalum clips are placed surgically before the start of radiotherapy. This is a burden for patients, as general anaesthesia is needed, and most patients perceive pain or discomfort afterwards. The clip surgery also results in delay in the treatment process, due to the recovery time needed and the availability of the operating room. A shorter, clipless, workflow could potentially contribute to optimizing survival, as delays in treatment can lead to an increased metastatic risk [3].

Several changes are required to perform image-based clipless ocular proton therapy. In the current workflow, many different uncertainties are combined in target volume definition, while patient positioning is very precise. In an image-based clipless workflow, these uncertainties in target volume definition will consist of less elements, since delineation would mainly be performed on one modality. However, without clips,

positioning of the eye and tumour will most likely be less accurate. In Figure 1, a new workflow is proposed and compared to the current workflow. In Table 1 and in the paragraphs below, uncertainties in both workflows are explored: while not intended as a complete margin recipe, they describe the shift in uncertainties between the current workflow and an image-based, clipless alternative.

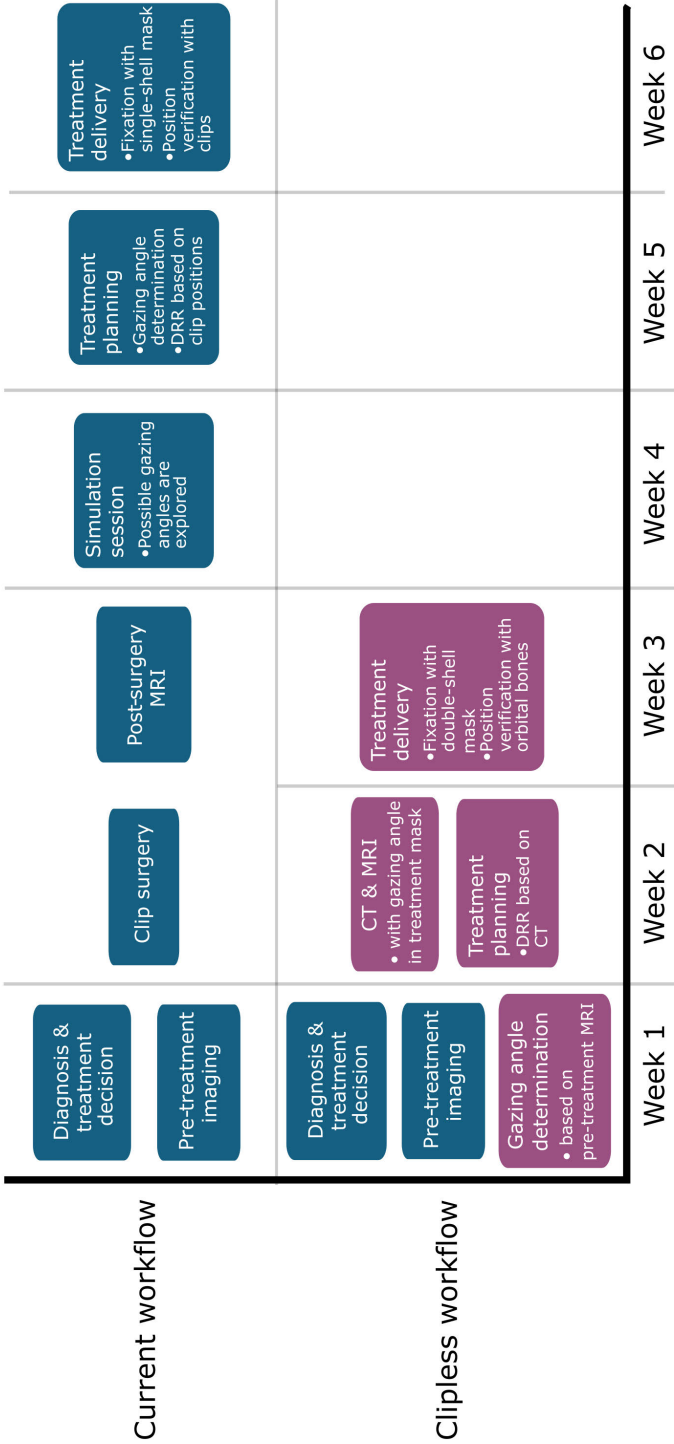


Figure 1: The current workflow and a proposal for an image-based, cliplless workflow. Changes are shown in pink. The timeframe shown is the shortest timeframe possible, variations may occur due to patient preferences or circumstances, OR and MRI planning, and eye treatment room availability. The timeframes described may differ in other centres.

Table 1: Shifts in uncertainties between the conventional and image-based, clipless workflow.

	Current workflow		Image-based clipless workflow	
	<i>Effect</i>	<i>Magnitude [mm]</i>	<i>Effect</i>	<i>Magnitude [mm]</i>
Target volume definition	Combined uncertainty of the polynomial tumour model on the fundus view	<i>~1-2 [4, 5]</i>	Target volume delineation:	0.4 [6]
	- uncertainty in clip-tumour distances		- Inter-observer variation of target volume delineation on MRI	
	- more than 1 possible shape of tumour base			
	- more than 1 possible option to place tumour base within clips			
	Thickness measurements			
	- difference 2D US/3D MRI	<i>0.3 [7]</i>		
	Use of a polynomial model to describe tumour	<i>0.6</i>	Not applicable	-
	Changes in tumour thickness between imaging and treatment	<i>0.4 [8]</i>	Shorter workflow but small increase possible	0.2 [8]
Patient positioning	Set-up: eye positioning based on clip match	<i>0.3 [5]</i>	Set-up: eye positioning based on orbital bone match	
			- MR delineation \diamond DRR	<i>~0.5</i>
			- Positioning based on orbital bones	<i>~0.4</i>

Uncertainties that are present in both workflows are not shown in this table. Numbers in italic are not a part of the current margin calculations, but are included in the target volume delineation.

Target volume delineation

Target volume definition in model-based treatment planning systems consists of determination of the tumour thickness, delineation of the tumour base, and choosing the best-fitting polynomial model to form the tumour top. Tumour thickness can be measured using both ultrasound and MRI. In this thesis, we showed that dedicated ocular MRI scans can be geometrically accurate (chapter 3, [9]) and that the mean absolute difference between these modalities was 0.3 mm for posterior tumours, with larger differences occurring in anteriorly located tumours (chapter 4, [7]). In these anteriorly located tumours, MRI seems more reliable due to visualization of the entire tumour, which is not always possible with the limited penetration depth of UBM. The delineation of the tumour base is performed based on the basal diameters, clip-tumour distances, and in some cases, the distance between tumour and optic nerve or ciliary body. Again, these clip-tumour distances can be measured during surgery or on MRI, with both methods having advantages and disadvantages. A previous study at our centre reported a mean absolute difference of 2.0 mm in clip-tumour distances, with larger deviations when the tumour cast a shadow under illumination through the pupil during surgery [4]. In these cases, MRI is more reliable. However, flat tumours or flat extensions might be difficult to visualize on MRI, in which case the surgical measurements might be preferred. Even when clip-tumour distances are certain, several options often remain for positioning the base between the clips and defining its shape (Figure 2), especially in treatment planning systems which do not support integration of imaging. In clinical practice, this effect is mitigated partly by performing a side-by-side comparison of the delineated tumour base and fundus imaging or MR imaging. However, residual uncertainty often persists. No studies have been performed on inter-observer variability of tumour base delineation in model-based systems. However, in my experience, different observers may end up with different base delineations.

After placement of the tumour base, a polynomial model is used to generate a 3D tumour volume. In chapter 5 [10], we demonstrated that tumour models like those used in treatment planning systems can accurately describe tumours if the correct degree for the polynomial is selected. Nonetheless, a median overestimation of 0.6 mm is present at a coverage level of 98% (Supplementary Table 6, chapter 5, [10]). Furthermore, choosing the correct degree is not always simple, since there is no overlay possible between the target volume in the treatment planning system and the tumour on MRI. This functionality does exist in other treatment planning systems such as OCTOPUS and RayOcular [11].

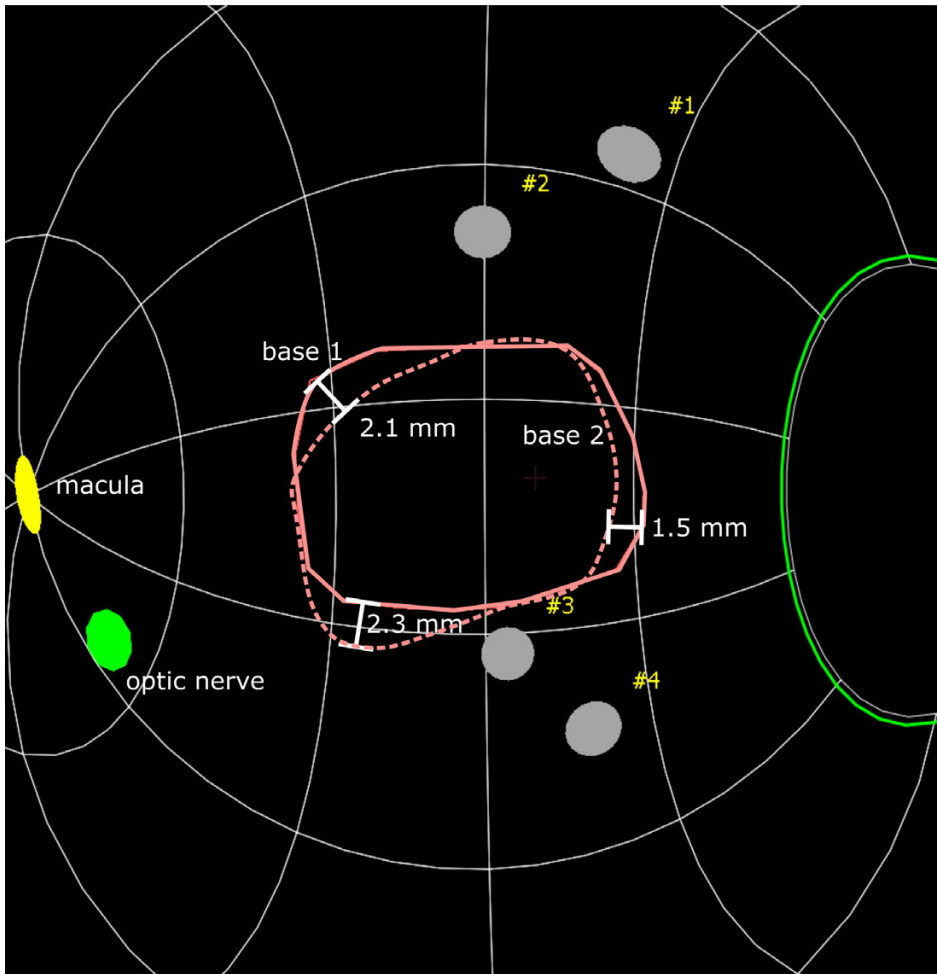


Figure 2: With the same clip-tumour distances, different options (base 1 and base 2) for placement of the tumour base within the fundus view are possible, with distances between the two contours of up to approximately 2.3 mm.

In steps described above, often, the largest measurement (or the measurement resulting in the largest target volume) is chosen to ensure tumour coverage, since no visual confirmation of one or the other option can be provided in the current treatment planning systems. These choices lead to a systematic overestimation of the tumour volume. An example of these choices is shown in Table 2. In the few papers on margins in ocular proton therapy, target volume delineation uncertainties are not explicitly considered [5] and are assumed to be included in the delineated target volume [12]. In an image-based clipless workflow, the tumour would be delineated on MR images, eliminating the previously mentioned uncertainties. In this thesis, we showed that

an eye-specific MRI protocol can produce geometrically accurate images of the eye, which enables using these scans for treatment planning (chapter 3, [9]). However, there remains an interobserver variability in the delineation of 0.4 mm [6], which is smaller than the uncertainties in target volume delineation in the current workflow. This variability is largest at the tumour edge. In both workflows, flat extensions and very thin tumours can be difficult to distinguish on MRI. This might be improved by accurate fusion of MRI and fundus images [13], or potentially by an increased spatial resolution of the MR images, although for some patients, clips may still be required.

A: Tumour measurements

	Ultrasound [mm]	MRI [mm]	Delineated GTV
Thickness	10.5	9.8	10.5
Largest diameter	16.0	14.3	17.0
Perpendicular diameter	12.4	13.0	13.5

B: Clip-tumour distances

	Surgery [mm]	MRI [mm]	Delineated GTV
Clip 1 - tumour	6.5	6.0	6.0
Clip 2 - tumour	0.5	2.9	0.5
Clip 3 - tumour	1.0	2.9	1.0
Clip 4 - tumour	8.5	9.2	8.5

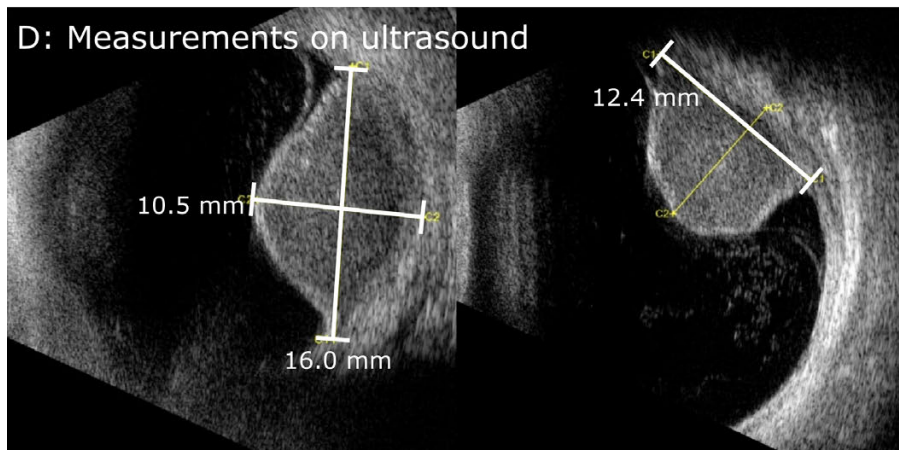
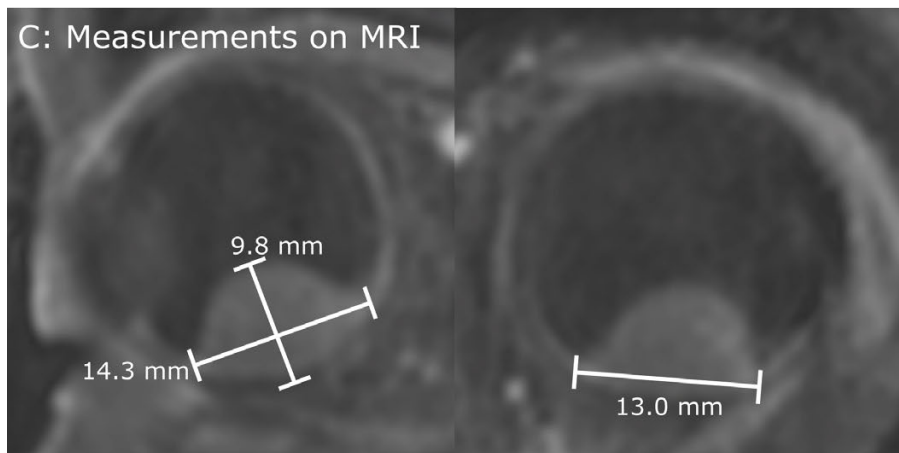


Figure 3: Example of patient where the resulting GTV is larger than the tumour measurements. Often, the measurement resulting in the largest tumour is chosen, in order to cover the entire tumour. This results in a systematic overestimation of the tumour: the diameters of the delineated GTV are 1.0 and 0.5 mm larger than the largest measured diameter.

In the current workflow, tumour growth is not considered, as uveal melanoma is regarded as a slow growing tumour. Given the high local control rates, it seems patients are treated adequately. However, we showed that tumours can change in the weeks between imaging and treatment delivery [8]. For example, an average increase in thickness of 0.4 mm was observed, which could be halved in the shorter clipless alternative (Figure 3).

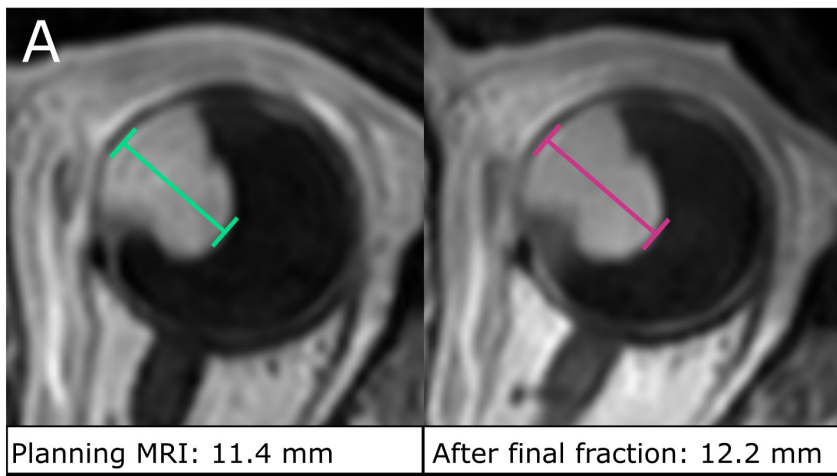
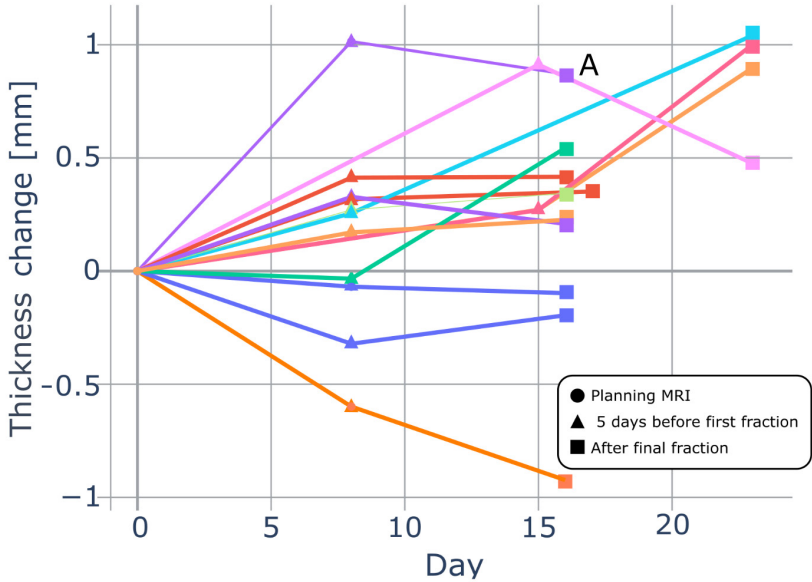


Figure 4: Changes in tumour thickness in ocular proton therapy [8]: a mean increase of 0.4 mm (range -0.9 – 1.0 mm) was observed between the planning MRI and end of treatment. Between the planning MRI and MRI 5 days before the first fraction (interval of 8 days), the

mean increase was 0.2 mm. An example of a patient with a 0.8 mm increase in prominence is shown in (A).

The work in this thesis can also be applied in other contexts, for example in ocular MR-linac treatments. Currently, there is no literature available about treating uveal melanoma on MR-linacs. A benefit would be the visualization of the target volume in the treatment position, instead of bony anatomy or tantalum clips only, potentially enabling smaller treatment margins compared to stereotactic radiotherapy. However, similar to SRT, the dose on the organs at risk might be higher compared to proton therapy, due to the larger lateral penumbra and distal fall-off of photons.

Patient positioning

The tantalum clips enable very accurate positioning, with a low remaining set-up uncertainty of about 0.3 mm [5, 14]. In a cliplless workflow, set-up uncertainty will most likely be larger: it consists of conversion of the MR delineation into a digitally reconstructed radiograph (DRR) to perform the bone match, the accuracy of the bone match itself, the difference in position of the eye within the orbit between a supine (imaging) and seated (treatment) position, and day-to-day variations in effective gazing angle. A preliminary analysis was performed within our project on a retrospective dataset [15] to quantify this combined effect. A bone match was performed on the kV images taken during patient positioning before the start of each fraction, where the first fraction served as a reference. Comparing the bone-matched clip positions with clip-matched clip positions, the average standard deviation was around 0.4 mm in each direction in patients gazing with their affected eye, giving an indication of the set-up error in a cliplless workflow. However, this number does not contain the contribution of the conversion of the supine CT data to a DRR and needs to be verified in a prospective cohort [16]. Here, the double-shell immobilization mask proposed for the cliplless workflow may contribute to minimizing rotations and therefore lowering the set-up uncertainty [17].

Other benefits of an image-based, cliplless workflow

Switching to an image-based, cliplless workflow has additional consequences, and not all of them may have an impact on irradiation of the target. For example, the image-based approach may improve definition of the organs at risk by improving the placement of the eye model. In model-based treatment planning systems, an ellipsoid eye model is constructed using the axial length and transverse diameter of the patient's eye. This eye model is then fitted to the location of the tantalum clips. The verification of this eye model is limited to the clip locations, leaving an uncertainty for the rest of the eye. In an image-based workflow, the placement and size of the eye model can be verified, decreasing this uncertainty.

Furthermore, in the current approach, the same mass density of 1.05 g/cm^3 is used for the entire eye, based on a mean of the densities of the eyes, liver and pancreas [18]. Preliminary results from our project show that although the mass density is similar between patients, the density of the vitreous is likely lower than the used value, and range differences up to 0.7 mm for posterior tumours could be present. In an image-based workflow, it would be possible to use the Hounsfield units from CT to determine the stopping power for each structure in the beam path, instead of the average value that is currently applied. This could decrease the contribution of density uncertainties in the distal margin, currently estimated at 1 mm [5].

Additionally, the optic nerve is modelled as a tube with fixed orientation and position. The true optic nerve position in the gazing angle used for treatment cannot be verified in the current treatment planning systems, which would be possible in the new workflow. Similarly, the distance from macula to optic nerve is assumed to be identical for all patients in the current eye model, while large studies show a standard deviation of 0.3 mm in macula-disk distance [19]. Although the macula is not visible on MRI, fusion with fundus imaging [13] or implementing an OCT measurement [20] could improve the placement of the macula in the eye model. Previous studies on macula and optic nerve dose report that they are independent predictors of vision loss after ocular proton therapy [21, 22]. Improving accuracy of OAR modelling could therefore improve sparing of these organs at risk during treatment planning, possibly preserving more vision.

Another advantage of a clipless workflow is that eliminating the clip surgery may reduce treatment-related costs, as OR time, surgeon time, and hospitalization are no longer required. Additionally, a clipless workflow could aid in making ocular proton therapy possible for frail patients who are not able to undergo general anaesthesia.

Context and conditions

In this subchapter, several uncertainties about the current and proposed clipless workflow are discussed. This comparison is based on the workflow as depicted in Figure 1 and includes a high-quality eye-specific MR and CT scan. Without these imaging modalities, uncertainties might be larger. In this thesis, we showed that the 3D MRI sequences proposed in earlier papers [4] are geometrically accurate, and thus suitable for radiotherapy planning (chapter 3, [9]).

The workflow above describes the use of MRI for delineation and verification of the eye model, which requires a treatment planning system that is able to integrate 3D imaging with the eye model. Currently, OCTOPUS and RayOcular are the only

treatment planning systems supporting this function [11]. OCTOPUS was in-house developed by the German Cancer Research Centre in collaboration with the Helmholtz-Zentrum Berlin and Charité [23] and its development is discontinued [11].

The uncertainties described above and in Table 1 cannot simply be added, as they might be interdependent. A careful margin determination must be performed for the new workflow. In the evaluation of this new margin, the systematic overestimations that are currently part of the target volume delineation must be considered: even if a slightly larger margin would be necessary, the total irradiated volume might still be smaller, as the current systematic overestimations are eliminated.

Not all uncertainties affect irradiated volume equally, due to the single beam set-up conventionally used in ocular proton therapy. Ultimately, irradiated volume is determined by the shape of the aperture and the penetration depth. Factors that have a large effect on one or both of these include the size of the tumour base and tumour thickness, whereas the influence of using a polynomial tumour model is likely smaller. Whether these uncertainties have an effect on aperture size or penetration depth (i.e. lateral or distal margin) depends on tumour location and gazing angle.

A clipless workflow might not be possible or beneficial for all patients. For example, patients with flat tumours might still need clips to reliably delineate the tumour, since flat tumours are sometimes difficult to distinguish on MRI. This might be especially the case when these tumours extend peripherally, in areas where fundus imaging is more difficult as well. For patients with tumours located 2-3 mm from the optic nerve or macula, where the size of the needed margin may result in either hitting or avoiding the structure. Here, the benefits of using 3D imaging could be combined with the benefits of accurate patient positioning with clips, although the longer treatment process due to the clip placement must be considered as well.

The workflow as shown in Figure 1 is based on a seated treatment position with a fixed, horizontal beamline. In the recent years, gantry-based systems with added patient-specific apertures have been proposed [24-26]. In such a set-up, no correction is needed between supine and seated positions, since both imaging and treatment are performed in a supine position. However, gantry-based solutions generally have a larger distal fall-off and lateral penumbra than dedicated horizontal beamlines, due to the redirection of the proton beam and the added equipment to use apertures on the gantry. The PTCOG Ocular Statement reported median distal falloffs of 1.0 mm (0.9-1.2 mm) for dedicated horizontal beamlines and 2.8 mm (1.5-6.0 mm) for gantry-based high-energy systems [11]. Differences in lateral penumbra were smaller, with

median lateral penumbras of 1.4 mm (1.2-1.9 mm) for dedicated horizontal beamlines and 1.6 mm (1.2-3.0 mm) for gantry-based systems. Depending on the exact set-up, I hypothesize that gantry-based ocular proton therapy could achieve similar or potentially smaller margins than the fixed horizontal beamlines.

Fractionation schemes

Dose on the organs at risk can be minimized by trying to minimize the irradiated volume, as described earlier. Another option would be to reconsider the total dose given to this patient group. In ocular proton therapy, the most commonly used fractionation schemes are 4-5 fractions with a total dose of 56-70 GyE [27]. In most centres, all tumours receive an identical dose. Some centres have reported outcomes for a lower dose for small to medium-sized tumours: for example, in a retrospective cohort of over 1000 patients with small to medium-sized tumours near the optic nerve or fovea, Lane et al. [28] reported a non-significantly higher remaining visual acuity in patients treated with a reduced dose of 50 GyE, compared to the standard dose of 70 GyE, both given in 5 fractions. In this study, severe visual impairment (visual acuity $\leq 6/60$) occurred in 50.7% of patients in the low-dose group, compared to 59.3% in the high-dose group ($p=0.056$). This possible improvement in visual acuity did not affect local control or disease-specific survival. Another earlier randomized controlled trial [29] compared the same doses in a group of 188 patients and found no improvement in visual acuity, but patients receiving the lower dose experienced significantly less visual field loss. Similar to the retrospective cohort, local recurrence and metastatic disease were not significantly different between the two dose groups. Both studies suggest that lowering the dose to 50 GyE can be done safely. Although differences in visual acuity were not significant, reducing the dose to 50 GyE in patients with small- and medium-sized might be reasonable.

Ocular proton therapy is traditionally hypofractionated. One study compared a conventional scheme of 4 x 13 GyE to a moderately hypofractionated scheme of 8 x 6.5 GyE for large uveal melanomas. While local control was similar with both schemes, no clear benefit in toxicity was observed [30]. Lowering the dose per fraction further (e.g. 30x2 GyE instead of 4x15 GyE) would result in an even lower biologically effective dose, potentially resulting in a lower local control, unless total dose is increased to compensate. Furthermore, the current hypofractionated schemes have logistic advantages, since patients often travel far from home to a specialized proton centre. Therefore, I would suggest first considering the total dose before adjusting the number of fractions.

9.2 TREATMENT RESPONSE ASSESSMENT

Even though proton beam therapy achieves excellent local control rates in uveal melanoma, patients report anxiety in the post-treatment period, partly due to uncertainty regarding the effectiveness of therapy [31]. Identifying and validating early biomarkers of treatment response could help reassure patients and ultimately improve quality of life during follow-up.

Response to radiotherapy can be classified into three categories: local control, in which the tumour responds well to treatment; non-response, in which tumour growth persists; and local recurrence, in which the tumour initially appears controlled but subsequently regrows. True non-responding uveal melanomas after proton therapy are rare and are not commonly distinguished from recurrences in the literature. Local recurrences can be further subclassified: marginal recurrences arise at the tumour edge, global or in-field recurrences affect larger portions or the entire tumour, and distant recurrences occur at sites not adjacent to the primary tumour.

With changes in workflow, such as the cliplless workflow, the adoption of smaller margins, or a lower dose, assessing treatment response will become particularly relevant. Perfusion-weighted MRI is shown to be an early marker of treatment response, even before a measurable reduction in tumour size is observed [32]. However, this is most likely primarily useful for detecting global recurrences or identifying non-responders, as marginal recurrences may initially be too flat or small to visualize reliably on MRI. In this thesis, we showed that a more complex, quantitative analysis of dynamic contrast-enhanced MRI using Tofts modelling does not substantially improve assessment of treatment response (chapter 7, [33]). Furthermore, current clinical semi-quantitative perfusion-weighted imaging methods have been shown to be reproducible and suitable for routine evaluation (chapter 8, [34]).

For detection of marginal recurrences, funduscopy combined with fundus angiography remains the primary imaging modality. Emerging imaging modalities may provide additional support for assessing treatment response in the future. For instance, after brachytherapy, mottling patterns observed on fundus autofluorescence imaging correspond to irradiated areas [35]. This approach could potentially be applied following proton therapy to verify the radiation field and monitor tumour response. A limitation of fundus autofluorescence, however, is its reduced applicability for peripherally located lesions.

In addition to anxiety regarding the treatment of the primary tumour, patients often experience concern about the development of metastases. Historically, few life-prolonging treatment options were available [36]. In recent years, tebentafusp has demonstrated a survival benefit in patients with metastatic uveal melanoma [37, 38]. Moreover, ongoing studies are investigating the adjuvant use of tebentafusp [39]. In this context, non-invasive methods to identify high-risk patients may provide additional clinical value. In this thesis, we showed that using ellipsoid tumour models based on 2D measurements are not a good predictor of tumour volume in individual patients (chapter 3, [40]), and should therefore not be used for the identification of high-risk patients.

Finally, continued attention to psychological support remains essential throughout patient follow-up.

9.3 CONCLUSION

In this thesis, we demonstrated that MRI is geometrically accurate and suitable for treatment planning in uveal melanoma. We quantified differences between tumour measurements obtained from MRI and conventional methods, and between MRI-based volumes and tumour models. These findings provide a foundation for an image-based, clipless workflow. Such a workflow could offer several advantages, including the elimination of surgical clip placement and the potential reduction of the effectively irradiated volume. Nonetheless, it is conceivable that, for specific patient subgroups, the use of tantalum clips may remain necessary.

Alternative strategies exist for the treatment of larger ocular tumours, some of which may provide advantages relative to dedicated horizontal eye lines. For example, gantry-based proton therapy systems can potentially achieve comparable treatment outcomes.

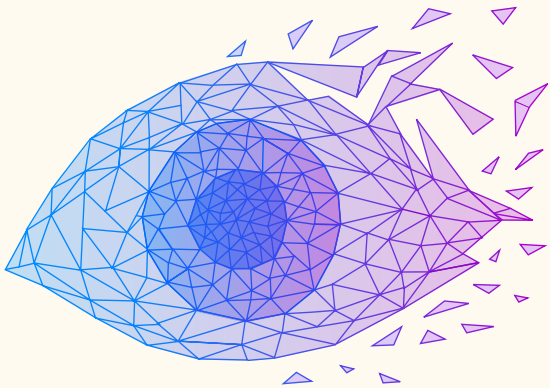
In addition to its role in treatment planning, MRI also has a role in follow-up after treatment. In this thesis, we demonstrated that semi-quantitative MRI methods are sufficient for monitoring treatment response and are reproducible, supporting their use in clinical practice. Overall, these results highlight the feasibility and potential benefits of integrating high-resolution MRI into the treatment planning and follow-up of ocular proton therapy, contributing to a more patient-friendly and accurate treatment.

REFERENCES

1. Marinkovic M, Pors LJ, van den Berg V, Peters FP, Schalenbourg A, Zografos L, et al. Clinical Outcomes after International Referral of Uveal Melanoma Patients for Proton Therapy. *Cancers (Basel)*. 2021;13:doi: 10.3390/cancers13246241.
2. Kujala E, Makitie T, Kivela T. Very long-term prognosis of patients with malignant uveal melanoma. *Invest Ophthalmol Vis Sci*. 2003;44:4651-9.doi: 10.1167/iovs.03-0538.
3. Stalhammar G. Delays between Uveal Melanoma Diagnosis and Treatment Increase the Risk of Metastatic Death. *Ophthalmology*. 2024;131:1094-104.doi: 10.1016/j.ophtha.2023.11.021.
4. Jaarsma-Coes MG, Ferreira TA, Marinkovic M, Vu THK, van Vught L, van Haren GR, et al. Comparison of Magnetic Resonance Imaging-Based and Conventional Measurements for Proton Beam Therapy of Uveal Melanoma. *Ophthalmol Retina*. 2023;7:178-88.doi: 10.1016/j.oret.2022.06.019.
5. Wulff J, Koska B, Ahmad Khalil D, Richter R, Maximilian Backer C, Baumer C, et al. Uncertainties in ocular proton planning and their impact on required margins. *Phys Med*. 2024;121:103358.doi: 10.1016/j.ejmp.2024.103358.
6. Jaarsma-Coes MG, Klaassen L, Verbist BM, Vu THK, Klaver YLB, Rodrigues MF, et al. Inter-Observer Variability in MR-Based Target Volume Delineation of Uveal Melanoma. *Adv Radiat Oncol*. 2023;8:101149.doi: 10.1016/j.adro.2022.101149.
7. Klaassen L, Jaarsma-Coes MG, Verbist BM, Vu THK, Marinkovic M, Rasch CRN, et al. Automatic Three-Dimensional Magnetic Resonance-based measurements of tumour prominence and basal diameter for treatment planning of uveal melanoma. *Phys Imaging Radiat Oncol*. 2022;24:102-10.doi: 10.1016/j.phro.2022.11.001.
8. Klaassen L, vd Steeg-Henzen, C.; Lengkeek, T.; Plug, G.P.; Bakker, P.A.C.; Vu, T.H.K.; Marinkovic, M.; Luyten, G.P.M.; Verbist, B.M.; Rasch, C.R.N.; Beenakker, J.W.M. Changes in tumour volume before and during ocular proton beam therapy. *ESTRO 2024*.
9. Klaassen L, Haasjes C, Hol M, Cambraia Lopes P, Spruijt K, van de Steeg-Henzen C, et al. Geometrical accuracy of magnetic resonance imaging for ocular proton therapy planning. *Phys Imaging Radiat Oncol*. 2024;31:100598.doi: 10.1016/j.phro.2024.100598.
10. Klaassen LR, C.R.N.; Beenakker, J.W.M. Comparison of model-based and delineation-based target volume definition for ocular proton therapy. Submitted to *Physica Medica*.
11. Hrbacek J, Kacperek A, Beenakker JM, Mortimer L, Denker A, Mazal A, et al. PTCOG Ocular Statement: Expert Summary of Current Practices and Future Developments in Ocular Proton Therapy. *Int J Radiat Oncol Biol Phys*. 2024;120:1307-25.doi: 10.1016/j.ijrobp.2024.06.017.
12. Bjorkman D, Via R, Lomax A, De Prado M, Baroni G, Weber DC, et al. The effect of intra- and inter-fractional motion on target coverage and margins in proton therapy for uveal melanoma. *Phys Med Biol*. 2024;69.doi: 10.1088/1361-6560/ad8297.
13. Haasjes C, Vu THK, Beenakker JM. Patient-specific mapping of fundus photographs to three-dimensional ocular imaging. *Med Phys*. 2025;52:2330-9.doi: 10.1002/mp.17576.
14. Hol M, Spruijt KH, Rodrigues MF, Klaver YLB, Kouwenberg J, Bakker PAC, et al. Accuracy of day-to-day patient positioning in ocular proton therapy with a dedicated beamline. *PLoS One*. 2025;20:e0333294.doi: 10.1371/journal.pone.0333294.
15. Hol M.; Astreinidou, E.; Klaassen, L.; Marinkovic, M.; Vu, T.H.K.; Rasch, C.R.N.; Beenakker, J.W.M. Clipless positioning for ocular proton therapy. Abstract for PTCOG 2026; Deauville.
16. CCMO: overview of medical research in the Netherlands. Clipless Positioning for Ocular Proton Therapy [Available from: <https://www.onderzoekmetmensen.nl/en/trial/57781>].

17. van der Burgh BJH, M.; Klaassen, L.; Astreimidou, E.; Rasch, C.R.N.; Herder, J.L.; Beenakker, J.W.M. Multi-posture head immobilization for ocular proton therapy. Submitted to Applied Clinical Medical Physics.
18. ICRP. Adult Reference Computational Phantoms. ICRP Publication 110. . 2009.
19. Jonas RA, Wang YX, Yang H, Li JJ, Xu L, Panda-Jonas S, et al. Optic Disc-Fovea Distance, Axial Length and Parapapillary Zones. The Beijing Eye Study 2011. PLoS One. 2015;10:e0138701.doi: 10.1371/journal.pone.0138701.
20. Wulff J, Koska B, Heufelder J, Janson M, Backer CM, Siregar H, et al. Commissioning and validation of a novel commercial TPS for ocular proton therapy. Med Phys. 2023;50:365-79.doi: 10.1002/mp.16006.
21. Polishchuk AL, Mishra KK, Weinberg V, Daftari IK, Nguyen JM, Cole TB, et al. Temporal Evolution and Dose-Volume Histogram Predictors of Visual Acuity After Proton Beam Radiation Therapy of Uveal Melanoma. Int J Radiat Oncol Biol Phys. 2017;97:91-7.doi: 10.1016/j.ijrobp.2016.09.019.
22. Thariat J, Grange JD, Mosci C, Rosier L, Maschi C, Lanza F, et al. Visual Outcomes of Parapapillary Uveal Melanomas Following Proton Beam Therapy. Int J Radiat Oncol Biol Phys. 2016;95:328-35.doi: 10.1016/j.ijrobp.2015.12.011.
23. Dobler B, Bendl R. Precise modelling of the eye for proton therapy of intra-ocular tumours. Phys Med Biol. 2002;47:593-613.doi: 10.1088/0031-9155/47/4/304.
24. Qi H, Hu L, Huang S, Lee YP, Chen Q, Yu F, et al. Proton Therapy for Uveal Melanoma on a Pencil Beam Scanning Gantry. Adv Radiat Oncol. 2025;10:101782.doi: 10.1016/j.adro.2025.101782.
25. Regmi R, Maes D, Nevitt A, Toltz A, Leuro E, Chen J, et al. Treatment of ocular tumors through a novel applicator on a conventional proton pencil beam scanning beamline. Sci Rep. 2022;12:4648.doi: 10.1038/s41598-022-08440-5.
26. Chou CY, Huang HC, Lee SH, Hsu SM. Dosimetric evaluation and clinical application of collimated apertures with proton beam line scanning in stereotactic radiotherapy. J Appl Clin Med Phys. 2025;26:e70128.doi: 10.1002/acm2.70128.
27. Hrbacek J, Mishra KK, Kacperek A, Dendale R, Nauraye C, Auger M, et al. Practice Patterns Analysis of Ocular Proton Therapy Centers: The International OPTIC Survey. Int J Radiat Oncol Biol Phys. 2016;95:336-43.doi: 10.1016/j.ijrobp.2016.01.040.
28. Lane AM, Oxenreiter MM, Hashmi M, Aronow ME, Trofimov AV, Shih HA, et al. A Comparison of Treatment Outcomes after Standard Dose (70 Gy) versus Reduced Dose (50 Gy) Proton Radiation in Patients with Uveal Melanoma. Ophthalmol Retina. 2022;6:1089-97.doi: 10.1016/j.oret.2022.05.006.
29. Gragoudas ES, Lane AM, Regan S, Li W, Judge HE, Munzenrider JE, et al. A randomized controlled trial of varying radiation doses in the treatment of choroidal melanoma. Arch Ophthalmol. 2000;118:773-8.doi: 10.1001/archophth.118.6.773.
30. Thariat J, Mathis T, Pace-Loscos T, Peyrichon ML, Maschi C, Rosier L, et al. Single-Masked Randomized Phase 2 Study Assessing 2 Forms of Hypofractionated Proton Therapy in Patients With Large Choroidal Melanomas. Int J Radiat Oncol Biol Phys. 2023;117:357-69. doi: 10.1016/j.ijrobp.2023.04.028.
31. Anchouche S, Liu J, Zaguia F, Nassrallah G, Deschenes J. Quality of life considerations in uveal melanoma patients: a systematic review. Can J Ophthalmol. 2020;55:413-23. doi: 10.1016/j.jcjo.2020.05.010.
32. Tang MCY, Ferreira TA, Marinkovic M, Jaarsma-Coes MG, Klaassen L, Vu THK, et al. MR-based follow-up after brachytherapy and proton beam therapy in uveal melanoma. Neuroradiology. 2023;65:1271-85.doi: 10.1007/s00234-023-03166-1.

33. Klaassen L, Jaarsma-Coes MG, Marinkovic M, Luyten GPM, Rasch CRN, Ferreira TA, et al. Quantitative Perfusion-Weighted Magnetic Resonance Imaging in Uveal Melanoma. *Invest Ophthalmol Vis Sci.* 2024;65:17.doi: 10.1167/iops.65.11.17.
34. Janssen P, Ferreira TA, Vu THK, Beenakker JWM, Klaassen L. Reproducibility of perfusion-weighted and diffusion-weighted MR imaging in patients with ocular tumours. Submitted to *Ocular Oncology & Pathology*.
35. Bindewald-Wittich A, Swenshon T, Carasco E, Dreyhaupt J, Willerding GD. Blue-Light Fundus Autofluorescence Imaging following Ruthenium-106 Brachytherapy for Choroidal Melanoma. *Ophthalmologica.* 2020;243:303-15.doi: 10.1159/000504715.
36. Rantala ES, Hernberg M, Kivela TT. Overall survival after treatment for metastatic uveal melanoma: a systematic review and meta-analysis. *Melanoma Res.* 2019;29:561-8.doi: 10.1097/CMR.0000000000000575.
37. Hassel JC, Piperno-Neumann S, Rutkowski P, Baurain JF, Schlaak M, Butler MO, et al. Three-Year Overall Survival with Tebentafusp in Metastatic Uveal Melanoma. *N Engl J Med.* 2023;389:2256-66.doi: 10.1056/NEJMoa2304753.
38. Nathan P, Hassel JC, Rutkowski P, Baurain JF, Butler MO, Schlaak M, et al. Overall Survival Benefit with Tebentafusp in Metastatic Uveal Melanoma. *N Engl J Med.* 2021;385:1196-206.doi: 10.1056/NEJMoa2103485.
39. EORTC EOfRaToC-. Adjuvant Tebentafusp in High Risk Ocular Melanoma (ATOM) 2025 [06-09-2025]. Available from: <https://clinicaltrials.gov/study/NCT06246149>.
40. Klaassen L, Ferreira TA, Luyten G, Beenakker JM. Estimating uveal melanoma volume with ellipsoid tumour models. *Acta Ophthalmol.* 2025;103:691-8.doi: 10.1111/aos.17492.



Appendix

PORTFOLIO

LIST OF PUBLICATIONS

DANKWOORD

CURRICULUM VITAE

PORTFOLIO

The PhD trajectory – an overview

I started my PhD within the MReye group, a multidisciplinary research group within the C.J. Gorter MRI Center with strong connections to the Ophthalmology and Radiology departments, after completing my master's thesis there as well. Building on that foundation, I first continued with a project comparing ultrasound and MRI measurements. One of my early goals was to implement the automatic measurement methods developed for this project into clinical software. Although implementation turned out not to be feasible due to limitations in the clinically used software packages, it was an important learning experience. I gained a better understanding of how different disciplines approach these measurements and how valuable a multidisciplinary perspective is when developing clinically relevant tools.

In parallel, I set up and managed a registration study for ocular proton therapy patients at the LUMC. This was a non-WMO study, where each patient is asked for permission to use their clinical data for research purposes. For three years, I maintained this database and coordinated data retrieval from collaborating centres. This experience helped me develop organizational skills and an understanding of the practical aspects of clinical research. Around the same time, I improved an existing DCE-MRI analysis method developed by a colleague and applied it to a large retrospective cohort of uveal melanoma patients, both before and after treatment. Later, I applied the same methods in collaboration with another researcher, reinforcing my expertise in quantitative imaging analysis and data interpretation.

During the course of my PhD, I also temporarily took over a study on uveal melanoma delineation on MRI during a colleague's leave, which broadened my understanding of the role of 3D imaging in radiation oncology. Together with the same colleague, I shared the first authorship of a review paper about the use of MRI in ocular oncology. In addition, I developed a phantom to verify the accuracy of the MRI scans we used, which resulted in a publication. I also coordinated a clinical study originally designed to take place before the COVID-19 pandemic, for which I wrote the amendment and served as the coordinating researcher.

As my PhD progressed, I wanted to become more critical in my scientific reasoning. To practice this skill, I initiated a journal club in the MReye research group. I also reviewed journal manuscripts and carried out a comparative analysis in response to a published paper, investigating different methods for estimating ocular tumor volume.

These activities helped me grow as an independent researcher and improved my ability to evaluate scientific work.

In the later years of my PhD, several new collaborations developed through the clipless ocular proton therapy project. I worked closely with PhD candidates from Radiotherapy, TU Delft, and Erasmus MC, for example during a feasibility study with healthy volunteers at TU Delft, and in setting up a new clinical study on clipless patient positioning. I also believe that a positive and connected research environment is key to good science. To contribute to this, I organized group activities, such as a visit to the MuZIEum, and participated in the annual Eye Fund Walk & Ride, where we raised funds for ophthalmic research through an 80-km bike ride. Furthermore, together with one of the ophthalmologists, I lead a closed-door session for the PhD students of the ophthalmology department.

At the start of my PhD, I was often involved in scanning patients as part of clinical care, especially since the ocular MRI program was still in development. I regularly attended multidisciplinary meetings between ophthalmology, radiotherapy, and radiology, which gave me valuable insight into clinical decision-making and the link between imaging and treatment. After about three years, I moved into a combined role as a part-time PhD candidate and part-time clinical technologist in ocular proton therapy at HollandPTC. This combination of research and clinical work proved very rewarding: the experience of working directly with patients gave me new insights for my research, while my research background allowed me to contribute to patient care from both a clinical and technical perspective.

Throughout my PhD, I have been active in teaching and student supervision. I led tutorial groups for the Clinical Technology program and supervised six bachelor's and master's students from various backgrounds, including (medical) physics, (technical) medicine, and Medical Imaging & Radiation Oncology. One of these student projects led to a paper, which was recently submitted. In my final year, I also joined the supervision team of a new PhD candidate and took part in several recruitment procedures.

Beyond my direct research work, I was a part of several committees. I served for multiple years in the Quality Committee of the Dutch Society of Technical Medicine (NVvTG), including two years as chair. In addition, I contributed to Communication Committee of the C.J. Gorter MRI Center. I also co-organized a cycling event between the radiology research groups of the AmsterdamUMC, UMCU and LUMC. In my free time, triathlon kept me busy, ranging from an olympic distance in the first year of my PhD to a full Ironman in the final months.

CREDIT TABLE

CRediT table for the thesis of Lisa Klaassen

Ch.	Type*	Short Title	Conceptualization	Data Curation	Formal Analysis	Funding Acquisition	Investigation	Methodology	Project Administration	Resources	Software	Supervision	Validation	Visualization	Writing – Original Draft	Writing – Review & Editing	Preregistered	Preprinted	Published with Peer Review
1	Introduction	Introduction	█														<input type="checkbox"/>	<input type="checkbox"/>	<input type="checkbox"/>
2	Collaboration chapter	MRI in UM - systematic review		█	█												<input type="checkbox"/>	<input checked="" type="checkbox"/>	<input checked="" type="checkbox"/>
3	PhD project chapter	Geometrical accuracy of ocular MRI	█	█	█		█	█									<input type="checkbox"/>	<input checked="" type="checkbox"/>	<input checked="" type="checkbox"/>
4	PhD project chapter	Automatic 3D measurements of UM	█	█	█		█	█		█	█			█			<input type="checkbox"/>	<input checked="" type="checkbox"/>	<input checked="" type="checkbox"/>
5	PhD project chapter	Model-based & delineation-based GTV	█	█	█		█	█			█						<input type="checkbox"/>	<input type="checkbox"/>	<input type="checkbox"/>
6	PhD project chapter	Estimating UM volume	█	█	█		█	█									<input type="checkbox"/>	<input checked="" type="checkbox"/>	<input checked="" type="checkbox"/>
7	PhD project chapter	Quantitative PWI in UM	█	█	█		█	█			█						<input type="checkbox"/>	<input checked="" type="checkbox"/>	<input checked="" type="checkbox"/>
8	Collaboration chapter	PWI & DWI reproducibility in UM	█	█	█		█	█				█					<input type="checkbox"/>	<input type="checkbox"/>	<input type="checkbox"/>
9	Discussion	Discussion	█											█	█		<input type="checkbox"/>	<input type="checkbox"/>	<input type="checkbox"/>

*PhD project chapters are the direct result of the PhD project of the PhD candidate. Some theses also include Collaboration Chapters, to which the PhD candidate has contributed but fall outside the PhD project.

DISSEMINATION TABLE

Jaarsma-Coes MG, <u>Klaassen L</u> , Marinkovic M, Luyten GPM, Vu THK, Ferreira TA, Beenakker JWM. Magnetic Resonance Imaging in the Clinical Care for Uveal Melanoma Patients-A Systematic Review from an Ophthalmic Perspective. Cancers (Basel). 2023 May 30;15(11):2995. doi: 10.3390/cancers15112995.	
<i>Shared first authorship</i>	
Chapter in this thesis	2
Publication in peer reviewed journal	doi: 10.3390/cancers15112995.
<u>Klaassen L</u> , Haasjes C, Hol M, Cambraia Lopes P, Spruijt K, van de Steeg-Henzen C, Vu K, Bakker P, Rasch C, Verbist B, Beenakker JWM. Geometrical accuracy of magnetic resonance imaging for ocular proton therapy planning. Phys Imaging Radiat Oncol. 2024 Jun 12;31:100598. doi: 10.1016/j.phro.2024.100598.	
Chapter in this thesis	3
Publication in peer reviewed journal	doi: 10.1016/j.phro.2024.100598.
Conference contributions	Abstract submitted and presented at PTCOG
<u>Klaassen L</u> , Jaarsma-Coes MG, Verbist BM, Vu THK, Marinkovic M, Rasch CRN, Luyten GPM, Beenakker JWM. Automatic Three-Dimensional Magnetic Resonance-based measurements of tumour prominence and basal diameter for treatment planning of uveal melanoma. Phys Imaging Radiat Oncol. 2022 Nov 7;24:102-110. doi: 10.1016/j.phro.2022.11.001.	
Chapter in this thesis	4
Publication in peer reviewed journal	doi: 10.1016/j.phro.2022.11.001.
Open code	https://github.com/MREYE-LUMC/OPT_tumourmodels
Conference contributions	Abstract submitted and presented at several conferences: EVER, ISMRM, ISMRM Benelux, NOG, ESTRO, ISOO

<u>Klaassen L</u> , Rasch CRN, Beenakker JWM. Comparing model-based and MR-based target volume definition for ocular proton beam therapy planning . Submitted to Physica Medica.	
Chapter in this thesis	5
Open code	https://github.com/MREYE-LUMC/OPT_tumourmodels
<u>Klaassen L</u> , Ferreira TA, Luyten G, Beenakker JWM. Estimating uveal melanoma volume with ellipsoid tumour models . Acta Ophthalmol. 2025 Sep;103(6):691-698. doi: 10.1111/aos.17492.	
Chapter in this thesis	6
Publication in peer reviewed journal	doi: 10.1111/aos.17492.
Conference contributions	Abstract submitted and presented at OOG conference
<u>Klaassen L</u> , Jaarsma-Coes MG, Marinkovic M, Luyten GPM, Rasch CRN, Ferreira TA, Beenakker JWM. Quantitative Perfusion-Weighted Magnetic Resonance Imaging in Uveal Melanoma . Invest Ophthalmol Vis Sci. 2024 Sep 3;65(11):17. doi: 10.1167/iovs.65.11.17.	
Chapter in this thesis	7
Publication in peer reviewed journal	doi: 10.1167/iovs.65.11.17.
Other forms of dissemination	Abstract submitted and presented at several conferences: OOG, NOG
Janssen PAM, Ferreira TA, Vu THK, Beenakker JWM, <u>Klaassen L</u> . Reproducibility of perfusion-weighted and diffusion-weighted MRI in Uveal Melanoma . Submitted to the Journal of Magnetic Resonance Imaging.	
Chapter in this thesis	8

Overview of completed courses and other training

Mandatory activities		
Year	Title	Hours
2021	Leiden University Onboarding Programme	5
2021	Basic Methods and Reasoning in Biostatistics	42

2022	Renewal Basiscursus Regelgeving en en Organisatie voor Klinisch Onderzoekers (BROK)	5
2022	Workshop Scientific Conduct for PhDs	5
Transferable skill courses		
2022	Academic Writing for PhDs	56
2023	Job Orientation course	12

Other scientific activities related to this thesis

Year	Description	Linked to chapter
2021	Poster presentation at EVER	4
	Digital poster at ISMRM	4
	Presentation at ISMRM Benelux	4
	Presentation at NOG	4
2022	Mini-oral and poster pitch at ESTRO	4*
	Two online power pitches at ISMRM	4*
	Poster at ISMRM Benelux	4*
	Two poster presentations at ISOO	4*
	Presentation at NOG	-
2023	Poster at PTCOG	3
	Poster at HollandPTC symposium	3
	Presentation at LUMC Cancer Research Day	7
	Presentation at OOG	7
	Presentation at NOG	7
2024	Poster at ESTRO	9
	Presentation at PTCOG-OPTIC	9
	Presentation at NOG	9
2025	Presentation at OOG	6

* One abstract presented at conferences in 2022 does not appear as a chapter in this thesis.

LIST OF PUBLICATIONS

Automatic Three-Dimensional Magnetic Resonance-based measurements of tumour prominence and basal diameter for treatment planning of uveal melanoma. **Klaassen L**, Jaarsma-Coes MG, Verbist BM, Vu THK, Marinkovic M, Rasch CRN, Luyten GPM, Beenakker JM. *Phys Imaging Radiat Oncol*. 2022 Nov 7;24:102-110. doi: 10.1016/j.phro.2022.11.001.

Inter-Observer Variability in MR-Based Target Volume Delineation of Uveal Melanoma. Jaarsma-Coes MG, **Klaassen L**, Verbist BM, Vu THK, Klaver YLB, Rodrigues MF, Nabarro C, Luyten GPM, Rasch CRN, van Herk M, Beenakker JM. *Adv Radiat Oncol*. 2022 Dec 24;8(3):101149. doi: 10.1016/j.adro.2022.101149.

Magnetic Resonance Imaging in the Clinical Care for Uveal Melanoma Patients-A Systematic Review from an Ophthalmic Perspective. Jaarsma-Coes MG, **Klaassen L**, Marinkovic M, Luyten GPM, Vu THK, Ferreira TA, Beenakker JM. *Cancers*. 2023 May 30;15(11):2995. doi: 10.3390/cancers15112995.

MR-based follow-up after brachytherapy and proton beam therapy in uveal melanoma. Tang MCY, Ferreira TA, Marinkovic M, Jaarsma-Coes MG, **Klaassen L**, Vu THK, Creutzberg CL, Rodrigues MF, Horeweg N, Klaver YLB, Rasch CRN, Luyten GPM, Beenakker JM. *Neuroradiology*. 2023 Aug;65(8):1271-1285. doi: 10.1007/s00234-023-03166-1. Epub 2023 May 30.

Geometrical accuracy of magnetic resonance imaging for ocular proton therapy planning. **Klaassen L**, Haasjes C, Hol M, Cambraia Lopes P, Spruijt K, van de Steeg-Henzen C, Vu K, Bakker P, Rasch C, Verbist B, Beenakker JW. *Phys Imaging Radiat Oncol*. 2024 Jun 12;31:100598. doi: 10.1016/j.phro.2024.100598.

Quantitative Perfusion-Weighted Magnetic Resonance Imaging in Uveal Melanoma. **Klaassen L**, Jaarsma-Coes MG, Marinkovic M, Luyten GPM, Rasch CRN, Ferreira TA, Beenakker JM. *Invest Ophthalmol Vis Sci*. 2024 Sep 3;65(11):17. doi: 10.1167/iovs.65.11.17.

Evaluation of MRI Safety of Ru-106 Eye Applicators. Tang MCY, **Klaassen L**, Marinkovic M, Vu THK, Luyten GPM, Creutzberg CL, Ketelaars M, Beenakker JM. *Ocul Oncol Pathol*. 2025 Apr;11(1):13-20. doi: 10.1159/000542712.

Estimating uveal melanoma volume with ellipsoid tumour models. **Klaassen L**, Ferreira TA, Luyten G, Beenakker JM. *Acta Ophthalmol*. 2025 Apr 3. doi: 10.1111/aos.17492.

DANKWOORD

Het is bijzonder om werk te hebben dat je uitdaagt, waar je energie van krijgt, en waarvan je het idee hebt dat het iets zou kunnen bijdragen aan de wereld. Daarbij is onderzoek doen een teamsport: in zowel de leuke als lastige momenten heb ik me altijd ontzettend gesteund gevoeld door collega's, vrienden en familie.

Tijdens mijn promotietraject heb ik geluk gehad met hele fijne supervisors. Allereerst Jan-Willem, dank je wel voor je vertrouwen, voor je humor en dat je altijd oog hebt voor de mens achter de werknemer. Ik kijk uit naar het voortzetten van onze samenwerking in de toekomst, en naar meer gesprekken over fietsen. Coen, dank voor je kritische blik. Jouw vragen dagen me uit om uit te zoomen en om scherper te formuleren. Professor Luyten, dank voor de bereidheid om mee te denken en voor het vertrouwen.

Onderdeel zijn van de MReye groep is een voorrecht. Ik geniet en heb genoten van de samenwerking met zowel huidige als voormalige collega's – en van alle inside jokes. Myriam, Luc, Kevin, Lennart, Corné, Martijn, Iris, Nadine, Anna Lisa en alle studenten die ik heb mogen begeleiden: bedankt voor de gezelligheid, de fun facts, de podcasts en de inspiratie. Daarnaast dank ik de leden van het cliploos project, onder andere Eleftheria, Bas, Mike en Ad, voor de fijne samenwerking.

Het C.J. Gorter MRI Center is een onderzoeksgroep met slimme en gezellige mensen (en een heleboel taart). In het bijzonder bedank ik mijn lieve (oud-)kamergenoten: Yiming, dank je wel voor de gezelligheid en de gastvrijheid tijdens de office dinners. Bea: jouw warmte en positiviteit zijn uniek. Rosanne: ik kijk met plezier terug op onze wandelingen naar de hertjes en de oliebollenkraam, en ben blij dat ik bij jou altijd even kan komen zeuren.

Ik heb ontzettend veel geleerd van het bijwonen van MDO's en spreekuren op de oogheelkunde. Heel veel dank aan Marina, Khanh, Jaco en Danial voor jullie betrokkenheid en jullie bereidheid om uitleg te geven. Daarnaast heb ik het contact met de verpleegkundigen oogoncologie (Joke, Susanne en Laura) als heel fijn ervaren, dank jullie wel! In het begin van mijn PhD heb ik veel tijd doorgebracht op K37 om de oogmelanoompatiënten te leren scannen. Daarom wil ik ook de MRI-laboranten in het LUMC bedanken. Kritisch naar die beelden kijken, leerde ik onder andere van Teresa Ferreira en Berit Verbist. Dank jullie wel voor de fijne samenwerking.

Ik heb het geluk niet één, maar twee werkplekken te hebben. Tijdens mijn PhD kwam ik in HollandPTC eerst aanraking met de MBB'ers MRI en de klinisch fysici voor de

MRPBT-studie en het geometrical accuracy-paper. Dat de samenwerking fijn was, blijkt wel uit het feit dat ik daarna graag meer tijd in HollandPTC wilde doorbrengen. Al mijn collega's bij HollandPTC bedank ik voor het vertrouwen – in mij persoonlijk, maar ook in de klinisch technoloog als zorgprofessional. De oog-MBB'ers (Paul, Carina, Eline, Leon, Mariëlle, Nienke en Dewy) wil ik daarnaast bedanken de fijne sfeer op de ooglijn. De radiotherapeuten, in het bijzonder Pauline en Michiel, dank ik voor de wijze woorden en alles wat ik van hen heb mogen leren.

Daarnaast wil ik mijn vrienden en familie bedanken. Beldie, Suus, Aniek, Marjolein, Romy, Renée, Eline, Fleur, Sybren, Derek, Bart: dank jullie wel voor alle peptalks, steun, avonturen en gezelligheid. Niels en Dagmar, pap en mam: jullie hebben al mijn dromen altijd gesteund met ongelofelijk veel enthousiasme. Dank jullie wel.

Als laatste gaat mijn dank uit naar de patiënten die ik tijdens het onderzoek of in een klinische setting heb mogen ontmoeten. Jullie veerkracht, humor en bereidheid om mee te doen aan wetenschappelijk onderzoek om de behandeling voor toekomstige patiënten te verbeteren, motiveren mij dagelijks.

CURRICULUM VITAE

Lisa Klaassen was born in Almelo on August 21st, 1996. After completing her secondary education (VWO) cum laude in 2014, she moved to Delft to study Clinical Technology, a joint bachelor's programme of Delft University of Technology, Leiden University Medical Center and Erasmus Medical Center. After her bachelor's degree, she continued with the master's programme in Technical Medicine, specializing in Imaging & Interventions. Fascinated by medical imaging and radiation oncology, she completed several internships at HollandPTC, LUMC, and Erasmus MC.

After having completed her master thesis internship in the MReye research group at the LUMC, she got the opportunity to pursue a PhD within the same group. Under supervision of dr. Jan-Willem Beenakker, and with the support of prof. dr. Gré Luyten and prof. dr. Coen Rasch, she was able to combine her interests in imaging and radiation oncology and apply it to ocular tumours within a highly multidisciplinary environment. The research performed during this period resulted in this thesis. During her PhD, Lisa joined the quality committee of the Dutch Society for Technical Medicine and contributed to the communication committee of the C.J. Gorter MRI Center. She always thoroughly enjoyed interacting with patients, and from April 2024, she got the opportunity to combine her research position with a part-time clinical position at HollandPTC.

After completion of this thesis, she will continue to combine research and patient care as a postdoctoral researcher at LUMC and clinical technologist at HollandPTC, aiming to keep improving clinical care for uveal melanoma patients.

